ORDRE n° 42470

THÈSE

Présentée à

l'Université de Lille – Sciences et Technologies
(Ecole Doctorale des Sciences de la Matière, du Rayonnement et de l'Environnement)

Pour l'obtention du grade de

Docteur
(Discipline ; Molécules et Matière Condensée)

Par

Hiroki NAGASHIMA

Development and application of through-bond and through-space correlation NMR experiments between spin-1/2 and quadrupolar nuclei in crystalline and amorphous solids
(Développement et applications d'expériences RMN de corrélation, à travers les liaisons et l'espace, entre noyaux de spin-1/2 et quadripolaires dans les solides cristallins et amorphes)

Soutenance prévue le 7 Novembre 2017

Composition du Jury :

Directeur de Thèse :
Olivier Lafon, Professeur, Université de Lille-Sciences et Technologies, UCCS
François Méar, Maître de Conférences, Université de Lille-Sciences et Technologies, UCCS
Frédérique Pourpoint, Maître de Conférences, École Nationale Supérieure de Chimie de Lille, UCCS

Rapporteurs :
Dominique Massiot, Directeur de Recherche, CNRS, CEMHTI
Christel Gervais, Professeur, Université Pierre et Marie Curie, LCMCP

Examinateurs :
Lionel Montagne, Professeur, Université de Lille-Sciences et Technologies, UCCS
Annie Pradel, Directrice de Recherche, CNRS, ICGM
Jonathan Yates, Professor, University of Oxford, department of materials

Acknowledgement

At first, I would like to express my gratitude to all supervisors. Prof. Olivier Lafon provided me the opportunity to be PhD student in his group and provided me a nice environment, good insight into NMR theory and great new ideas for the SS-NMR study. His passion and ability to understand the physics for the SS-NMR always encouraged me to do my best. Thanks to Dr. François Méar for the advices from chemical point of view and kind support of my PhD in thin film NMR. Thanks to Dr. Frédérique Pourpoint for her support of the experiment, the presentation, the article and the advices.

I would like to thank other menbers of group. Thanks to Dr. Julien Trébosc for guiding me SS-NMR experiment, processing and simulation and giving me great new ideas for my study. His skills and knowledges are greatest in the SS-NMR field. I learned many SS-NMR techniques from him. Thanks to Prof. Jean-Paul Amoureux for help in writing the articles and giving me the new idea and the advices. Thanks to Prof. Lionel Montagne for giving me many advices and suggestions from chemical point of view in the thin film NMR project. Thank to Dr. Laurent Delevoye for the coordination of 'NMR and inorganic material' group.

I acknowledge all members of the defense committee: Prof. Dominique Massiot, Prof. Christel Gervais, Prof. Annie Pradel, and Prof. Jonathan Yates for evaluating my thesis in spite of their busy schedule.

The DNP NMR experimental studies would not be possible without the support from Dr. Torsten Gutmann and Dr. Aany Sofy Lilly Thankamony in Darmstadt, Dr. Fabien Aussenac and Patrick Dorffer in Wissembourg, Dr. Sachin Rama Chaudhari in Lyon, Dr. Nicolas.Birlirakis, Dr. Diego Carnevale and Dr. Mathieu Baudin in Paris. Also, the simulation study for DNP, ^{14}N overtone and adiabatic SFAM would not be possible without the support from Prof. Ilya Kuprov, Dr. Frédéric Mentink-Vigier, Dr. Zhehong Gan and Dr. Gwendal Kervern. I would like to thank NMR facility staff in Lille: Dr. Xavier Trivelli, Dr. Bertrand Revel, Dr. Bertrand.Doumert, Dr. Gregory Tricot and Dr. Marc Bria for their support.

I would like to thank my colleagues: Dr. Baudouin Dillmann, Dr. Ming Shen, Dr. Yixuan Li, Dr. Thibault Carlier, Dr. Denys Grekov, Raynald Giovine, Pauline.Glatz, Kadiali.Bodiang and Pereira Luiz for their help and good atmosphere in the lab. Thanks to Luc Noureux, Alison Mclellan and Shantanu Lanke for the opportunity of the SS-NMR teaching.

I would like to thank Robert and Hiromi ADANT for the support of life in France.

Finally, I would like to special thank my parents and my wife for encouraging and trust me for my challenges.

Contents

Abstract

My PhD thesis focuses on the development of the through-bond and through-space correlation solid state NMR experiments involving half-integer quadrupolar nuclei in order to characterize chemical structure of inorganic material at atomic level. This thesis consists of two part.

First, we introduce two-dimensional (2D) ^{71}Ga-^{77}Se through-bond and through-space heteronuclear correlation (HETCOR) experiments. Such correlations are achieved using (i) the *J*-mediated Refocused Insensitive Nuclei Enhanced by Polarization Transfer (*J*-RINEPT) method with ^{71}Ga excitation and ^{77}Se Carr-Purcell-Meiboon-Gill (CPMG) detection, as well as (ii) the *J*- or dipolar-mediated Heteronuclear Multiple-Quantum Correlation (*J*- or *D*-HMQC) schemes with ^{71}Ga excitation and quadrupolar CPMG (QCPMG) detection. These methods are applied to the crystalline β-Ga_2Se_3 and the $0.2Ga_2Se_3$-$0.8GeSe_2$ glass. We also report 2D ^{71}Ga Satellite Transition Magic-Angle Spinning (STMAS) spectrum of β-Ga_2Se_3 using QCPMG detection at high magnetic field, high Magic-Angle Spinning frequency, and high rf-field.

Second, we introduce novel sequences using indirect detection to correlate quadrupolar nuclei and spin-1/2 isotopes, other than ^{1}H and ^{19}F. These sequences use γ-encoded symmetry-based RN_n^v schemes that reintroduce the space component $|m| = 1$ of the heteronuclear dipolar coupling. These schemes can be applied to the indirectly detected spin in Dipolar-mediated Heteronuclear Multiple-Quantum Correlation (*D*-HMQC) sequence or to the detected isotope in a novel sequence, named Dipolar-mediated Heteronuclear Universal-Quantum Correlation (*D*-HUQC). The performance of the sequences have been compared to conventional *D*-HMQC with R^3 and SFAM recoupling via SIMPSON simulations and NMR experiments, including ^{13}C-{^{15}N} heteronuclear correlation on glycine and ^{31}P-^{27}Al ones on VPI-5 and $Na_7(AlP_2O_7)_4PO_4$.

Chapter 1: General introduction

This thesis focuses on the heteronuclear correlation NMR experiments involving half-integer quadrupolar nuclei. Hence, chapter 1 summarizes the important tool, concept and the state of the art in this field. The section 1.1 introduces the basic principles of solid-state NMR experiments. The section 1.2 describes the property of quadrupolar nuclei. The section 1.3 and 1.4 summarizes sensitivity enhancement and high resolution methodology for quadrupolar nuclei. The section 1.5 describes the heteronuclear dipolar recoupling sequence applied to single channel in HETCOR sequence. The section 1.6 is the review of 2D HETCOR experiments between spin-1/2 and half-integer quadrupolar nuclei.

1.1. Theoretical basis

A brief description of the theoretical basis of solid-state NMR spectroscopy is provided here. More detailed description can be found in the references [1-5]. The dynamics of nuclear spins during NMR experiments is described by the Liouville-von Neuman equation:

$$\frac{d}{dt}\hat{\rho}(t) = -i[\hat{H}(t), \hat{\rho}(t)] \tag{1.1}$$

where $\hat{\rho}(t)$ and $\hat{H}(t)$ represent the density operator and the Hamiltonian, respectively. The formal solution of the time evolution of the density operator can be recast in Hilbert space as follow

$$\hat{\rho}(t) = \hat{U}(t)\hat{\rho}(0)\hat{U}^{\dagger}(t) \tag{1.2}$$

with

$$\hat{U}(t) = \hat{T}e^{-\mathrm{i}\int_0^t \hat{H}(t)dt} \tag{1.3}$$

where $\hat{U}(t)$ is called propagator, and $\hat{T}$ is the Dyson time-ordering operator. Signal detection can be performed as

$$S(t) = \langle \hat{Q} \rangle(t) = Tr\{\hat{\rho}(t)\hat{Q}\} \tag{1.4}$$

The Hamiltonian consists of external and internal terms

$$\hat{H}(t) = \hat{H}_{ext} + \hat{H}_{int} \tag{1.5}$$

where the first term represents external interactions, including Zeeman and radiofrequency (rf) interaction, while the second one contains internal parts of the nuclear spin Hamiltonian. In the laboratory (LAB) frame, the external Hamiltonian takes the form

$$\hat{H}_{ext} = \hat{H}_0 + \hat{H}_1(t) = \omega_0\hat{I}_z + 2\omega_1\cos(\omega_{\mathrm{ref}}t + \phi)\hat{I}_z \tag{1.6}$$

with $\omega_1 = -\gamma B_1$, ω_{ref} and ϕ denoting the rf nutation angular frequency, the angular carrier frequency and phase of the rf-field, respectively, and B_1 the rf field amplitude and γ the gyromagnetic ratio.

The internal components of the Hamiltonian may conveniently be expressed in an irreducible tensor representation

$$\hat{H}_{int} = \sum_{\lambda} \hat{H}_{\lambda} \; ; \qquad \hat{H}_{\lambda} = C^{\lambda} \sum_{j=0}^{2} \sum_{m=-j}^{j} (-1)^m \left[A_{j,-m}^{\lambda}\right]^{L} \hat{T}_{j,m}^{\lambda} \tag{1.7}$$

where $A_{j,m}^{\lambda}$ and $\hat{T}_{j,m}^{\lambda}$ represents spatial and spin dependencies, respectively, and C^{λ} is a fundamental interaction dependent constant. j describe the rank of the tensor, while the superscript L designate that the description applies in LAB frame.

The analytical procedure of NMR experiments is as follows:

(i) Transformation into an appropriate interaction frame,

(ii) The calculation of the effective Hamiltonian,

(iii) The calculation of the response of the initial density operator to the effective Hamiltonian

We need to introduce the concept of the rotations, average Hamiltonian (AH) and interaction frame to carry out those analytical calculations.

1.1.1. Rotations

Rotation of spin operators in cyclic 3D subspace

Assume that $\hat{\rho}(0) = \hat{A}$, $H(t) = \omega(t)\hat{B}$, and the operator $\hat{A}$, $\hat{B}$, and $\hat{C}$ is cyclic commutative ($[\hat{A}, \hat{B}] = i\hat{C}$, $[\hat{B}, \hat{C}] = i\hat{A}$, $[\hat{C}, \hat{A}] = i\hat{B}$), the time-evolution of the density operator is given by

$$\hat{\rho}(t) = e^{-i\phi\hat{B}}\hat{A}e^{i\omega\phi\hat{B}} = \cos(\phi)\hat{A} - \sin(\phi)i\left[\hat{B}, \hat{A}\right] = \cos(\phi)\hat{A} - \sin(\phi)\hat{C} \tag{1.8}$$

where $\phi = \int_0^t \omega(t)dt$ (e.g., $\phi = \omega_1 t$ for constant amplitude rf irradiation). The important things is to calculate the commutator $\left[\hat{B}, \hat{A}\right]$. If the commutator can be calculated easily (for instance, typical sets of non-commuting operators are $\{\hat{I}_x, \hat{I}_y, \hat{I}_z\}$, $\{\hat{I}_x, 2\hat{I}_y\hat{S}_z, 2\hat{I}_z\hat{S}_z\}$, $\{2\hat{I}_x\hat{S}_z, \hat{I}_y, 2\hat{I}_z\hat{S}_z\}$), this representation is preferable.

Rotation of irreducible spherical tensor operators

In irreducible spherical tensor representation, operator T of rank-j transforms as

$$\left[\hat{T}_{j,m}^{\lambda}\right]^{F2} = \sum_{m'=-j}^{j} \left[\hat{T}_{j,m'}^{\lambda}\right]^{F1} D_{m',m}^{(j)}(\Omega) \tag{1.9}$$

where $D^{(j)}$ is a rank-j Wigner rotation matrix and $\Omega = \{\alpha, \beta, \gamma\}$ is the Euler angles separating the two frames F1 and F2. We consider here positive angles referring to counter-clockwise rotations, with the Wigner rotation being: a rotation by α around the original *z*-axis, rotation by β around the new *y*-axis, and finally rotation by γ around resulting *z*-axis. The Wigner matrix may be conveniently expressed in terms of reduced Wigner matrix ($d^{(j)}$) elements

$$D^{(j)}_{m',m}(\Omega) = e^{-im'\alpha} d^{(j)}_{m',m}(\beta) e^{-im\gamma} \tag{1.10}$$

First and second rank reduced Wigner matrix elements are given in **Table.1.1**.

Table 1.1. Reduced Wigner matrix elements $d^{(j)}_{m',m}(\beta)$ for j = 1, 2

j	$m' \backslash m$	-2	-1	0	1	2
1	-1		$\frac{1}{2}(1+c_\beta)$	$\frac{1}{\sqrt{2}}s_\beta$	$\frac{1}{2}(1-c_\beta)$	
	0		$-\frac{1}{\sqrt{2}}s_\beta$	c_β	$\frac{1}{\sqrt{2}}s_\beta$	
	1		$\frac{1}{2}(1-c_\beta)$	$-\frac{1}{\sqrt{2}}s_\beta$	$\frac{1}{2}(1+c_\beta)$	
2	-2	$\frac{1}{4}(1+c_\beta)^2$	$\frac{1}{2}(1+c_\beta)s_\beta$	$\sqrt{3/8}\,s_\beta^2$	$\frac{1}{2}(1-c_\beta)s_\beta$	$\frac{1}{4}(1-c_\beta)^2$
	-1	$-\frac{1}{2}(1+c_\beta)s_\beta$	$c_\beta^2-\frac{1}{2}(1-c_\beta)$	$\sqrt{3/8}\,s_{2\beta}$	$\frac{1}{2}(1+c_\beta)-c_\beta^2$	$\frac{1}{2}(1-c_\beta)s_\beta$
	0	$\sqrt{3/8}\,s_\beta^2$	$-\sqrt{3/8}\,s_{2\beta}$	$\frac{1}{2}(3c_\beta^2-1)$	$\sqrt{3/8}s_{2\beta}$	$\sqrt{3/8}\,s_\beta^2$
	1	$-\frac{1}{2}(1-c_\beta)s_\beta$	$\frac{1}{2}(1+c_\beta)-c_\beta^2$	$-\sqrt{3/8}\,s_{2\beta}$	$c_\beta^2-\frac{1}{2}(1-c_\beta)$	$\frac{1}{2}(1+c_\beta)s_\beta$
	2	$\frac{1}{4}(1-c_\beta)^2$	$-\frac{1}{2}(1-c_\beta)s_\beta$	$\sqrt{3/8}\,s_\beta^2$	$-\frac{1}{2}(1+c_\beta)s_\beta$	$\frac{1}{4}(1+c_\beta)^2$

* s_β and c_β stand for $\sin\beta$ and $\cos\beta$

1.1.2. Effective Hamiltonian

In NMR theory, most Hamiltonian is time dependent. It is effective to obtain time independent Hamiltonian by approximation methods in order to calculate density operator. Typical approximative expression of the Hamiltonian series is as follow.

$$\hat{H}_{eff}(t) = \bar{\hat{H}}^{(1)} + \bar{\hat{H}}^{(2)} + \ldots \tag{1.11}$$

There are some approximation procedure to drive this effective Hamiltonian. Most popular approximation theory is average Hamiltonian theory (AHT) [3,4] and Floquet theory.[6] AHT treatment is sufficient in this thesis. Advantage of Floquet theory is in the situation of asynchronous condition. In AHT, lowest order terms are defined as

$$\bar{\hat{H}}^{(1)} = \frac{1}{\tau_c}\int_0^{\tau_c} \hat{H}(t')dt' \tag{1.12}$$

$$\bar{\bar{H}}^{(2)} = \frac{1}{i\tau_c}\int_0^{\tau_c} dt^{"} \int_0^{t^{"}} \left[\hat{H}(t^{"}), \hat{H}(t')\right] dt' \tag{1.13}$$

where τ_c denoting the period over which the averaging is performed. This simple expansion and later variants have proven extremely useful for simplifying the description of NMR experiments, for example, using a first-order approximation of the Hamiltonian in an interaction frame parameterizing out the dependency on rf-fields.

1.1.3. Interaction frame

In the analysis of NMR experiments, it is useful to transform to interaction frame when considering only the effect of the interesting internal parts of the Hamiltonian, which truly affects the spin dynamics. Frequently, Zeeman interaction itself complicates the contribution of internal Hamiltonian to the evolution of the density operator. The transformation to the frame of Zeeman interaction permits to simplify the calculation of the evolution of the density operator. A typical Hamiltonian in NMR consists of large terms, such as Zeeman interaction and small ones, such as chemical shift, dipolar coupling and quadrupolar coupling etc. as follow.

$$\hat{H}(t) = \hat{H}_{big}(t) + \hat{H}_{small}(t) \tag{1.14}$$

Here, if we only want to discuss the effect of $\hat{H}_{small}$ on the spin system, we decompose the propagator into $\hat{U}(t) = \hat{U}_{big}(t)\tilde{\hat{U}}(t)$ and then by manipulating the density operator and Hamiltonian with $\hat{U}_{big}$ as follows.

$$\tilde{\hat{\rho}}(t) = \hat{U}_{big}^{\dagger}\hat{\rho}(t)\hat{U}_{big} \tag{1.15}$$

$$\tilde{\hat{H}}(t) = \hat{U}_{big}^{\dagger}\hat{H}(t)\hat{U}_{big} - i\hat{U}_{big}^{\dagger}\frac{d}{dt}\hat{U}_{big}(t) = \tilde{\hat{H}}_{small}(t) \tag{1.16}$$

H_{big} can be removed and converted to interaction frame. Eq.(1.15) and (1.16) fulfill the Liouville-von Neuman equation $\frac{d}{dt}\tilde{\hat{\rho}}(t) = -i[\tilde{\hat{H}}(t), \tilde{\hat{\rho}}(t)]$. In the thesis, the interaction frame symbol "~" is abbreviated from below.

Truncated Hamiltonian in high magnetic field can be derived from combination of AHT and Zeeman interaction frame:

$$\overline{\hat{H}_{\lambda}}^{(1)} = C^{\lambda}\left\{\left[A_{0,0}^{\lambda}\right]^{L}\hat{T}_{0,0}^{\lambda} + \left[A_{2,0}^{\lambda}\right]^{L}\hat{T}_{2,0}^{\lambda}\right\} \tag{1.17}$$

Thus, all components with $m \neq 0$ vanish in a first-order approximation and only the terms which commute with $\hat{I}_z$ are remained. Truncated Hamiltonians of all internal interaction are given in **Table.1.2** and **1.3.**

Table.1.2. Construction of Truncated Hamiltonian [5]

λ	C^{λ}	$\left[A_{0,0}^{\lambda}\right]^{L}$	$\hat{T}_{0,0}^{\lambda}$	$\hat{H}_{\lambda}^{iso}$	$\left[A_{2,0}^{\lambda}\right]^{L}$	$\left[\hat{T}_{2,0}^{\lambda}\right]^{L}$	$\hat{H}_{\lambda}^{aniso}$
CS	$-\gamma_I$	$-\sqrt{3}\delta_{iso}$	$-\frac{1}{\sqrt{3}}B_0\hat{I}_z$	$\delta_{iso}\omega_0\hat{I}_z$	$\left[A_{2,0}^{CS}\right]^{L}$	$-\sqrt{\frac{2}{3}}B_0\hat{I}_z$	$\sqrt{\frac{2}{3}}\omega_{CSA}\hat{I}_z$
D_{II}	1				$\left[A_{2,0}^{D,II}\right]^{L}$	$\frac{1}{\sqrt{6}}\left(3\hat{I}_z^j\hat{I}_z^k-\hat{I}^j\cdot\hat{I}^k\right)$	$\omega_{D,II}\left(3\hat{I}_z^j\hat{I}_z^k-\hat{I}^j\cdot\hat{I}^k\right)$
D_{IS}	1				$\left[A_{2,0}^{D,IS}\right]^{L}$	$\sqrt{\frac{2}{3}}\hat{I}_z\hat{S}_z$	$\omega_{D,IS}\,2\hat{I}_z\hat{S}_z$
J_{II}	1	$-2\pi\sqrt{3}J_{II}^{iso}$	$-\frac{1}{\sqrt{3}}\hat{I}^j\cdot\hat{I}^k$	$2\pi J_{II}^{iso}\hat{I}^j\cdot\hat{I}^k$	$\left[A_{2,0}^{J,II}\right]^{L}$	$\frac{1}{\sqrt{6}}\left(3\hat{I}_z^j\hat{I}_z^k-\hat{I}^j\cdot\hat{I}^k\right)$	$\omega_{J,II}^{aniso}\left(3\hat{I}_z^j\hat{I}_z^k-\hat{I}^j\cdot\hat{I}^k\right)$
J_{IS}	1	$-2\pi\sqrt{3}J_{IS}^{iso}$	$-\frac{1}{\sqrt{3}}\hat{I}\cdot\hat{S}$	$2\pi J_{IS}^{iso}\hat{I}\cdot\hat{S}$	$\left[A_{2,0}^{J,IS}\right]^{L}$	$\sqrt{\frac{2}{3}}\hat{I}_z\hat{S}_z$	$\omega_{J,IS}^{aniso}\,\hat{I}_z\hat{S}_z$
Q *(1st)*	$\frac{2\pi C_Q}{2I(2I-1}$				$\left[A_{2,0}^{Q}\right]^{L}$	$\frac{1}{\sqrt{6}}\left(3\hat{I}_z^2-I(I+1)\right)$	$\frac{\omega_Q}{3\sqrt{6}}\left[A_{2,0}^{Q}\right]^{L}\left(3\hat{I}_z^2-I(I+1)\right)$

Table.1.3. Second rank spatial tensor in the principal axis system [5]

λ	$\left[A_{2,0}^{\lambda}\right]^{P}$	$\left[A_{2,\pm1}^{\lambda}\right]^{P}$	$\left[A_{2,\pm2}^{\lambda}\right]^{P}$
CS	$\sqrt{\frac{3}{2}}\delta_{aniso}$	0	$-\frac{1}{2}\eta\delta_{aniso}$
D_{II}	$\sqrt{6}\,b_{II}$	0	0
D_{IS}	$\sqrt{6}\,b_{IS}$	0	0
J_{II}	$2\pi\sqrt{\frac{3}{2}}J_{II}^{aniso}$	0	$-\frac{1}{2}\eta\,J_{II}^{aniso}$
J_{IS}	$2\pi\sqrt{\frac{3}{2}}J_{IS}^{aniso}$	0	$-\frac{1}{2}\eta\,J_{IS}^{aniso}$
Q *(1st order)*	$\sqrt{\frac{3}{2}}$	0	$-\frac{1}{2}\eta_Q$

* Second rank spatial tensor in LAB frame, $\left[A_{2,0}^{\lambda}\right]^{L}$ is defined as $\left[A_{2,0}^{\lambda}\right]^{L}=\sum_{m=-2}^{2}\left[A_{2,m}^{\lambda}\right]^{P}D_{m,0}^{(2)}(\Omega_{PL})$ in the case of static condition . $\left[A_{2,m}^{\lambda}\right]^{P}$ with $m=0,\pm1,\pm2$ is necessary in order to obtain $\left[A_{2,0}^{\lambda}\right]^{L}$. The anisotropies of the spatial tensors (e.g., δ_{aniso} and J_{II}^{aniso}) are defined as $A_{aniso}=[A_{zz}]^{P}-A_{iso}$ with $A_{iso}=1/3\left([A_{xx}]^{P}+\left[A_{yy}\right]^{P}+[A_{zz}]^{P}\right)$. The asymmetry parameter is defined by $\eta=\left(\left[A_{yy}^{\lambda}\right]^{P}-\left[A_{xx}^{\lambda}\right]^{P}\right)/\left(\left[A_{zz}^{\lambda}\right]^{P}-A_{iso}\right)$. The dipolar coupling constatnts are defined by $b_{II}=-\left(\frac{\gamma_I^2}{r^3}\right)\frac{\mu_0\hbar}{4\pi}$ and $b_{IS}=-\left(\frac{\gamma_I\gamma_S}{r^3}\right)\frac{\mu_0\hbar}{4\pi}$ in rads^{-1} where $\mu_0=4\pi\cdot10^{7}$ NC^{-2}s^{2} is the permeability of a vacuum, γ is gyromagnetic ratio, r is the internuclear distance. $C_Q=(e^2qQ)/h$ (see section. 1.2 in detail) with $h=6.62608\cdot10^{-34}$ Js is Planck's constant. $\hbar$ is Planck's constant divided by 2π.

1.1.4. Magic angle spinning

The sensitivity and resolution of NMR spectra of disordered solids may be improved significantly by rapidly rotating the sample about an axis at the "magic angle", $\beta_{RL} = \tan^{-1}\sqrt{2} \approx 54.74$, with respect to the static magnetic field (**Fig.1.1**). This technique is called magic-angle spinning (MAS). The spatial rotation of the sample causes the orientation-dependent anisotropic spin interactions to become time-dependent and to be averaged out in the case of rapid sample spinning.

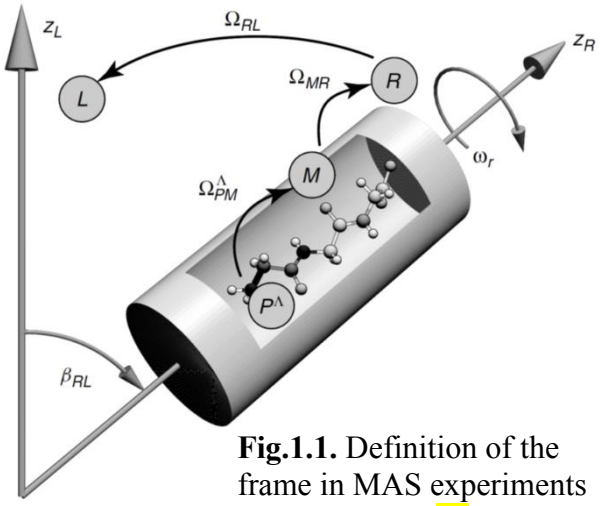

Fig.1.1. Definition of the frame in MAS experiments (adapted from [36])

Let us check how heteronuclear dipolar coupling is averaged out by MAS. The coefficient (including spatial part) of dipolar coupling is given by

$$\omega_{D,IS}(t) = \frac{1}{\sqrt{6}} C^{\lambda} \left[A^{DIS}_{2,0}\right]^{L} \tag{1.18}$$

In the static case of the powder sample, assuming Euler angle $\Omega_{PL} = \{\alpha_{PL}, \beta_{PL}, \gamma_{PL}\}$ between principal axis system (PAS) frame and LAB frame,

$$\omega_{D,IS} = \frac{1}{\sqrt{6}} C^{\lambda} \left[A^{DIS}_{2,0}\right]^{P} d^{(2)}_{0,0}(\beta_{PL}) = \frac{1}{2} b_{IS}(3\cos^2(\beta_{PL}) - 1) \tag{1.19}$$

where the constant and the spatial tensor in PAS frame is shown in **Table.1.2** and **1.3**. In static condition of the powder sample, $\omega_{D,IS}$ only depend on β_{PL} angle. $b_{IS} = -\left(\frac{\gamma_I \gamma_S}{r^3}\right)\frac{\mu_0}{4\pi}$ is the dipolar coupling constant in rads^{-1}.

In the spinning case, LAB frame is associated with PAS frame via rotor-fixed (ROTOR) frame. Euler angle is defined as $\Omega_{PR} = \{\alpha_{PR}, \beta_{PR}, \gamma_{PR}\}$, $\Omega_{PL} = \{\omega_R, \beta_{RL}, \gamma_{RL}\}$. $\omega_{D,IS}(t)$ under MAS is

$$\omega_{D,IS}(t) = \sum_{m=-2}^{2} \omega^{(m)}_{D,IS} e^{im\omega_R t} \tag{1.20}$$

with

$$\omega^{(m)}_{D,IS} = b_{IS} e^{im\gamma_{PR}} d^{(2)}_{0,-m}(\beta_{PR}) d^{(2)}_{-m,0}(\beta_{RL}) \tag{1.21}$$

In MAS case, $\omega_{D,IS}(t)$ depends on not only β_{PR} angle but also γ_{PR} angle unlike static case. Since γ_{RL} angle is related to the rotation around MAS axis, γ_{RL} angle is especially important in rotating solids. In MAS case, $\omega^{(m)}_{D,IS}$ for m = 0, ±1, ±2 are

$$\omega_{D,IS}^{(0)} = \frac{1}{4} b_{IS}(3\cos^2(\beta_{PR}) - 1)(3\cos^2(\beta_{RL}) - 1) = 0 \quad (1.22)$$

$$\omega_{D,IS}^{(\pm 1)} = -\frac{1}{2\sqrt{2}} b_{IS} \sin(2\beta_{PR})\, e^{\pm i\gamma_{PR}} \quad (1.23)$$

$$\omega_{D,IS}^{(\pm 2)} = \frac{1}{4} b_{IS} \sin^2(\beta_{PR})\, e^{\pm i2\gamma_{PR}} \quad (1.24)$$

Assuming sampling at rotor echo and magic angle $\beta_{RL} = \tan^{-1}\sqrt{2}$

$$\phi = \sum_{m=-2}^{2} \int_0^{n\tau_R} \omega_{D,IS}^{(m)} e^{im\omega_R t}\, dt = \omega_{D,IS}^{(0)} = 0 \quad (1.25)$$

Dipolar coupling is averaged out. As mentioned later, rotor synchronized t_1 acquisition in 2D experiments is necessary for averaging dipolar coupling, CSA and quadrupolar interaction (especially, first-order terms).

In infinite spinning case, by AHT treatment

$$\overline{\widehat{H}_{D,IS}}^{(1)} = \frac{\omega_R}{2\pi} \int_0^{\frac{2\pi}{\omega_R}} \widehat{H}_{D,IS}\, dt = \omega_{D,IS}^{(0)} 2\hat{I}_z \hat{S}_z = 0 \quad (1.26)$$

implying that the dipolar coupling does not affect the spin evolution. The above derivation is only valid for commuting dipolar interactions. However, in the case of non-commuting homonuclear dipolar interactions (homogeneous case), it is difficult to remove the dipolar coupling only by MAS. High resolution spectrum can be obtained by combination of MAS and decoupling sequence (which manipulate spin part in Hamiltonian).

1.1.5. Cross polarization

Cross polarization (CP) enhances the NMR signal of low-γ nuclei coupled through dipolar interaction with high-γ nuclei. The pulse sequence is shown in **Fig.1.2**. The cross polarization consists in

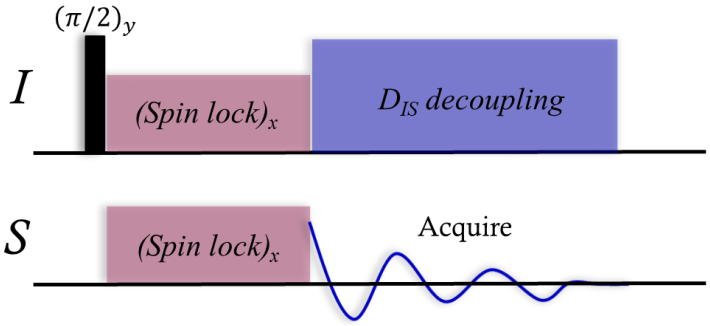

Fig.1.2 schematic diagram of the basic $I \rightarrow S$ cross polarization experiment.

(i) Generating transverse magnetization on the I channel by π/2 pulse and applying a rf-field $\omega_{1,I}$, sufficient to lock it.

(ii) Satisfying the Hartmann-Hahn (HH) matching condition with a suitable rf-field $\omega_{1,S}$.

(iii) Adjusting the contact time for which two rf-fields are applied. The optimal contact time depends on b_{IS}.

Under MAS, it is complicated task to understand HH matching condition at quantum mechanics level.[7] Heteronuclear dipolar recoupled AH under MAS is

0Q condition: $\omega_{1,I} - \omega_{1,S} = n\omega_R$

$$\overline{\widehat{H}_{D,IS}}^{(1)} = \frac{1}{4}\omega_{D,IS}^{|n|}\{\cos(\gamma_{PR})(\hat{I}_+\hat{S}_- + \hat{I}_-\hat{S}_+) \pm \sin(\gamma_{PR})(\hat{I}_+\hat{S}_- - \hat{I}_-\hat{S}_+)\} \quad (1.27)$$

2Q condition: $\omega_{1,I} + \omega_{1,S} = n\omega_R$

$$\overline{\widehat{H}_{D,IS}}^{(1)} = \frac{1}{4}\omega_{D,IS}^{|n|}\{\cos(|n|\gamma_{PR})(\hat{I}_+\hat{S}_+ + \hat{I}_-\hat{S}_-) \pm \sin(|n|\gamma_{PR})(\hat{I}_+\hat{S}_+ - \hat{I}_-\hat{S}_-)\} \quad (1.28)$$

with n = ±1, ±2 and

$$\omega_{D,IS}^{|n|=1} = -\frac{1}{2\sqrt{2}} b_{IS} \sin(2\beta_{PR}) \quad (1.29)$$

$$\omega_{D,IS}^{|n|=2} = \frac{1}{4} b_{IS} \sin^2(\beta_{PR}) \quad (1.30)$$

$\omega_{1,I} - \omega_{1,S} = n\omega_R$ condition is called zero quantum (0Q) matching because of flip-flop transition. $\omega_{1,I} + \omega_{1,S} = n\omega_R$ condition is called double quantum (2Q) matching because of flip-flip (or flop-flop) transition.

Hence, HH matching condition under MAS is summarized as follow.

$$\omega_{1,S} = \varepsilon\omega_{1,I} + n\omega_R \quad (\varepsilon = \pm 1; n = \pm 1, \pm 2) \quad (1.31)$$

From this results, in case of moderate spinning speed region (ν_R = 10 ~ 20 kHz) or large rf-amplitude, 0Q condition (ε = +1) can be chosen. On the other hand, in case of very high spinning speed or low rf-amplitude, 2Q condition (ε = –1) can be better than 0Q condition.

1.2. NMR of quadrupolar nuclei

1.2.1. Quadrupolar interaction

Around 75% of NMR-active nuclei are quadrupolar (i.e. have a spin quantum number I > 1/2).[8-12] A quadrupolar nucleus possesses an electric quadrupolar moment, eQ, which interacts with the electric field gradient (EFG) created by the charges (electrons, other nuclei). The EFG is defined by three components, V_{xx}, V_{yy} and V_{zz}, where $V_{zz} = eq$, in its principal axis system. This interaction between eQ and the EFG is generally described in terms of the quadrupolar coupling constant, $C_Q = e^2qQ/h$ and the asymmetry parameter, $\eta_Q = (V_{xx} - V_{yy})/V_{zz}$. The quadrupolar Hamiltonian in the LAB frame can be written as

$$\hat{H}_Q = \frac{\omega_Q}{3} \sum_{m=-2}^{2} (-1)^m \left[A^Q_{2,-m}\right]^L \hat{T}_{2,m} \tag{1.32}$$

with

$$\omega_Q = 2\pi \frac{3C_Q}{2I(2I-1)} \tag{1.33}$$

The quadrupolar Hamiltonian can then be approximated in the high field case using AHT and expressed with Clebsch-Gordan coefficients for second-order term. First- and second-order quadrupolar Hamiltonian under fast MAS speed are

$$\overline{\hat{H}_Q}^I = \frac{\omega_Q}{3\sqrt{6}} \left[A^Q_{2,0}\right]^R d^{(2)}_{0,0}(\beta_{RL}) \left(3\hat{I}_z^2 - I(I+1)\right) \tag{1.34}$$

$$\overline{\hat{H}_Q}^{II} = \frac{\omega_Q^2}{9\omega_0} \left(\left[B^Q_{0,0}\right]^R \hat{K}_0 + \left[B^Q_{2,0}\right]^R d^{(2)}_{0,0}(\beta_{RL}) \hat{K}_2 + \left[B^Q_{4,0}\right]^R d^{(2)}_{0,0}(\beta_{RL}) \hat{K}_4\right) \tag{1.35}$$

Where

$$\hat{K}_0 = \frac{1}{\sqrt{5}} \hat{I}_z \left(3\hat{I}_z^2 - I(I+1)\right), \qquad \hat{K}_2 = -\frac{1}{2\sqrt{14}} \hat{I}_z \left(12\hat{I}_z^2 - 8I(I+1) + 3\right),$$
$$\hat{K}_4 = -\frac{1}{2\sqrt{70}} \hat{I}_z \left(34\hat{I}_z^2 - 18I(I+1) + 5\right) \tag{1.36}$$

$$\left[B^Q_{l,0}\right]^R = \sum_{n=-m}^{m} \left[B^Q_{l,n}\right]^p D^{(2)}_{n,0}(\Omega_{PR}) \tag{1.37}$$

$$\left[B^Q_{0,0}\right]^p = \frac{3+\eta_Q^2}{2\sqrt{5}}, \quad \left[B^Q_{2,0}\right]^p = \frac{-3+\eta_Q^2}{\sqrt{14}}, \quad \left[B^Q_{2,\pm 2}\right]^p = \sqrt{\frac{3}{7}}\eta_Q,$$
$$\left[B^Q_{4,0}\right]^p = \frac{18+\eta_Q^2}{2\sqrt{70}}, \quad \left[B^Q_{4,\pm 2}\right]^p = \frac{3\eta_Q}{2\sqrt{7}}, \quad \left[B^Q_{4,\pm 4}\right]^p = \frac{\eta_Q^2}{4}, \tag{1.38}$$

Transition frequency between eigenstates $|s\rangle$ and $|r\rangle$ can be derived from

$$\omega_{p,q} = \omega_{s\to r} = \left\langle r\left|\overline{\hat{H}_Q}\right|r\right\rangle - \left\langle s\left|\overline{\hat{H}_Q}\right|s\right\rangle \tag{1.39}$$

It is convenient to express transition frequency in terms of $p = r - s$ (coherence order) and $q = r^2 - s^2$ (satellite order).[2]

For the first-order quadrupolar interaction, transition frequency is given by

$$\omega^I_{p,q} = q \frac{\omega_Q}{\sqrt{6}} \left[A^Q_{2,0}\right]^R d^{(2)}_{0,0}(\beta_{RL}) \tag{1.40}$$

For half-integer spins, 1Q Central Transition (CT: -1/2 ↔ 1/2) and symmetric Multiple Quantum (MQ: $-p/2 \leftrightarrow p/2$) coherence ($q = 0$) are not affected by the first-order term. On the other hand, the Satellite transitions (STs: $m-1 \leftrightarrow m$) ($q \neq 0$) are not strongly affected by the first-order quadrupolar interaction.

For the second-order quadrupolar interaction, transition frequency is given by

$$\omega_{p,q}^{II} = \omega_{p,q}^{(0)} + \omega_{p,q}^{(2)} + \omega_{p,q}^{(4)} \tag{1.41}$$

where

$$\omega_{p,q}^{(0)} = -p\frac{\left(1+\eta_Q^2/3\right)}{30}\frac{\left(\omega_Q\right)^2}{\omega_0}\left(I(I+1) - \frac{3}{4}\left(p^2 + 3\frac{q^2}{p^2}\right)\right) \tag{1.42}$$

$$\omega_{p,q}^{(2)} = C_2(\Omega_{PR})\left(3\left(p^2 + \frac{3q^2}{p^2}\right) - p(8I(I+1) - 3)\right)d_{0,0}^{(2)}(\beta_{RL}) \tag{1.43}$$

$$\omega_{p,q}^{(4)} = C_4(\Omega_{PR})\left(\frac{17}{2}\left(p^2 + \frac{3q^2}{p^2}\right) - p(18I(I+1) - 5)\right)d_{0,0}^{(4)}(\beta_{RL}) \tag{1.44}$$

with

$$C_2(\Omega_{PR}) = -\frac{1}{9}\frac{\omega_Q^2}{\omega_0}\frac{\left[B_{2,0}^Q\right]^R}{2\sqrt{14}} \tag{1.45}$$

$$C_4(\Omega_{PR}) = -\frac{1}{9}\frac{\omega_Q^2}{\omega_0}\frac{\left[B_{4,0}^Q\right]^R}{2\sqrt{70}} \tag{1.46}$$

$$d_{0,0}^{(4)}(\beta_{RL}) = \frac{1}{8}\left[35\cos^4(\beta_{RL}) - 30\cos^2(\beta_{RL}) + 3\right] \tag{1.47}$$

$\omega_{p,q}^{(0)}$ term is an isotropic quadrupolar-induced frequency which do not broaden the spectrum. $\omega_{p,q}^{(2)}$ and $\omega_{p,q}^{(4)}$ terms are anisotropic and broaden the CT spectrum of powder samples. Especially, $\omega_{p,q}^{(4)}$ term cannot be removed completely by MAS owing to $d_{0,0}^{(4)}(\beta_{RL})$. Second-order quadrupolar broadening is proportional to $1/\omega_0$. Hence, the use of high magnetic fields improves the spectral resolution. The energy level diagram of I = 3/2 is shown in **Fig.1.3**.

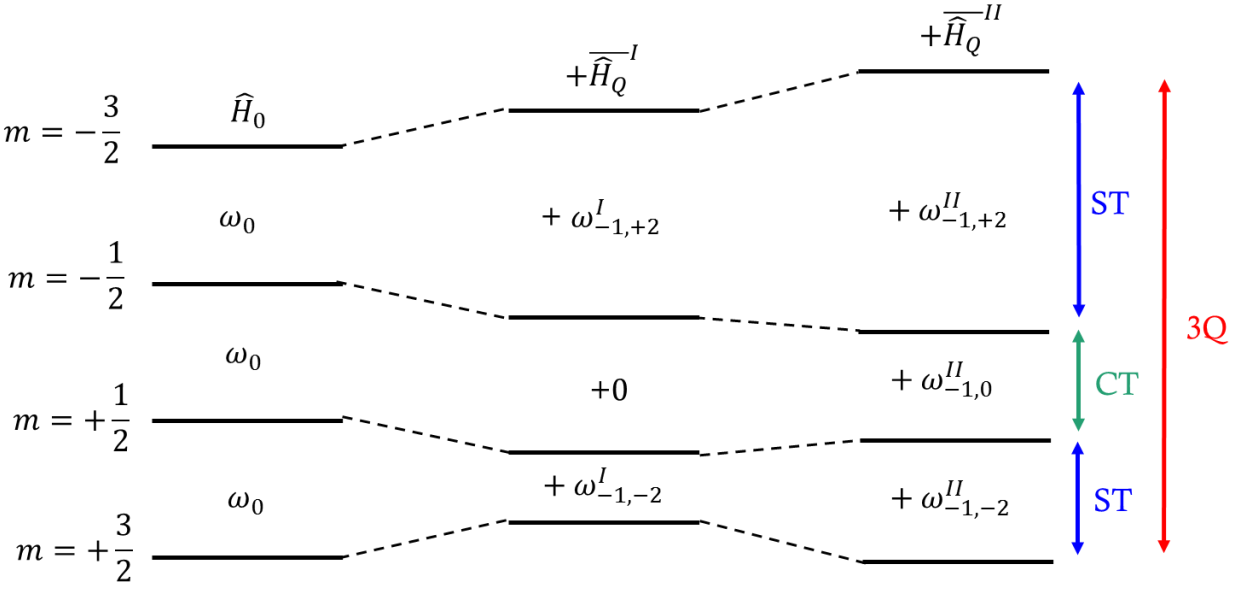

Fig.1.3 schematic energy level diagram of a nucleus with I = 3/2.

1.2.2. CT selective pulse

Another difficulty for quadrupolar nuclei is the manipulation of the magnetization using a rf-field since such field ranging from tens to hundreds kilohertz is typically weaker than the strength of the first-order quadrupolar interaction. In the limit case, where the rf-field is much smaller than the quadrupolar interaction, the CT is selectively excited and the general formula for rf nutation frequency is

$$\omega_{nut} = \left(I + \frac{1}{2}\right)\omega_1 \tag{1.48}$$

An additional result of selective excitation is that it reduces the intensity of the resulting central transition signal. If the signal following a non-selective pulse of length can be described by

$$S(\tau_p) = S_0 \sin(\omega_1 \tau_p) \tag{1.49}$$

then the signal following a CT selective pulse is

$$S(\tau_p) = \frac{S_0}{I + 1/2} \sin\left((I + 1/2)\omega_1 \tau_p\right) \tag{1.50}$$

The π/2 and π CT-selective pulses are employed in numerous pulse sequences described below. Therefore, setting up a spin echo experiment using π/2 and π CT-selective on a model sample or better on target sample is always useful.

1.2.3. Non selective pulse

The excitation pulses using larger rf-field yield more intense NMR signals than CT-selective ones. In general, the maximal possible rf-field remains smaller than or comparable to the strength of the quadrupolar interaction. In this intermediate regime, the spin dynamics of quadrupolar nuclei becomes complex and highly dependent on the strength of the quadrupolar interaction. These non-selective rf pulses are notably employed for the acquisition of 1D NMR spectra. Furthermore, for quantitative NMR spectra, the quadrupolar nuclei are excited by a single non-selective pulse producing small flip angle of the CT magnetization. Non-selective pulses are also employed to excite the STs as well as MQ transitions.

1.3. Sensitivity enhancement methodology for half-quadrupolar nuclei

1.3.1. Population transfer from satellite transitions

The intensity enhancement of the CT of half-integer spin quadrupolar nuclei can be achieved via a change of the populations of the various energy levels.[13] Two limit cases are by saturation or inversion of the ST populations. Simultaneous saturation of the STs equalizes the populations of all the lower and upper energy levels and enhances CT signal intensity by a

factor of (I +1/2). On the other hand, population inversion enhance CT signal intensity by a factor of 2I.

RAPT. In 1999, Madhu et al. used a phase-alternating pulse train (Fast Amplitude Modulation: FAM) to enhance MQ to 1Q coherence transfer in MQMAS experiment.[14] Yao et al. employed the same pulse train in 1D experiments to obtain enhancement and proposed Rotor Assisted Population Transfer (RAPT).[15] The RAPT pulse train with alternating phases creates sidebands generated from the carrier frequency, ν_{ref}, at frequency intervals of

$$\nu_{\phi} - \nu_{\mathrm{ref}} = (\Delta\phi/360°)\tau_{\mathrm{p}} \tag{1.51}$$

where ϕ is the phase increment between the pulses in degree and τ_p, which is equal to the sum of d_{RAPT} and P_{RAPT}, is the RAPT time in seconds shown in **Fig.1.4**.

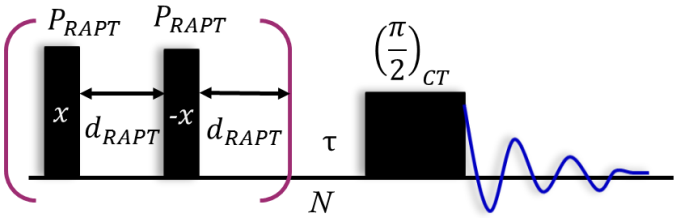

Fig.1.4. Schematic diagram of RAPT pulse sequence

Two parameters, the RAPT modulation frequency, $\nu_m = [2(d_{RAPT} + P_{RAPT})]^{-1}$, and the rf-amplitude are expected to have a greater influence on the signal enhancement. Yao et al. observed maximum enhancement (I +1/2) around $\nu_m = C_Q/4$ for I = 3/2 nucleus. [15]

DFS. Kentgens et al. proposed Double Frequency Sweep (DFS).[16] These pulses simultaneously sweep both the high- and low- frequency STs in a symmetric manner with the use of an amplitude-modulated pulse. A linear DFS is obtained if the rf-amplitude is varied smoothly from a start frequency (ω_s) to a final frequency (ω_f) in a cosinusoidal fashion as follows

$$\omega_1(t) = \omega_1^{max} \cos\left(\omega_s t - (\omega_s - \omega_f)\frac{t^2}{2\tau_p}\right) \tag{1.52}$$

where ω_1^{max} is the maximum rf-amplitude and τ_p is the length of the DFS pulse. This generates rf carrier sidebands which are swept over the STs. The carrier sidebands are swept smoothly over the STs which yields a more complete ST population inversion. When a powdered sample is spun rapidly at the magic angle, different crystallites will experience largely different sweep rates, as well as a different number of sweeps. Different crystallites will experience different enhancements ranging from 1 to 2I. The effect of the DFS, when applied to spinning samples, is generally to saturate the STs.

HS. Wasylishen and co-workers used hyperbolic secant (HS) inversion pulse to induce perfect inversion of spin population.[17] The pulse is smoothly turned on and off as the amplitude is modulated by a hyperbolic secant function, whereas the phase is modulated to induce a sweep with a hyperbolic tangent profile

$$\omega_1(t) = \omega_1^{max}\,\mathrm{sech}\left(\beta\left(\frac{2t}{\tau_\mathrm{p}} - 1\right)\right) \tag{1.53}$$

$$\phi(t) = \left(\frac{\lambda}{\beta}\right)\left(\frac{\tau_p}{2}\right) ln\left[\mathrm{sech}\left(\beta\left(\frac{2t}{\tau_\mathrm{p}} - 1\right)\right)\right] + \Delta\omega_\mathrm{ref}\, t \tag{1.54}$$

where the parameters λ and β are associated with the maximum frequency and truncation of the sech function, respectively. $\Delta\omega_\mathrm{ref}$ is a rf-offset. The amplitude may be further modulated with a cosine function so that the HS pulse affects both the high- and low-frequency STs.

Under MAS conditions, it was possible to approach the theoretical maximum enhancements expected for complete inversion of the STs in spinning samples. A key aspect of their breakthrough was that the largest enhancements were obtained if the HS sweep width equaled the spinning frequency such that only a single ST sideband was targeted. Generally, HS outperform RAPT and DFS under MAS condition.

1.3.2. (Q)CPMG acquisition

The CPMG (Carr-Purcell-Meiboom-Gill) experiment is a very common technique in NMR spectroscopy.[18] The CPMG experiment consists of a π pulses as in **Fig.1.4**, refocusing the signal during acquisition. The Fourier transformed spectrum is composed of a series of regularly spaced sharp peaks (spikelet). CPMG is most successful on samples with long T_2' relaxation times, as the signal can be refocused multiple times.

The CPMG experiment has been used to obtain signal enhancement for I = 1/2 nuclei as well as the measurement T_2' before being applied to quadrupolar nuclei.[19] CPMG experiments on quadrupolar nuclei are termed QCPMG, although the method is not fundamentally different from the conventional CPMG except for CT selective pulse.

The condition. Under MAS, the CPMG echo period (t_e) is chosen to be rotor synchronized as illustrated in **Fig.1.4**.

$$t_e = 2m\tau_R = t_\pi + t_a + 2de \tag{1.55}$$

with t_a is the one echo acquisition period, and *de* the dead time during which the Free-Induction Decay (FID) is not recorded. A factor of 2 in $t_\mathrm{e} = 2m\tau_\mathrm{R}$ is originated from the rotor synchronization of the period between π /2 pulse and π pulse. *NE* is a number of echoes which is set to acquire as many echoes as possible.

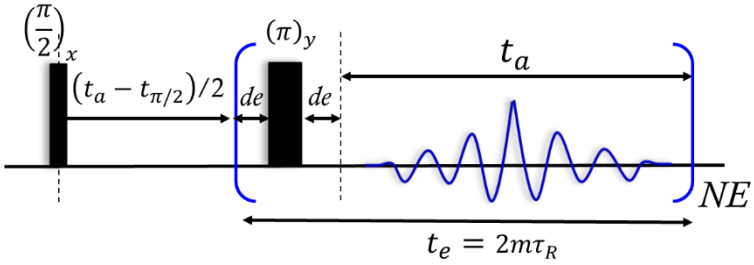

Fig.1.4 Schematic diagram of the CPMG pulse sequence

The resolution of CPMG spectrum is determined by the spikelet spacing, $1/(t_e)$, and the width of the spikelet is related to T_2'. There is also the option to add all of the echoes together to form a full-echo, and to recover the original lineshape instead of spikelets.

0Q coherence. If the refocusing pulse is not a perfect π pulse, some signal will be passed through 0Q coherence. This is so-called stimulated echoes. Modulation of the spikelet manifold arises due to the difference in time at which Hahn and stimulated echoes form. Hence, the severity of the spectral distortion is correlated to an increase in the magnitude of the 0Q coherences as the flip angle deviates from 180°. This 0Q coherence can be completely filtered by phase cycle (16 step phase cycle or PIETA method) after every π pulse keeping only the ±1Q coherences.[19,20] However, if filtration of 0Q coherence is carried out, the first echo remains completely unperturbed, while a significant loss of intensity is observed for subsequent echoes. Thus, the first echo is a pure Hahn echo, while subsequent echoes are a combination of Hahn and stimulated echoes, i.e., echoes which form due to coherence transfer pathways that pass through 0Q order. Moreover, 0Q coherence can result in slower decay rates since it depends on the spin-lattice relaxation T_1 which is larger than T_2' in solids. The amount of observable signal is therefore maximized by the use of a minimal phase cycling scheme.

Modified CPMG. The CPMG can refocus the anisotropic interaction such as CSA, second-order quadrupolar coupling and heteronuclear dipolar coupling. On the other hand, homonuclear dipolar coupling cannot be refocused by CPMG as Hahn echo and paramagnetic center affect T_2' to be short as known paramagnetic relaxation enhancement (PRE). Hence, T_2' will be shorter and the width of spikelets will be broadened in the presence of homonuclear dipolar couplings and paramagnetic substances. R. Siegel et al. proposed modified CPMG sequence in which π pulse is replaced into π/2 pulse except for first π pulse.[21] By this sequence, the property of homonuclear dipolar decoupling is more effective than regular CPMG and T_2' will be longer for non-dilute system without spectral distortion although second and third echo intensity of a modified CPMG is a less than that of regular CPMG. Consequently, Modified CPMG is 1.5 ~ 2 times efficient than regular CPMG in non-dilute system.[22]

However, utilizing CPMG is basically preferable for dilute spin system and non-paramagnetic system. This CPMG with minimal phase cycling have been combined with CP, PRESTO and MQMAS so far and significant sensitivity enhancement have been observed.

1.4. High resolution methodology for half-integer quadrupolar nuclei

A major issue with half-integer quadrupolar nuclei ($I > 1/2$) is that even under MAS, the second-order quadrupolar broadening is not completely eliminated. As a consequence, overlapping of resonances with distinct isotropic chemical shifts, δ_{iso}, often occurs and a simple determination of the number of sites in a compound is rendered difficult. In order to overcome this problem, a few research groups have proposed in the late 80s, two methods where the sample is rotated at two different angles either simultaneously (DOuble Rotation, DOR) [23] or sequentially (Dynamic Angle Spinning, DAS).[24] The set of angles are chosen to cancel both first and second-order terms of the quadrupolar interaction. Even if the development of DOR and DAS methods has been very important in the beginning of the 90s, their use is nowadays limited to rare applications due to the obvious technical challenge that is associated to them. From 1995 on, two 2D pulse sequences, the Multiple-Quantum MAS (MQMAS)[25] and the Satellite Transition MAS (STMAS)[26] have been proposed to cancel out the broadening due to the whole quadrupolar interaction.

1.4.1. MQMAS

MQMAS is designed to remove the second-order broadening of the CT transition in NMR spectra of half-integer spin quadrupolar nuclei (I >1/2). From Eq.(1.40), the contribution from the 1st order quadrupolar perturbation for the symmetric transition vanishes. We then only consider the second order effect. In Eq.(1.41 – 1.47), The $d^{(2)}_{0,0}(\beta_{RL})$ terms vanishes owing to MAS and isotropic part can be ignored since it does not contribute to phase dispersion and only induce an isotropic quadrupolar induced shift. Therefore, only the rank-4 term in Eq.(1.44) remains. In conventional MQMAS sequence, first rf pulse excites symmetrical MQ coherence ($-p/2 \leftrightarrow p/2$), which evolve during t_1 period, and then second rf pulse converts them to 1Q coherence which can be detected (**Fig.1.5**).

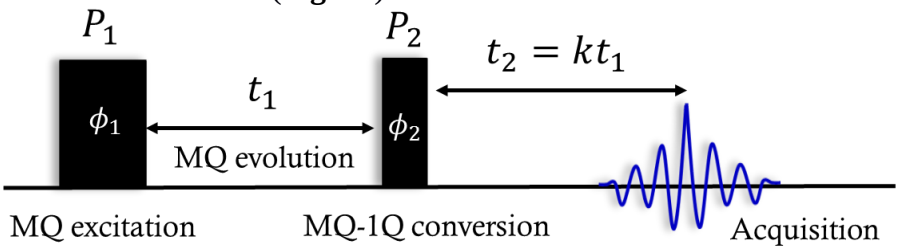

Fig.1.5. Schematic diagram of the original MQMAS experiment

The total evolution phase is given by

$$\Phi(t) = \omega^{(4)}_{p,0}(\beta_{RL})t_1 + \omega^{(4)}_{-1,0}(\beta_{RL})t_2 \qquad (1.56)$$

From this equation, the isotropic echo can be observed by satisfying following condition

$$t_2 = -\frac{\omega_{p,0}^{(4)}(\beta_{RL})}{\omega_{-1,0}^{(4)}(\beta_{RL})} t_1 = \frac{1}{9}\frac{p(-17p^2 + 36I(I+1) - 10)}{4I(I+1) - 3} = kt_1 \qquad (1.57)$$

Thus, rank-4 terms are cancelled out. The values *k* for various spin *I* is shown in **Table.1.4**.

Table.1.4. The value *k* for various half-integer quadrupolar spin.

$I \setminus p$	3	5	7	9
3/2	-7/9			
5/2	19/12	-25/12		
7/2	101/45	11/9	-161/45	
9/2	91/36	95/36	7/18	-31/6

MQMAS spectra are presented after a shearing transformation to obtain pure absorption 2D spectrum [27]. However, the original MQMAS sequence does not give pure absorption 2D spectra. In order to overcome this problem, some modified MQMAS sequences have been proposed.

Z filter method.[28] The z-filter approach was thus added to the original sequence in order to symmetrize the echo and anti-echo coherence transfer pathways. This method can be used on samples with both long and very short T_2'. It needs shearing.

Split-t_1 method.[29] The split-t_1 sequence divides the t_1 time between MQ and 1Q evolution periods in a proportion *k*, that avoids the post-acquisition shearing procedure. The disadvantage is that the shifted-echo type pulse sequences depend on the decay rate, $1/T_2'$, of transverse losses, which is not refocused by a CT-selective π pulse, and the z-filter should thus be preferred when facing short T_2' relaxation values

There are several approaches for sensitivity improvement approach.

3Q to 1Q conversion. The main disadvantage of the MQMAS method lies in its lack of sensitivity that suffers from a very inefficient conversion rate from 3Q to 1Q (or 0Q for the z-filter sequence) coherences. Therefore, several studies have been carried out to increase this conversion by modifying conversion pulse with FAM, DFS or HS. [30]

MQMAS-QCPMG. Another sensitivity improvement approach is to combine MQMAS with QCPMG detection. F.H.Larsen et al. introduced QCPMG acquisition into MQMAS experiment.[31] This represents the amplitude-modulated split-t_1 preparation for 3Q-QCPMG-MAS sequence with z filter applied to spin I = 3/2.

1.4.2. STMAS

The main limitation of MQMAS is its low sensitivity, which is due to the low efficiency in excitation and conversion of MQ transitions. STMAS 2D experiment, which correlates the 1Q ST and CT coherences, was proposed in 2000 by Gan as an alternative to MQMAS to obtain a high-resolution spectrum for half-integer quadrupolar nucleus, since ST excitation and conversion show superior efficiencies. Like MQMAS, the STMAS pulse sequence is based on a quadrupolar echo but with pulse conditions and phase cycling optimized to excite STs. Likewise, we assume the spin system at magic angle and ignore isotropic part. First rf pulse excite non-symmetrical ($m-1 \leftrightarrow m$) ST coherence, which evolve during t_1 period, and then second rf pulse converts them to 1Q coherence which can be detected. The total evolution phase is given by

$$\Phi(t) = \omega_{-1,q}^{(4)}(\beta_{RL})t_1 + \omega_{-1,0}^{(4)}(\beta_{RL})t_2 \tag{1.58}$$

From this equation, the isotropic echo can be observed by satisfying following condition

$$t_2 = -\frac{\omega_{-1,q}^{(4)}(\beta_{RL})}{\omega_{-1,0}^{(4)}(\beta_{RL})}t_1 = \frac{17}{3}\frac{q^2}{(4I(I+1)-3)} - 1 = k't_1 \tag{1.59}$$

Thus, rank-4 terms are cancelled out. The values *k'* for various spin *I* is represented in **Table.1.5.**

Table.1.5. The value *k'* for various half-integer quadrupolar spin

I \ *m*	3/2	5/2	7/2	9/2
3/2	-8/9			
5/2	7/24	-11/6		
7/2	28/45	-23/45	-12/5	
9/2	55/72	1/18	-9/8	-25/9

Disadvantage of STMAS.

(i) Since those STs are affected by the first-order quadrupolar interaction, the STMAS experiment is extremely sensitive to a precise setting of the magic angle. STs evolve during t_1 period and rotor-synchronization t_1 acquisition is mandatory to eliminate the first-order quadrupolar broadening of STs. The required precision is about 0.002–0.005°.

(ii) Even when taking all necessary precautions, STMAS spectra always contain an unwanted autocorrelation signal stemming from the CT evolution during t_1 and t_2 periods, which cannot be cancelled out by phase cycling. In order to avoid this problem, some approaches have been proposed so far.

DQF methods.[32] the transfer between 1Q and 2Q coherences is performed with an additional soft CT-selective π pulse just before 1Q conversion pulse, called Double Quantum Filter (DQF), which also inverts the CT magnetization (1Q ↔ −1Q), and does not affect outer satellite 1Q coherences of spin 5/2, 7/2, and 9/2. Since ±2Q is selected by phase cycle, CT-CT correlations are removed.

Split-t_1 method.[33] An additional soft CT-selective π pulse is placed on after $t_1 = n/9\tau_R$ evolution. The magnetization spends $1/9^{th}$ of the evolution time on ±1Q levels, and $8/9^{th}$ on ±2Q levels. Likewise, since ±2Q is selected by phase cycle, CT-CT correlations are removed. The post-acquisition shearing procedure is not needed for split-t_1 STMAS. Both DQF and split-t_1 have z filter duration after 1Q conversion pulse.

1.5. Heteronuclear dipolar recoupling

This thesis focuses on 2D HETCOR between spin-1/2 and half-integer quadrupolar nuclei. Under magic-angle spinning (MAS) for resolution purpose, these heteronuclear dipolar (D_{IS}) couplings between two isotopes *I* and *S* are averaged out and their exploitation requires the use of D_{IS} recoupling sequences. Here, we concentrate on recoupling schemes which can reintroduce dipolar interactions between spin-1/2 and quadrupolar nuclei. In that case, the D_{IS} recoupling must be achieved without the application of rf-field to the quadrupolar nucleus because of the intricate spin dynamics of quadrupolar nuclei in the presence of rf-field. An ideal D_{IS} recoupling method should have the following characteristics:

(i) The spin interactions other than the desired D_{IS} coupling must be suppressed from the average Hamiltonian (AH) or must have no influence on the time evolution of the density matrix; (these undesired interactions comprise homonuclear dipolar (D_{II}) coupling, D_{IS} coupling, isotropic chemical shift, chemical shift anisotropy (CSA), quadrupole interaction, and interaction between nuclei and unpaired electrons in the case of paramagnetic compounds);

(ii) The magnitude of the scaled recoupled D_{IS} coupling must be larger than the decay rate of the signal (due to effective T_2' or $T_{1\rho}$ under the recoupling if applied to the observed nucleus);

(iii) The employed rf-field in the D_{IS} recoupling must be compatible with the probe specifications;

(iv) The D_{IS} recoupling sequence must be robust to rf-inhomogeneities;

(v) The D_{IS} recoupling sequence must be robust to MAS frequency instabilities;

(vi) When the goal is to measure internuclear distances, the sampling frequency of the recoupling sequence must be faster than the signal dephasing produced by the recoupled dipolar interaction.

However, there is no ideal D_{IS} recoupling method possessing the properties (i) to (vi) and choice of the method thus depends on its application.

γ encoding in heteronuclear case. The property of D_{IS} recoupling methods depend on γ_{PR} Euler angle. The definition of γ encoding is that the norm of D_{IS} recoupled average Hamiltonian does not depend on γ_{PR} Euler angle.[34] This norm is equal to effective dipolar coupling ($\omega_{D,IS}$). The property regarding γ encoding is as follow.

(i) Non-γ encoding recoupling sequence is 25 % less efficient than γ encoding recoupling;

(ii) Dipolar oscillation of build-up curve of non-γ encoding is less pronounced, compared to γ encoding sequence;

(iii) γ encoding recoupling is more robust to MAS fluctuation, since γ encoding does not depend on γ_{PR} angle around MAS axis;

(iv) In case of D_{IS} recoupling, dipolar truncation effect $\left[\hat{H}_{(i)}, \hat{H}_{(j)}\right] \neq 0$ is linked to γ encoding. Non-γ encoded D_{IS} recoupled AH is formed by longitudinal-two-order-spin ($\hat{I}_z\hat{S}_z$). On the other hand, γ encoded D_{IS} recoupled AH contains 1Q terms which lead to dipolar truncation.

(v) Also, γ encoded D_{IS} recoupled AH does not commute with CSA recoupled AH. This lead to detrimental effect on the efficiency. On the other hand, non-γ encoded D_{IS} recoupling sequence is not affected by CSA since D_{IS} recouped AH commute with CSA recoupled AH.

For instance, as already described in Eq.(1.27-1.30), CP is γ-encoded recoupling and dipolar truncated although CP is not a single channel recoupling. In the following, frequently used single channel D_{IS} recoupling sequences are presented.

1.5.1. R^3

Rotary-Resonance Recoupling (R^3) [34, 35] consists in the rf irradiation of a single-spin system, the spin-1/2 here, with a rf-amplitude equal to a multiple (q = 1, 2) of the MAS frequency. The q = 1 condition recouples both D_{IS} coupling and D_{II} while the q = 2 recouples only D_{IS} coupling. Therefore, the latter condition must be used in the presence of a strong D_{II} coupling.

Under MAS, assuming rf irradiation of single channel $\omega_1\hat{S}_x$ and *S* spin subject to CSA and D_{IS} coupling with *I* spin, first order AH is

$$\begin{aligned}\overline{\widehat{H}}^{(1)} = &\frac{1}{2}\left(\omega_{CSA,S}^{(-q)} + \omega_{CSA,S}^{(q)}\right)\hat{S}_z - \frac{i}{2}\left(\omega_{CSA,S}^{(-q)} - \omega_{CSA,S}^{(q)}\right)\hat{S}_y \\ &+ \left(\omega_{D,IS}^{(-q)} + \omega_{D,IS}^{(q)}\right)\hat{I}_z\hat{S}_z - i\left(\omega_{D,IS}^{(-q)} - \omega_{D,IS}^{(q)}\right)\hat{I}_z\hat{S}_y + (\omega_1 - q\omega_R)\hat{S}_x\end{aligned} \tag{1.60}$$

where $\omega_{CSA,S}^{(\pm q)}$ and $\omega_{D,IS}^{(\pm q)}$ are the complex amplitudes of the Hamiltonian. If not $\sup\left\{\left|\omega_{CSA,S}^{(-q)} \pm \omega_{CSA,S}^{(q)}\right|, \left|\omega_{D,IS}^{(-q)} \pm \omega_{D,IS}^{(q)}\right|\right\} \gg |\omega_1 - q\omega_R|$, R^3 is strongly sensitive to rf-inhomogeneity. Hence, in the case of small CSA and small D_{IS} coupling, R^3 exhibits poor efficiency due to rf-inhomogeneity inside the MAS rotor. Therefore, R^3 often practically is not chosen. D_{IS} recoupled AH of R^3 (q = 1, 2) can be written as

$$\overline{\widehat{H}_{D,IS}}^{(1)} = 2\omega_{D,IS}^{|m|}\left[\cos(q\varphi)\hat{I}_z\hat{S}_z - \sin(q\varphi)\hat{I}_z\hat{S}_y\right] \tag{1.61}$$

with

$$\varphi = \gamma_{PR} + \alpha_{RL}^0 - \omega_R t^0 \tag{1.62}$$

q = 1: $$\omega_{D,IS}^{|m|=1} = -\frac{1}{2\sqrt{2}} b_{IS}\sin(2\beta_{PR}) \tag{1.63}$$

q = 2: $$\omega_{D,IS}^{|m|=2} = \frac{1}{4} b_{IS}\sin^2(\beta_{PR}) \tag{1.64}$$

Since effective dipolar coupling ($\omega_{D,IS}$) is independent of γ_{PR} angle, R^3 has γ encoding property. This means that R^3 benefits from a good robustness to MAS fluctuations and dipolar truncation effect. Inverse supercycled R^3 (SPI-R^3) improve the robustness to rf-inhomogeneity, but γ encoding is lost. The setup of R^3 consists in finding the optimal recoupling time as well as the optimum rf-field. Such setting must be precise in the case of small CSA.

1.5.2. REDOR

The REDOR scheme for D_{IS} recoupling has been extensively used for distance measurements.[36, 37] It is constituted of π pulses applied every half rotor period under with a variety of rf phasing scheme $x\bar{x}$-4, $x\bar{x}$-4 and supercycles (*xy*-4, *xy*-8 or *xy*-16) designed to increase the robustness to rf-offset and rf-inhomogeneity. D_{IS} recoupled AH of REDOR *xy*-4 and *xx*-4 are

REDOR xy-4 $$\overline{\widehat{H}_{D,IS}}^{(1)} = 2\omega_{D,IS}\hat{I}_z\hat{S}_z \tag{1.65}$$

with $$\omega_{D,IS}^{|m|=1} = -\frac{\sqrt{2}}{\pi}\kappa b_{IS}\sin(2\beta_{PR})\cos(\varphi) \tag{1.66}$$

REDOR xx-4 $$\overline{\widehat{H}_{D,IS}}^{(1)} = \omega_{D,IS}\left[\cos(\varphi)\,2\hat{I}_z\hat{S}_z - \psi\sin(\varphi)\,\hat{I}_z\hat{S}_y\right] \tag{1.67}$$

with $$\omega_{D,IS}^{|m|=1} = -\frac{\sqrt{2}}{\pi}\kappa b_{IS}\sin(2\beta_{PR}) \quad (1.68)$$

where $$\kappa = \frac{\cos(\psi\,\pi/2)}{1-\psi^2} \quad (1.69)$$

$$\psi = \frac{2\tau_{\mathrm{p}}}{\tau_{\mathrm{R}}} \quad (1.70)$$

The factor κ describes the finite π pulse effect and ψ is the fraction of the rotor period occupied by the pulses. In the case of infinite π pulse (i.e. $\psi = 0$, κ =1), REDOR *xy*-4 and *xx*-4 have non-γ encoding property and non-dipolar truncation effect. In case of windowless RF irradiation (i.e. $\psi = 1$, $\kappa = \pi/4$), REDOR *xx*-4 and REDOR *xy*-4 are analogous to R^3 (q = 1) and SPI-R^3 (q = 1) respectively. Thus, the factor κ decrease with increasing π pulse length.

REDOR also recouples D_{II} couplings, and the size of the recoupled terms depends on the ratio of pulse width with respect to the period of the sample rotation. Hence, only in the limit of short pulses with respect to the rotation period, D_{II} decoupling is achieved, while under very fast MAS substantial recoupling of the D_{II} occurs.

Nevertheless, in the D-HMQC context, the REDOR scheme may be an interesting option as it is a well-established technique in the measurement of distances and because its setup is easy, as only rf-amplitude and the length of the π pulses must be determined.

1.5.3. Symmetry based recoupling

The symmetry-based rotor-synchronized pulse sequence CN_n^ν and RN_n^ν has been developed by M Levitt et al.[38, 39] They make use of symmetry properties of the spin interactions of quantum numbers l, m, λ, and μ (**Table.1.6**). The beauty of CN_n^ν and RN_n^ν is that they can remove those components of spin interaction we do not want and to keep those we do. Hundreds of composition can be useful for different type of dipolar coupling manipulation. Here we concentrate on D_{IS} recoupled RN_n^ν sequence which is more restricted than C-type sequence.

Table.1.6. Components of spin interactions in the interaction frame under MAS

Interaction	Space rank l	Space component m	Spin rank λ	Spin component μ
δ_{iso}	0	0	1	-1, 0, 1
CSA	2	-2, -1, 1, 2	1	-1, 0, 1
D_{II}	2	-2, -1, 1, 2	2	-2, -1, 0, 1, 2
D_{IS}	2	-2, -1, 1, 2	1	-1, 0, 1
J_{II}	0	0	0	0
J_{IS}	0	0	1	-1, 0, 1

RN_n^ν construction. RN_n^ν can be constructed by following procedures:

(i) Determine the pulse sequence element R with duration $n\tau_R/N$. R must rotate 180° about the *x*-axis of the rotating frame. R may be a single π pulse of phase $\phi = 0$ or a composite pulse (for example, 270°-90°). Note that scaling factor κ strongly depend on a basic element R.

(ii) Derive a 'mirror image' element R*'* from R by reversing the sign of all phases.

(iii) Concatenate *N*/2 phase switched RR*'* pairs, according to

$$RN_n^\nu = \{R_\phi R'_{-\phi}\}_{N/2} \tag{1.71}$$

where the phase shift ϕ is given by $\phi = \pi\nu/N$. The complete RN_n^ν sequence spans n rotational periods which characterize the rf-amplitude of R element. rf-amplitude is given by

$$\omega_1 = \frac{N\omega_R}{2n} \tag{1.72}$$

This symmetry imposes the following selection rule on the components of the recoupled first order AH

$$\overline{\widehat{H}_{lm\lambda\mu}}^{(1)} = 0 \quad \text{if } mn - \mu n \neq \frac{N}{2}\cdot Z_\lambda \tag{1.73}$$

Here *l* refers to the rank of the spin interaction with respect to spatial rotations, *m* refers to the spatial rotational component ($m = -l, -l+1, , , +l$); λ is the rank of the interaction with respect to rotations of resonant spins, and μ is the spin rotational component ($\mu = -\lambda, -\lambda+1, , , +\lambda$). The symbol Z_λ indicates an integer with the same parity as λ, e.g., if λ is even, then Z_λ = 0, ±2, ±4, . . , while if λ is odd, then Z_λ = 1, ±3, ±5, . . To understand this selection rule for each interaction, space-spin-selection diagram (SSS) diagrams is useful (see [38]).

$R18_2^5$ symmetry. As an example, let us check $R18_2^5 = \{(180^o)_{50^o}(180^o)_{-50^o}\}^9$ which is used in PRESTO transfer as mentioned later.[40] For D_{IS} and CSA interaction $\{l, m, \lambda, \mu\}$ = {2, ±2, 1, ∓1},

$$\begin{aligned} mn - \mu\nu = 2\cdot 2 - 5\cdot(-1) = 9 = \frac{N}{2}Z_\lambda \ \text{ or} \\ mn - \mu\nu = 2\cdot(-2) - 5\cdot 1 = -9 = \frac{N}{2}Z_\lambda \end{aligned} \tag{1.74}$$

The recoupling for D_{IS} and CSA interaction are performed. Here, the association of each *m* term with a single value of μ indicate that the recoupling is 'γ-encoding'. In case of 0Q recoupling of D_{IS} interaction $\{l, m, \lambda, \mu\}$ = {2, ±1 or ±2, 1, 0}, the recoupling should be non-γ encoding. For D_{II} coupling, $mn - \mu n \neq N/2\cdot Z_\lambda$. $R18_2^5$ symmetry imposes D_{II} decoupling at the same time as γ-encoded recoupling of CSA and D_{IS} coupling. D_{IS} recoupled AH of $R18_2^5$ is

$$\overline{\widehat{H}_{D,IS}}^{(1)} = 2\omega_{D,IS}^{|m|=2}\left[\cos(2\varphi)\hat{I}_z\hat{S}_x - \sin(2\varphi)\hat{I}_z\hat{S}_y\right] \quad (1.75)$$

with

$$\omega_{D,IS}^{|m|=2} = \kappa\frac{3\sqrt{2}}{4}b_{IS}\sin^2(\beta_{PR}) \quad (1.76)$$

where κ is equal to 0.1754 (for $R18_2^5$) in case of R element of an simple π pulse. $R18_2^5$ has dipolar truncation effect owing to 1Q D_{IS} recoupling. The Hamiltonian form of $R18_2^5$ bracketed by $\pi/2$ pulse will be identical to R^3 (q = 2) except for scaling factor.

$$\overline{\widehat{H}_{D,IS}}^{(1)}(R^3) = \frac{1}{\kappa\,3\sqrt{2}}\exp\left(i\frac{\pi}{2}\hat{I}_y\right)\cdot\overline{\widehat{H}_{D,IS}}^{(1)}(R18_2^5)\cdot\exp\left(-i\frac{\pi}{2}\hat{I}_y\right) \quad (1.77)$$

Relationship of the symmetry. R^3 (q = 1, 2) corresponds to $R2_1^0$ (q = 1) and $R4_1^0$ (q = 2) symmetry, respectively. Note that R^3 is the special case in view of γ encoding. The CSA and D_{IS} interaction terms with quantum number {l, m, λ, ν} = {2, ±q, 1, 0}, {2, ±q, 1, 1} and {2, ±q, 1, 1} are symmetry-allowed. Therefore, there is no bijection between symmetry-allowed {l, m} and {λ, ν} quantum numbers. However, R^3 is categorized γ encoding as explained in 1.5.1.

REDOR *xy*-4 corresponds to $R4_2^1$ symmetry. This symmetry implements selection of the {l, m, λ, μ} = {2, ±1, 1, 0} terms. However, the $R4_2^1$ symmetry also allows D_{II} coupling terms of the form {2, ±2, 2, 0}, {2, ±1, 2, ±2} and {2, ±1, 2 ∓2}. These recoupled D_{II} interactions interfere with the operation of REDOR in non-dilute spin systems. REDOR *xy*-8 and REDOR *xy*-16 correspond to supercycle version of $R4_2^1$ symmetry which are $R4_2^1R4_2^{-1}$ and $[R4_2^1R4_2^{-1}]_0[R4_2^1R4_2^{-1}]_{180}$ respectively.

Above discussion is only for first order AH. Second order AH is also important for characterizing detail performance of the recoupling sequence.

1.5.4. $SR4_1^2$

The $SR4_1^2$ has been introduced by Brinkmann and Kentgens to measure ^{1}H-^{17}O distances. [41, 42] The method is based on the symmetry theory ($R4_1^2 = \{(180^o)_{90^o}(180^o)_{-90^o}\}_2$) with two additional supercycling: a phase inversion ($R4_1^2R4_1^{-2}$) to eliminate D_{II} couplings and a threefold cycling ($SR4_1^2 = [R4_1^2R4_1^{-2}]_0[R4_1^2R4_1^{-2}]_{120}[R4_1^2R4_1^{-2}]_{240}$) to improve the robustness to rf-offset. Moreover, it has a very good robustness to rf-inhomogeneities. The D_{IS} recoupled AH is

$$\overline{\widehat{H}_{D,IS}}^{(1)} = 2\omega_{D,IS}^{|m|=2}\hat{I}_z\hat{S}_z \quad (1.78)$$

with

$$\omega_{D,IS}^{|m|=2} = \frac{1}{4}b_{IS}\sin^2(\beta_{PR})\cos(2\varphi) \quad (1.79)$$

$SR4_1^2$ is non-γ encoded and not dipolar truncated. $SR4_1^2$ is very well suited to recouple D_{IS} coupling in the presence of strong ^{1}H D_{II} couplings.

It is also very easy and fast to optimize. The only parameter to consider for optimization is the recoupling time. Indeed, the theoretical optimum rf-amplitude, $\omega_1 = 2\omega_R$, shows a broad optimum and does not require further optimization. MAS frequency values used in the actual experiment lead to moderate rf-amplitude that do not represent technical limitation for probeheads. However, at slow spinning speeds, the theoretical rf-amplitude may not be large enough to properly eliminate ^{1}H D_{II} coupling.

1.5.5. SFAM

SFAM (Simultaneous Frequency and Amplitude Modulation) have been proposed to overcome REDOR limitation.[43] The rf-field is modulated in amplitude $\omega_1(t)$ and carrier frequency, $\omega_{\mathrm{ref}} + \Delta\omega_{\mathrm{ref}}(t)$, according to the MAS frequency ω_R:

$$\omega_1(t) = \omega_1^{max} \sin(N\omega_R t) \tag{1.80}$$

$$\Delta\omega_{\mathrm{ref}}(t) = \Delta\omega_{\mathrm{ref}}^{max} \cos(N\omega_R t) \tag{1.81}$$

where ω_1^{max} is the maximum of the rf-field amplitude modulation and $\Delta\omega_{\mathrm{ref}}^{max}$ is the maximum amplitude of the rf-field frequency modulation around its average value. The modulation is done at N = 1 or 2 times the MAS frequency. According to the value of N, SFAM-N will behave differently. For each N, two regions of efficient D_{IS} recoupling can be distinguished.[44] D_{IS} recoupled AH is

Region 1: $$\overline{\widehat{H}_{D,IS}}^{(1)} = 2\omega_{D,IS}^{|m|}\left[\cos(\psi)\hat{I}_z\hat{S}_z - \sin(\psi)\hat{I}_y\hat{S}_z\right] \tag{1.82}$$

Region 2: $$\overline{\widehat{H}_{D,IS}}^{(1)} = 2\omega_{D,IS}^{|m|}\hat{I}_z\hat{S}_z \tag{1.83}$$

with

$$\psi = \frac{\omega_1^{max}}{N\omega_R} \tag{1.84}$$

N=1: $$\omega_{D,IS}^{|m|=1} = \kappa b_{IS} \sin(2\beta_{PR}) \cos(\varphi) \tag{1.85}$$

N=2: $$\omega_{D,IS}^{|m|=2} = \kappa b_{IS} \sin^2(\beta_{PR}) \cos(2\varphi) \tag{1.86}$$

where κ depend on N and region, and ψ is close to 90°. Therefore, SFAM-N is non-γ encoded recoupling and not dipolar truncated.[44] With N = 1, both D_{IS} and D_{II} coupling are recoupled ($|m|$ = 1), while with N = 2, D_{IS} coupling only is recoupled ($|m|$ = 2). Therefore, when D_{II} couplings are weak, the use of SFAM-1 recoupling is recommended since this $|m|$ = 1 recoupling method benefits from a $\sqrt{2}$ shorter recoupling time than the $|m|$ = 2 recoupling methods.

SFAM setup requires three parameters to be optimized: recoupling time, ω_1^{max} and $\Delta\omega_{\mathrm{ref}}^{max}$. For practical applications, $\omega_1^{max} \sim 1.5N\omega_R$ and $\Delta\omega_{\mathrm{ref}}^{max} \sim 0.5N\omega_R$ should be used for region 1 and $\omega_1^{max} = \Delta\omega_{\mathrm{ref}}^{max} \sim kN\omega_R$ with k = 3, 5, 7… for region 2. These recoupling conditions will speed up the optimization of SFAM-*N* recoupling by reducing the number of adjustable parameters from three to one. The type of SFAM-*N* scheme and experimental parameters should be selected depending on D_{II} coupling and CSA, the MAS frequency and the probe limitations. The parameter values present a broad optimum, and once N and $\Delta\omega_{\mathrm{ref}}(t)$ are chosen, the corresponding rf-amplitude barely needs adjustment.

1.6. 2D HETCOR between half-integer quadrupolar nuclei and spin-1/2

Two-dimensional (2D) heteronuclear correlation (HETCOR) nuclear magnetic resonance (NMR) spectroscopy is a valuable tool for the characterization and structural investigation of solid state compounds under MAS. Two possible way exist for building up internuclear high resolution correlation spectra:

(i) The first method makes use of the non-vanishing isotropic terms of *J*-coupling, which directly characteristic of the existence of a chemical bond like in liquid state NMR;

(ii) The second method is to restore the through-space dipolar interaction. This interaction vanishes under MAS and need to be reintroduced using continuous wave or modulated rf irradiation dipolar recoupling methods.

These methods facilitate spectral assignment owing to the improved resolution and extracted information. The HETCOR methods using coherence transfers via the *J*-coupling (*J*-HETCOR) or via the dipolar couplings (*D*-HETCOR) are complementary. The *J*-HETCOR techniques help in identifying the molecular entities in solid state compound, while the *D*-HETCOR techniques can be used to establish their 3 dimensional structures and to reveal the noncovalent intra- and intermolecular interaction.

A variety of *J*-HETCOR and *D*-HETCOR pulse sequences have been proposed so far. **Fig.1.6** is their classification.[42] The sequences are classified according to the mode of detection, direct or indirect, and the order of coherences during the t_1 evolution period.

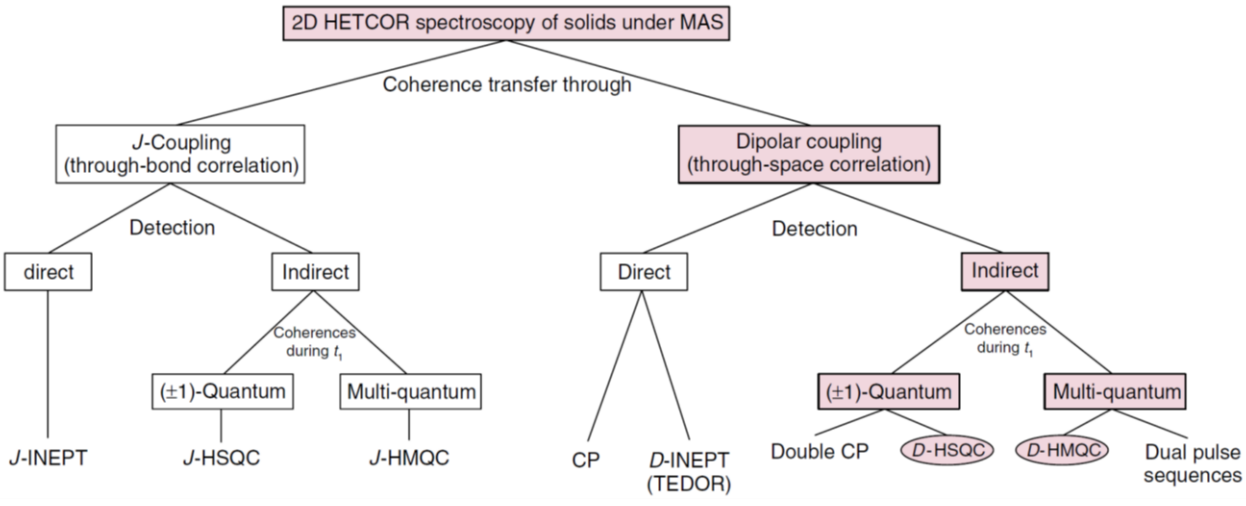

Fig.1.6. Schematic classification of 2D HETCOR NMR experiments in solids (adapted from [42])

1.6.1. Through-bond correlation

One of the most informative classes of solution-state NMR experiments consists in correlating the signals of distinct isotopes through the use of heteronuclear multiple quantum coherences (HMQC) or using the Insensitive Nuclei Enhanced by Polarization Transfer (INEPT) pulse sequence. These methods have been adapted in the last decades for the study of solids under MAS conditions.[45,46]

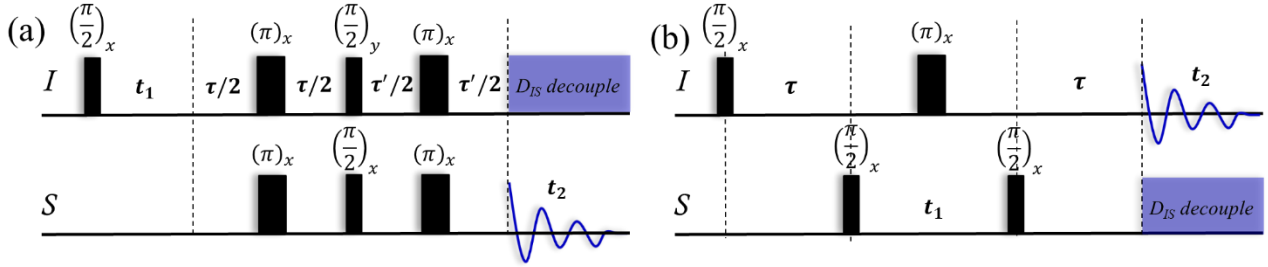

Fig.1.7. Schematic diagram of (a) *J*-RINEPT and (b) *J*-HMQC

We start by considering the standard *J*-RINEPT experiment, shown in **Fig.1.7(a)**, involving an isolated pair of chemically bonded I and S nuclei. Density operator evolution can be calculated and the signal intensity (build-up curve) observed in the S channel can be derived as

$$S(t_1,t_2)_{RINEPT} \sim \alpha \sin(\pi J_{IS}\tau')\sin(\pi J_{IS}\tau)\cos(\omega_I t_1)\exp\left(-\frac{\tau}{T'_{2,I}}-\frac{\tau'}{T'_{2,S}}\right) \quad (1.87)$$

where $\alpha = \gamma_I\gamma_S^2\exp(i\omega_S t_2)$, J_{IS} is the scalar coupling, γ_I and γ_S are the nuclear gyromagnetic ratio, while τ and τ' denote the defocusing and refocusing delays, respectively.

In the *J*-HMQC experiment (**Fig.1.7(b)**), similarly, density operator evolution can be calculated and the signal is observed as

$$S(t_1,t_2)_{HMQC} \sim \beta \sin^2(\pi J_{IS}\tau)\cos(\omega_S t_1)\exp\left(-\frac{2\tau}{T'_{2,I}}\right) \quad (1.88)$$

where $\beta = \gamma_I^3\exp(i\omega_I t_2)$. When the experiments are optimized, i.e., $\tau_{opt} = \tau'_{opt} = 1/(2\,J_{IS})$ for an isolated spin pair. In addition, signal expression of many spin system given in [47].

The relative sensitivity of RINEPT (direct:DD) and HMQC(indirect:ID) per unit of time is derived from[48]

$$\xi = \frac{(S/N)_{ID}}{(S/N)_{DD}} \approx \frac{f_{ID}^2}{f_{DD}}\left[\frac{(FWHM)_S Q_I}{(FWHM)_I Q_S}\right]^{\frac{1}{2}}\left(\frac{\gamma_I}{\gamma_S}\right)^{\frac{3}{2}}\frac{1}{\sqrt{2\pi}} \quad (1.89)$$

where $(FWHM)_{I(S)}$ are full width at half maximum (in Hz), $Q_{I(S)}$ are the quality factors of the sample coil, and $f_{ID(DD)}$ the polarization transfer efficiencies. There is only one transfer in the case of direct detection (f_{DD}), whereas two are required with indirect detection (f_{ID}). The direct

and indirect transfer efficiencies is assumed the same value, $f_{ID} = f_{DD}$. From this equation, the gain increase when increasing γ_I/γ_S, $FWHM_S/FWHM_I$ and f_{ID}.

Both pulse sequence will be optimized in such way that

(i) Under MAS, the delay in the experiments are performed with rotor synchronization.

(ii) CT selective pulse must be sent on the quadrupolar nuclei channel. Therefore, CT selective pulse must be optimized on the sample prior to the experiments.

(iii) The delay (τ and τ') should be optimized on the sample. Theoretically set to $1/(2\,J_{IS})$ for an isolated spin pair, which may be of several ms if one wants to transfer coherence through small *J*-couplings.

In addition, a quick determination of the T_2' for a target sample using an echo sequence, is also a good option. If the T_2' turns out to be short, for example in the presence of paramagnetic centers in the sample, or for amorphous samples, the *J*-RINEPT and *J*-HMQC build-up signal may be weak and it is difficult to obtain the 2D spectra. In the case of using ^{1}H, D_{II} decoupling sequence, such as FSLG, PMLG and DUMBO, should be applied on ^{1}H channel since D_{II} coupling significantly shorten T_2' decay.[46, 49]

It is well known that the magnetization transfer in the *J*-HMQC experiment between spin-1/2 and quadrupolar nuclei for solids is achieved not only through *J* coupling but also through residual dipolar splitting (RDS) resulting from the second-order cross-terms between the quadrupolar and dipolar interactions unlike in the solution.[50] In some case, RDS can be larger than *J* coupling. Nevertheless, regularly, RDS is still small and suffer from short T_2' decay in solids. The RDS is out of scope in this thesis.

Even if the 2D *J*-RINEPT and *J*-HMQC experiment provides a more selective means of correlation than its dipolar counterpart, the *D*-RINEPT and *D*-HMQC experiment, which highlights proximities between close nuclei, should be an alternative.

1.6.2. Through-space correlation

Two type of experiments are described here to obtain 2D correlations using dipolar couplings to highlight proximities between two different nuclei, one of them being a quadrupolar one. First type of experiments are based on direct method, which is similar to *J*-RINEPT. This type of experiments are CP, TEDOR, *D*-RINEPT and PRESTO. Second type of experiments are based on indirect method, which corresponds to Double CP, *D*-HSQC and *D*-HMQC pulse sequences. In the case of solid state NMR, *D*-HSQC is less advantageous than *D*-HMQC.[42] Therefore, *D*-HMQC is only described and emphasized for indirect method.

1.6.2.1. The CP-HETCOR experiment

CP-HETCOR between spin-1/2 and half-integer quadrupolar nuclei is identical to the familiar HETCOR scheme employed to correlate spin-1/2 isotopes.[51] However, CT selective rf-irradiation should be employed for the half-integer quadrupolar channel.

CP dynamics between one spin-1/2 nucleus (I) and one half-integer ($S = n/2$, $n > 1$) nucleus presents a considerable challenge due to the very complex spin dynamics involved in both the spin-locking of S nucleus and the $I \rightarrow S$ CP transfer itself. The set up procedure is as follow.

(i) The rf-amplitude on the quadrupolar channel during the CP transfer, $\omega_{1,S}$, must be optimized so that it achieves efficient spin-lock of the CT.

The effect of MAS on spin-locking of S magnetization can be categorized based on the magnitude of the adiabaticity parameter:

$$\alpha_{ad} = \frac{\omega_{1,S}^2}{\omega_Q \omega_R} \tag{1.90}$$

that is related to the speed at which the quadrupole interaction crosses zero as the sample rotates.[52] The efficiency of spin-locking increases when $\alpha_{ad} \ll 1$ or when $\alpha_{ad} \gg 1$, whereas the intermediate case $\alpha_{ad} \sim 1$ results in a loss of spin-locked states. In case of strong quadrupole interaction and fast spinning speed, only the first case, called sudden passage, is most of the time accessible.

Under typical conditions, in the sudden passage condition, selective manipulation of the CT requires rf-amplitudes in the order of a few kHz (ranging from 5 to 20 kHz), but must still be large enough so that nuclei resonating at different offsets are efficiently spin-locked. Furthermore, the detrimental R^3 conditions where is multiple of MAS frequency, must be avoided.

$$\left(S + \frac{1}{2}\right)\omega_{1,S} = q\omega_R \quad (q : \text{integer}) \tag{1.91}$$

(ii) In the case of weak $\omega_{1,S}$, the nutation frequency acting on the central-transition (CT) is multiplied by (S + 1/2), and the fast MAS previous Hartmann–Hahn matching condition between spin-1/2 nucleus translates into:

$$\left(S + \frac{1}{2}\right)\omega_{1,S} = \varepsilon\omega_{1,I} + n\omega_R \quad (\varepsilon = \pm 1\,;\ \mathrm{n} = \pm 1, \pm 2) \tag{1.92}$$

(iii) Finally CP contact time is optimized. Optimal values are on the order of a few milliseconds.

As a conclusion, the CP method applied to quadrupolar nuclei is not an easy and not robust experiment. The efficiency of the CP transfer being C_Q dependent, sites with very different C_Q

may not be observable simultaneously. To be efficient, the rf-amplitude must be weak, which leads to a large sensitivity to off-resonance irradiation and rf-mismatch. In order to overcome the sensitivity to rf-offset, Multi Pulse (MP)-CP have been proposed.[53]

1.6.2.2. *D*-RINEPT experiments

D-RINEPT is an alternative to CP. This method derives from *J*-RINEPT[54] but R^3 is applied on spin-1/2 channel during the defocusing, τ, and refocusing delays, τ', of *D*-RINEPT sequence (**Fig.1.8**).

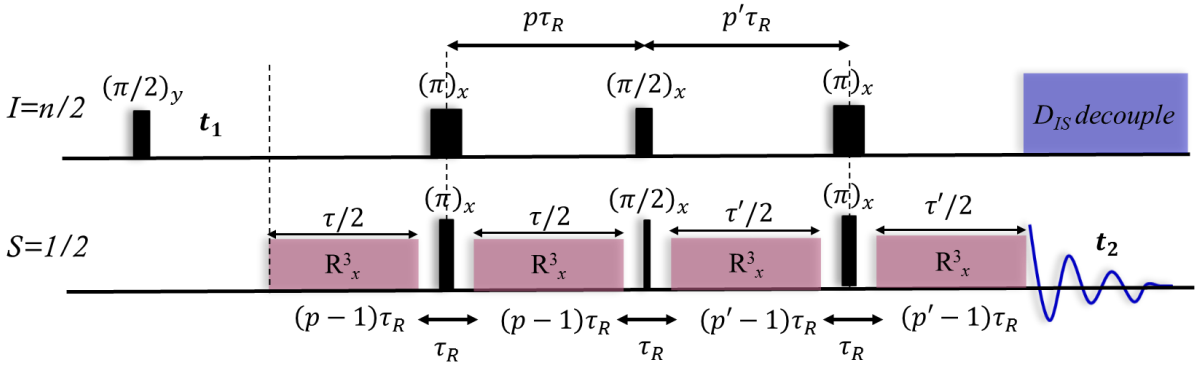

Fig.1.8. Schematic diagram of *D*-RINEPT where R^3 is sent to *S* channel and *I* channel is a half spin quadrupolar nuclei, in which CT selective pulse is applied.

Density operator evolution can be calculated. During the R^3 (q = 1) recoupling applied on the *S* channel (observed channel), the density operator evolves under the effect of the AH given by Eq.(1.61) and assuming $\tau = \tau'$:

$$\begin{aligned}
\hat{I}_x &\xrightarrow{\overline{\hat{H}_{D,IS}}^{(1)}} \cancel{\cos\left(\omega_{D,IS}^{|m|=1}\tau\right)\hat{I}_x} + 2\sin\left(\omega_{D,IS}^{|m|=1}\tau\right)\{\cos(\varphi)\hat{I}_y\hat{S}_z + \sin(\varphi)\hat{I}_y\hat{S}_y\} \\
&\xrightarrow{\frac{\pi}{2}\hat{I}_x,\ \frac{\pi}{2}\hat{S}_x,} 2\sin\left(\omega_{D,IS}^{|m|=1}\tau\right)\{\cos(\varphi)\hat{I}_z\hat{S}_y + \sin(\varphi)\hat{I}_z\hat{S}_z\} \\
&\xrightarrow{\overline{\hat{H}_{D,IS}}^{(1)}} \sin^2\left(\omega_{D,IS}^{|m|=1}\tau\right)\{\cos^2(\varphi) + \sin^2(\varphi)\}\hat{S}_x
\end{aligned} \tag{1.93}$$

The first term in Eq.(1.93) is not transferred to the *S* nucleus and is discarded.

In the *D*-RINEPT sequences,

(i) CSA dephasing of spin-1/2 is refocused by a hard π pulse in the middle of a one-rotor period delay (**Fig.1.8**), whereas D_{IS} refocusing is prevented by a CT selective π pulse on the quadrupolar nucleus;

(ii) The spin-1/2 isotropic chemical shifts and J_{IS} couplings, which are not modulated by MAS, have their dephasings canceled by R^3-irradiation;

(iii) To prevent any quadrupolar modulation, the delays in between the three CT-selective pulses must be rotor synchronized: $p\tau_R$ and $p'\tau_R$. By also taking into account the gap delays (τ_R), each R^3 period must therefore last $(p-1)\tau_R$ and $(p'-1)\tau_R$. D_{IS} dephasings onto the spin-1/2 nucleus, related to other not manipulated active nuclei, are cancelled due to the π pulse in the middle of each echo period;

(iv) For 2D correlation experiment, t_1 evolution block is inserted after first $\pi/2$ pulse.

The *D*-RINEPT is easier to optimize than CP-HETCOR and less dependent on the C_Q value. Moreover, R^3 methods are less sensitive to rf-offset. On the other hand, a disadvantage of R^3 is poor efficiency owing to poor robustness to rf-inhomogeneity. Recently, Rossini et al reported *D*-RINEPT method using $SR4_1^2$ recoupling, instead of R^3.[55]

1.6.2.3. PRESTO experiments

Xin Zhao et al. proposed heteronuclear polarization transfer methods utilizing single channel recoupling based on symmetries $R18_1^7$ and $R18_2^5$ which produces 1Q Hamiltonian.[56] This class of methods was called PRESTO (Phase-shifted Recoupling Effects a Smooth Transfer of Order). PRESTO also has an advantage of no continuous irradiation to quadrupolar nuclei, compared to CP. There are three type of PRESTO (I, -II, -III) sequence (**Fig.1.9**).

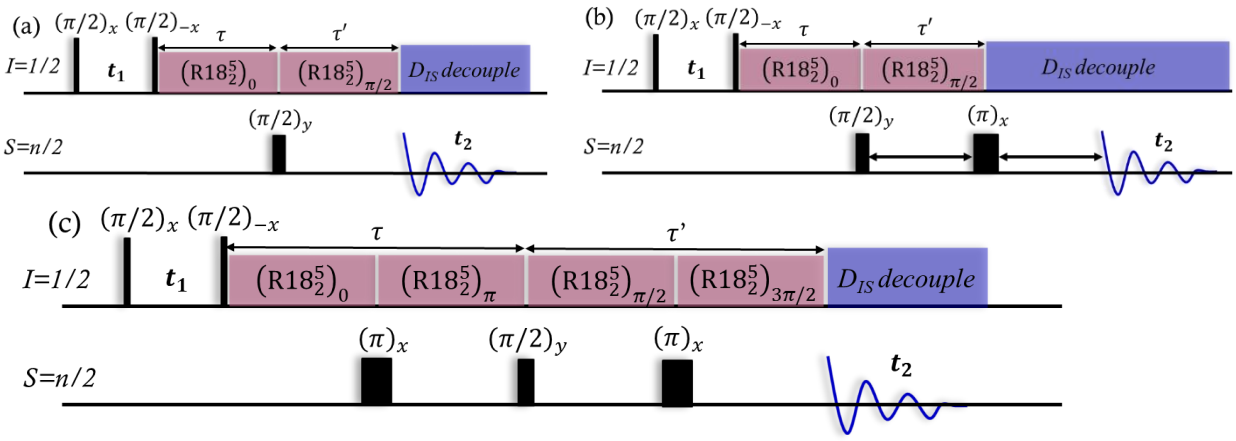

Fig.1.9. Schematic diagram of (a) PRESTO-I, (b) PRESTO-II, (c) PRESTO-III where *I* and *S* channel are assumed to be spin-1/2 and half-integer quadrupolar nuclei, respectively.

If CSA is neglected, density operator evolution ($\tau = \tau'$) of PRESTO-I is calculated as

$$\hat{I}_z \xrightarrow{\left(\overline{\hat{H}_{D,IS}^{(1)}}\right)_0} e^{(-i2\varphi\hat{I}_z)}\{\cancel{\cos(\omega_{D,IS}^{|m|=2}\tau)\hat{I}_z} - 2\sin(\omega_{D,IS}^{|m|=2}\tau)\hat{I}_y\hat{S}_z\}e^{(i2\varphi\hat{I}_z)} \xrightarrow{\frac{\pi}{2}\hat{S}_x} e^{(-i2\varphi\hat{I}_z)}\{-2\sin(\omega_{D,IS}^{|m|=2}\tau)\hat{I}_y\hat{S}_x\}e^{(i2\varphi\hat{I}_z)} \quad (1.94)$$

$$\left(\overline{\widehat{H}_{D,IS}}^{(1)}\right)_{\pi/2} \xrightarrow{} \sin^2\left(\omega_{D,IS}^{|m|=2}\tau\right)\hat{S}_y$$

where

$$\left(\overline{\widehat{H}_{D,IS}}^{(1)}\right)_0 = \omega_{D,IS}^{|m|=2}\exp(-i2\varphi I_z)2\hat{I}_x\hat{S}_z\exp\left(i2\varphi\hat{I}_z\right) \quad (1.95)$$

$$\left(\overline{\widehat{H}_{D,IS}}^{(1)}\right)_{\pi/2} = \omega_{D,IS}^{|m|=2}\exp\left(-i2\varphi\hat{I}_z\right)2\hat{I}_y\hat{S}_z\exp\left(i2\varphi\hat{I}_z\right) \quad (1.96)$$

Thus, *S*-spin transverse magnetization is generated at the beginning of the acquisition period. The feature of each PRESTO sequence is below.

PRESTO-I. *S*-spin isotropic chemical shift evolve during the refocusing delay. This is not preferable in the case of *S* spin with different chemical shifts.

PRESTO-II. This sequence includes an additional spin echo element on the *S*-spin channel in order to refocus *S*-spin isotropic chemical shift, but PRESTO-II cannot refocus *I*-spin CSA which can interfere with the D_{IS} recoupling since D_{IS} recoupled AH generated by $R18_1^7$ and $R18_2^5$ does not commute with *I*-spin CSA recoupled AH.

PRESTO-III. A π pulse on the S-spin channel is inserted at the exact center of the τ interval. The phase of the *I*-spin irradiation is shifted by π at the same instant. Such procedure refocuses S-spin isotropic chemical shift as well as the CSA of *I*-spin. A disadvantage of PRESTO-III is the larger step for the recoupling time, compared to PRESTO-II. In the case of the system with large heteronuclear dipolar coupling, such large steps can prevent the adjustment of the recoupling time to its value leading to maximal transfer efficiency.

For 2D correlation experiment, t_1 evolution period with π/2 bracket is inserted before the defocusing delay.[57]

The PRESTO is easier to optimize than CP-HETCOR. $R18_1^7$ and $R18_2^5$, which have D_{II} decoupling property, is suitable 1Q D_{IS} recoupling for the nuclei subject to strong D_{II} coupling, such as ^{1}H. Furthermore, these symmetry-based recoupling are more robust to rf-mismatch and rf inhomogeneity than R^3. So far, the PRESTO sequence has only been reported with recoupling applied to the non-observed channel. Recently, the usefulness of PRESTO sequence to transfer DNP-enhanced ^{1}H polarization to quadrupolar nuclei has been demonstrated.[57]

1.6.2.4. *D*-HMQC experiment.

D-HMQC sequence with R^3

In 2006, Z. Gan et al. and S. Cavadini et al. proposed *D*-HMQC with R^3 recoupling.[50, 58] Although these experiments were initially proposed for the indirect observation of ^{14}N via ^{1}H or ^{13}C, they can be also employed for half-integer quadrupolar nuclei. **Fig.1.10(a)** shows *D*-

HMQC sequence, for which the recoupling is applied on the direct channel (denoted DR for direct recoupling hereafter) proposed by Z Gan.[58] The evolution of the density operator during *D*-HMQC sequence with R^3 (q = 2)is as follow (assuming t_1 = 0).

$$\begin{aligned}
\hat{I}_x &\xrightarrow{\overline{\hat{H}_{D,IS}}^{(1)}} \cancel{\cos\left(\omega_{D,IS}^{|m|=2}\tau\right)\hat{I}_x} + \sin\left(\omega_{D,IS}^{|m|=2}\tau\right)\left\{\cos(2\varphi)\,2\hat{I}_y\hat{S}_z + \sin(2\varphi)\,2\hat{I}_z\hat{S}_z\right\} \\
&\xrightarrow{\frac{\pi}{2}\hat{S}_x} \sin\left(\omega_{D,IS}^{|m|=2}\tau\right)\left\{-\cos(2\varphi)\,2\hat{I}_y\hat{S}_y - \sin(2\varphi)\,2\hat{I}_z\hat{S}_y\right\} \\
&\xrightarrow{\pi\hat{I}_y} \sin\left(\omega_{D,IS}^{|m|=2}\tau\right)\left\{\cos(2\varphi)\,2\hat{I}_y\hat{S}_y + \cancel{\sin(2\varphi)\,2\hat{I}_z\hat{S}_y}\right\}
\end{aligned} \tag{1.97}$$

Second term can be removed by the phase cycle of π pulse in *I* channel

$$\xrightarrow{\frac{\pi}{2}\hat{S}_x} \sin\left(\omega_{D,IS}^{|m|=2}\tau\right)\cos(2\varphi)\,2\hat{I}_y\hat{S}_z$$

$$\xrightarrow{\overline{\hat{H}_{D,IS}}^{(1)}} -\sin^2\left(\omega_{D,IS}^{|m|=2}\tau\right)\cos^2(2\varphi)\,\hat{I}_x$$

where

$$\overline{\hat{H}_{D,IS}}^{(1)} = 2\omega_{D,IS}^{|m|=2}\left[\cos(2\varphi)\hat{S}_z\hat{I}_z - \sin(2\varphi)\hat{S}_z\hat{I}_y\right] \tag{1.98}$$

It is noted that final result of the density operator evolution in this *D*-HMQC sequence depend on γ_{PR} angle owing to selecting ± 1 coherence on the *I* channel by the phase cycle.

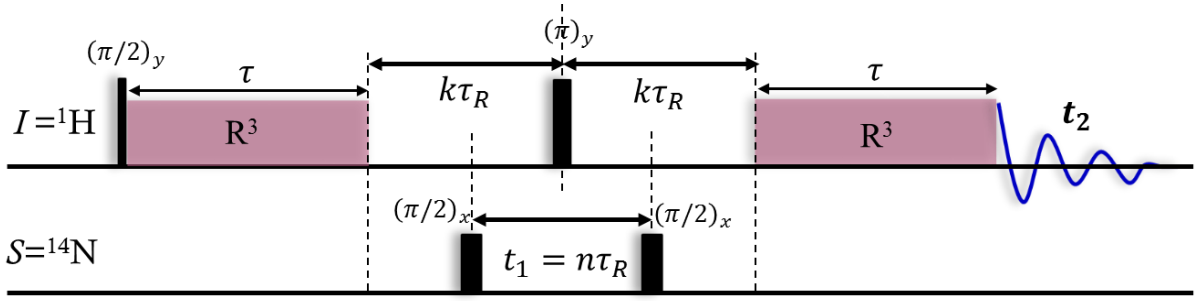

Fig.1.10. Schematic diagram of ^{1}H-{^{14}N}*D*-HMQC presented by Z Gan

Although *D*-HMQC sequence looks similar to *J*-HMQC sequence, there are some important differences for the optimization of the pulse sequence:

(i) Rotary-resonance has the specific property that a delay introduced during the R^3 irradiation may change the AH acting on the spins. As an example, a gap in R^3 irradiation of half (q = 1) or a quarter (q = 2) rotor period changes the sign of the CSA and D_{IS} recoupled AH, as would do a π pulse in a Hahn echo experiment.[59, 60] This sign change create a rotary resonance echo for CSA and D_{IS}. When a spin echo π pulse is added in the middle of the gap, the timing of the two R^3 periods must be continuous in rotor position. The spin echo segment (between the end of defocusing and beginning of refocusing of R^3 block) must be integer (q = 1) or half integer (q = 2) numbers of rotor period. In practical applications,

even numbers of rotor period ($2k\tau_R$) are often used to avoid any kind of modulation. This rotary resonance concept is also applied to *D*-RINEPT sequence as seen in 1.6.2.2.

(ii) The spin-echo segment increments $2\tau_R$ for every two t_1 increments. However, this increment could lead to sidebands occurring at $\nu_R/2$ since detected signal decrease by the contribution from T_2' decay of ^{1}H every $2\tau_R$. T_2' decay of ^{1}H is relatively shorter owing to homonuclear dipolar coupling. Similarly, short T_2' decay of the observed nucleus broaden the resolution in the indirect dimension in 2D spectra of *D*-HMQC.

(iii) R^3 irradiation must be q = 2 condition ($\omega_1 = 2\omega_R$) which include D_{II} decoupling.

(iv) Finite pulse length should be included in the rotor-synchronization conditions. Therefore, t_1 period set to $t_1 = n\tau_R$ (the pulse length on the ^{14}N channel must be counted) in order to refocus first order quadrupolar interaction as well as the careful adjustment of the delay between the recoupling and π/2 pulse before t_1 evolution.

Thus, unlike *J*-HMQC, there are several careful set-up points owing to recoupling sequence, MAS and some kind of anisotropic interactions. After building the sequence, the *D*-HMQC is easier to optimize than CP-HETCOR. However, R^3 is sensitive to rf maladjustement and inhomogeneity.

Recoupling on direct channel and Indirect channel.

The recoupling sequence can only be efficiently applied to the spin-1/2 nucleus. The observed signal can either be that of the spin-1/2 nucleus (**Fig.1.11(a)**) or that of the quadrupolar nucleus (**Fig.1.11(b)**).[42, 44, 54] -DR and -IR stand for Direct (observed) channel Recoupling and Indirect (non-observed) channel Recoupling.

As exhibited in **Fig.1.11**, the rotor synchronization in *D*-HMQC is redefined as follows.[44]

$$T_A + \tau + T_B + \frac{t_1}{2} = n\tau_R \quad (1.99)$$

$$\tau = k\tau_R \quad (1.100)$$

$$2T_A + t_1 = p\tau_R \quad (1.101)$$

Eq.(1.99) insures that the observed spin anisotropy (quadrupolar or CSA) does not modulate the signal that could lead to sidebands occurring at $\nu_R/2$ for example. Eq.(1.100) is required by the definition of rotor synchronized recoupling sequences. Eq.(1.101) is critical for non-γ encoded recoupling. Delay T_A and T_B are recalculated every t_1 increment based on the minimum delay required to fit $t_1$and pulses between the recoupling pulses. If *S* spin is integer quadrupolar nucleus, as mentioned in *D*-HMQC-DR with R^3, $t_1$must be rotor synchronized ($t_1 = j\tau_R$) to refocus first order quadrupolar interaction. . In case of ^{1}H-{X} *D*-HMQC-DR,

relation.(1.99) can be relaxed to $T_A + \tau + T_B + \frac{t_1}{2} = \frac{1}{2}n\tau_R$ since the main signal modulation originates from homonuclear dipolar coupling that has a $\tau_R/2$ modulation. In that case, a τ_R t_1 increment can be fulfilled with $T_B = 0$. Moreover it is important to have a steady increment of n with t_1 in relation.(1.99) to remove a potential modulation induced by T_2' relaxation.

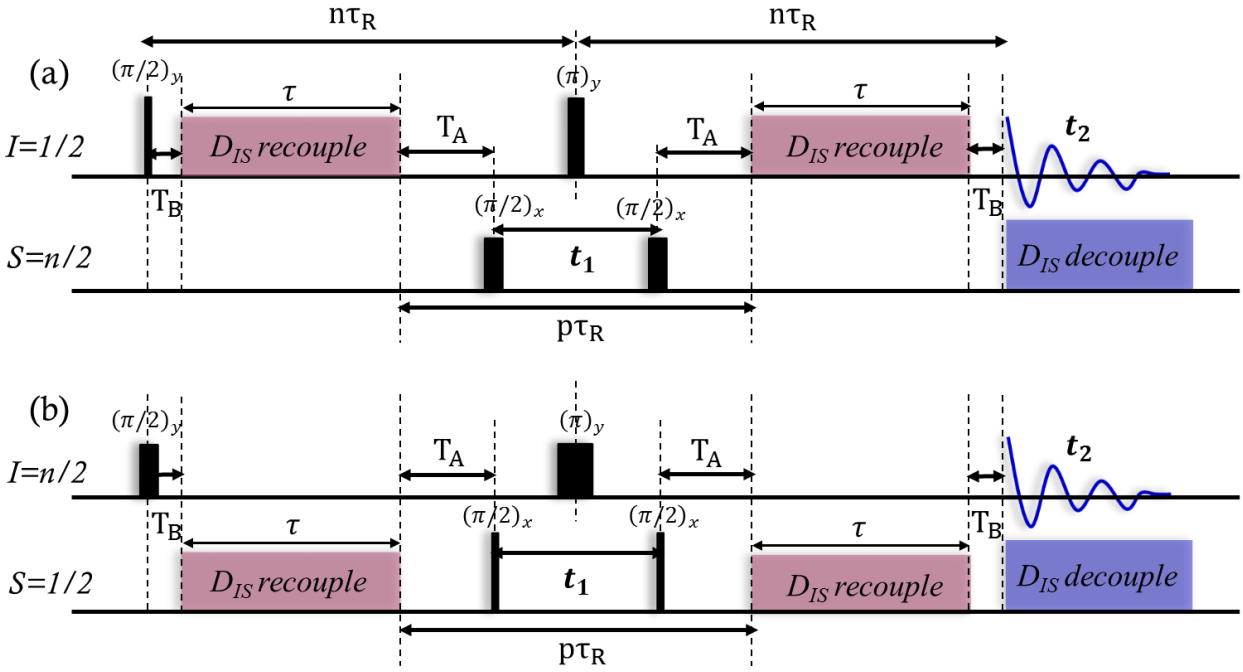

Fig.1.11. Schematic diagram of (a) *D*-HMQC-DR, (b) *D*-HMQC-IR

Most of the time, *D*-HMQC-IR benefits from higher sensitivity owing to the short quadrupolar longitudinal relaxation time and the possibility of using population transfer technique before first π/2 pulse, in order to enhance the population difference across the CT. Moreover, this version also leads to a better robustness with respect to spinning speed fluctuation since the D_{IS} recoupling is sent on the non-observed channel and the CSA of the observed nucleus is not reintroduced.

Conversely, *D*-HMQC-DR can be frequently used in the case of the experiment involving integer quadrupolar, such as ^{14}N, because of the absence of refocusing π pulse for such isotopes. In the case of quadrupolar nuclei subject to large quadrupolar interactions, *D*-HMQC-DR profits from the shorter maximum value of t_1, owing to observation along F1 of a second-order line-width. Furthermore, for protonated compounds, *D*-HMQC-DR might benefit from higher sensitivity since the quadrupolar nuclei can be detected via ^{1}H isotope or the sensitivity can be increased by replacing the first π/2 pulse by an initial ^{1}H → *I* CP transfer. For ^{1}H-{X} *D*-HMQC-DR experiment, D_{II} decoupling scheme can be applied during both t_1 and t_2 periods in order to enhance the spectral resolution.[61] However, *D*-HMQC-DR is more sensitive to MAS

frequency instabilities since the CSA of the observed I nucleus (CSA_I) is reintroduced and can only be refocused by the perfect rotor-synchronization of the two D_{IS} recoupling periods. Such rotor-synchronization is more difficult to achieve for long t_1 period.

Comparison of several recoupling sequence in *D*-HMQC.

The choice of the D_{IS} recoupling influences the performances of *D*-HMQC experiment. Although *D*-HMQC-DR with R^3 recoupling have been successfully applied to observe ^{14}N nuclei indirectly via ^1H, R^3 is less robust to rf inhomogeneity and has the property of dipolar truncation effect (long range recoupling is not possible).

Therefore several recoupling sequences have been explored and their performances have been compared. These methods can be classified in four different groups: R^3, symmetry-based sequences ($R12_3^5$, $R20_5^9$ and $SR4_1^2$), REDOR, and SFAM.

Except for R^3 (q = 1, 2), these recouplings are non-γ-encoded and can accomplish a 'longitudinal two-spin-order' ($\hat{I}_z\hat{S}_z$) recoupling of the dipolar interactions. Therefore, density operator evolution of *D*-HMQC is the same as that of *J*-HMQC. This D_{IS} recoupled AH commutes across different spin pairs and therefore does not suffer from dipolar truncation and hence, both short- and long- range distance can be observed simultaneously. In non-γ encoded recoupling schemes, $SR4_1^2$ and SFAM recoupling show better performance than REDOR and other non-γ encoded symmetry based recoupling.[62] Moreover, X. Lu et al. further investigated the performance of SFAM and $SR4_1^2$ in *D*-HMQC-DR and –IR.[44] Recommended recouplings are shown in **Table.1.7** with respect to the size of D_{II} and CSA.

Table.1.7. Recommended recouplings as function of the magnitude of D_{II} and CSA or rf-offset.

Channel	*D*-HMQC-DR				*D*-HMQC-IR			
D_{II}	large		small		large		small	
CSA or rf-offset	large	small	large	small	large	small	large	small
recoupling	$SR4_1^2$ or SFAM-2^{reg2} or $R^3(q=2)$	$SR4_1^2$	SFAM-1^{reg2} or $R^3(q=1)$	SFAM-1^{reg2}	$SR4_1^2$ or SFAM-2^{reg2}	$SR4_1^2$	SFAM-1^{reg2}	

In case of *D*-HMQC-IR, $SR4_1^2$ or SFAM recoupling schemes should be used for their robustness to rf inhomogeneity. Furthermore, the robustness to MAS fluctuation of these recoupling methods is generally sufficient. If D_{II} coupling are small, SFAM-1^{reg2} scheme should

be selected since it results in shorter mixing time. This will limit the losses due to T_2' relaxation on the observed spin. Otherwise, $SR4_1^2$ or SFAM-2 can be employed but $SR4_1^2$ often outperform SFAM-2. If the spin-1/2 exhibits large CSA or rf-offsets, SFAM-2^{reg2} allows selecting a recoupling condition for larger rf-amplitude ($\omega_1 = 3, 5, 9\omega_R$) than $SR4_1^2$ ($\omega_1 = 2\omega_R$) that will increase the robustness with respect to these interactions. For *D*-HMQC-DR, the choice of the recoupling sequences is similar when the CSA is small. In the case of large CSA, R^3 offers high robustness to MAS fluctuations and rf inhomogeneity.

R^3 and $SR4_1^2$ schemes only require the optimization of two parameters (recoupling time and rf-amplitude). In case of SFAM, a third parameter should be optimized, the frequency offset.

Note that among these recoupling schemes, R^3 (q = 1, 2) method is the only which is γ encoded. γ encoded recoupling are more robust to MAS fluctuation and exhibits 25 % higher efficiency than non-γ encoded ones. Furthermore, they are affected by dipolar truncation, which allows selecting correlation with 1st neighbors, thus facilitating the spectral assignment.

Comparison of CP-HETCOR and D-HMQC

G Tricot et al. demonstrated the performance of *D*-HMQC compared to CP-HETCOR.[63] The performances of ^{27}Al-{^{31}P} *D*-HMQC-IR using SFAM-1 recoupling have been compared to those ^{31}P-{^{27}Al}CP-HETCOR for a potassium alumino-phosphate glass (with composition $50K_2O$-$10Al_2O_3$-$40P_2O_5$). **Fig.1.12** display the ^{27}Al-{^{31}P}*D*-HMQC and ^{31}P-{^{27}Al} CP-HETCOR 2D spectra obtained at 18.8 T using the same MAS frequency of 20 kHz and the same sample volume (3.2 mm probe-head). The spectrum was acquired, setting the rf-offset on resonance for AlO_5 species. Experimental time is 17 and 68 hours for *D*-HMQC and CP-HETCOR respectively.

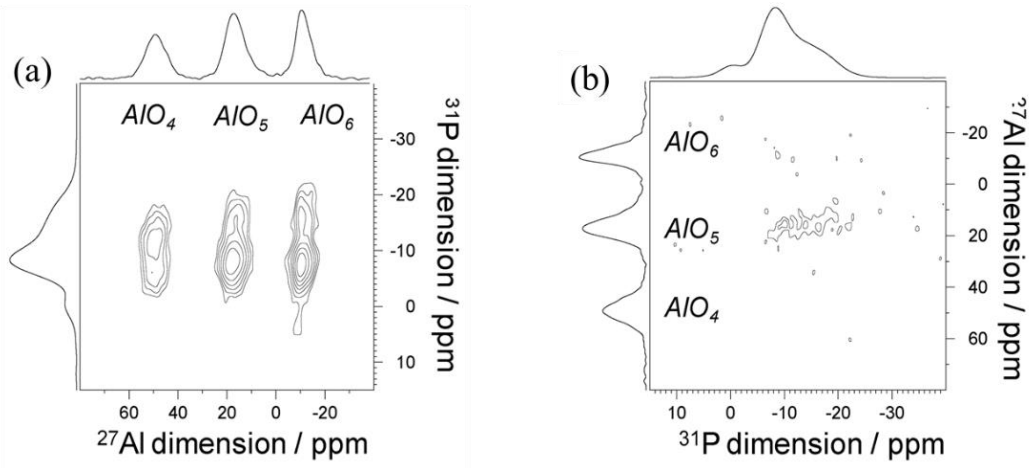

Fig.1.12. ^{31}P/^{27}Al correlation NME spectra of $50K_2O$-$10Al_2O_3$-$40P_2O_5$ glass acquired using (a) ^{27}Al-{^{31}P}*D*-HMQC-IR and (b)^{31}P-{^{27}Al}CP-HETCOR at 18.8 T under MAS frequency of 20 kHz. (Adapted from [63])

The comparison of these two spectra clearly indicates the superiority of the *D*-HMQC technique at high field. Indeed, the *D*-HMQC spectrum shows a correlation scheme similar to that obtained at 9.4 T with an improved resolution in both dimensions, whereas the CP-HETCOR spectrum only displays a weak correlation involving AlO_5 species. The absence of cross-peaks for AlO_6 and AlO_4 environments illustrates the high sensitivity to rf-offset for CP transfer. The enhanced *D*-HMQC spectral resolution at 18.8 T allows improving the structural analysis by showing clear evidence of two P species in the vicinity of tetrahedral aluminium, whereas the experiment performed at 9.4 T only evidences a single P-AlO_4 species.

As mentioned in section *D*-HMQC with R^3, the resolution in the indirect dimension of a 2D *D*-HMQC spectrum suffer from the T_2' decay of the observed nucleus during the echo. Hence, analysis of indirect linewidth must be done with care. On the other hand, for CP, only single-quantum coherences are involved such that the resolution in the indirect dimension is the same as for one-dimensional experiment.

The experiments with frequency splitter

In the periodic table of elements, there are many NMR-active nuclei with small Larmor frequency difference. However, due to the limitation of commercial solid state-NMR probes, double-resonance experiment for ^{13}C-^{27}Al, ^{13C}-^{51}V, ^{27}Al-^{51}V, ^{23}NA-^{27}Al and ^{23}Na-^{51}V is hardly achieved. A solution consists in the use of an external frequency splitter (such as the REDOR-box device commercialized by NMR Service GmbH) connected to a single rf channel of probe head. Such device enables double resonance experiments involving nuclei with close Larmor frequencies. The major limitation of the frequency splitter is the impossibility of simultaneous rf irradiation at both resonance frequencies, precluding some experiments, such as CP. *D*-HMQC is compatible with frequency splitter since *D*-HMQC does not require simultaneous rf irradiation on the channels of correlated isotopes. Organoaluminium compounds have been analyzed by ^{13}C-^{27}Al *J*- and *D*-HMQC with frequency splitter.[64, 65] Recently, 2D ^{13}C-^{27}Al correlation spectra for Al-based MOFs have been acquired using a frequency splitter, ^{13}C-{^{27}Al} CP-*D*-HMQC sequence, in which ^{13}C transverse magnetization is created using ^{1}H→^{13}C CP transfer, the ^{1}H magnetization being enhanced by Dynamic Nuclear Polarization.[66]

t_1 noise problem in 2D experiment

One key drawback of the *D*-HMQC pulse sequence is that both the MAS frequency and spectrometer must be very stable to avoid excessive t_1-noise because the signals from uncorrelated spins are imperfectly suppressed by phase cycling alone. Especially, in case of *D*-

HMQC-DR, non-γ encoded recoupling is very sensitive to MAS fluctuation since each crystallite must have the same orientation at the beginnings of defocusing and refocusing periods. Such condition is especially difficult to achieve in *D*-HMQC-DR experiment when the t_1 evolution time and recoupling time are long due to narrow peaks and weak dipolar interactions, respectively. Such MAS fluctuations lead to random change in the detected signal intensity and it is difficult to suppress the t_1 noise by phase cycle.

In the case of double CP, uncoupled spin magnetization is reduced by inserting purging (2Q filter) period into between t_1 evolution and signal detection.[67] However, this purging period cannot be applied to *D*-HMQC sequence in principle. Therefore, it may be difficult to apply *D*-HMQC-DR to the isotopes with very low abundance, when the heteronuclei are dilute or when there are multiple overlapping ^{1}H signals.

If completely uncoupled signal exist in the spectrum, the signal can be suppressed by inserting a single, long, low amplitude selective saturation pulse before the start of *D*-HMQC (**Fig.1.13**).[68] If completely uncoupled signal is removed, t_1-noise from completely uncoupled signal is suppressed and this method cleans the 2D spectrum. However, this approach does not suppress the t_1-noise for coupled nuclei. Hence, the t_1-noise problem of 2D *D*-HMQC experiments still unsolved.

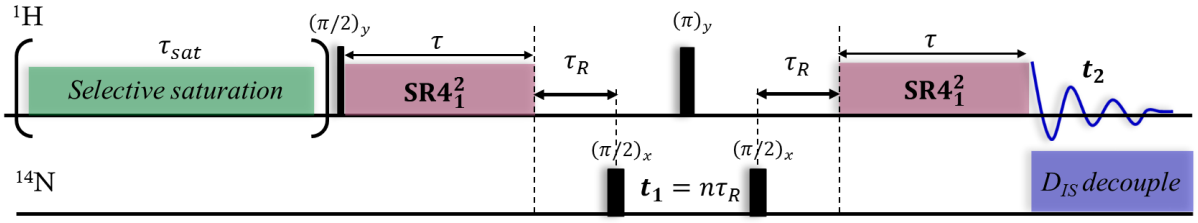

Fig.1.13. Schematic diagram of *D*-HMQC-DR with selective saturation pulse

Constant time *D*-HMQC approach

Recently, A. Rossini. et al. proposed constant time *D*-HMQC approach to indirectly detect via spin-1/2 nuclei wideline spectrum which consists of many sidebands owing to large anisotropic interaction, such as CSA.[69] **Fig.1.14** illustrates constant time *D*-HMQC pulse sequence. The spin echo block in the middle of the sequence is fixed to a constant duration ($2k\tau_R > t_{1,max}$) and the θ pulses are stepped outwards to enable arbitrary, rotor asynchronous t_1 increments. θ pulse should be optimized to achieve broadband excitation. Owing to constant time between recouplings, detected signal is not modulated with T_2' decay. The sensitivity

gain, ξ, provided by the indirect detection of wideline spectrum using constant time *D*-HMQC experiment with respect to direct detection strongly depends on the investigated sample.

They demonstrated that constant time *D*-HMQC-DR with $SR4_1^2$ enabled rapid acquisition of 2D ^{1}H-^{195}Pt correlation of cis-platin and trans-platin in experimental time of 2 hours. This indirect detection strategy provides sensitivity gains between 1 to 2 orders of magnitude compared to direct detection. On the other hand, constant time ^{1}H-^{71}Ga *D*-HMQC-DR experiments required slightly longer experimental time than direct detection due to relatively low ξ. However, the advantage of this method is that overlapping sites could potentially be resolved by correlation to different ^{1}H chemical shifts. This method also suffers from t_1 noise. If large t_1 noise appears in the 2D spectra, the sensitivity is significantly decreased.

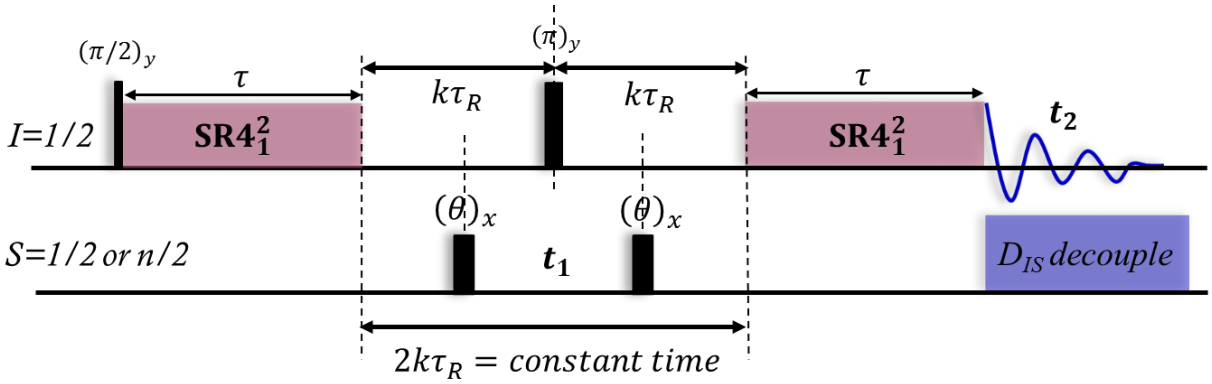

Fig.1.14. Schematic diagram of constant time *D*-HMQC-DR sequence

Indirect ST spectrum in *D*-HMQC

In the case of integer quadrupolar nucleus, such as ^{14}N, the spectrum does not exhibit central transition but only the transitions between energy levels $1 \leftrightarrow 0$ and $0 \leftrightarrow -1$. Hence, for the indirect observation of ^{14}N spectrum, the complete rotor-synchronized t_1 acquisition is required to average out first order quadrupolar interaction.

In the case of half-integer quadrupolar nucleus, first order quadrupolar interaction also affect the ST. Therefore, ST can be indirectly detected using complete rotor synchronized t_1 acquisition and hard π/2 pulse instead of CT selective pulse in indirect channel of half-integer quadrupolar nuclei.

If only CT spectrum is required (sometimes, observation of ST spectrum contaminate CT spectrum), rotor-asynchronous t_1 acquisition is preferable. On the other hand, the duration between two recoupling blocks should be rotor- synchronized.

Recently, Y. Nishiyama and co-worker demonstrated that CT spectrum and ST spectrum (center band and spinning side band) can be indirectly detected using conventional and constant

time *D*-HMQC-DR with various condition of t_1 acquisition (synchronous or asynchronous) and the rf pulses (hard or soft pulse with appropriate rf-offset) of indirectly detected channel.[70, 71]

The observation of center band of ST_1 spectrum has the benefit from a more accurate determination of quadrupolar coupling constant. Quadrupolar product $P_Q = C_Q\left(1+\eta_Q^2/3\right)^{1/2}$ can be estimated from the frequency difference between CT and the center band of ST_1. In the case of I = 5/2, the CT and the center band of ST_1 are preferred since ST_2 line-width is broader than the other two transition. However, sometimes CT and center band ST_1 may not be resolved. This prevents the accurate determination of ST_1 shift. They resolved this problem by measuring spinning sideband of ST_1.

1.6.3. More advanced 2D-HETCOR method

MQ-HETCOR

It has been shown by several groups that CP-HETCOR can be coupled with the MQMAS experiment.[72] Numerous applications of the so-called MQ-HETCOR have been published, many of them related to the characterization of the aluminophosphate molecular sieves. The 3Q-HETCOR spectrum exhibits a better resolution in the ^{27}Al dimension compared to the ^{27}Al-^{31}P CP HETCOR spectrum.

Alternatively, the MQMAS block was combined with a *J*-RINEPT sequence in order to avoid the complexity of spin locking the quadrupolar nucleus.[73]

The MQMAS block has also been combined with *D*-RINEPT, for which the coherence of quadrupolar isotope is transferred to that of spin-1/2 nuclei via D_{IS} couplings reintroduced by the application of D_{IS} recoupling sequences, such as R^3, to the spin-1/2 isotope during the defocusing and refocusing delays of the RINEPT block (**Fig.1.15**).[34]

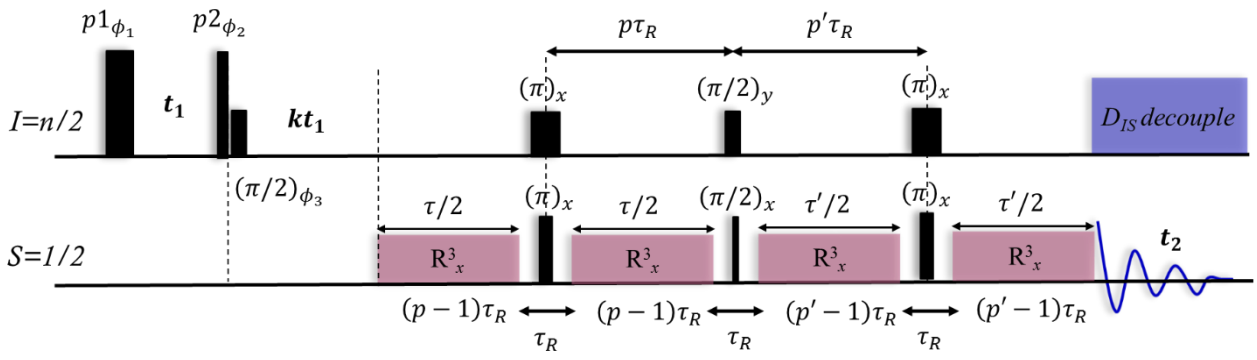

Fig.1.15. Schematic diagram of MQ-*D*-RINEPT sequence

HMQC-ST

HMQC and HSQC sequences are fundamentally symmetrical with respect to time, and it is, therefore, difficult to introduce an unsymmetrical MQMAS or STMAS second order quadrupolar filter. For spin-3/2, this limitation can nevertheless be overcome by inserting during the t_1 period a symmetrical t_1 STMAS sequence on the non-observed channel [74]:

0Q→±1Q ($n\tau_R/18$) → ± 2Q ($8n\tau_R/9$) → ±1Q ($n\tau_R/18$) → ±0Q (**Fig.1.16**).

This symmetrical t_1-split STMAS sequence was also used in STARTMAS experiment.[75]

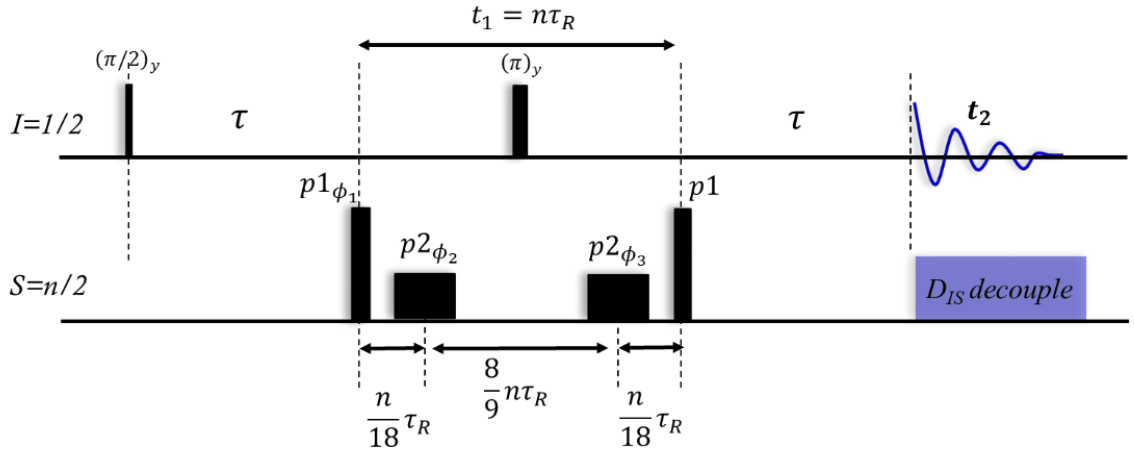

Fig.1.16. Schematic diagram of HMQC-ST sequence.

PT *J*/*D*-HMQC

Q. Wang et al. have shown recently that for *J*- or *D*-HMQC experiments indirectly detecting half-integer spin quadrupolar nuclei, the population transfer can be accelerated by manipulating their satellite transition (**Fig.1.17**).[76] Such approach is notably useful to enhance the sensitivity of ^{27}Al-^{17}O *J*-HMQC experiments.

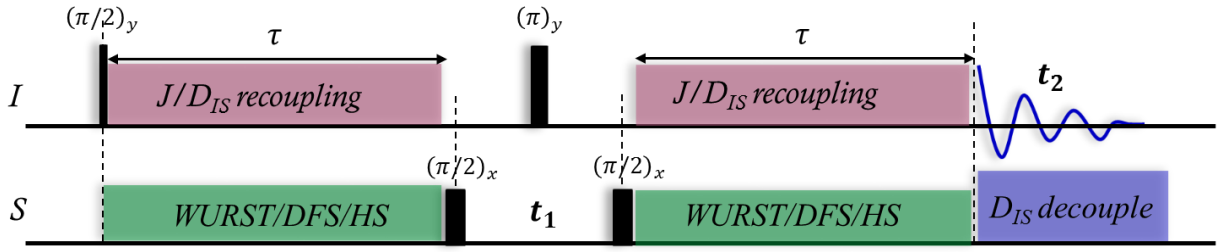

Fig.1.17. Schematic diagram of PT *J*/*D*-HMQC sequence.

1.7. Objectives of the thesis

We have reviewed at solid-state NMR method for quadrupolar nuclei, including high-resolution techniques, methods to enhance sensitivity as well as 2D HETCOR experiments. In the past, these techniques were only used by the experts, but today they have more and more often used for structural analysis of materials. In recent years, many improvements of these methods have been reported. In this thesis, we aim to further improve these methods. A disadvantage of these methods is often the lack of sensitivity. In recent years the sensitivity issue has been partially improved by the development of high field Dynamic Nuclear Polarization (DNP). Nevertheless, DNP is not a universal sensitivity improvement method since it requires the impregnation of radical solution to the sample and the use of specific equipment. In particular, DNP is difficult to apply for bulk samples, such as inorganic glass and crystals since it is impossible to impregnate radical solution.

However, high resolution methods such as MQMAS and STMAS that analyze these materials are low sensitivity, and also for 2D HETCOR methods, there are systems that cannot be applied owing to low sensitivity problem at present. For these methods, the improvement in this thesis are two points of interest.

In Chapter 2, we show how to analyze Gallium Selenide material which was difficult for MQ or STMAS and HETCOR experiment because of low sensitivity. Specifically, the pulse sequence of STMAS and various HETCOR method will be developed by adding the CPMG acquisition and population transfer irradiation.

Chapter 3 presents a new *D*-HMQC sequence with γ encoded recoupling, which is experimentally demonstrated to acquire ^{27}Al-^{31}P 2D correlation on aluminophosphate material. As reviewed in section 1.5 and 1.6, R^3 has low sensitivity due to poor robustness to rf-inhomogeneity and is not used much in practice. Therefore, we investigated symmetry-based γ encoded recoupling techniques, which must be more robust to rf inhomogeneity than R^3. Nevertheless, these methods should benefit from good robust to MAS fluctuations, thus limiting the magnitude of t_1 noise.

1.8. References

[1] Sakurai, J. J. *Modern Quantum Mechanics, Revised Edition*. (Addison Wesley, 1993).
[2] Levitt, M. H. *Spin Dynamics: Basics of Nuclear Magnetic Resonance*. (Wiley, 2008).
[3] Mehring, M. *Principles of High Resolution NMR in Solids*. (Springer-Verlag, 2012).
[4] Charles P. Slichter *Principles of Magnetic Resonance* (Springer, 2013)
[5] Edén, M. Computer simulations in solid-state NMR. I. Spin dynamics theory. *Concepts Magn. Reson.* **17A,** 117–154 (2003).
[6] Leskes, M., Madhu, P. K. & Vega, S. Floquet theory in solid-state nuclear magnetic resonance. *Progress in Nuclear Magnetic Resonance Spectroscopy* 57, 345–380 (2010).
[7] Rovnyak, D. Tutorial on analytic theory for cross-polarization in solid state NMR. *Concepts in Magnetic Resonance Part A* **32A,** 254–276 (2008).
[8] Man, P. P. Quadrupolar Interactions. in *Encyclopedia of Magnetic Resonance* (ed. Harris, R. K.) (John Wiley & Sons, Ltd, 2011).
[9] Vega, A. J. Quadrupolar Nuclei in Solids. in *Encyclopedia of Magnetic Resonance* (ed. Harris, R. K.) (John Wiley & Sons, Ltd, 2010).
[10] Ashbrook, S. E. & Duer, M. J. Structural information from quadrupolar nuclei in solid state NMR. *Concepts in Magnetic Resonance Part A* **28A,** 183–248 (2006).
[11] Jerschow, A. From nuclear structure to the quadrupolar NMR interaction and high-resolution spectroscopy. *Progress in Nuclear Magnetic Resonance Spectroscopy* **46,** 63–78 (2005).
[12] Fernandez, C. & Pruski, M. Probing Quadrupolar Nuclei by Solid-State NMR Spectroscopy: Recent Advances. in *Solid State NMR* (ed. Chan, J. C. C.) **306,** 119–188 (Springer Berlin Heidelberg, 2011).
[13] Siegel, R., Nakashima, T. T. & Wasylishen, R. E. Sensitivity enhancement of NMR spectra of half-integer quadrupolar nuclei in the solid state via population transfer. *Concepts Magn. Reson.* **26A,** 47–61 (2005).
[14] Madhu, P. K., Goldbourt, A., Frydman, L. & Vega, S. Sensitivity enhancement of the MQMAS NMR experiment by fast amplitude modulation of the pulses. *Chemical Physics Letters* **307,** 41–47 (1999).
[15] Yao, Z., Kwak, H.-T., Sakellariou, D., Emsley, L. & Grandinetti, P. J. Sensitivity enhancement of the central transition NMR signal of quadrupolar nuclei under magic-angle spinning. *Chemical Physics Letters* **327,** 85–90 (2000).
[16] Kentgens, A. P. M. & Verhagen, R. Advantages of double frequency sweeps in static, MAS and MQMAS NMR of spin I=3/2 nuclei. *Chemical Physics Letters* **300,** 435–443 (1999).
[17] Siegel, R., Nakashima, T. T. & Wasylishen, R. E. Signal enhancement of NMR spectra of half-integer quadrupolar nuclei in solids using hyperbolic secant pulses. *Chemical Physics Letters* **388,** 441–445 (2004).
[18] Hung, I. & Gan, Z. On the practical aspects of recording wideline QCPMG NMR spectra. *Journal of Magnetic Resonance* **204,** 256–265 (2010).
[19] Larsen, F. H., Jakobsen, H. J., Ellis, P. D. & Nielsen, N. C. Sensitivity-Enhanced Quadrupolar-Echo NMR of Half-Integer Quadrupolar Nuclei. Magnitudes and Relative Orientation of Chemical Shielding and Quadrupolar Coupling Tensors. *J. Phys. Chem. A* **101,** 8597–8606 (1997).
[20] Baltisberger, J. H. *et al.* Communication: Phase incremented echo train acquisition in NMR spectroscopy. *The Journal of Chemical Physics* **136,** 211104 (2012).
[21] Siegel, R., Nakashima, T. T. & Wasylishen, R. E. Application of Multiple-Pulse Experiments to Characterize Broad NMR Chemical-Shift Powder Patterns from Spin-1/2 Nuclei in the Solid State. *J. Phys. Chem. B* **108,** 2218–2226 (2004).

[22] Siegel, R., Nakashima, T. T. & Wasylishen, R. E. Signal-to-noise enhancement of NMR spectra of solids using multiple-pulse spin-echo experiments. *Concepts Magn. Reson.* **26A,** 62–77 (2005).
[23] Samoson, A., Lippmaa, E. & Pines, A. High resolution solid-state N.M.R.: Averaging of second-order effects by means of a double-rotor *Molecular Physics* **65,** 1013–1018 (1988).
[24] Mueller, K. T. *et al.* Dynamic-angle spinning of quadrupolar nuclei. *Journal of Magnetic Resonance (1969)* **86,** 470–487 (1990).
[25] Medek, A., Harwood, J. S. & Frydman, L. Multiple-Quantum Magic-Angle Spinning NMR: A New Method for the Study of Quadrupolar Nuclei in Solids. *J. Am. Chem. Soc.* **117,** 12779–12787 (1995).
[26]Z Gan, Satellite transition magic-angle spinning nuclear magnetic resonance spectroscopy of half-integer quadrupolar nuclei. *The Journal of Chemical Physics* **114,** 10845–10853 (2001).
[27] Amoureux, J.-P., Huguenard, C., Engelke, F. & Taulelle, F. Unified representation of MQMAS and STMAS NMR of half-integer quadrupolar nuclei. *Chemical Physics Letters* **356,** 497–504 (2002).
[28] Amoureux, J.-P., Fernandez, C. & Steuernagel, S. *ZFiltering in MQMAS NMR*. (Academic Press, 1996).
[29] Brown, S. P. & Wimperis, S. Two-Dimensional Multiple-Quantum MAS NMR of Quadrupolar Nuclei: A Comparison of Methods. *Journal of Magnetic Resonance* **128,** 42–61 (1997).
[30] Siegel, R., Nakashima, T. T. & Wasylishen, R. E. Sensitivity enhancement of MQMAS NMR spectra of spin 3/2 nuclei using hyperbolic secant pulses. *Chemical Physics Letters* **403,** 353–358 (2005).
[31] Vosegaard, T., Larsen, F. H., Jakobsen, H. J., Ellis, P. D. & Nielsen, N. C. Sensitivity-Enhanced Multiple-Quantum MAS NMR of Half-Integer Quadrupolar Nuclei. *J. Am. Chem. Soc.* **119,** 9055–9056 (1997).
[32] Kwak, H.-T. & Gan, Z. Double-quantum filtered STMAS. *Journal of Magnetic Resonance* **164,** 369–372 (2003).
[33] Trebosc, J., Amoureux, J.-P. & Gan, Z. Comparison of high-resolution solid-state NMR MQMAS and STMAS methods for half-integer quadrupolar nuclei. *Solid State Nuclear Magnetic Resonance* **31,** 1–9 (2007).
[34] Martineau, C. *et al.* High-resolution through-space correlations between spin-1/2 and half-integer quadrupolar nuclei using the MQ-D-R-INEPT NMR experiment. *Phys. Chem. Chem. Phys.* **14,** 7112–7119 (2012).
[35] Jaroniec, C. P. Dipolar recoupling: heteronuclear. *eMagRes* (2009).
[36] Gullion, T. Introduction to rotational-echo, double-resonance NMR. *Concepts Magn. Reson.* **10,** 277–289 (1998).
[37] Jaroniec, C. P., Tounge, B. A., Rienstra, C. M., Herzfeld, J. & Griffin, R. G. Recoupling of Heteronuclear Dipolar Interactions with Rotational-Echo Double-Resonance at High Magic-Angle Spinning Frequencies. *Journal of Magnetic Resonance* **146,** 132–139 (2000).
[38] Levitt, M. H. Symmetry-Based Pulse Sequences in Magic-Angle Spinning Solid-State NMR. in *eMagRes* (John Wiley & Sons, Ltd, 2007).
[39] Brinkmann, A. & Levitt, M. H. Symmetry principles in the nuclear magnetic resonance of spinning solids: Heteronuclear recoupling by generalized Hartmann–Hahn sequences. *The Journal of Chemical Physics* **115,** 357 (2001).
[40] Zhao, X., Edén, M. & Levitt, M. H. Recoupling of heteronuclear dipolar interactions in solid-state NMR using symmetry-based pulse sequences. *Chemical Physics Letters* **342,** 353–361 (2001).

[41] Brinkmann, A. & Kentgens, A. P. M. Proton-Selective 17O−H Distance Measurements in Fast Magic-Angle-Spinning Solid-State NMR Spectroscopy for the Determination of Hydrogen Bond Lengths. *J. Am. Chem. Soc.* **128,** 14758–14759 (2006).
[42] Lafon, O. *et al.* Indirect Detection via Spin-1/2 Nuclei in Solid State NMR Spectroscopy: Application to the Observation of Proximities between Protons and Quadrupolar Nuclei. *The Journal of Physical Chemistry A* **113,** 12864–12878 (2009).
[43] Fu, R., Smith, S. A. & Bodenhausen, G. Recoupling of heteronuclear dipolar interactions in solid state magic-angle spinning NMR by simultaneous frequency and amplitude modulation. *Chemical Physics Letters* **272,** 361–369 (1997).
[44] Lu, X. *et al.* Observation of proximities between spin-1/2 and quadrupolar nuclei: Which heteronuclear dipolar recoupling method is preferable? *The Journal of Chemical Physics* **137,** 144201 (2012).
[45] Fyfe, C. A., Wong-Moon, K. C., Huang, Y. & Grondey, H. INEPT Experiments in Solid-State NMR. *J. Am. Chem. Soc.* **117,** 10397–10398 (1995).
[46] Lesage, A., Sakellariou, D., Steuernagel, S. & Emsley, L. Carbon−Proton Chemical Shift Correlation in Solid-State NMR by Through-Bond Multiple-Quantum Spectroscopy. *J. Am. Chem. Soc.* **120,** 13194–13201 (1998).
[47] Amoureux, J. P., Trebosc, J., Wiench, J. & Pruski, M. HMQC and refocused-INEPT experiments involving half-integer quadrupolar nuclei in solids. *Journal of Magnetic Resonance* **184,** 1–14 (2007).
[48] Ishii, Y. & Tycko, R. Sensitivity Enhancement in Solid State 15N NMR by Indirect Detection with High-Speed Magic Angle Spinning. *Journal of Magnetic Resonance* **142,** 199–204 (2000).
[49] Elena, B., Lesage, A., Steuernagel, S., Böckmann, A. & Emsley, L. Proton to Carbon-13 INEPT in Solid-State NMR Spectroscopy. *J. Am. Chem. Soc.* **127,** 17296–17302 (2005).
[50] Cavadini, S., Lupulescu, A., Antonijevic, S. & Bodenhausen, G. Nitrogen-14 NMR Spectroscopy Using Residual Dipolar Splittings in Solids. *J. Am. Chem. Soc.* **128,** 7706–7707 (2006).
[51] Fyfe, C. A., Grondey, H., Mueller, K. T., Wong-Moon, K. C. & Markus, T. Coherence transfer involving quadrupolar nuclei in solids: aluminum-27 .tautm. phosphorus-31 cross-polarization NMR in the molecular sieve VPI-5. *J. Am. Chem. Soc.* **114,** 5876–5878 (1992).
[52] Vega, A. J. CPMAS of quadrupolar S= 32 nuclei. *Solid State Nuclear Magnetic Resonance* **1,** 17–32 (1992).
[53] Hu, B., Amoureux, J. P., Trébosc, J. & Hafner, S. Through-space MP-CPMAS experiments between spin-1/2 and half-integer quadrupolar nuclei in solid-state NMR. *Journal of Magnetic Resonance* **192,** 8–16 (2008).
[54] Trebosc, J., Hu, B., Amoureux, J. P. & Gan, Z. Through-space R3-HETCOR experiments between spin-1/2 and half-integer quadrupolar nuclei in solid-state NMR. *Journal of Magnetic Resonance* **186,** 220–227 (2007).
[55] Venkatesh, A., Hanrahan, M. P. & Rossini, A. J. Proton detection of MAS solid-state NMR spectra of half-integer quadrupolar nuclei. *Solid State Nuclear Magnetic Resonance* **84,** 171–181 (2017).
[56] Zhao, X., Hoffbauer, W., Schmedt auf der Günne, J. & Levitt, M. H. Heteronuclear polarization transfer by symmetry-based recoupling sequences in solid-state NMR. *Solid State Nuclear Magnetic Resonance* **26,** 57–64 (2004).
[57] Perras, F. A., Kobayashi, T. & Pruski, M. Natural Abundance 17O DNP Two-Dimensional and Surface-Enhanced NMR Spectroscopy. *J. Am. Chem. Soc.* **137,** 8336–8339 (2015).
[58] Gan, Z., Amoureux, J. P. & Trébosc, J. Proton-detected 14N MAS NMR using homonuclear decoupled rotary resonance. *Chemical Physics Letters* **435,** 163–169 (2007).

[59] Z. Gan, D.M. Grant, R.R. Ernst, NMR chemical shift anisotropy measurements by RF driven rotary resonance., Chem. Phys. Lett. 254 (1996)
[60]Z. Gan, Rotary resonance echo double resonance for measuring heteronuclear dipolar coupling under MAS., J. Magn. Reson. 183 (2006) 235–241.
[61] Shen, M. *et al.* Improving the resolution in proton-detected through-space heteronuclear multiple quantum correlation NMR spectroscopy. *Journal of Magnetic Resonance* **245,** 38–49 (2014).
[62] Hu, B., Trébosc, J. & Amoureux, J. P. Comparison of several hetero-nuclear dipolar recoupling NMR methods to be used in MAS HMQC/HSQC. *Journal of Magnetic Resonance* **192,** 112–122 (2008).
[63] Tricot, G. *et al.* Structural characterisation of phosphate materials: new insights into the spatial proximities between phosphorus and quadrupolar nuclei using the D-HMQC MAS NMR technique. *Phys. Chem. Chem. Phys.* **13,** 16786–16794 (2011).
[64] Pourpoint, F. *et al.* Advances in Structural Studies on Alkylaluminum Species in the Solid State via Challenging 27Al–13C NMR Spectroscopy and X-ray Diffraction. *J. Phys. Chem. C* **117,** 18091–18099 (2013).
[65] Li, S. *et al.* Host–Guest Interactions in Dealuminated HY Zeolite Probed by 13C–27Al Solid-State NMR Spectroscopy. *J. Phys. Chem. Lett.* **5,** 3068–3072 (2014).
[66] Pourpoint, F. *et al.* Probing 27Al–13C proximities in metal–organic frameworks using dynamic nuclear polarization enhanced NMR spectroscopy. *Chem. Commun.* **50,** 933–935 (2013).
[67] Wiench, J. W., Bronnimann, C. E., Lin, V. S.-Y. & Pruski, M. Chemical Shift Correlation NMR Spectroscopy with Indirect Detection in Fast Rotating Solids: Studies of Organically Functionalized Mesoporous Silicas. *J. Am. Chem. Soc.* **129,** 12076–12077 (2007).
[68] Robertson, A. J., Pandey, M. K., Marsh, A., Nishiyama, Y. & Brown, S. P. The use of a selective saturation pulse to suppress t 1 noise in two-dimensional 1 H fast magic angle spinning solid-state NMR spectroscopy. *Journal of Magnetic Resonance* **260,** 89–97 (2015).
[69] J. Rossini, A., P. Hanrahan, M. & Thuo, M. Rapid acquisition of wideline MAS solid-state NMR spectra with fast MAS, proton detection, and dipolar HMQC pulse sequences. *Physical Chemistry Chemical Physics* **18,** 25284–25295 (2016).
[70] Pandey, M. K., Kato, H., Ishii, Y. & Nishiyama, Y. Two-dimensional proton-detected 35Cl/1H correlation solid-state NMR experiment under fast magic angle sample spinning: application to pharmaceutical compounds. *Phys. Chem. Chem. Phys.* **18,** 6209–6216 (2016).
[71] Duong, N. T. & Nishiyama, Y. Satellite and central transitions selective 1H/{27Al} D-HMQC experiments at very fast MAS for quadrupolar couplings determination. *Solid State Nuclear Magnetic Resonance* (2017).
[72] Wang, S. H., De Paul, S. M. & Bull, L. M. High-Resolution Heteronuclear Correlation between Quadrupolar and Spin-12 Nuclei Using Multiple-Quantum Magic-Angle Spinning. *Journal of Magnetic Resonance* **125,** 364–368 (1997).
[73] Wiench, J. W. & Pruski, M. Probing through bond connectivities with MQMAS NMR. *Solid State Nuclear Magnetic Resonance* **26,** 51–55 (2004).
[74] Trébosc, J., Lafon, O., Hu, B. & Amoureux, J.-P. Indirect high-resolution detection for quadrupolar spin-3/2 nuclei in dipolar HMQC solid-state NMR experiments. *Chemical Physics Letters* **496,** 201–207 (2010).
[75] Thrippleton, M. J., Ball, T. J., Steuernagel, S., Ashbrook, S. E. & Wimperis, S. STARTMAS: A MAS-based method for acquiring isotropic NMR spectra of spin I=3/2 nuclei in real time. *Chemical Physics Letters* **431,** 390–396 (2006).
[76] Wang, Q. *et al.* Signal enhancement of J-HMQC experiments in solid-state NMR involving half-integer quadrupolar nuclei. *Chem. Commun.* **49,** 6653–6655 (2013).

Chapter 2: ^{71}Ga-^{77}Se connectivities and proximities in gallium selenide crystal and glass probed by solid-state NMR

2.1. Introduction

Chalcogenide glasses are technologically important materials that can be suitably designed to exhibit many interesting physical properties including high transparency in the infrared range, low phonon energy, high optical nonlinearity, large photo-sensitivity, and high ionic conductivity.[1–7] Beyond the usual systems based on Ge-Sb-Se or Ge-As-Se moieties, one of the pseudo-binary systems that display glass-forming ability over a significant composition range is Ga_2Se_3-$GeSe_2$.[8] Previous studies using Raman, X-ray photo-electron (XPS), extended X-ray absorption fine-structure (EXAFS), as well as ^{77}Se and ^{71}Ga solid-state NMR (SS-NMR) spectroscopies, have shown that the structure of these gallium and germanium selenide glasses (denoted GGS hereafter) is composed predominantly of a network of corner-sharing (CS) $GaSe_4$ and/or $GeSe_4$ tetrahedra and a small fraction of edge-shared (ES) $GaSe_4$ and/or $GeSe_4$ tetrahedra, in which the Ga, Ge, and Se atoms are covalently bonded to 4, 4, and 2 neighboring atoms, respectively.[9–13] The tetra-coordinated Ga and Ge sites as well as the di-coordinated Se ones are denoted Ga^{IV}, Ge^{IV} and Se^{II} hereafter. XPS and ^{71}Ga SS-NMR spectroscopy have demonstrated that the addition of Ga_2Se_3 increases the deficiency in Se and leads to the formation of Ge-Ge bonds and $_3(Se^{II})$-Ge-Ge-$(Se^{II})_3$ units, which are distributed in such way that any clustering of these units is avoided.[11,12] Furthermore, Raman spectroscopy and ^{77}Se SS-NMR studies, including two-dimensional (2D) ^{77}Se MATPASS/CPMG (Magic-Angle Turning-Phase Adjusted Spinning Sidebands with Carr-Purcell-Meiboon-Gill detection) experiments, have shown the formation of tri-coordinated Se atoms (Se^{III}) in GGS glasses with high content of Ga_2Se_3 (> 25 % mol).[12,13] The formation of these sites provides another mechanism to accommodate the deficiency in Se atoms. These Se^{III} atoms mainly replace the Se^{II} ones in the CS $GaSe_4$ and/or $GeSe_4$ tetrahedra.

As mentioned above, SS-NMR is a precious tool to characterize the local environment of atoms in GGS glasses. ^{77}Se isotope possesses a nuclear spin of 1/2, a gyromagnetic ratio similar to that of ^{29}Si nucleus ($\gamma_{77Se} \approx 0.96\gamma_{29Si} \approx 0.76\gamma_{13C}$) and a low natural abundance, $NA_{77Se} \approx 7.63$ %.[14] As ^{29}Si nuclei, ^{77}Se isotope exhibits long longitudinal relaxation times, T_1, in solids. Furthermore, ^{77}Se NMR resonances are often broad, notably for glasses. Such broadening further reduces the sensitivity since the total integrated intensity is spread over a broad spectral width. Ga element has two stable NMR-active isotopes, ^{69}Ga and ^{71}Ga, both with spin-3/2. ^{69}Ga

is more abundant than ^{71}Ga ($NA_{69Ga} \approx 60.4$ % and $NA_{71Ga} \approx 39.6$ %), but the latter possesses higher gyromagnetic ratio ($\gamma_{69Ga} \approx 0.96\gamma_{13C}$ and $\gamma_{71Ga} \approx 1.22\gamma_{13C}$) and smaller quadrupole moment ($Q_{69Ga} = 17.1$ and $Q_{71Ga} = 10.7$ fm^2). Therefore, ^{71}Ga NMR experiments are more sensitive than ^{69}Ga ones. Nevertheless, even for ^{71}Ga isotope, the quadrupole interaction broadens the NMR resonance over hundreds of kHz and the detection of these broad powder patterns is often challenging. Finally, the detection of ^{73}Ge nuclei by SS-NMR spectroscopy remains extremely challenging owing to the unfavorable properties of this isotope: low gyromagnetic ratio ($\gamma_{73Ge} \approx 0.14\gamma_{13C}$), low natural abundance ($NA_{73Ge} \approx 7.76\%$) and large quadrupole moment ($Q_{73Ge} = -19.6$ fm^2). Nevertheless, ^{73}Ge SS-NMR spectra of germanium selenide glasses have been reported.[15]

A major limitation of this study is the lack of resolution of 1D NMR spectra of GGS glasses since the resonances are broaden by the distribution of local environments as well as the anisotropic interactions, such as Chemical Shift Anisotropy (CSA) for ^{77}Se nuclei and quadrupole interaction for ^{71}Ga and ^{73}Ge isotopes. Recently, 2D ^{77}Se CPMG experiments have allowed the measurement of one-bond *J*-coupling between ^{77}Se nuclei in arsenic selenide glasses.[16] Furthermore, it has been shown that the 2D MATPASS/CPMG sequence can improve the resolution of ^{77}Se signals for germanium selenide and GGS glasses by separating the isotropic chemical shift and the CSA in two distinct dimensions.[13,17] Nevertheless, to the best of our knowledge, the *J*-couplings between ^{77}Se and ^{71}Ga nuclei have not been measured so far. Similarly, neither through-bond nor through-space ^{77}Se-^{71}Ga hetero-nuclear correlation (*J*-HETCOR and *D*-HETCOR, respectively) 2D spectrum has been reported hitherto.

In this article, we introduce 2D ^{77}Se-^{71}Ga *J*-HETCOR and *D*-HETCOR experiments. These sequences are first tested on β-Ga_2Se_3 crystalline sample. Using high-magnetic field (21.1 T) and high Magic-Angle Spinning (MAS) frequency, $\nu_R = 62.5$ kHz, we observe for this sample, two distinct ^{71}Ga NMR signals, a narrow peak, accounting for 12 % of the total intensity, and a broad one. The narrow peak is assigned to Quenched phase in β-Ga_2Se_3 crystal. Previous SS-NMR studies at lower field and MAS frequency have only reported the observation of the narrow peak.[12] We also report high-resolution ^{71}Ga 2D spectrum of β-Ga_2Se_3 acquired by introducing Satellite Transition MAS (STMAS) experiment [18,19] using quadrupolar CPMG (QCPMG) detection [20] at 21.1 T and $\nu_R = 62.5$ kHz. The 2D ^{71}Ga STMAS-QCPMG spectrum allows separating the NMR signals of the Quenched phase and Annealed phase, but not those of the two Ga sites in Annealed phase.[21]

The 2D ^{77}Se-^{71}Ga through-bond spectra are acquired by introducing (i) the Refocused Insensitive Nuclei Enhanced by Polarization Transfer (*J*-RINEPT) experiment [22] with ^{71}Ga excitation and ^{77}Se CPMG detection [16], called ^{77}Se-{^{71}Ga}, as well as (ii) the Hetero-nuclear Multiple-Quantum Correlation (*J*-HMQC) experiment [23] with ^{71}Ga excitation and QCPMG detection, the ^{77}Se signal being indirectly detected, called ^{71}Ga-{^{77}Se}. Both ^{77}Se-{^{71}Ga} *J*-RINEPT-CPMG and ^{71}Ga-{^{77}Se} *J*-HMQC-QCPMG 2D spectra show the expected correlation between the broad ^{71}Ga signal of β-Ga_2Se_3 and the $^{77}Se^{II}$ and $^{77}Se^{III}$ signals. Furthermore, those spectra also exhibit a cross-peak between the ^{71}Ga narrow signal of the Quenched phase and the $^{77}Se^{III}$ signals. Such observation indicates that the Quenched phase is composed of Se^{III} sites. In addition, by fitting the evolution of the ^{77}Se-{^{71}Ga} *J*-RINEPT-CPMG and ^{71}Ga-{^{77}Se} *J*-HMQC-QCPMG signals as function of the defocusing and/or refocusing delays, τ and τ' (see **Fig.2.1**), we measure for the first time the one-bond and three-bonds *J*-couplings, denoted ^1J and ^3J, respectively, between ^{71}Ga isotope and $^{77}Se^{II}$ as well as $^{77}Se^{III}$ nuclei. The 2D ^{77}Se-^{71}Ga through-space spectrum is acquired by introducing the ^{71}Ga-{^{77}Se} dipolar-mediated HMQC experiment (*D*-HMQC) [24,25] with QCPMG detection. The ^{71}Ga-^{77}Se dipolar couplings are reintroduced under MAS conditions by applying the Simultaneous Frequency and Amplitude Modulation ($SFAM_1$) recoupling [26–28] during the defocusing and refocusing delays. The sensitivity between through-space and through-bond correlation experiment is compared.

These 2D ^{77}Se-^{71}Ga *J*- and *D*-HETCOR experiments are then applied to characterize the GGS glass xGa_2Se_3–(1-x) $GeSe_2$ with x = 0.2 (denoted $GGS_{0.2}$ hereafter). The GGS_x glass-ceramics are a good alternative to single-crystalline Ge and polycrystalline ZnSe materials for making lenses transparent in the IR range for thermal imaging applications. The $GGS_{0.2}$ composition leads to a homogeneous and reproducible glass-ceramic using suitable heat treatment over its glass transition temperature. For this sample, the controlled nucleation rate is assumed to be due to a specific phenomenon of phase separation.[8] The same behavior has been observed as well in sulfide based glasses of the same composition, highlighting the important role of gallium during the nucleation process.[11,29] The obtained glass-ceramics present enhanced mechanical properties, while keeping an excellent transparency in the mid-infrared range. The ^{77}Se-^{71}Ga *J*- and *D*-HETCOR 2D spectra permit to resolve and identify molecular units containing Ga and Se atoms in $GGS_{0.2}$ glass. Furthermore, the evolution of ^{77}Se-{^{71}Ga} *J*-RINEPT-CPMG and ^{71}Ga-{^{77}Se} *J*-HMQC-QCPMG signals as function of the τ delay allows the estimate of the $^1J_{^{71}Ga\text{-}^{77}Se}$ couplings and indicates that the ^{71}Ga-^{77}Se covalent bonds in $GGS_{0.2}$ glass are similar to those of β-Ga_2Se_3.

2.2. Methods

2.2.1. NMR methods

2.2.1.1. Acquiring ^{71}Ga 1D MAS spectra

As seen below, ^{71}Ga isotope in β-Ga_2Se_3 crystal and $GGS_{0.2}$ glass is subject to large quadrupole interactions. In order to improve the spectral resolution, ^{71}Ga 1D spectra were acquired at high magnetic field, B_0 = 21.1 T, and high MAS frequency, ν_R = 62.5 kHz, since for quadrupolar nuclei the resolution is proportional to $(B_0)^2$ and MAS can improve the spectral resolution by a factor of ca. 3 by partially averaging the second-order broadening, at least when the spinning sidebands are separated from the center-bands. As seen in **Fig.2.5(b), (d)**, the MAS averaged line-width of the central transition (CT) between energy levels ±1/2 of ^{71}Ga nuclei extends over 60 kHz in β-Ga_2Se_3 crystal and $GGS_{0.2}$ glass, and hence a high MAS frequency of $\nu_R \geq 60$ kHz is required.

2.2.1.2 CPMG and QCPMG.

As explained in the introduction, ^{71}Ga and ^{77}Se spectra of GGS glasses exhibit wide powder patterns, which result in low sensitivity. Nevertheless, for these isotopes, the decay of the maximum of the echo signal for increasing spin echo delay is often much slower than that the Free-Induction Decay. Consequently, the sensitivity can be enhanced by acquiring multiple rotor-synchronized echoes in the form of the CPMG scheme for ^{77}Se nuclei [16] and QCPMG sequence for ^{71}Ga one.[30]

2.2.1.3. ^{71}Ga STMAS-QCPMG.

A high-resolution ^{71}Ga spectrum was acquired by introducing the STMAS-QCPMG sequence. The STMAS method offers the advantage to be typically 2-8 times more sensitive than the Multiple-Quantum MAS (MQMAS) scheme. Another advantage of STMAS for the acquisition of high-resolution ^{71}Ga spectra is that the sensitivity of this technique does not depend on the MAS frequency, and hence, STMAS-QCPMG spectra can be acquired at MAS frequency ($\nu_R \geq 60$ kHz) sufficiently high to separate the spinning sidebands from the center-bands. Conversely, for MQMAS, the sensitivity decreases with increasing MAS frequency.[31] The employed STMAS-QCPMG sequence is shown in **Fig.2.1**. A z-filter is used to produce pure absorption line-shapes.[18] Furthermore, the split-t_1 approach is used so that the isotropic spectrum results from a projection onto the F_1 dimension, without any shearing data treatment.[19] As ^{71}Ga is a spin-3/2 isotope, the t_1 period is partitioned into two delays $t_1/9$ and $8t_1/9$. The CT-selective pulse separating the two parts converts the ±1Q single-quantum

coherences evolving during $t_1/9$ into ±2Q double-quantum coherences evolving during $8t_1/9$. The coherence pathways are selected using phase cycling. The selection of 2Q coherences eliminates the undesired CT-CT diagonal ridge. QCPMG recycling was applied during the acquisition period, t_2. The delay between the QCPMG π-pulses was long enough so that both echo and anti-echo signals could be detected without truncation. The quadrature along the indirect dimension was achieved using the States-TPPI procedure [32] by incrementing the phase of the initial π/2-pulse.

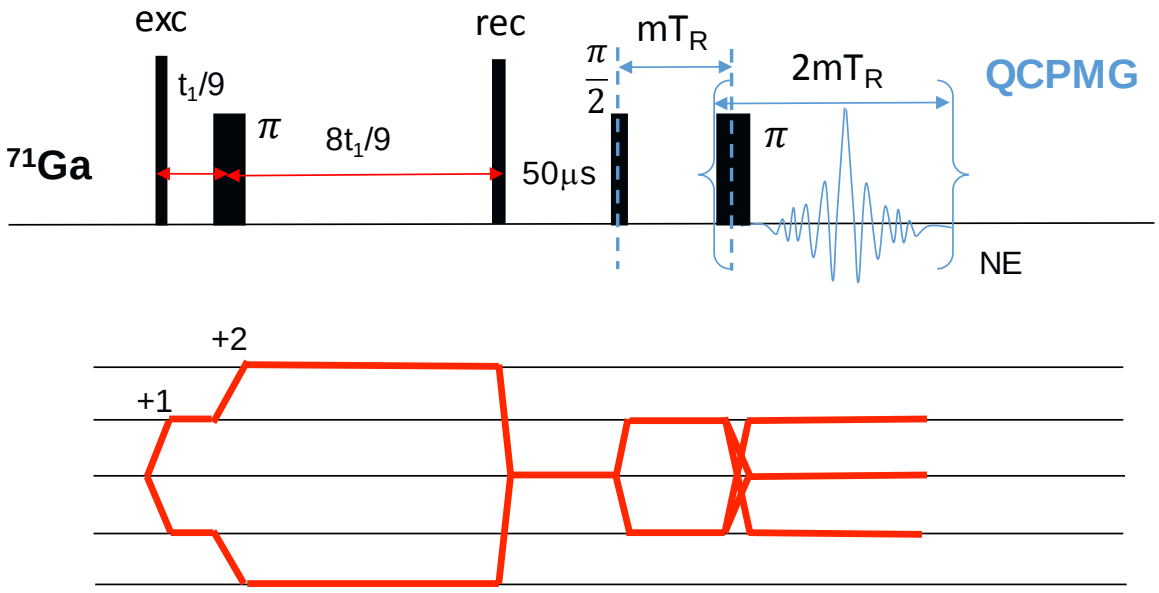

Fig.2.1. Employed pulse sequence and coherence pathways diagram for 2D ^{71}Ga split-t_1 amplitude-modulated *z*-filter STMAS-QCPMG experiment. The first and third pulses are applied with high rf-fields to excite and reconvert both CT and satellite transition (ST) of ^{71}Ga nuclei, whereas the other pulses are applied with low rf-field so that they are CT selective.

2.2.1.4. ^{77}Se-{^{71}Ga} *J*-RINEPT-CPMG.

The ^{77}Se-{^{71}Ga} *J*-RINEPT-CPMG scheme is shown in **Fig**.2.2(a). It derives from the *J*-RINEPT sequence [22] by applying the CPMG recycling of magnetization during the t_2 period. The initial selective π/2-pulse excites the ^{71}Ga CT magnetization, which is encoded by ^{71}Ga isotropic chemical shifts and second-order quadrupolar couplings as well as $J_{71Ga\text{-}77Se}$ couplings during the t_1 period. During the defocusing period, τ, the simultaneous π-pulses on the ^{71}Ga and ^{77}Se channels refocus the evolution under ^{71}Ga isotropic shifts but not that under the $J_{71Ga\text{-}77Se}$ couplings and hence, the ^{71}Ga in-phase CT with respect to ^{77}Se is converted into antiphase CT. The simultaneous π/2-pulses on ^{71}Ga and ^{77}Se channels convert this antiphase CT of ^{71}Ga nuclei

into antiphase ^{77}Se 1Q coherences. During the refocusing period, τ', ^{77}Se isotropic shift is refocused and the antiphase ^{77}Se 1Q coherences evolve under ^{71}Ga-^{77}Se *J*-couplings into in-phase ^{77}Se magnetization. Thus, the refocusing period yields in phase multiplets, for which the intensities of the different components add constructively, and hence, enhance signal intensity since the different components of the multiplets overlap and the decay of ^{77}Se 1Q coherence during τ' delay is slow.

2.2.1.5. ^{71}Ga-{^{77}Se} *J*- or *D*-HMQC-QCPMG.

The ^{71}Ga-{^{77}Se} *J*-HMQC-QCPMG scheme is displayed in **Fig.2.2(b)**. The sequence is similar to the *J*-HMQC scheme,[23] but the QCPMG recycling of magnetization is employed during the t_2 period. During the defocusing delay, τ, the in-phase ^{71}Ga CT evolves into antiphase one and is then converted into ^{71}Ga-^{77}Se multiple-quantum coherences by the π/2-pulse on ^{77}Se channel. These coherences are encoded by the ^{77}Se isotropic chemical shift before being converted back into anti-phase ^{71}Ga CT by the second ^{77}Se π/2-pulse. The ^{71}Ga-{^{77}Se} *D*-HMQC-QCPMG sequence is similar to that shown in **Fig.2.2(b)**, but $SFAM_1$ recoupling is applied on the ^{77}Se channel during the two delays τ in order to refocus the evolution under $J_{^{71}Ga-^{77}Se}$ couplings, while reintroducing the ^{71}Ga-^{77}Se dipolar couplings.

2.2.1.6. Measurement of $T'_{2,^{71}Ga}$ and $T'_{2,^{77}Se}$ time constants.

The T'_2 time constant characterizes the exponential decay of the maximum signal in spin-echo experiments. As explained below, these time constants for ^{71}Ga and ^{77}Se nuclei appear in the analytical expression of ^{77}Se-{^{71}Ga} *J*-RINEPT-CPMG and ^{71}Ga-{^{77}Se} *J*-HMQC-QCPMG experiments. Therefore, the independent measurement of these T'_2 values yields more accurate ^{71}Ga-^{77}Se *J*-couplings by better constraining the fit of signals to the analytical expression. Here, the $T'_{2,^{71}Ga}$ constant was measured using a spin echo experiment with QCPMG detection (see **Fig.2.2(d)**). The $T'_{2,^{77}Se}$ constants were determined using a spin echo experiment with CPMG detection. However, the sensitivity was improved by replacing the initial π/2-pulse by a ^{71}Ga → ^{77}Se *J*-RINEPT polarization transfer. Such transfer improves the sensitivity since the ^{71}Ga gyromagnetic ratio is higher than that of ^{77}Se isotope and the longitudinal relaxation times of ^{71}Ga nuclei (about 0.6 s for the investigated samples) are much shorter than those of ^{77}Se isotopes (larger than 100 s).

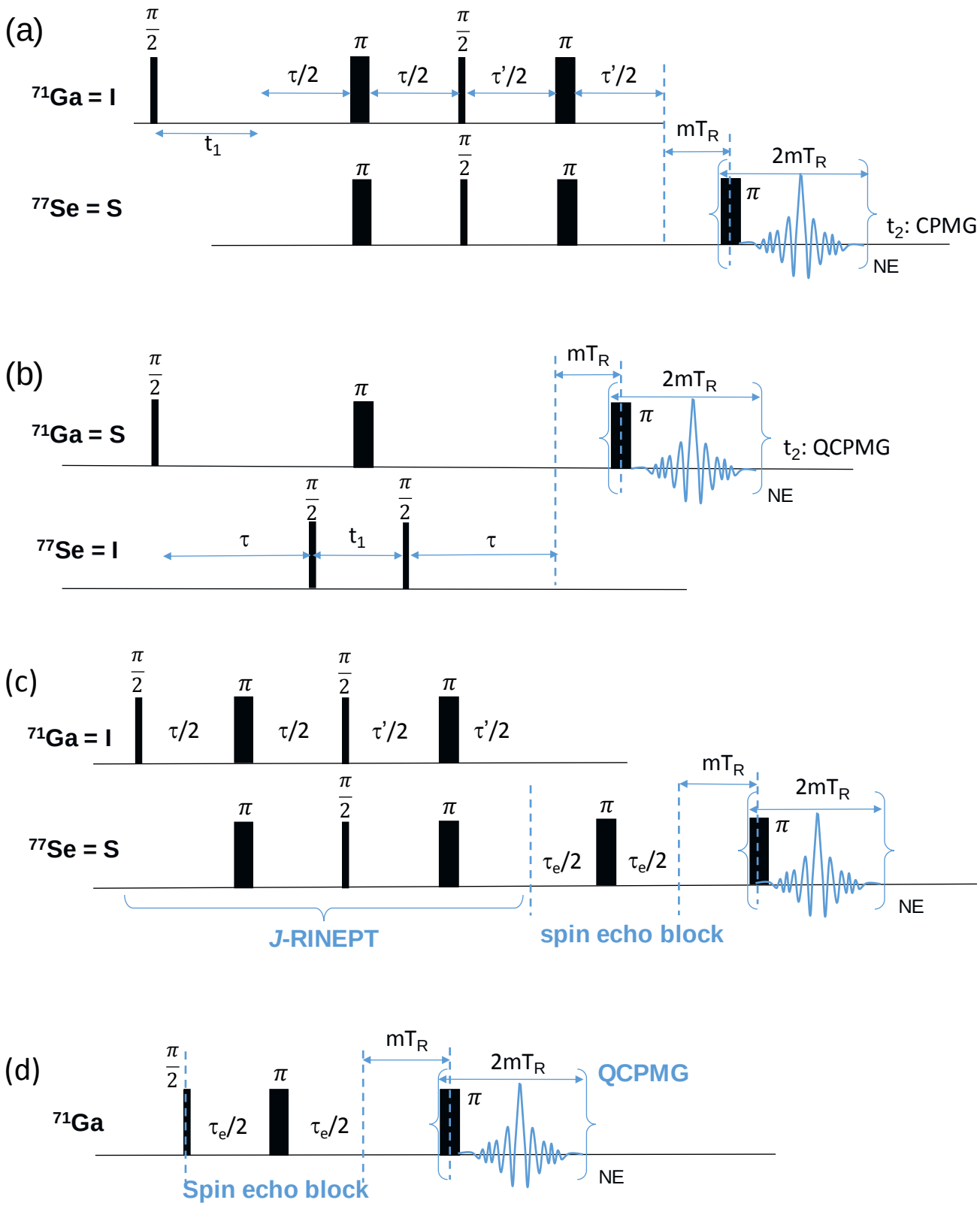

Fig.2.2. (a,b) Employed 2D ^{71}Ga-^{77}Se through-bond correlation sequences: (a) ^{77}Se-{^{71}Ga} *J*-RINEPT-CPMG and (b) ^{71}Ga-{^{77}Se} *J*-HMQC-QCPMG. (c,d) Sequences used to measure the (c) ^{77}Se and (d) ^{71}Ga T'_2 values. All sequences employ ^{71}Ga excitation in order to improve the sensitivity since the longitudinal relaxation of ^{71}Ga nuclei is much faster than that of ^{77}Se. All pulses applied to the ^{71}Ga nuclei in these sequences selectively excite the CT.

2.2.2. Analytical expression of ^{77}Se-{^{71}Ga} *J*-RINEPT and ^{71}Ga-{^{77}Se} *J*-HMQC

The analytical expressions of ^{77}Se-{^{71}Ga} *J*-RINEPT-CPMG and ^{71}Ga-{^{77}Se} *J*-HMQC-QCPMG transfer efficiencies are required for the determination of $J_{71Ga\text{-}77Se}$ couplings by the fit of the evolution of their experimental signals as function of the τ and τ' delays.

The global transfer efficiencies are the sum of those for the different spin systems in the sample, weighted by their abundance since the analytical expression of the transfer efficiency depends on the number of ^{71}Ga and ^{77}Se nuclei in the spin system. As seen below, the fit of the evolution of *J*-RINEPT and *J*-HMQC signals as function of the τ and τ' delays only allows the determination of a limited number of adjustable parameters. In order to reduce this number, we assumed that the *J*-couplings through a given number of bonds between ^{71}Ga isotope and ^{77}Se nucleus occupying both sites, Se^{II} or Se^{III}, are all identical. Such assumption is a simplification since for instance, the $^3J_{71Ga\text{-}77Se}$ coupling through the ^{71}Ga-Se-Ga-^{77}Se three bonds must depend a priori on the torsion angle around the Se-Ga middle bond. Furthermore, for β-Ga_2Se_3, the $^1J_{71Ga\text{-}77Se}$ couplings were not sufficient to describe the evolution of the *J*-RINEPT and *J*-HMQC signals and the contribution of coherence transfer through $^3J_{71Ga\text{-}77Se}$ couplings had to be included.

Using the above assumption, it can be shown that the transfer efficiency, *f*, of ^{71}Ga-{^{77}Se} *J*-HMQC-QCPMG scheme is given by

$$f(\tau) = \left\{ \begin{matrix} m\left[\sum_{p=1}^{m} p\alpha_p^m \, s_{1J}^2 c_{1J}^{2p-2}\left(\alpha_0^n + \sum_{q=1}^{n} q\alpha_q^n c_{3J}^{2q}\right)\right] \\ +n\left[\sum_{q=1}^{n} q\alpha_q^n \, s_{3J}^2 c_{3J}^{2q-2}\left(\alpha_0^m + \sum_{p=1}^{m} p\alpha_p^m c_{1J}^{2p}\right)\right] \end{matrix} \right\} \exp\left(-\frac{2\tau}{T'_{2,71Ga}}\right) \quad (2.1)$$

where *m* and *n* denotes the numbers of Se atoms connected to one ^{71}Ga nucleus by one- and three-bonds, respectively, α_r^l with *l* = *m* or *n* and *r* = *p* or *q* denotes the fraction of *r* ^{77}Se nuclei among the *l* Se atoms connected to the Ga atom, $c_{xJ}^y = \cos^y(\pi\, {}^xJ\tau)$ and $s_{xJ}^y = \sin^y(\pi\, {}^xJ\tau)$. In Eq.(2.1), the first and second terms correspond to ^1J and ^3J transfers, respectively. The α_r^l fraction are given by

$$\alpha_r^l = C_r^l (1 - \mathrm{NA}_{77Se})^{l-r} . \mathrm{NA}_{77Se}^r \quad (2.2)$$

where C_r^l denotes the *r*-combination of a set *l*. In β-Ga_2Se_3, according to the crystal structure [21], we have *m* = 4 and *n* = 18.

Similarly, it can be shown that the transfer efficiency of ^{77}Se-{^{71}Ga} *J*-RINEPT-CPMG scheme is given by

$$f(\tau,\tau') = \left\{ m\left[\sum_{p=1}^{m} p\alpha_p^m \left[m' \sum_{p'=1}^{m'} p'\alpha'^{m'}_{p'}\, s_{1J}s'_{1J}c_{1J}^{p-1}c'^{p'-1}_{1J}\left(\alpha_0^n + \sum_{q=1}^{n} q\alpha_q^n c_{3J}^q\right)\left(\alpha'^{n'}_0 + \sum_{q'=1}^{n'} q'\alpha'^{n'}_{q'}c_{3J}^{q'}\right)\right]\right] + n\left[\sum_{q=1}^{n} q\alpha_q^n \left[n' \sum_{q'=1}^{n'} q'\alpha'^{n'}_{q'}\, s_{3J}s'_{3J}c_{3J}^{q-1}c'^{q'-1}_{3J}\left(\alpha_0^m + \sum_{p=1}^{m} p\alpha_p^m c_{1J}^p\right)\left(\alpha'^{m'}_0 + \sum_{p'=1}^{m'} p'\alpha'^{m'}_{p'}c_{1J}^{p'}\right)\right]\right]\right\} \exp\left(-\frac{\tau}{T'_{2,71Ga}} - \frac{\tau'}{T'_{2,77Se}}\right) \quad (2.3)$$

where *m*' and *n*' denotes the numbers of Ga atoms connected to a given ^{71}Se site by one- and three-bonds, respectively. In β-Ga_2Se_3, we have *m*' = 2 and *n*' = 11 for Se^{II} sites, *m*' = 3 and *n*' = 13 for $Se^{III,1}$ sites and *m*' = 3 and *n*' = 11 for $Se^{III,2}$ sites. As the ^{77}Se NMR signals of the two Se^{III} sites are not resolved (see **Fig.2.5**) and the unit cell contains identical number of $Se^{III,1}$ and $Se^{III,2}$ sites, we consider *m*' = 3 and *n*' = 12 for Se^{III} sites hereafter. The α'^l_r fraction are given by

$$\alpha'^l_r = C_r^l (1 - \mathrm{NA}_{71Ga})^{l-r}\, \mathrm{NA}_{71Ga}^r \quad (2.4)$$

2.3. Experimental section

2.3.1. Synthesis of crystalline β-Ga_2Se_3

β-Ga_2Se_3 crystals were synthesized according to the already published process.[3,16] High purity raw elements Ga (5N purity), and Se (N purity) were weighted (5 g), transferred into a 9 mm diameter silica tube, and sealed under a vacuum of 10^{-3} Pa. The ampoule was heated (+1.5 °C/min) up to 1100 °C and maintained at this temperature for 10 hours. The temperature was then decreased down to 950 °C and maintained for 12 hours in order to promote the crystallization of the Ga_2Se_3 compound. Then, the temperature was decreased with a ramp of -0.5 °C/min down to 880 °C. After 30 minutes at this temperature, the solid was quenched into water, then annealed at 550 °C for 840 hours, and finally removed out from the silica tube. The $GGS_{0.2}$ glass has been prepared following the classical melt-quenching way used for making infrared chalcogenide glasses. Further details have been given previously.[8]

2.3.2. Solid-state NMR

NMR spectra were recorded on Bruker BioSpin spectrometers operating either at B_0 = 9.4 T (wide-bore magnet equipped with Avance-II console) or 21.1 T (narrow-bore magnet equipped with Avance-IV console). Samples were spun either at ν_R = 20 kHz using 3.2 mm triple-resonance HXY probes for the 9.4 T magnet or at ν_R = 62.5 kHz using 1.3 mm double-resonance HX probe for the 21.1 T magnet. The ^{71}Ga and ^{77}Se isotropic chemical shifts were referenced to the resonance (0 ppm) of saturated aqueous solutions of $Ga(NO_3)_3$ and H_2SeO_3.

The 1D direct excitation ^{71}Ga MAS spectra were acquired using spin echo experiments, in which the refocusing pulse is bracketed by T_E delays. All other spectra were acquired using CPMG recycling in the case of ^{77}Se detection or QCPMG one in the case of ^{71}Ga detection. These schemes enhance the sensitivity by collecting a large number of echoes, *NE*. In the case of β-Ga_2Se_3 1D spectra, we have always used trains of π-pulses for the CPMG and QCPMG parts. However, ^{77}Se and ^{71}Ga spectra of $GGS_{0.2}$ are ca. twice broader than those of β-Ga_2Se_3. Therefore, (i) we have then used the maximum rf-fields available with our probes, and (ii) in the case of 1D spectra we have used trains of π/2-pulses for the CPMG/QCPMG recycling to broaden the excitation rf-profiles. Indeed, it has been recently shown that ‘π-pulses only provide a maximum intensity at the transmitter frequency’ and that one observes ‘only a slight loss in intensity at the transmitter frequency, accompanied by an increase in bandwidth, when the pulse-length of the train is shortened’.[33] Without the CPMG/QCPMG recycling, the RINEPT and HMQC sequences include two (**Fig.2.2(a)**) or one (**Fig.2.2(b)**) π-pulses on the detected

nucleus. Therefore, the rf-profile cannot be broadened by the use of π/2 pulses in the train of echoes, and hence we used π-pulses in these trains to maximize the S/N. A delay of 2ms rotor-periods between the CPMG or QCPMG pulses was used (**Fig.2.2**), leading to a total echo-time of $T_E = 2mT_R$. The amount of signal was maximized by using a minimal phase cycling of the (Q)CPMG scheme, i.e. a fixed phase of the pulses in the (Q)CPMG train. The phase of the (Q)CPMG pulses was shifted by 90° with respect to the preceding 90° pulse. This limited phase cycling avoids the destructive interferences between the two coherence pathways, and all possible coherence transfer pathways (i.e., 0Q and ±1Q) form echoes simultaneously if the sequence is correctly rotor-synchronized.[33] After the CPMG/QCPMG recycling, all echoes can be added on top of each other's with data processing and the spectra are then represented in a classical way, without any spikelet.

For split-t_1 STMAS experiment, the lengths and the radiofrequency (rf) nutation frequencies were equal to 1.25/0.8 μs and 215 kHz, respectively, whereas 155 kHz was used for the CT selective pulse.

$T'_{2,71Ga}$ measurements were recorded with a spin-echo-QCPMG sequence (**Fig.2.2(d)**). $T'_{2,77Se}$ measurements were performed with the J-RINEPT spin-echo-CPMG sequence as mentioned above (**Fig.2.2(c)**). In both cases, the spin-echo block was phase-cycled with four steps and always rotor synchronized.

For β-Ga_2Se_3, the separate evolutions for Se^{II} and Se^{III} species of the *J*-HMQC-QCPMG signal as function of τ delay were acquired by recording twenty-nine ^{71}Ga-{^{77}Se} 2D spectra. The pulse programs are given in the Appendix. All experimental specifications corresponding to spectra are given in **Table.2.1**.

Table.2.1. Experimental parameters for the spectra

Fig	B_0 /T	ν_R /kHz	$\nu_{1,77Se}$ /kHz	$\nu_{1,71Ga}$ /kHz	CPMG Tilt angle	T_E /ms	*NS*	*NE*	τ_{RD} /s	T_{exp} /h	τ /ms
2.5a	9.4	20	40	X	180	1	256	200	300	21.6	X
2.5b	21.1	62.5	X	155	90	0.48	102400	X	0.5	14.2	X
2.5c	9.4	20	63	X	90	0.2	72	1200	1200	24	X
2.5d	21.1	62.5	X	155	90	0.48	102400	X	0.5	14.2	X
2.6a,b	9.4	20	40	95	π	0.3	128	800	1.2	0.73	0.8
2.6c,d	9.4	20	X	95	π	0.2	64	600	1.0	0.57	X
2.7	21.1	62.5	X	215(1^{st},3^{rd}) 155 others	180	1.09	3072	20	0.6	14.3	X
2.8a	9.4	20	X	25	π	0.8	256	200	1	0.07	X
2.8b	9.4	20	X	95	$\pi/2$	0.8	256	200	1	0.07	X
2.9a-f	9.4	20	40	95	180	0.3	128	800	1.2	5.6	X
2.9g,h	9.4	20	40	95	180	0.1	128	600	1	17	X
2.10a-d	9.4	20	40	95	π	0.3	128	800	1.2	5.6	X
2.10e,f	9.4	20	40	95	π	0.1	128	600	1	17	X
2.11a	9.4	20	40	95	180	0.4	128	800	1	4.6	0.7
2.11b	9.4	20	40	95	180	0.1	128	600	1	1.2	0.8
2.11c	9.4	20	40	95	180	0.1	256	600	1	2.3	4
2.13	9.4	20	X	95	$\pi/2$	0.5	4096	100	1	1.13	X
2.14a	9.4	20	X	95	π	0.1	64	800	1.0	0.44	X
2.14b	9.4	20	63	95	π	0.2	512	1200	1.2	2.73	0.8
2.15a	9.4	20	40 63	95	180	0.3 0.2	128 1024	800 1200	1 1.2	4.6 25.5	X
2.15b	9.4	20	40 63	95	180	0.1	32 1024	600	1	1.4 20.6	X
2.16	9.4	20	63	95	π	0.4	30000	500	1.2	10	0.8
2.17a	9.4	20	63	95	180	0.3	2048	800	1	9.9	0.8
2.17b	9.4	20	63	95	180	0.1	512	500	1	10.7	0.8
2.17c	9.4	20	63	95	180	0.1	1024	500	1	21.5	3

2.4. Results and discussion

2.4.1. Crystalline β-Ga_2Se_3

The crystal structure of β-Ga_2Se_3 is composed of Annealed phase and Quenched phase according to this reference.[34] X-ray diffraction data of β-Ga_2Se_3 is shown in **Fig.2.3**.

For Annealed phase, the crystal system is the monoclinic (space group: B11b). There are two types of 4 fold coordinated Ga sites which are called $Ga^{IV,2}$ and $Ga^{IV,2}$. There are one 2 fold coordinated Se (Se^{II}) and two types of 3 fold coordinated Se site ($Se^{III,1}$ and $Se^{III,2}$).
In Gallium environment, $Ga^{IV,1}$ is connected to Se^{II}, $Se^{III,1}$ and two $Se^{III,2}$. On the other hand, $Ga^{IV,2}$ is connected to Se^{II}, two $Se^{III,1}$ and $Se^{III,2}$. $Ga^{IV,1}$ and $Ga^{IV,2}$ possess similar symmetry environment. In Selenium environment, Se^{II} is connected to $Ga^{IV,1}$ and $Ga^{IV,2}$. $Se^{III,1}$ is connected to $Ga^{IV,1}$ and two $Ga^{IV,2}$. $Se^{III,2}$ is connected to two $Ga^{IV,1}$ and $Ga^{IV,2}$. $Se^{III,1}$ and $Se^{III,2}$ possess similar symmetry environment. (see **Fig.2.4**).
In addition, Se^{II} – Ga^{IV} bond length is shorter than Se^{III} – Ga^{IV} bond length. This different bond length lead to distort the Ga tetrahedral environment. Each bond length value is represented in **Table.2.2**.
Ga vacancy get organized. It can be described as a ABCA'B'C' stacking (**Fig.2.5**). This ordering has effect on the cell

For Quenched phase, the crystal system is the cubic (Space group: F-43m) where all Ga^{IV} sites form regular tetrahedron with four Se. All Se are composed of Se^{III}. All Se^{III} – Ga^{IV} bond length is 2.358 (Å). Ga vacancy is random where Ga occupancy is 0.666 in the structure.

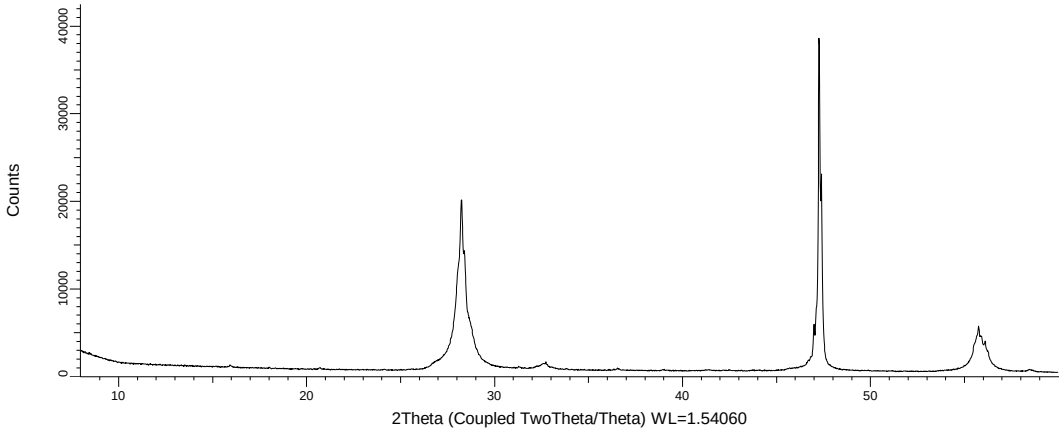

Fig.2.3. X-ray diffraction data of β-Ga_2Se_3.

Table.2.2. Each bond length of Se^{II} – Ga^{IV} in Annealed phase for β-Ga_2Se_3. Each value is adopted from [34].

Se^{II} – Ga^{IV} bond length (Å)		Se^{III} – Ga^{IV} bond length (Å)	
Se^{II} – $Ga^{IV,1}$	2.316	$Se^{III,1}$ – $Ga^{IV,1}$	2.466
Se^{II} – $Ga^{IV,2}$	2.338	$Se^{III,1}$ – $Ga^{IV,2}$	2.464
		$Se^{III,1}$ – $Ga^{IV,2}$	2.468
		$Se^{III,2}$ – $Ga^{IV,1}$	2.422
		$Se^{III,2}$ – $Ga^{IV,1}$	2.477
		$Se^{III,2}$ – $Ga^{IV,2}$	2.454

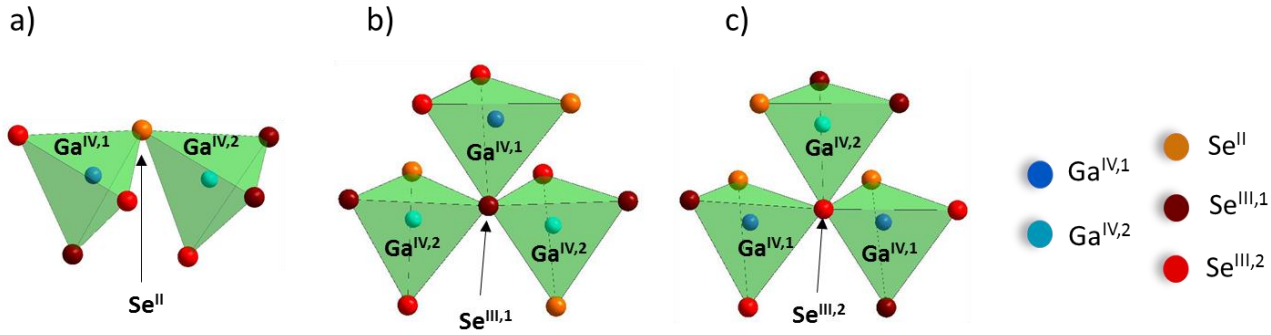

Fig.2.4. Representation of the three distinct selenium sites in Annealed phase of β-Ga_2Se_3.

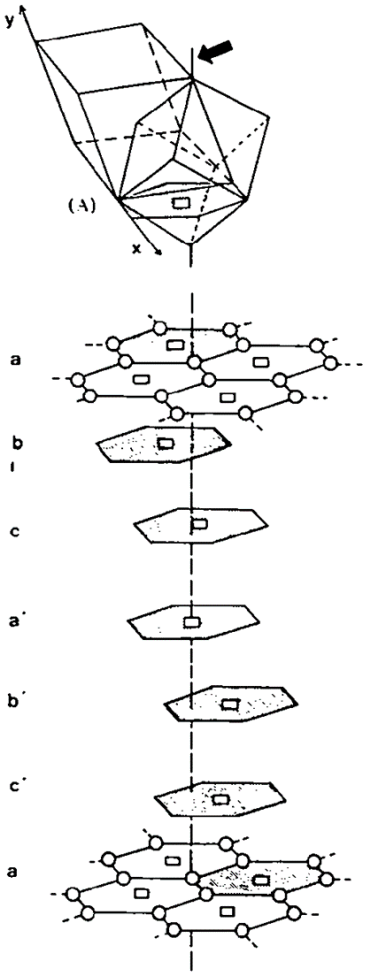

Fig.2.5. Organization of Ga vacancy in Annealed phase of β-Ga_2Se_3. Adopted from [34]

2.4.1.1. 1D MAS spectra

^{77}Se. The ^{77}Se 1D MAS spectrum is shown in **Fig.2.6(a)**. The Se^{II} and Se^{III} resonances are resolved but not those of crystallographically inequivalent $Se^{III,1}$ and $Se^{III,2}$ sites (see **Fig.2.4**). A quantitative measurement of the relative amounts of the different selenium sites is precluded using a CPMG sequence since the T'_2 values can differ between the Se^{II} and Se^{III} environments. Here, the T'_2 values of $^{77}Se^{II}$ and $^{77}Se^{III}$ nuclei were measured using *J*-RINEPT-CPMG sequence (**Fig.2.2(c)**). The attenuation of the ^{77}Se signals versus the echo-delay τ_e is shown in **Fig.2.7(a,b)** and it provides $T'_{2,Se}$ = 21 and 24 ms for Se^{II} and Se^{III}, respectively (**Table.2.3**).

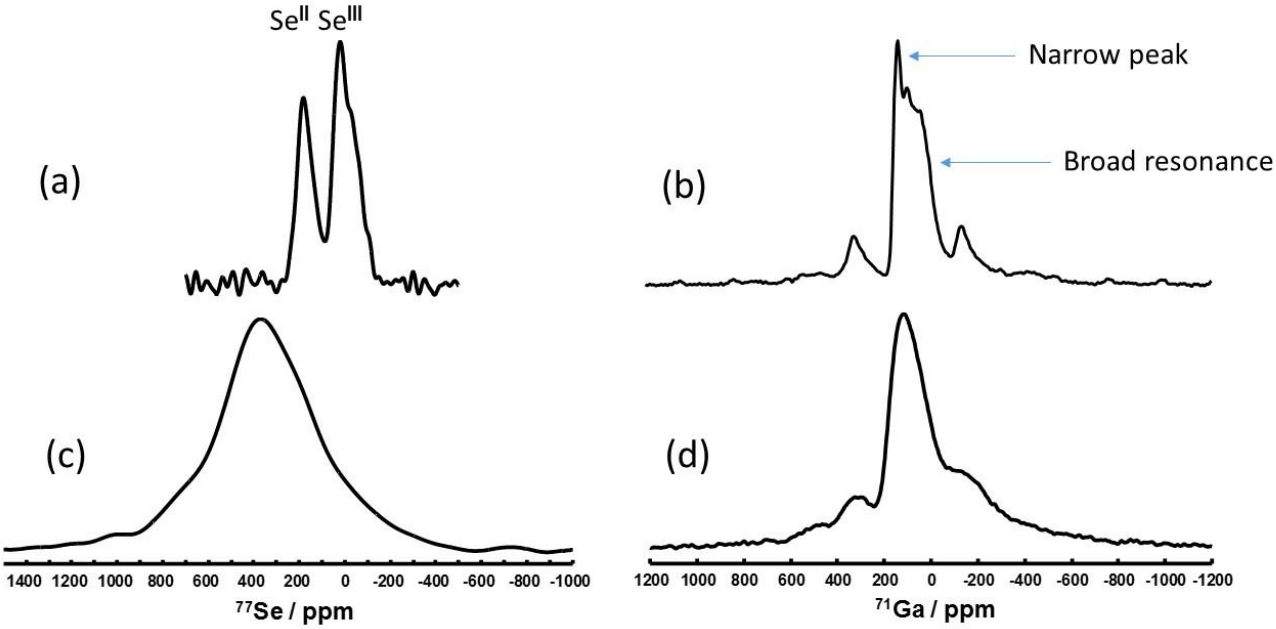

Fig.2.6. 1D MAS spectra of (a,b) β-Ga_2Se_3 and (c,d) $GGS_{0.2}$. (a,c) ^{77}Se CPMG spectra with B_0 = 9.4 T and ν_R = 20 kHz. (b,d) ^{71}Ga QCPMG spin echo spectra with B_0 = 21.1 T and ν_R = 62.5 kHz.

^{71}Ga. The MAS spectrum was recorded with a spin-echo at 21.1 T and ν_R = 62.5 kHz. The spectrum shows two signals: one narrow resonance on the top of a broad 2nd-order quadrupolar spectrum with only one spinning sideband of the broad resonance on each side (**Fig.2.6(b)**). The sharp signal is probably due to Quenched phase, whereas the broad resonance is attributed to both $Ga^{IV,1}$ and $Ga^{IV,2}$ species of Annealed phase since these species has distorted tetrahedron.

In an attempt to disentangle these two broad contributions, we have recorded at 21.1 T and ν_R = 62.5 kHz a 2D high-resolution ^{71}Ga STMAS spectrum with a full-echo detection and QCPMG recycling. The spectrum shown in **Fig.2.8** displays two different contributions: one presenting a small C_Q value with a large distribution of isotropic chemical shift, and another one exhibiting a large C_Q value. These two signals correspond to the narrow and broad

resonances in **Fig.2.6(b)**, respectively. The isotropic chemical shifts of both narrow and broad resonances correspond to $GaSe_4$ environments. The smaller C_Q value for the narrow resonance with respect to the broad one indicates that the $GaSe_4$ environments are more symmetrical in the Quenched phase than in the Annealed phase of β-Ga_2Se_3 crystal. Unfortunately, the 2D STMAS spectrum does not permit us to resolve the $Ga^{IV,1}$ and $Ga^{IV,2}$ sites in Annealed phase of β-Ga_2Se_3 crystal, and the 1D spectrum was thus fitted assuming only two species (one narrow and one broad) with the DMfit software.[35] Such fit (not shown) provided the relative amounts of the two sites and their quadrupolar parameters (Conc (%), C_Q (MHz), η_Q) ≈ (88, 17.4, 0.5) and (12, 4.4, 0.3) for the broad and narrow resonances, respectively.

Whereas at B_0 = 21.1 T and ν_R = 62.5 kHz, the sidebands are well resolved from the center-band in the 1D ^{71}Ga spectrum, at B_0 = 9.4 T and ν_R = 20 kHz, only the narrow resonance was detected for $\nu_{1,71Ga}$ = 25 kHz (see **Fig.2.9(a)**) as well as a part of the broad signal for $\nu_{1,71Ga}$ = 95 kHz (see **Fig.2.9(b)**). The first spectrum is rather similar to the one already published.[12] These results highlight the need of high magnetic field and high MAS frequency for the acquisition of ^{71}Ga MAS spectra. $T'_{2,71Ga}$ measurements were performed at 9.4 T with ν_R = 20 kHz, and the evolutions are surprisingly identical for the narrow and broad resonances (**Fig.2.7(c,d)**, **Table.2.3**): $T'_{2,71Ga}$ = 5.7 and 5.0 ms, respectively. It must be noted that those values are approximately four times smaller than the $T'_{2,77Se}$ ones (**Fig.2.7(a,b)**, **Table.2.3**).

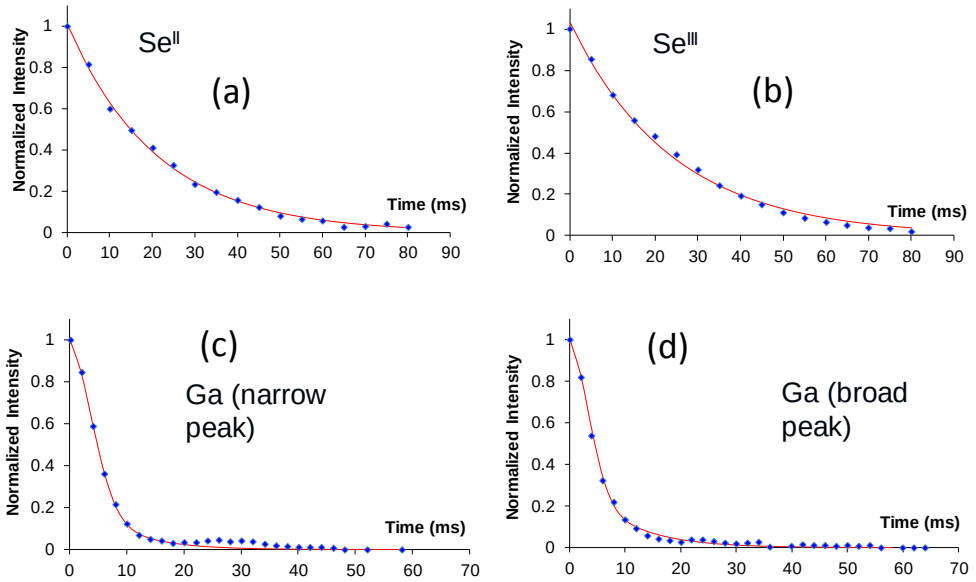

Fig.2.7. β-Ga_2Se_3: experimental decay of (a,b) ^{77}Se signals in *J*-RINEPT-spin-echo-CPMG experiment and of (c,d) ^{71}Ga signals in spin-echo-QCPMG sequence as function of the spin echo delay. The red continuous curves correspond to the best fit of experimental data points to a decaying mono-exponential function with T'_2 = (a) 21, (b) 24, (c) 5.7, and (d) 5.0 ms.

Table.2.3. Experimental T'_2 values of β-Ga_2Se_3 and $GGS_{0.2}$.

	T'_2 /ms	
	β-Ga_2Se_3	**$GGS_{0.2}$**
Se^{II}	21	18
Se^{III}	24	
Ga (Broad resonance)	5	8
Ga (Narrow resonance)	5.7	

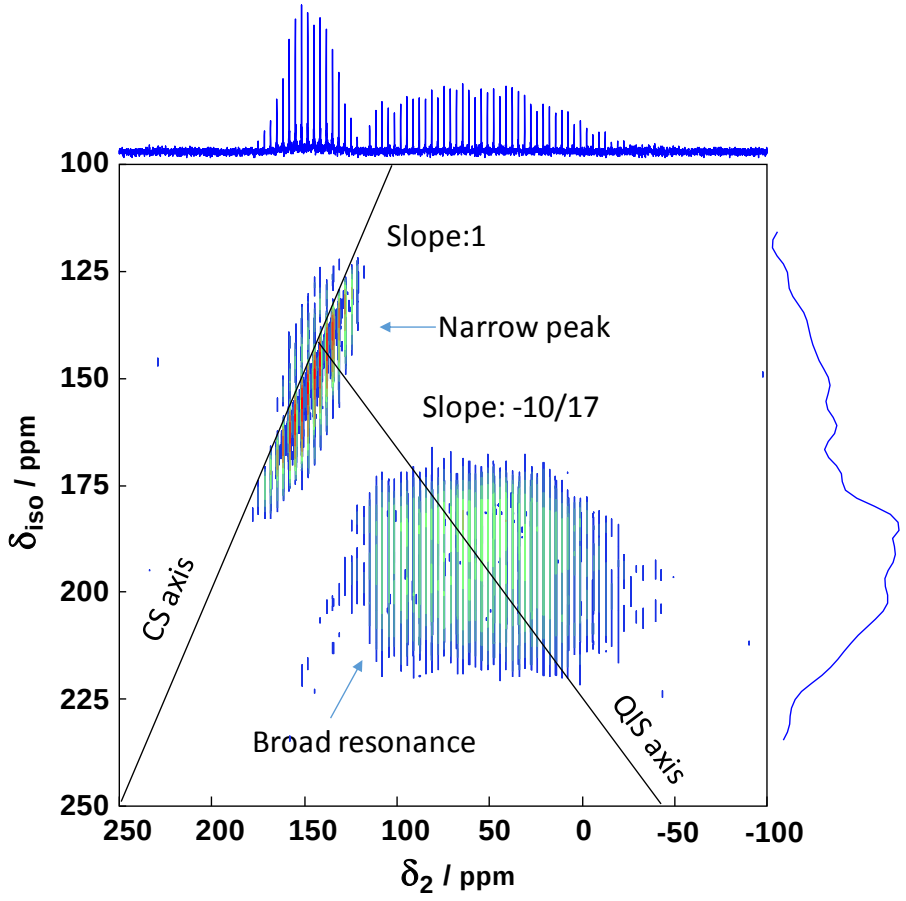

Fig.2.8. 2D ^{71}Ga STMAS-QCPMG spectrum of β-Ga_2Se_3 recorded at B_0 = 21.1 T and ν_R = 62.5 kHz.

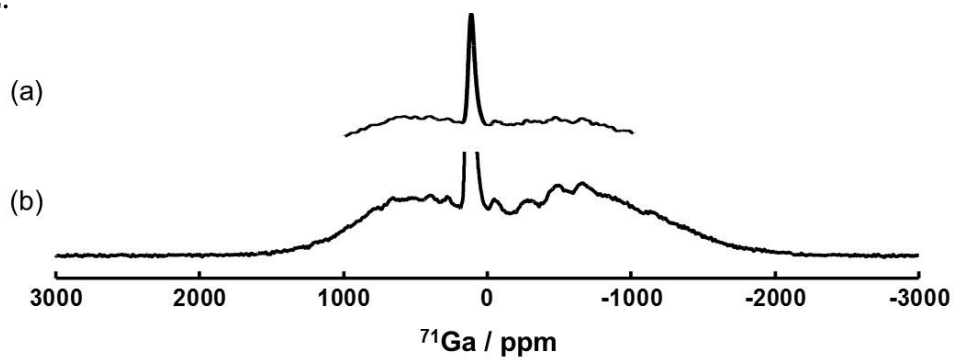

Fig.2.9. 1D ^{71}Ga QCPMG spectrum of β-Ga_2Se_3 recorded at B_0 = 9.4 T and ν_R = 20 kHz using (a) $\nu_{1,^{71}Ga}$ = 25 or (b) 95 kHz.

2.4.1.2. *J*-RINEPT and *J*-HMQC build-up curves

J-RINEPT

The ^{77}Se-{^{71}Ga} *J*-RINEPT-CPMG build-up curves of Se^{II} and Se^{III} signals for β-Ga_2Se_3 are shown in **Fig.2.10(a-f)**. They were obtained by acquiring 1D ^{77}Se-{^{71}Ga} *J*-RINEPT-CPMG spectra with $t_1 = 0$**.** When τ = τ' (**Fig.2.10(a,b)**), maximum transfer is achieved for τ = τ' ≈ 0.7 ms. These values suggest that the one-bond $^1J_{71Ga\text{-}77Se}$ couplings are much larger than 100 Hz. Therefore, it is possible to keep fixed a recoupling time (τ or τ') to this optimum value and to vary the other one (τ' or τ respectively) (**Fig.2.10(c-f)** and **Fig.2.11(a-d)**). The experimental points are normalized with respect to the maximum intensity observed with the Se^{III} site. The Se^{II} signal maximum intensities are always equal to ca. 0.40 that for Se^{III}. This value is smaller than that (0.5) predicted from the crystal structure of Annealed phase, which contains two Se^{III} sites for one Se^{II} site. This may be due to the shorter $T'_{2,}$ value for $^{77}Se^{II}$ nuclei with respect to $^{77}Se^{III}$ ones (**Fig.2.7(a,b)** and **Table.2.3**).

For the fit of the ^{77}Se-{^{71}Ga} *J*-RINEPT build-up curves to Eq. (2.3), we used the T'_2 values of **Table.2.3** and then the only adjustable parameters in Eq.(2.3) are $^1J_{71Ga\text{-}77Se}$ and $^3J_{71Ga\text{-}77Se}$ values. One additional parameter was the intensity of the signal. The best fits are displayed in **Fig.2.10** as continuous red curves. The best fit $^1J_{71Ga\text{-}77Se}$ and $^3J_{71Ga\text{-}77Se}$ values as well as the ratio of the signal intensities of Se^{II} and Se^{III} sites, I^{II}/I^{III}, are given in **Table.2.4**. As seen in that table and **Table.2.4**, we obtained similar *J*-coupling values and I^{II}/I^{III} ratios from the fit of build-up curves with τ = τ', τ' = 0.7 ms and τ = 0.7 ms. The scalar couplings with the first neighbors are slightly larger for $^{77}Se^{II}$ nuclei with respect to Se^{III} ones $^1J_{71Ga\text{-}77SeII} \approx 760 \pm 30$ Hz and $^1J_{71Ga\text{-}77SeIII} \approx 530 \pm 20$ Hz. This result is consistent with the shorter Se^{II}-Ga distances with respect to Se^{III}-Ga ones, as seen in the crystal structure.[36] In addition, $^3J_{71Ga\text{-}77Se}$ couplings are much smaller than with the $^1J(^{71}Ga\text{-}^{77}Se)$ ones: $^3J(^{71}Ga\text{-}^{77}Se) \approx 11 \pm 5$ and 5 ± 1 Hz, for Se^{II} and Se^{III} sites, respectively. I^{II}/I^{III} ratios are slightly smaller than the ratio between the number of Se^{II} and Se^{III} sites in the crystal structure, probably owing to the shorter $T'_{2,}$ value for $^{77}Se^{II}$ nuclei with respect to $^{77}Se^{III}$ ones, as mentioned above. The best fit curves deviate from the experimental build-up curves. Such deviation stems from (i) the contribution of the Quenched phase signal to these curves and (ii) the distribution of $^1J_{71Ga\text{-}77Se}$ and $^3J_{71Ga\text{-}77Se}$ coupling values, whereas we assumed identical *J*-coupling values through a given number of bonds.

J-HMQC

In 1D ^{71}Ga-{^{77}Se} *J*-HMQC-QCPMG experiments, the ^{77}Se signal is encoded in the indirect dimension, and hence 1D experiments do not allow the separation of Se^{II} and Se^{III} *J*-HMQC build-up curves. Such separation can only be achieved by recording a series of 2D experiments. These measurements require a long experimental time since many (29 here) 2D experiments had to be recorded. However, these 2D experiments permit us to separate the build-up curves for the broad ^{71}Ga resonance of β-Ga_2Se_3 (see **Fig.2.10(g,h)**) and the narrow one corresponding to the Quenched (**Fig.2.11(e,f)**). The fit of these curves to Eq.(2.1) yields $^1J_{71Ga\text{-}77Se}$ couplings and I^{II}/I^{III} ratio similar to those determined from 1D ^{77}Se-{^{71}Ga} *J*-RINEPT-CPMG build-up curves (see **Table.2.5**). It must be noted that the $^3J_{71Ga\text{-}77Se}$ values determined from the fit of 2D ^{71}Ga-{^{77}Se} *J*-HMQC-QCPMG build-up curves are much larger than those fitted from 1D ^{77}Se-{^{71}Ga} *J*-RINEPT-CPMG ones: 28 and 16 with respect to 11 and 5 Hz, for Se^{II} and Se^{III} sites, respectively.

The fit of the *J*-HMQC build-up curves for the ^{71}Ga narrow resonance to Eq.(2.1) yields $^1J_{71Ga\text{-}77Se}$ couplings for Quenched phase (see **Table.2.5**), which are similar to those measured for the broad resonance (**Table.2.4**). Hence, the ^{71}Ga-^{77}Se bonds are similar in Annealed phase and in Quenched phase. However, the I^{II}/I^{III} ratio is smaller for the Quenched phase than for Annealed phase. In the Annealed phase, the Ga sites are bonded to one Se^{II} and three Se^{III} sites. The narrow resonance must correspond to Ga atoms attached to four Se^{III} sites. Thus, the lower amount of Se^{II} sites in the Quenched phase is consistent with the more symmetrical environment of ^{71}Ga nuclei, deduced from its lower C_Q value.

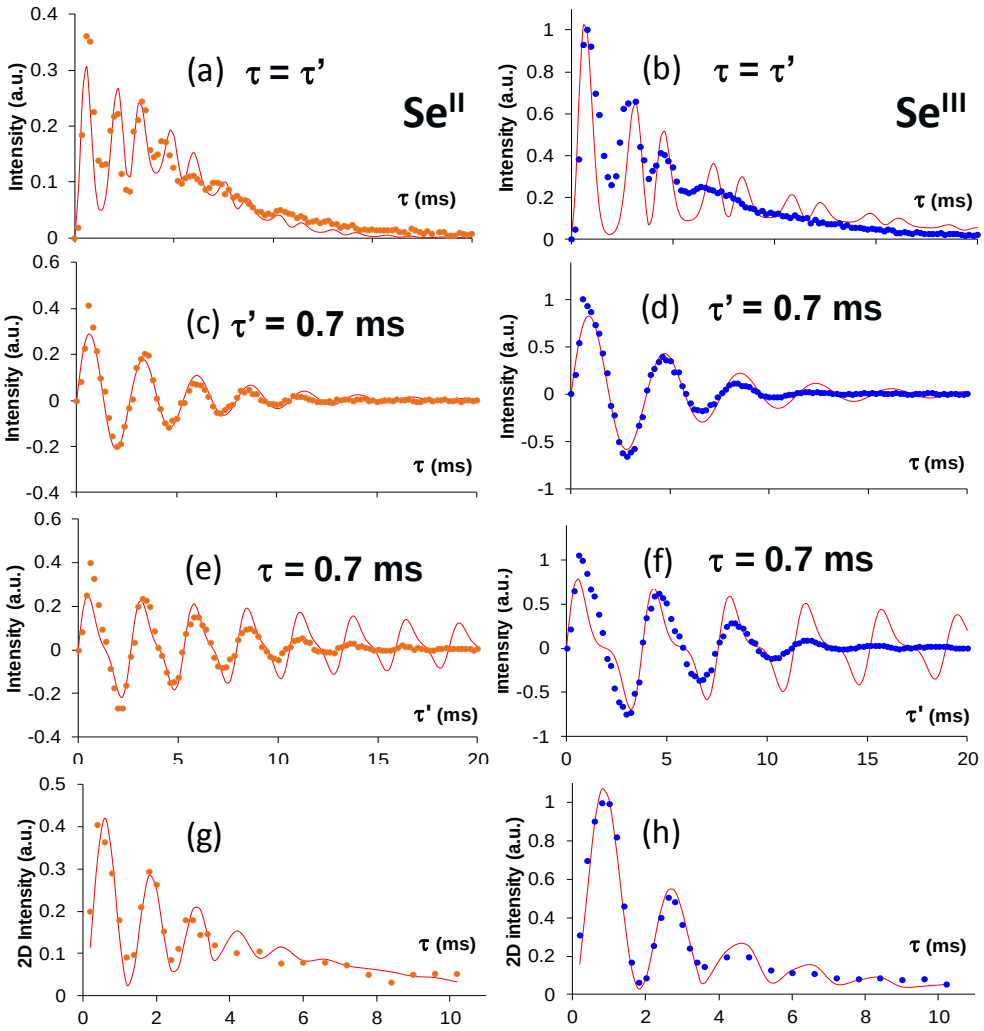

Fig.2.10. (a-f) Evolution of 1D ^{77}Se-{^{71}Ga} J-RINEPT-CPMG Se^{II} (left) and Se^{III} (right) signals of β-Ga_2Se_3 versus either (a,b) τ = τ', (c,d) τ with τ' = 0.7 ms, or (e,f) τ' with τ = 0.7 ms. (g,h) Evolution of 2D ^{71}Ga-{^{77}Se} *J*-HMQC-QCPMG signals of cross-peaks between the broad ^{71}Ga resonance and (g) Se^{II} (left) or (h) Se^{III} (right) signals. The points are the experimental values, normalized to their maximum observed for Se^{III}, whereas the continuous curves correspond to the best fits with the parameters given in **Table.2.4**.

Table.2.4. Best fit $^{1}J(^{71}Ga\text{-}^{77}Se)$ and $^{3}J(^{71}Ga\text{-}^{77}Se)$ values and I^{II}/I^{III} ratio for the fit of the experimental curves of **Fig.2.10** to Eq.(2.3) for 1D ^{77}Se{^{71}Ga} *J*-RINEPT-CPMG build-up curves and to Eq.(2.1) for ^{71}Ga{^{77}Se} *J*-HMQC-QCPMG build-up curves.

Fig Se Method	I^{II}/I^{III}	$^{1}J_{71Ga\text{-}77Se}$ /Hz	$^{3}J_{71Ga\text{-}77Se}$ /Hz
(a) Se^{II} *J*-RINEPT	0.32	734	18
(b) Se^{III}		518	5
(c) Se^{II}	0.40	752	8
(d) Se^{III}		528	5
(e) Se^{II}	0.36	744	7
(f) Se^{III}		523	5
(g) Se^{II} *J*-HMQC	0.35	801	28
(h) Se^{III}		543	16

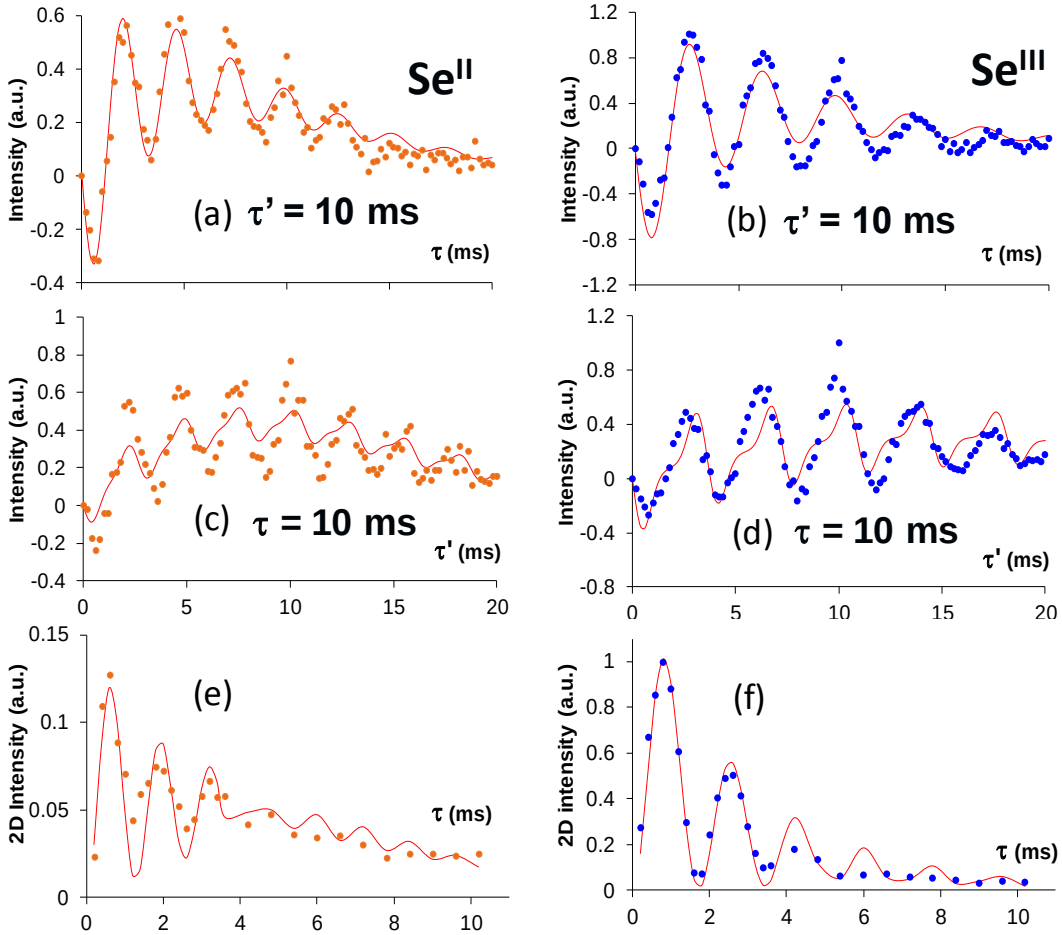

Fig.2.11. (a-d) Evolution of 1D ^{77}Se-{^{71}Ga} *J*-RINEPT-CPMG Se^{II} (left) and Se^{III} (right) signals of β-Ga_2Se_3 versus (a,b) τ with τ' = 10 ms or (c,d) τ' with τ = 10 ms. (e,f) Evolution versus τ of 2D ^{71}Ga-{^{77}Se} *J*-HMQC-QCPMG cross-peaks between the narrow ^{71}Ga resonance and (g) Se^{II} (left) and (h) Se^{III} (right) signals. The points are the experimental values, normalized to their maximum observed for Se^{III}, whereas the continuous curves correspond to the best fits with the parameters given in **Table.2.5**.

Table.2.5. Best $^1J_{71Ga\text{-}77Se}$ and $^3J_{71Ga\text{-}77Se}$ values and I^{II}/I^{III} ratio for the fit of the experimental curves of **Fig.2.11** to Eq.(2.3) for 1D ^{77}Se-{^{71}Ga} *J*-RINEPT-CPMG build-up curves and to Eq.(2.1) for ^{71}Ga-{^{77}Se} *J*-HMQC-QCPMG build-up curves.

Fig	Se	Method	I^{II}/I^{III}	$^1J_{71Ga\text{-}77Se}$ /Hz	$^3J_{71Ga\text{-}77Se}$ /Hz
(a)	Se^{II}	J-RINEPT	0.55	755	10
(b)	Se^{III}			565	8
(c)	Se^{II}		0.51	747	13
(d)	Se^{III}			551	6
(e)	Se^{II}	*J*-HMQC	0.11	773	22
(f)	Se^{III}			580	9

2.4.1.3. Comparison of the 2D *J*-RINEPT and *D*- or *J*-HMQC spectra

The 2D spectra of the ^{77}Se-{^{71}Ga} *J*-RINEPT-CPMG and ^{71}Ga-{^{77}Se} *J*- and *D*-HMQC-QCPMG experiments are displayed in **Fig.2.12**. The ^{77}Se projections of these 2D spectra are shown in **Fig.2.13**. In agreement with the crystal structure of Annealed phase,[21], the 2D *J*-RINEPT and *J*-HMQC spectra show cross-peaks between the broad ^{71}Ga resonance and both ^{77}Se^{II} and ^{77}Se^{III} signals, indicating that the Ga atoms are bonded to both Se^{II} and Se^{III} sites. The 2D *D*-HMQC spectrum allows the observation of the through-space proximities between Ga atom and both Se^{II} and Se^{III} sites. In the three 2D heteronuclear correlation spectra, the narrow ^{71}Ga resonance assigned to the Quenched phase correlates mainly with the Se^{III} signal. This observation is consistent with the low I^{II}/I^{III} ratio determined from the fit of the build-up curves of the narrow resonance in 2D ^{71}Ga-{^{77}Se} *J*-HMQC-QCPMG spectra (see **Table.2.5**).

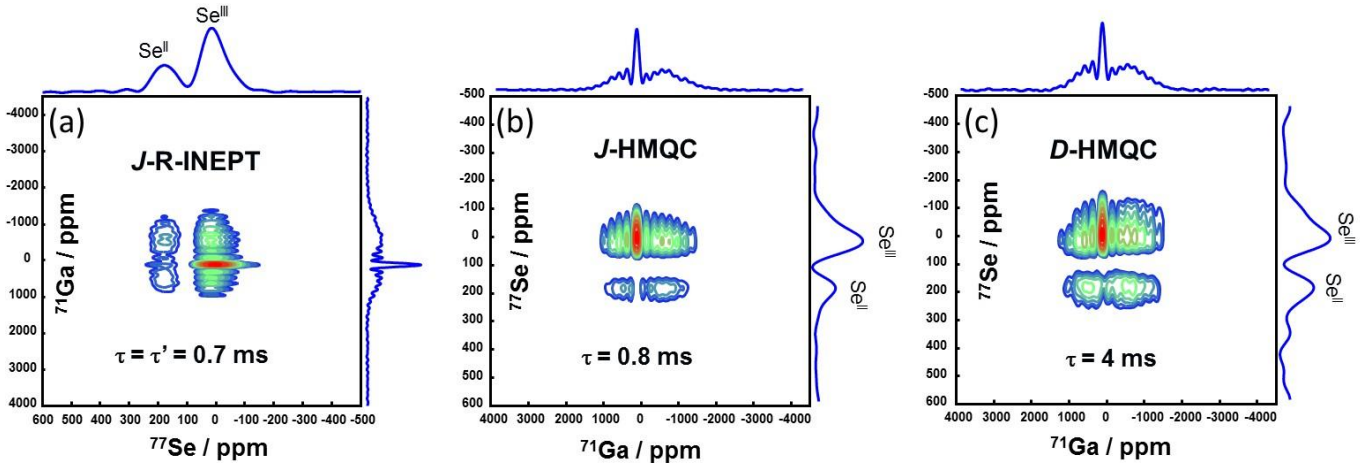

Fig.2.12. 2D spectra of β-Ga_2Se_3 at B_0 = 9.4 T and ν_R = 20 kHz: (a) ^{77}Se-{^{71}Ga} *J*-RINEPT-CPMG with τ = τ' = 0.7 ms, (b) ^{71}Ga-{^{77}Se} *J*-HMQC-QCPMG with τ = 0.8 ms, (c) ^{71}Ga-{^{77}Se} *D*-HMQC-QCPMG with τ = 4 ms.

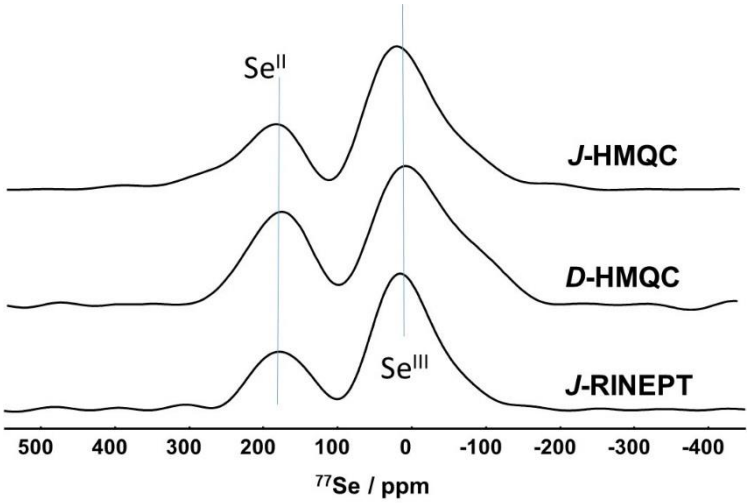

Fig.2.13. ^{77}Se projections of the 2D spectra of β-Ga_2Se_3 shown in **Fig.2.12**. The intensities are normalized so that Se^{III} signal has the same intensity in the three projections.

Table.2.6. S/N ratios in one hour for the Se^{II} and Se^{III} signals of 2D ^{77}Se-{^{71}Ga} *J*-RINEPT-CPMG and ^{71}Ga-{^{77}Se} *J*- and *D*-HMQC-QCPMG spectra of β-Ga_2Se_3.

	S/N in one hour	
	Se^{II}	Se^{III}
^{71}Ga{^{77}Se} *J*-HMQC	139	307
^{71}Ga{^{77}Se} *D*-HMQC	24	36
^{77}Se{^{71}Ga} *J*-RINEPT	20	47

For the three experiments, the S/N ratios in one hour of experiment are reported in **Table.2.6**. ^{71}Ga-{^{77}Se} *J*-HMQC-QCPMG experiment yields the highest *S/N* ratio since (i) the detected isotope is ^{71}Ga, which has a higher gyromagnetic ratio than ^{77}Se ($\gamma_{^{71}Ga} \approx 1.6\gamma_{^{77}Se}$) and (ii) the $^1J_{^{71}Ga\text{-}^{77}Se}$ couplings (760 and 530 Hz) greatly exceed the dipolar couplings (ca. 200 Hz) between the same nuclei and hence, the ^{71}Ga-^{77}Se coherence transfer is much faster through the *J*-couplings than through the dipolar couplings, i.e. optimal τ delay of 0.7-0.8 ms for *J*-HMQC experiment instead of 4 ms for *D*-HMQC one, which limits the signal losses.

Despite (i) the low natural abundance of ^{77}Se, (ii) the broad line-shape of ^{71}Ga spectra, and (iii) the relatively low Larmor frequency of ^{77}Se, experimental times of these 2D experiments were always less than 5 hours. These preliminary encouraging results prove the high efficiency of the developed sequences and such methods were thus applied to characterize a non-crystalline sample.

2.4.2. ^{71}Ga-^{77}Se correlations for $0.2Ga_2Se_3$ - $0.8GeSe_2$ glass ($GGS_{0.2}$)

The methods employed for the characterization of β-Ga_2Se_3 were applied to that of the binary glass system $0.2Ga_2Se_3$-$0.8GeSe_2$ ($GGS_{0.2}$). The ^{77}Se 1D spectrum of $GGS_{0.2}$ exhibits only one resonance, as already reported for a similar glass composition (x = 0.3).[12,13] This resonance is ca. twice broader than the ^{77}Se spectrum of β-Ga_2Se_3 (compare **Fig.2.6(a,c)**). Such broadening stems from the presence of additional molecular units with the incorporation of Ge element, such as CS and ES $GaSe_4$ and $GeSe_4$ tetrahedra and $(Se^{II})_3$-Ge-Ge-$(Se^{II})_3$ units, as well as the glass structural disorder producing a distribution in ^{77}Se isotropic chemical shifts. The ^{71}Ga spectrum displays a broad resonance at B_0 = 21.1 T and ν_R = 62.5 kHz, as already observed for the crystalline β-Ga_2Se_3 (compare **Fig.2.6(b,d)**). At B_0 = 9.4 T and ν_R = 20 kHz, the ^{71}Ga spectrum is broader (**Fig.2.14**) and it displays many spinning sidebands. T'_2 constant times of ^{71}Ga and ^{77}Se nuclei were measured in $GGS_{0.2}$ using sequences in **Fig.2.2(c,d)**, and we found $T'_{2,71Ga} \approx 8$ ms and $T'_{2,77Se} \approx 18$ ms (**Fig.2.15**). These values are similar to those found in β-Ga_2Se_3 (**Table.2.4**).

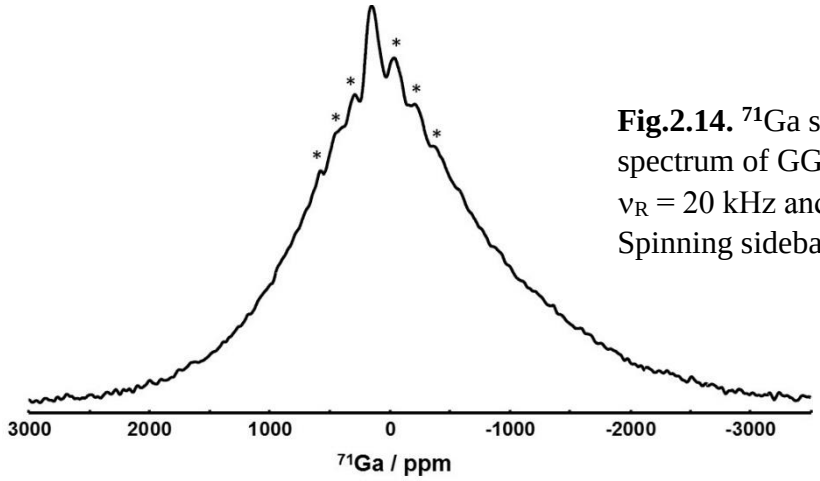

Fig.2.14. ^{71}Ga spin-echo-QCPMG spectrum of $GGS_{0.2}$ recorded at 9.4 T with ν_R = 20 kHz and $\nu_{1,71Ga}$ = 95 kHz. Spinning sidebands are indicated with *.

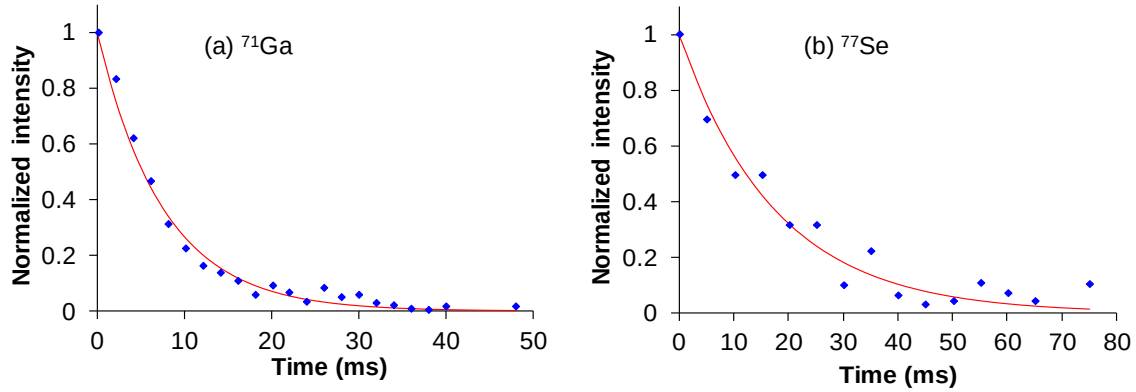

Fig.2.15. Experimental decay of (a) ^{71}Ga spin-echo-QCPMG signal and (b) ^{77}Se-{^{71}Ga} *J*-RINEPT-spin-echo-CPMG signal of $GGS_{0.2}$. The red continuous curves correspond to the best fit curves with T'_2 = (a) 8 and (b) 18 ms.

Fig.2.16 displays the build-up curves of ^{77}Se-{^{71}Ga} *J*-RINEPT experiments with $\tau = \tau'$ and ^{71}Ga-{^{77}Se} *J*-HMQC ones of crystalline β-Ga_2Se_3 and $GGS_{0.2}$ glass. As Se^{II} and Se^{III} resonances are not separated in the 1D spectra of $GGS_{0.2}$, the build-up curves of the glass are compared to the sum of Se^{II} and Se^{III} *J*-RINEPT build-up curves in crystalline β-Ga_2Se_3 weighted by the fractions of the Se^{II} and Se^{III} signals in the 1D ^{77}Se-{^{71}Ga} *J*-RINEPT-CPMG. Moreover, ^{71}Ga-{^{77}Se} *J*-HMQC spectra of $GGS_{0.2}$ (see **Fig.2.21(a)** and **(c)**) are displayed for comparison purpose. Therefore, the oscillations are slightly smoothed as compared to **Fig.2.10**. At short defocusing and refocusing times ($\tau < 1.2$ ms), glass and crystal exhibit identical build-up curves, which indicates that the $^1J_{71Ga\text{-}77Se}$ couplings, and hence Ga-Se bonds, are similar in both samples. However, for longer times ($\tau > 1.2$ ms), the curves of both materials deviate. Such difference stems notably from different $^3J_{71Ga\text{-}77Se}$ couplings since the torsion angles differ between the glass and the crystal. Similarly, the lack of signal oscillation for long τ values in the case of the glass stems from the distribution of $^3J_{71Ga\text{-}77Se}$ coupling values.

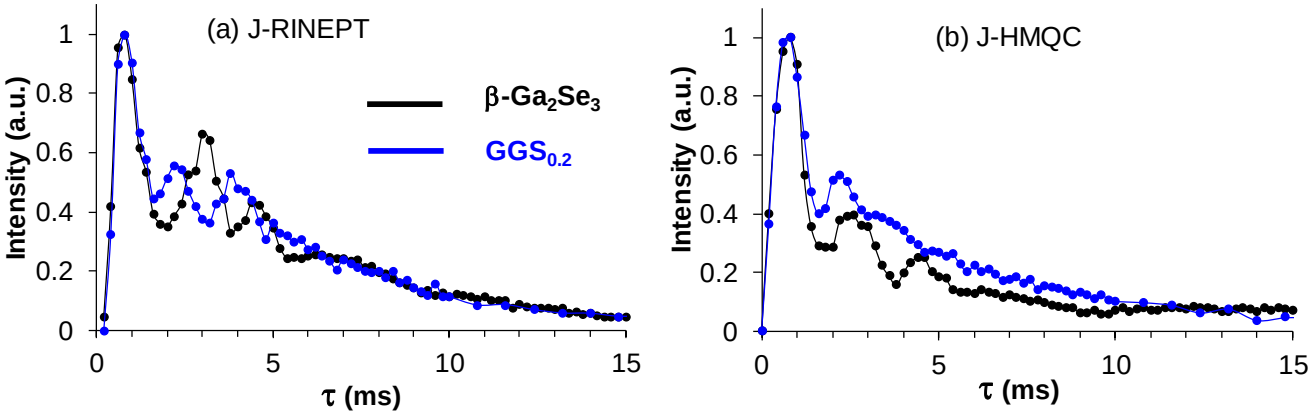

Fig.2.16. Evolution of (a) 1D ^{77}Se-{^{71}Ga} *J*-RINEPT-CPMG signals of β-Ga_2Se_3 (black) and $GGS_{0.2}$ (blue) versus $\tau = \tau'$ and (b) 1D ^{71}Ga-{^{77}Se} *J*-HMQC-QCPMG versus τ. To compare both materials, the weighted intensity of the two selenium resonances (**Fig.2.10(a** + **b)** and **Fig.2.10(g** + **h)**) were added for crystalline β-Ga_2Se_3.

To be sure that all ^{71}Ga and ^{77}Se sites are well excited, 1D ^{77}Se-{^{71}Ga} *J*-RINEPT and 2D ^{71}Ga-{^{77}Se} *J*-HMQC spectra were recorded with different carrier frequencies. **Fig.2.17** shows the 1D ^{77}Se-{^{71}Ga} *J*-RINEPT-CPMG spectra acquired with different carrier frequencies and it indicates that the total frequency range of ^{77}Se spectrum of $GGS_{0.2}$ glass is excited by *J*-RINEPT sequence using centered carrier frequency.

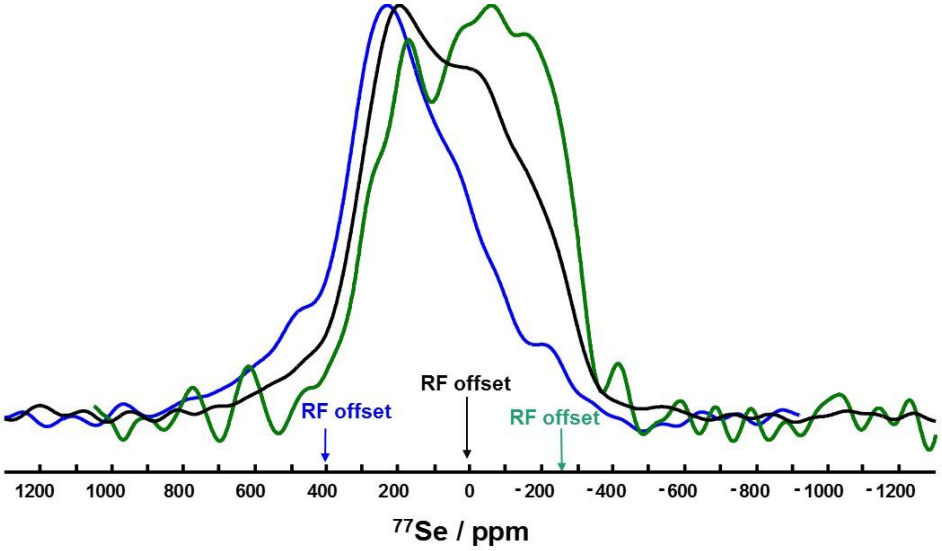

Fig.2.17. ^{77}Se-{^{71}Ga} 1D *J*-RINEPT-CPMG spectra of $GGS_{0.2}$ at B_0 = 9.4 T and ν_R = 20 kHz, $\nu_{1,71Ga}$ = 95, $\nu_{1,77Se}$ = 63 kHz and various ^{77}Se rf offsets indicated on the figure.

Fig.2.18 shows the 2D ^{77}Se-{^{71}Ga} *J*-RINEPT and ^{71}Ga-{^{77}Se} *J*- and *D*-HMQC spectra of $GGS_{0.2}$ glass. The ^{77}Se projections of these 2D spectra are shown in **Fig.2.19**. These projections exhibit higher resolution than the 1D ^{77}Se CPMG spectrum shown in **Fig.2.6(c)**. Furthermore, as seen in **Fig.2.20**, the ^{77}Se nuclei connected or close to ^{71}Ga isotopes resonate at lower isotropic chemical shifts than those that are only bonded to Ge atoms.

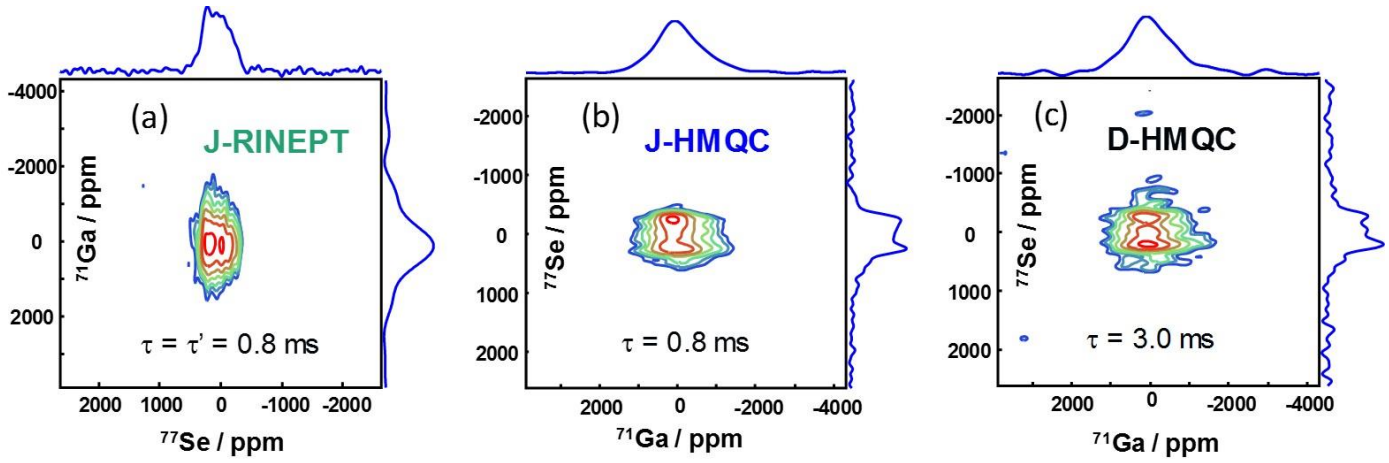

Fig.2.18. 2D spectra of $GGS_{0.2}$ at B_0 = 9.4 T with ν_R = 20 kHz: (a) ^{77}Se-{^{71}Ga} *J*-RINEPT-CPMG with $\tau = \tau' = 0.8$ ms, (b) ^{71}Ga-{^{77}Se} *J*-HMQC-QCPMG with τ = 0.8 ms, (c) ^{71}Ga-{^{77}Se} *D*-HMQC-QCPMG spectrum with τ = 3 ms.

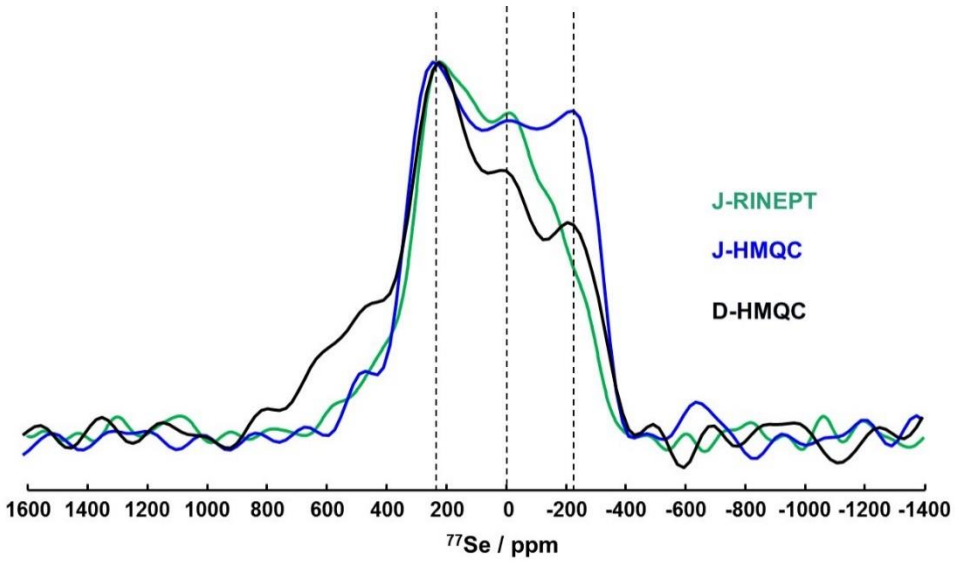

Fig.2.19. Comparison of the ^{77}Se projections of the ^{71}Ga-^{77}Se HETCOR 2D spectra of $GGS_{0.2}$ shown in **Fig.2.18**.

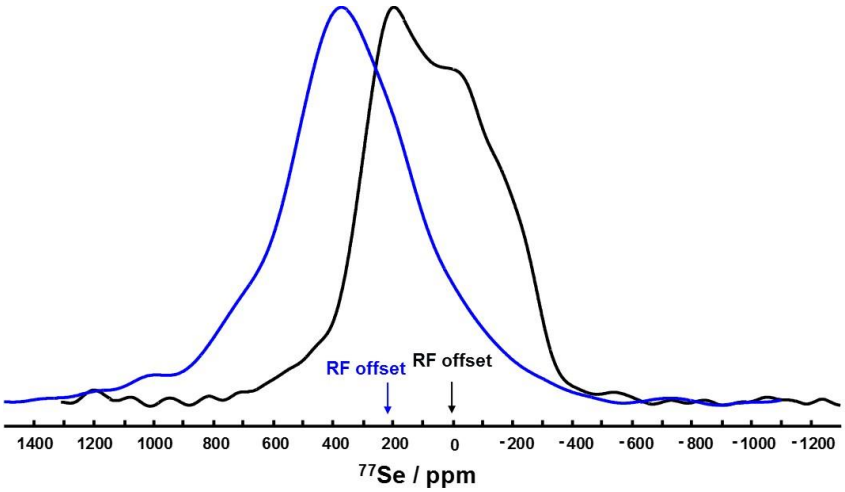

Fig.2.20. Comparison of 1D ^{77}Se spectra of $GGS_{0.2}$: CPMG (blue) and ^{77}Se-{^{71}Ga} *J*-RINEPT-CPMG (black).

Fig.2.21 shows the deconvolution of the ^{77}Se projection of 2D ^{71}Ga-^{77}Se HETCOR spectra as well as the 1D ^{77}Se CPMG spectrum of $GGS_{0.2}$ glass. In a first step, the ^{77}Se projections of *J*-RINEPT-CPMG and *J*-HMQC-QCPMG 2D spectra were simulated using the NMR parameters of already observed local environments of ^{77}Se nuclei in GGS_x glass, i.e. $^{77}Se^{II}$ sites of CS $GeSe_4$ and $GaSe_4$ tetrahedra resonating at 400 ppm and bonded to Ge-Ge bond resonating at 250 ppm as well as $^{77}Se^{III}$ sites of these CS tetrahedra resonating at −20 ppm.[13] Nevertheless, additional signals resonating at 128, −144 and −250 ppm were required to simulate the ^{77}Se projections of 2D *J*-RINEPT and *J*-HMQC spectra. The resonance at −144 ppm can be assigned to Se^{III} nuclei bonded to Ga-Ga bond since the GaSe, which consists of layers of $(Se^{III})_3$-Ga-Ga-$(Se^{III})_3$, moieties exhibits a single resonance at -80 ppm. The 2D spectra

exhibit ^{71}Ga signal at 1200 ppm characteristic of Ga nuclei in such environment.[37] The resonances at 128 and −250 ppm are tentatively assigned to Se^{III} sites of ES $GeSe_4$ and $GaSe_4$ tetrahedra and bonded to Ge-Ge bond. Nevertheless, further studies, including Density Functional Theory (DFT) calculations, would be required to confirm this assignment. The simulation of the ^{77}Se projection of 2D *D*-HMQC spectra includes the same contributions as those employed to simulate the ^{77}Se projections of the ^{71}Ga-^{77}Se J-HETCOR 2D spectra. However, the signal of ES $GeSe_4$ tetrahedra resonating at 600 ppm must also be included.[12] The absence of this signal for the through-bond correlations indicates that most of Se atoms in ES tetrahedra are bonded to Ge metal and the coherence transfer to ^{71}Ga is achieved through the dipolar couplings. In the simulation of 1D ^{77}Se CPMG spectrum, the relative integrated intensity of $^{77}Se^{II}$ sites of CS $GeSe_4$ and $GaSe_4$ tetrahedra and ES $GeSe_4$ is larger than in the ^{77}Se projections of the 2D spectra since most ES tetrahedra and a large fraction of CS ones contain Ge metal. Additional contribution resonating at 850 ppm is also required to simulate the 1D ^{77}Se CPMG spectrum. It is assigned to Se-Se^{II}-Se environment.[38]

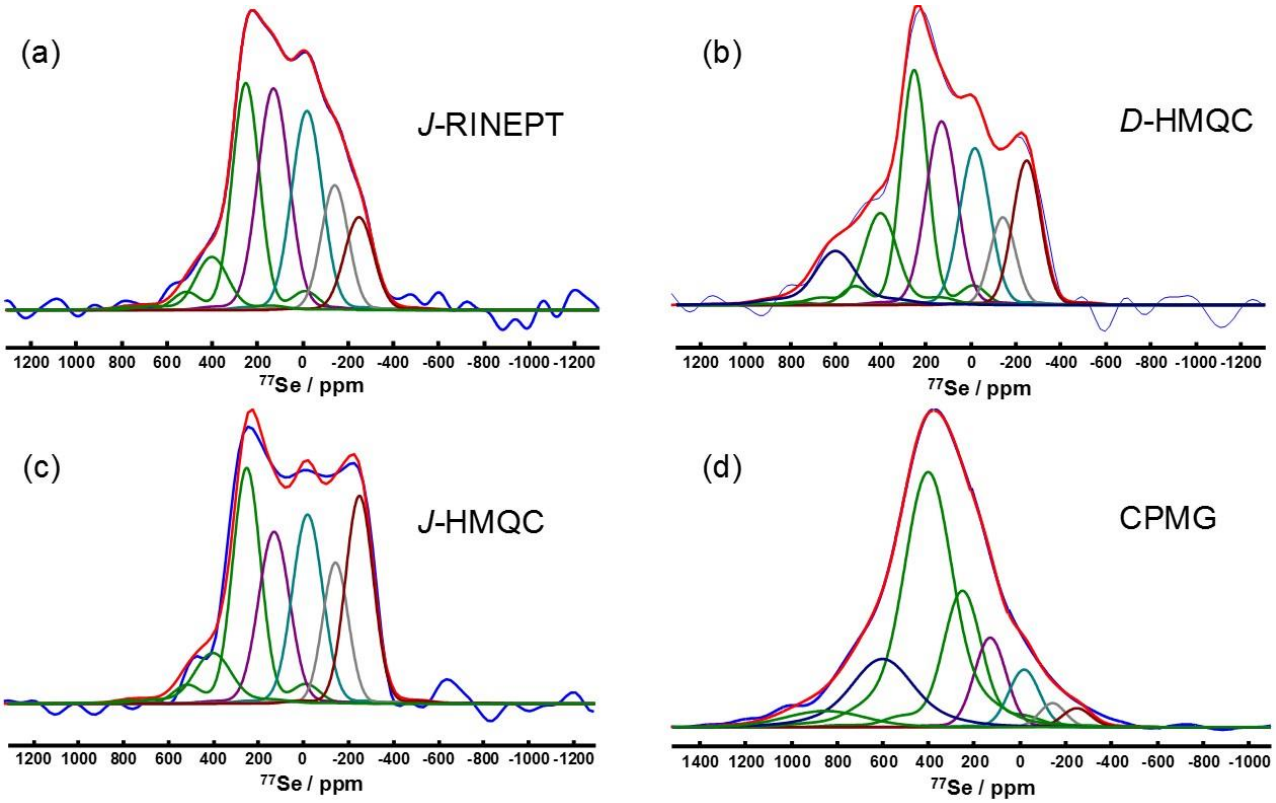

Fig.2.21. Deconvolution of the ^{77}Se projections of 2D spectra of $GGS_{0.2}$: (a) ^{77}Se-{^{71}Ga} *J*-RINEPT-CPMG, (b) ^{71}Ga-{^{77}Se} *D*-HMQC-QCPMG, (c) ^{71}Ga-{^{77}Se} *J*-HMQC-QCPMG, so that (d) the 1D ^{77}Se CPMG spectrum.

Table.2.7. Simulation parameters for the deconvolution of 1D ^{77}Se CPMG spectra of $GGS_{0.2}$ shown in **Fig.2.21**. -$Ge^{IV/3}$ = -$GeSe_3$ and -$Ge^{IV/2}$- = -$GeSe_2$- mean one Ge atom ***additionally*** bonded to 3 and 2 Se atoms. Ge/$Ga^{IV/3}$ = -$GeSe_3$ or -$GaSe_3$ means either a Ge or a Ga atom ***additionally*** bonded to 3 Se atoms.

	δ_{iso} /ppm	δ_{aniso} /ppm	η	FWHM /ppm	Fraction /%
$Ge^{IV/3}$-$Ge^{IV/2}$-**Se^{III}**-(Ge/$Ga^{IV/3}$)$_2$	-250	-120	0	145	1.65
$Ga^{IV/3}$-$Ga^{IV/2}$-**Se^{III}**-(Ge/$Ga^{IV/3}$)$_2$	-144	-120	0	133	1.91
Se^{III}-(Ge/$Ga^{IV/3}$)$_3$ (CS)	-20	-120	0	158	5.60
Se^{III}-(Ge/$Ga^{IV/3}$)$_3$ (ES)	128	-120	0	163	9.09
$Ge^{IV/3}$-$Ge^{IV/2}$-**Se^{II}**-(Ga/$Ge^{IV/3}$)	250	250	0.9	194	18.98
Se^{II}-(Ge/$Ga^{IV/3}$)$_2$ (CS)	400	250	0.9	243	44.17
Se^{II}-($Ge^{IV/3}$)$_2$ (ES)	600	280	0.9	298	14.74
Se-**Se^{II}**-Se	850	-150	0.8	400	3.85

2.5. Conclusion

We have introduced 2D ^{71}Ga-^{77}Se through-bond and through-space correlation experiments, including ^{77}Se-{^{71}Ga} *J*-RINEPT-CPMG and ^{71}Ga-{^{77}Se} *J*- or *D*-HMQC-QCPMG methods. These experiments have been demonstrated experimentally on β-Ga_2Se_3 crystal and $GGS_{0.2}$ glass. For the glass, these experiments improve the resolution of the ^{77}Se signal by selecting the ^{77}Se nuclei connected or close to ^{71}Ga nuclei. We show that the ^{71}Ga-{^{77}Se} *J*-HMQC-QCPMG experiment exhibit the highest sensitivity. Furthermore, the analysis of the build-up curves of the ^{71}Ga-^{77}Se through-bond correlation experiments allows the estimate of both $^1J_{^{71}Ga\text{-}^{77}Se}$ and $^3J_{^{71}Ga\text{-}^{77}Se}$ couplings in β-Ga_2Se_3 crystal. By introducing ^{71}Ga STMAS-QCPMG experiment at high field and high MAS frequency, we also resolve the ^{71}Ga signal of Annealed phase and that of Quenched phase. ^{71}Ga-^{77}Se correlation experiments identify Annealed phase and Quenched phase in β-Ga_2Se_3 crystal.

2.6. References

[1] B. Bureau, X.H. Zhang, F. Smektala, J.-L. Adam, J. Troles, H. Ma, C. Boussard-Plèdel, J. Lucas, P. Lucas, D. Le Coq, M.R. Riley, J.H. Simmons, Recent advances in chalcogenide glasses, J. Non-Cryst. Solids. 345 (2004) 276–283. doi:10.1016/j.jnoncrysol.2004.08.096.
[2] N. Chbani, A. Ferhat, A.-M. Loireau-Lozac'h, J. Dugué, Electrical conductivity of Ag2S–Ga2S3–GeS2 glasses, J. Non-Cryst. Solids. 231 (1998) 251–256. doi:10.1016/S0022-3093(98)00410-4.
[3] J. Saienga, S.W. Martin, The comparative structure, properties, and ionic conductivity of LiI+Li2S+GeS2 glasses doped with Ga2S3 and La2S3, J. Non-Cryst. Solids. 354 (2008) 1475–1486. doi:10.1016/j.jnoncrysol.2007.08.058.
[4] J.S. Sanghera, I.D. Aggarwal, Active and passive chalcogenide glass optical fibers for IR applications: a review, J. Non-Cryst. Solids. 256 (1999) 6–16. doi:10.1016/S0022-3093(99)00484-6.
[5] V.K. Tikhomirov, Photoinduced effects in undoped and rare-earth doped chalcogenide glasses: review, J. Non-Cryst. Solids. 256 (1999) 328–336. doi:10.1016/S0022-3093(99)00399-3.
[6] A. Zakery, S.R. Elliott, Optical properties and applications of chalcogenide glasses: a review, J. Non-Cryst. Solids. 330 (2003) 1–12. doi:10.1016/j.jnoncrysol.2003.08.064.
[7] J.-L. Adam, X.H. Zhang, On chalcogenide glasses, Woodhead Publishing, 2014. doi:10.1016/B978-0-85709-345-5.50020-9.
[8] M. Rozé, L. Calvez, Y. Ledemi, M. Allix, G. Matzen, X.-H. Zhang, Optical and Mechanical Properties of Glasses and Glass–Ceramics Based on the Ge–Ga–Se System, J. Am. Ceram. Soc. 91 (2008) 3566–3570. doi:10.1111/j.1551-2916.2008.02684.x.
[9] P. Němec, B. Frumarová, M. Frumar, Structure and properties of the pure and Pr3+-doped Ge25Ga5Se70 and Ge30Ga5Se65 glasses, J. Non-Cryst. Solids. 270 (2000) 137–146. doi:10.1016/S0022-3093(00)00066-1.
[10] K. Maeda, T. Sakai, K. Sakai, T. Ikari, M. Munzar, D. Tonchev, S.O. Kasap, G. Lucovsky, Effect of Ga on the structure of Ge–Se–Ga glasses from thermal analysis, Raman and XPS measurements, J. Mater. Sci. Mater. Electron. 18 (2007) 367–370. doi:10.1007/s10854-007-9238-0.
[11] R. Golovchak, L. Calvez, E. Petracovschi, B. Bureau, D. Savytskii, H. Jain, Incorporation of Ga into the structure of Ge–Se glasses, Mater. Chem. Phys. 138 (2013) 909–916. doi:10.1016/j.matchemphys.2012.12.084.
[12] A.W. Mao, B.G. Aitken, R.E. Youngman, D.C. Kaseman, S. Sen, Structure of Glasses in the Pseudobinary System Ga2Se3–GeSe2: Violation of Chemical Order and 8-N Coordination Rule, J. Phys. Chem. B. 117 (2013) 16594–16601. doi:10.1021/jp410017k.
[13] A.W. Mao, D.C. Kaseman, I. Hung, Z. Gan, B.G. Aitken, S. Sen, Mechanisms of structural accommodation of Se deficiency in binary Ga2Se3–GeSe2 glasses: Results from 77Se MATPASS/CPMG NMR spectroscopy, J. Non-Cryst. Solids. 410 (2015) 14–19. doi:10.1016/j.jnoncrysol.2014.12.003.
[14] B.A. Demko, R.E. Wasylishen, Solid-state selenium-77 NMR, Prog. Nucl. Magn. Reson. Spectrosc. 54 (2009) 208–238. doi:10.1016/j.pnmrs.2008.10.002.
[15] S. Sen, Z. Gan, Chemical order around Ge atoms in binary germanium selenide glasses:

Results from 73Ge solid-state NMR spectroscopy at 19.6 Tesla, J. Non-Cryst. Solids. 356 (2010) 1519–1521. doi:10.1016/j.jnoncrysol.2010.04.043.
[16] M. Deschamps, C. Roiland, B. Bureau, G. Yang, L. Le Pollès, D. Massiot, 77Se solid-state NMR investigations on AsxSe1−x glasses using CPMG acquisition under MAS, Solid State Nucl. Magn. Reson. 40 (2011) 72–77. doi:10.1016/j.ssnmr.2011.06.001.
[17] D.C. Kaseman, I. Hung, Z. Gan, S. Sen, Observation of a Continuous Random Network Structure in GexSe100–x Glasses: Results from High-Resolution 77Se MATPASS/CPMG NMR Spectroscopy, J. Phys. Chem. B. 117 (2013) 949–954. doi:10.1021/jp311320t.
[18] Z. Gan, Isotropic NMR Spectra of Half-Integer Quadrupolar Nuclei Using Satellite Transitions and Magic-Angle Spinning, J. Am. Chem. Soc. 122 (2000) 3242–3243. doi:10.1021/ja9939791.
[19] J. Trebosc, J.-P. Amoureux, Z. Gan, Comparison of high-resolution solid-state NMR MQMAS and STMAS methods for half-integer quadrupolar nuclei, Solid State Nucl. Magn. Reson. 31 (2007) 1–9. doi:10.1016/j.ssnmr.2006.09.002.
[20] F.H. Larsen, H.J. Jakobsen, P.D. Ellis, N.C. Nielsen, Sensitivity-Enhanced Quadrupolar-Echo NMR of Half-Integer Quadrupolar Nuclei. Magnitudes and Relative Orientation of Chemical Shielding and Quadrupolar Coupling Tensors, J. Phys. Chem. A. 101 (1997) 8597–8606.
[21] D. Lübbers, V. Leute, The crystal structure of β-Ga2Se3, J. Solid State Chem. 43 (1982) 339–345. doi:10.1016/0022-4596(82)90250-X.
[22] J.W. Wiench, M. Pruski, Probing through bond connectivities with MQMAS NMR, Solid State Nucl. Magn. Reson. 26 (2004) 51–55. doi:10.1016/j.ssnmr.2003.10.004.
[23] D. Massiot, F. Fayon, B. Alonso, J. Trebosc, J.-P. Amoureux, Chemical bonding differences evidenced from J-coupling in solid state NMR experiments involving quadrupolar nuclei, J. Magn. Reson. 164 (2003) 160–164. doi:10.1016/S1090-7807(03)00134-4.
[24] Z. Gan, 13C/14N heteronuclear multiple-quantum correlation with rotary resonance and REDOR dipolar recoupling, J. Magn. Reson. 184 (2007) 39–43. doi:10.1016/j.jmr.2006.09.016.
[25] J. Trebosc, B. Hu, J.P. Amoureux, Z. Gan, Through-space R3-HETCOR experiments between spin-1/2 and half-integer quadrupolar nuclei in solid-state NMR, J. Magn. Reson. 186 (2007) 220–227. doi:10.1016/j.jmr.2007.02.015.
[26] B. Hu, J. Trébosc, J.P. Amoureux, Comparison of several hetero-nuclear dipolar recoupling NMR methods to be used in MAS HMQC/HSQC, J. Magn. Reson. 192 (2008) 112–122. doi:10.1016/j.jmr.2008.02.004.
[27] O. Lafon, Q. Wang, B. Hu, F. Vasconcelos, J. Trébosc, S. Cristol, F. Deng, J.-P. Amoureux, Indirect Detection via Spin-1/2 Nuclei in Solid State NMR Spectroscopy: Application to the Observation of Proximities between Protons and Quadrupolar Nuclei, J. Phys. Chem. A. 113 (2009) 12864–12878. doi:10.1021/jp906099k.
[28] X. Lu, O. Lafon, J. Trébosc, G. Tricot, L. Delevoye, F. Méar, L. Montagne, J.P. Amoureux, Observation of proximities between spin-1⁄2 and quadrupolar nuclei: Which heteronuclear dipolar recoupling method is preferable?, J. Chem. Phys. 137 (2012) 144201. doi:10.1063/1.4753987.
[29] C. Lin, L. Calvez, M. Rozé, H. Tao, X. Zhang, X. Zhao, Crystallization behavior of 80GeS2 · 20Ga2S3 chalcogenide glass, Appl. Phys. A. 97 (2009) 713–720.

doi:10.1007/s00339-009-5304-1.
[30] L.A. O'Dell, R.W. Schurko, QCPMG using adiabatic pulses for faster acquisition of ultra-wideline NMR spectra, Chem. Phys. Lett. 464 (2008) 97–102. doi:10.1016/j.cplett.2008.08.095.
[31] S.E. Ashbrook, S. Wimperis, Satellite-Transition MAS NMR of Spin I=3/2, 5/2, 7/2, and 9/2 Nuclei: Sensitivity, Resolution, and Practical Implementation, J. Magn. Reson. 156 (2002) 269–281. doi:10.1006/jmre.2002.2557.
[32] D. Marion, M. Ikura, R. Tschudin, A. Bax, Rapid recording of 2D NMR spectra without phase cycling. Application to the study of hydrogen exchange in proteins, J. Magn. Reson. 1969. 85 (1989) 393–399. doi:10.1016/0022-2364(89)90152-2.
[33] I. Hung, Z. Gan, On the practical aspects of recording wideline QCPMG NMR spectra, J. Magn. Reson. 204 (2010) 256–265. doi:10.1016/j.jmr.2010.03.001.
[34] P G. Ghemard, S. Jaulmes, J. Etienne, J.Flahaut, Structure de la Phase Ordonnee du Sesquiseleniure de Gallium, Ga2Se3, Acta Cryst. (1983). C39, 968-971
[35] D. Massiot, F. Fayon, M. Capron, I. King, S. Le Calvé, B. Alonso, J.-O. Durand, B. Bujoli, Z. Gan, G. Hoatson, Modelling one- and two-dimensional solid-state NMR spectra, Magn Reson Chem. 40 (2002) 70–76.
[36] T. Nakayama, M. Ishikawa, Bonding and Optical Anisotropy of Vacancy-Ordered Ga 2Se 3, J. Phys. Soc. Jpn. 66 (1997) 3887–3892. doi:10.1143/JPSJ.66.3887.
[37] A.W. Mao, D.C. Kaseman, R.E. Youngman, B.G. Aitken, S. Sen, Structure and bonding characteristics of chalcogenide glasses in the system BaSeGa2Se3GeSe2, J. Non-Cryst. Solids. 375 (2013) 40–46. doi:10.1016/j.jnoncrysol.2013.04.061.
[38] D.C. Kaseman, K.M. Oliveira, T. Palazzo, S. Sen, Selenium Chain Length Distribution in GexSe100–x Glasses: Insights from 77Se NMR Spectroscopy and Quantum Chemical Calculations, J. Phys. Chem. B. 120 (2016) 4513–4521. doi:10.1021/acs.jpcb.6b02747.

Chapter 3: γ-independent through-space heteronuclear correlation between spin-1/2 and quadrupolar nuclei in solids

3.1. Introduction

Two-dimensional (2D) through-space dipolar heteronuclear correlation (*D*-HETCOR) NMR experiments allow in solids the unambiguous identification of proximities between sites occupied by different isotopes. Therefore, these methods are essential tools to facilitate the assignment of solid-state NMR spectra and to investigate the local atomic-level structures of materials. In this article, we focus on correlations between quadrupolar nuclei (e.g. ^{11}B, ^{14}N, ^{17}O, ^{27}Al…) and spin-1/2 isotopes (e.g. ^{13}C, ^{31}P, ^{29}Si…), other than ^{1}H and ^{19}F, which represent about 3/4 and 1/4 of stable NMR-active nuclei, respectively.[1–3] For instance, correlations between ^{31}P nuclei and ^{27}Al, ^{11}B or ^{51}V have been used to investigate the association between P_2O_5 and other glass-former oxides, such as Al_2O_3, B_2O_3 or V_2O_5.[4–6] ^{31}P-^{27}Al and ^{31}P-^{51}V correlations have also been used to investigate the structure of crystalline alumino- and vanado-phosphate materials, respectively.[7–9] Similarly, correlations between ^{29}Si and ^{27}Al nuclei have been employed to study crystalline and amorphous silicate materials, such as zeolites, clays and glasses.[10–13] More recently, ^{13}C-^{27}Al proximities in organo-aluminum solids and zeolites have also been probed using *D*-HETCOR experiments.[14–17]

These *D*-HETCOR experiments between spin-1/2 and quadrupolar nuclei should be efficient and robust to quadrupole interactions, electron shielding, inhomogeneity of the radiofrequency (rf) field, and instabilities of the Magic-Angle Spinning (MAS) frequency. Several pulse sequences have been proposed to correlate spin-1/2 and quadrupolar nuclei. Initially, such correlations have been achieved using cross-polarization (CP).[18] However, the efficiency and the robustness of CP transfers between spin-1/2 and quadrupolar nuclei are limited by the complex spin dynamics during spin locking, which depends on several factors, including (i) the amplitude and the orientation of the electric field gradient, (ii) the MAS frequency, ν_R, and (iii) the rf field amplitude, ν_1.[19] These shortcomings can be alleviated by the use of other *D*-HETCOR methods, such as the Dipolar-mediated Refocused Insensitive-Nuclei Enhanced by Polarization-Transfer (*D*-RINEPT) [8,9] and the Dipolar-mediated Heteronuclear Multiple Quantum Correlation (*D*-HMQC) experiments.[20,21] In these sequences, the heteronuclear dipolar couplings with the quadrupolar nuclei are reintroduced by irradiating only the spin-1/2 isotope, hence limiting the interference of the quadrupole interaction with the recoupling sequence. The *D*-RINEPT and *D*-HMQC methods complement each other since the former

employs direct detection, i.e. the excited and detected isotopes differ, whereas the latter uses indirect detection, i.e. the detected isotope is the same as the excited one. The relative sensitivities of the direct and indirect detections depend on the gyromagnetic ratios, the longitudinal relaxation times, and the spectral widths of the correlated nuclei.[22] This work focuses on sequences based on indirect detection.

In *D*-HMQC sequence, the dipolar couplings between spin-1/2, other than ^{1}H and ^{19}F, and quadrupolar nuclei have been reintroduced by applying to the spin-1/2 isotope heteronuclear dipolar schemes, such as Rotational-Echo DOuble Resonance (REDOR),[20] Simultaneous Frequency and Amplitude Modulation ($SFAM_1$),[23–25] and the Rotary Resonance Recoupling, $R^3(q = 1)$, with $\nu_1 = \nu_R$.[21] These recoupling schemes reintroduce the space component $|m| = 1$ for the dipolar coupling and the chemical shift anisotropy (CSA) of the spin-1/2 isotope. The $|m| = 1$ recoupling schemes benefit from larger scaling factors for the heteronuclear dipolar coupling than the $|m| = 2$ schemes and hence, require shorter recoupling periods in indirectly detected experiments, thus limiting the signal losses during coherence transfers.[25] Contrary to the $|m| = 2$ schemes, the $|m| = 1$ ones do not remove the homonuclear dipolar couplings between the irradiated spin-1/2 nuclei. Nevertheless, for nuclei other than ^{1}H and ^{19}F, the remaining homonuclear dipolar couplings are usually much smaller than the recoupled ones between spin-1/2 and quadrupolar nuclei, especially at high spinning speeds, and they lead to limited signal losses during the recoupling periods of indirectly detected *D*-HETCOR experiments.

Among the existing $|m| = 1$ recoupling schemes, it has been shown that $SFAM_1$ offers high robustness to rf inhomogeneity and resonance offset. In particular, it has been shown that when incorporated into the *D*-HMQC sequence, the $SFAM_1$ recoupling provides higher efficiencies than REDOR and $R^3(q = 1)$ methods.[25] However, the $SFAM_1$ recoupling is non-γ-encoded since the contribution of the heteronuclear dipolar coupling to the average Hamiltonian has a norm which depends on the Euler angle, $\gamma_{PR}^{D,IS}$, relating the internuclear vector between the coupled spins to the MAS rotor-fixed frame.[26] Because of this non-γ-encoding, each crystallite must have the same orientation at the beginnings of the two $SFAM_1$ parts, i.e. at the beginnings of defocusing and refocusing periods.[25] In other words, the delay between the beginnings of the two $SFAM_1$ parts must be rotor-synchronized, i.e. be an integer multiples of a rotor period, T_R. Such condition is especially difficult to achieve in *D*-HETCOR experiments when the t_1 evolution time is long due to weak dipolar interactions. Consequently, the *D*-HMQC sequence employing $SFAM_1$ recoupling is sensitive to fluctuations of the MAS frequency.

On the contrary to the REDOR recoupling, the $R^3(q = 1)$ scheme is γ-encoded,[26] but this does not mean that when introduced in an NMR experiment the signal is independent on the $\gamma_{PR}^{D,IS}$ angle. A sequence, the signal of which does not depend on this angle, will be termed γ-independent hereafter. The γ-encoding of the recoupling scheme is a necessary, but not sufficient, condition for th e γ-independence of the whole sequence. *D*-HMQC sequences with $R^3(q = 1)$ recoupling have been reported but these sequences are not necessarily γ-independent.[20,21] Furthermore, a major limitation of $R^3(q = 1)$ scheme is its sensitivity to rf inhomogeneity, especially when the irradiated spin is subject to small CSA.[23,26] The CSA of ^{13}C and ^{15}N nuclei have been reintroduced using γ-encoded $|m| = 1$ symmetry-based recoupling sequences, such as $R8_1^3$, $R10_1^4$, $R12_1^5$ or $R14_2^5$.[27,28] However, to the best of our knowledge, these sequences have not been used so far to reintroduce the heteronuclear dipolar coupling.

In the present article, we introduce novel γ-independent *D*-HETCOR experiments to correlate spin-1/2 nuclei, other than ^1H and ^{19}F, and quadrupolar ones. To reintroduce the dipolar interaction under MAS, these experiments employ γ-encoded $|m| = 1$ RN_n^ν schemes, which are applied either on the detected or the undetected channel.

In the theoretical section, we explain how the RN_n^ν schemes are selected and give the expression of the contribution of the heteronuclear dipolar coupling to the first-order average Hamiltonian. We describe how these recoupling schemes have been incorporated into the *D*-HETCOR sequences. In particular, how γ-independent *D*-HETCOR experiments with RN_n^ν schemes on the detected spin are achieved by introducing a novel sequence, named Dipolar-mediated Heteronuclear Universal-Quantum Correlation (*D*-HUQC). We then provide the analytical signal expressions for the various sequences.

Numerical simulations are then employed to test the validity of these expressions and the robustness of the various recouplings to offset, CSA, rf-field inhomogeneity and MAS instabilities.

The performances of the various recouplings and *D*-HMQC and *D*-HUQC sequences are finally compared between ^{13}C and ^{15}N nuclei in glycine and between ^{31}P and ^{27}Al in VPI-5 and $Na_7(AlP_2O_7)_4PO_4$.

3.2. Theory

In the following, we will always assume that the recoupling is applied to *I* spin.

3.2.1. Recoupling schemes

The heteronuclear dipolar interaction is characterized by a space rank $l = 2$ and a spin rank $\lambda = 1$. Hence, it can be regarded as the superposition of 15 components, with component indexes $m = -2, -1, 0, +1$ or $+2$ and $\mu = -1, 0$ or $+1$. As mentioned in the introduction, the γ-encoding of the heteronuclear recoupling scheme is desirable in order to improve the robustness of the sequence to instabilities of the MAS frequency. It has been shown that a bijection between the m and μ indexes is a sufficient condition to achieve γ-encoded recoupling.[29,30] In other words, schemes reintroducing two components, $\{2, m, 1, \mu\}$ and $\{2, -m, 1, -\mu\}$, of the heteronuclear dipolar interaction are γ-encoded. Furthermore, the scaling factor of the $|m| = 1$ components is usually $\sqrt{2}$ higher than that of the $|m| = 2$ ones. High scaling factors limit the signal losses during the recoupling periods. Hence, γ-encoded $|m| = 1$ schemes require selecting the $\{2, 1, 1, \mu\}$ and $\{2, -1, 1, -\mu\}$ components of the heteronuclear dipolar interaction, with $\mu = \pm 1$.

Setting up periodic symmetry relationships between the space and spin rotations facilitates the design of heteronuclear dipolar recoupling since these symmetry arguments allow generating a first-order average Hamiltonian containing the desired rotational components, $\{2, 1, 1, \mu\}$ and $\{2, -1, 1, -\mu\}$, while other components are suppressed.[29,31] Among the symmetry-based recoupling sequences, the RN_n^ν class leads to selection rules on the first-order average Hamiltonian, which are more selective than the CN_n^ν class.[32,33] Consequently, the number of higher-order terms in the effective Hamiltonian tends to be larger for CN_n^ν schemes than for RN_n^ν ones, which are thus often more robust.

A total of 269 RN_n^ν schemes were found, with $2 \leq N \leq 30$, $1 \leq n \leq 10$ and $1 \leq \nu \leq 21$, which only recouple the two components of the heteronuclear dipolar coupling and CSA in the first-order average Hamiltonian. Here, we only considered RN_n^ν schemes, where *N* must be even, built around π-pulses. These schemes result from the *N*/2-fold repetition of the pair $\pi_\phi\pi_{-\phi}$ of pulses, involving the phase shift $\phi = \pi\nu/N$. Each of the π-pulses has the same duration, nT_R/N, and rf-field requirement, $\nu_1 = N\nu_R/(2n)$. **Fig.3.1(a)** shows that the phase ϕ of the γ-encoded $|m| = 1$ recoupling scheme monotonically increases with rf-field when $\nu_1 \geq \nu_R$ and asymptotically converges towards 90°. The scaling factor, κ, of the allowed components of the heteronuclear dipolar coupling was calculated by using the 'C and R symmetries' Mathematica package. [32–

35] As seen in **Fig.3.1(b)**, κ monotonically increases with rf-field and asymptotically converges towards 0.26. We also calculated the number, $N^{(2)}$, of symmetry-allowed 2nd-order cross-terms involving commutators of two CSA Hamiltonians, two offset ones, and between one CSA and one offset Hamiltonians.[35] Among the 269 RN_n^ν schemes mentioned above, the minimal $N^{(2)}$ value is 42. Therefore, a total of 51 RN_n^ν recoupling were pre-selected with $\kappa > 0.24$, $\nu_1 < 3.6\nu_R$ and $N^{(2)} = 42$, and the properties of the finally chosen 4 schemes are listed in **Table.3.1**. The related *D*-HMQC and *D*-HUQC sequences were further investigated by numerical simulations and experiments.

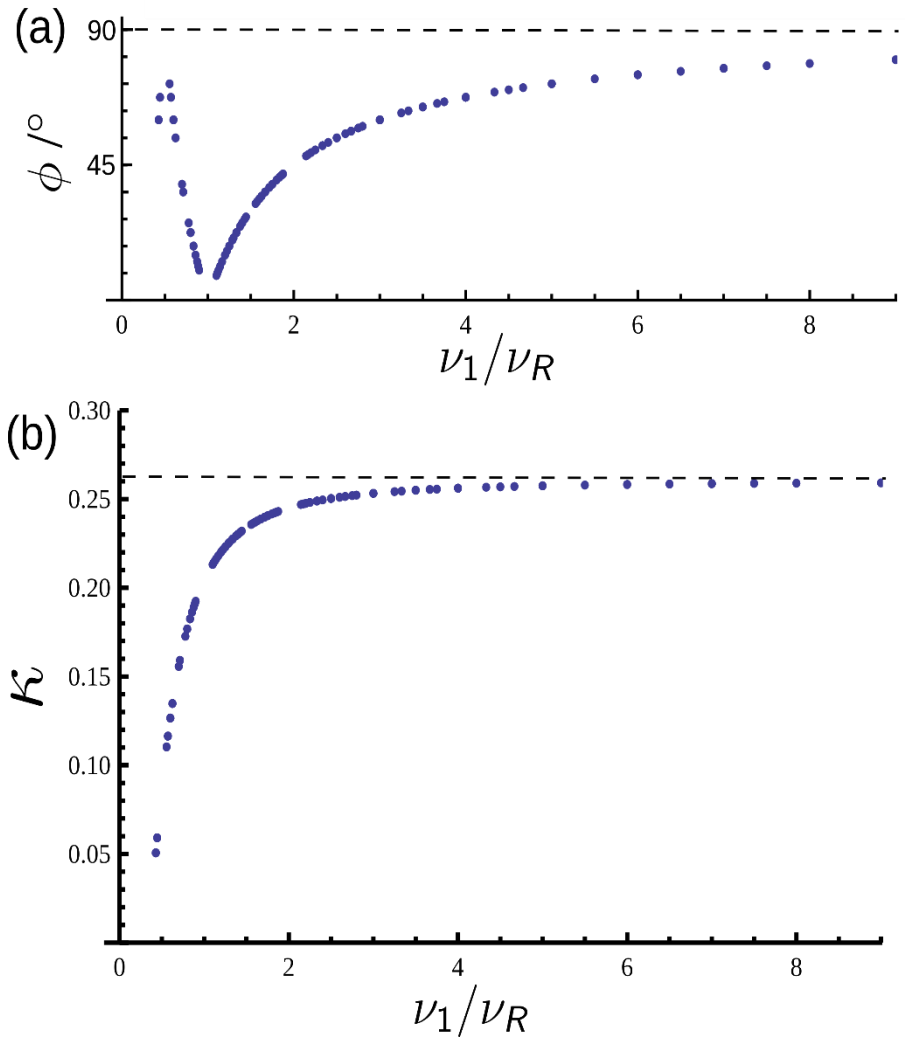

Fig.3.1. (a) Phase ϕ (°) and (b) scaling factor κ versus the ratio ν_1/ν_R for γ-encoded $|m| = 1$ RN_n^ν heteronuclear recoupling schemes with $2 \leq N \leq 30$, $1 \leq n \leq 10$ and $1 \leq \nu \leq 21$. It must be noted that for each ν_1/ν_R ratio the complementary phase, 180 - ϕ, also works with the same κ scaling factor.

Table.3.1. Properties of the selected RN_n^ν heteronuclear schemes recoupling the {2, 1, 1, -1} and {2, -1, 1, 1} components.

RN_n^ν	ϕ °	ν_1/ν_R	κ
$R18_4^5$	50.0	2.25	0.248
$R10_2^3$	54.0	2.50	0.250
$R16_3^5$	56.25	2.67	0.251
$R14_2^5$	64.28	3.5	0.254

The γ-encoded $|m| = 1$ RN_n^ν contribution of *I*-*S* dipolar interaction to the average Hamiltonian is equal to:

$$\overline{\widehat{H}_{D,IS}}^{(1)}(RN_n^\nu) = \omega_{D,IS}\left[\hat{S}_z\hat{I}^+\exp(i\varphi) + \hat{S}_z\hat{I}^-\exp(-i\varphi)\right]$$
$$= 2\omega_{D,IS}\left[\hat{S}_z\hat{I}_x\cos(\varphi) - \hat{S}_z\hat{I}_y\sin(\varphi)\right] \quad (3.1)$$

where the magnitude, $\omega_{D,IS}$, and the phase, φ, of the recoupled *I*-*S* coupling are given by

$$\omega_{D,IS} = \kappa\frac{\sqrt{3}}{2}b_{IS}\sin\left(2\beta_{PR}^{D,IS}\right) \quad (3.2)$$

and

$$\varphi = \gamma_{PR}^{D,IS} + \alpha_{RL}^0 - \omega_R t^0 \quad (3.3)$$

In Eqs.(3.2) and (3.3), (i) b_{IS} is the dipolar coupling constant in rad.s^{-1}, (ii) the Euler angles {0, $\beta_{PR}^{D,IS}$, $\gamma_{PR}^{D,IS}$} relate the internuclear direction to the MAS rotor-fixed frame, (iii) $\omega_R = 2\pi\nu_R$, and (iv) t^0 refers to the starting time of the RN_n^ν scheme. As seen in Eq.(3.1), the γ-encoded $|m| = 1$ RN_n^ν scheme reintroduces single-quantum (1Q) heteronuclear dipolar coupling terms. The evolutions of product operators for two coupled spin-1/2 nuclei *I* and *S* are given in **Table.3.1**. Under $\overline{\widehat{H}_{D,IS}}^{(1)}(RN_n^\nu)$, the z-magnetization of the *I*-spin is converted into heteronuclear multiple-quantum (MQ) coherences described by $2\hat{S}_y\hat{I}_y$ and $2\hat{S}_y\hat{I}_x$ operators, whereas the *x*-magnetization of the *S*-spin evolves into heteronuclear MQ coherences described by $2\hat{S}_y\hat{I}_x$ and $2\hat{S}_y\hat{I}_y$ operators. In both cases, the phase of the heteronuclear MQ coherences depends on φ angle. $\overline{\widehat{H}_{D,IS}}^{(1)}(RN_n^\nu)$ depends on φ phase, and hence $\gamma_{PR}^{D,IS}$ angle, but conversely its norm does not, which confirms the γ-encoding of these RN_n^ν sequences.[26]

In the case of R^3 scheme applied to *I* spin, the contribution of *I*-*S* dipolar interaction to the average Hamiltonian is tilted by -π/2 around $\hat{I}_y$ with respect to Eq.(3.1):

$$\overline{\widehat{H}_{D,IS}}^{(1)}(R^3) = \exp\left(\iota\frac{\pi}{2}\hat{I}_y\right)\cdot\overline{\widehat{H}_{D,IS}}^{(1)}(\mathrm{R}N_n^{\nu})\cdot\exp\left(-\iota\frac{\pi}{2}\hat{I}_y\right) \tag{3.4}$$

with $\kappa = 1/\sqrt{6} \approx 0.408$. Hence, the R^3 scheme is also γ-encoded.

The simultaneous frequency and amplitude modulation ($SFAM_1$) scheme has been proposed to recouple the hetero-nuclear dipolar interactions.[36] The carrier frequency, $\nu_{\mathrm{ref}} + \Delta\nu_{\mathrm{ref}}(t)$, of the rf-field is modulated with a cosine, while its amplitude, $\nu_1(t)$, is modulated with a sine, both in a rotor-synchronized way:

$$\nu_1(t) = \nu_1^{\max}\sin(2\pi\nu_{\mathrm{R}}t) \qquad \Delta\nu_{\mathrm{ref}}(t) = \Delta\nu_{\mathrm{ref}}^{\max}\cos(2\pi\nu_{\mathrm{R}}t) \tag{3.5}$$

When the $SFAM_1$ scheme in the region 2 is applied to the *I* spin, $\Delta\nu_{\mathrm{ref}}^{\max} \approx \nu_1^{\max} \approx 3\nu_{\mathrm{R}}$, the average Hamiltonian of the *I*-*S* dipolar interaction is

$$\overline{\widehat{H}_{D,IS}}^{(1)}(\mathrm{SFAM}) = 2\omega_{D,IS}\hat{S}_z\hat{I}_z \tag{3.6}$$

where

$$\omega_{D,IS} = \kappa b_{IS}\sin\left(2\beta_{PR}^{D,IS}\right)\cos(\varphi) \tag{3.7}$$

with $\kappa = -C_1/\left(2\sqrt{2}\right)$ and $C_1 \approx 1$ is the first coefficient of the Fourier series expansion of $\cos[\theta(t)]$, where $\theta(t)$ is the tilt angle between B_0 and the effective field.[25] As seen in Eq.(3.7), the $SFAM_1$ scheme is non-γ-encoded since its norm depends on φ, and hence on $\gamma_{PR}^{D,IS}$ angle.

RN_n^{ν} and R^3 schemes are dipolar-truncated (single-quantum coherences $\hat{S}_z\hat{I}_{x/y}$ in Eq.(3.1 and 3.4), whereas $SFAM_1$ is not (two-spin-order coherences $\hat{S}_z\hat{I}_z$ in Eq.(3.6)). In the first case, a small dipolar coupling between two spins is only weakly reintroduced if one or both spins are also strongly dipolar coupled to other spins. On the contrary, in the second case long distances correlations can be observed.

Table 3.2. Evolution of product operators for two coupled spin-1/2 nuclei, *I* and *S*, during γ-encoded $|m| = 1$ RN_n^v heteronuclear recoupling when such scheme is applied to the spin *I*.

$\hat{\boldsymbol{O}}(0)$	$\exp\left(-i\overline{\hat{H}_{D,IS}}^{(1)}\tau\right)\hat{\boldsymbol{O}}(0)\exp\left(i\overline{\hat{H}_{D,IS}}^{(1)}\tau\right)$
$\hat{S}_x$	$\hat{S}_x\cos(\omega_{D,IS}\tau) + 2\hat{S}_y\{\hat{I}_x\cos(\varphi) - \hat{I}_y\sin(\varphi)\}\sin(\omega_{D,IS}\tau)$
$\hat{S}_y$	$\hat{S}_y\cos(\omega_{D,IS}\tau) - 2\hat{S}_x\{\hat{I}_x\cos(\varphi) - \hat{I}_y\sin(\varphi)\}\sin(\omega_{D,IS}\tau)$
$\hat{S}_z$	$\hat{S}_z$
$2\hat{S}_x\hat{I}_z$	$2\hat{S}_x\hat{I}_z$
$2\hat{S}_y\hat{I}_z$	$2\hat{S}_y\hat{I}_z$
$2\hat{S}_z\hat{I}_z$	$2\hat{S}_z\hat{I}_z\cos(\omega_{D,IS}\tau) - \{\hat{I}_y\cos(\varphi) + \hat{I}_x\sin(\varphi)\}\sin(\omega_{D,IS}\tau)$
$\hat{I}_x$	$\hat{I}_x\{\cos^2(\varphi) + \cos(\omega_{D,IS}\tau)\sin^2(\varphi)\} - \hat{I}_y\sin^2\left(\frac{\omega_{D,IS}\tau}{2}\right)\sin(2\varphi) + 2\hat{S}_z\hat{I}_z\cos(\varphi)\sin(\omega_{D,IS}\tau)$
$\hat{I}_y$	$\hat{I}_y\{\cos(\omega_{D,IS}\tau)\cos^2(\varphi) + \sin^2(\varphi)\} - \hat{I}_x\sin^2\left(\frac{\omega_{D,IS}\tau}{2}\right)\sin(2\varphi) + 2\hat{S}_z\hat{I}_z\cos(\varphi)\sin(\omega_{D,IS}\tau)$
$\hat{I}_z$	$\hat{I}_z\cos(\omega_{D,IS}\tau) - 2\hat{S}_y\{\hat{I}_y\cos(\varphi) + \hat{I}_x\sin(\varphi)\}\sin(\omega_{D,IS}\tau)$
$2\hat{S}_z\hat{I}_x$	$2\hat{S}_z\hat{I}_x\{\cos^2(\varphi) + \cos(\omega_{D,IS}\tau)\sin^2(\varphi)\} - 2\hat{S}_z\hat{I}_y\sin^2\left(\frac{\omega_{D,IS}\tau}{2}\right)\sin(2\varphi) + \hat{I}_z\sin(\varphi)\sin(\omega_{D,IS}\tau)$
$2\hat{S}_z\hat{I}_y$	$2\hat{S}_z\hat{I}_x\{\cos(\omega_{D,IS}\tau)\cos^2(\varphi) + \sin^2(\varphi)\} + 2\hat{S}_z\hat{I}_y\sin^2\left(\frac{\omega_{D,IS}\tau}{2}\right)\sin(2\varphi) + \hat{I}_z\cos(\varphi)\sin(\omega_{D,IS}\tau)$
$2\hat{S}_x\hat{I}_x$	$2\hat{S}_x\hat{I}_x\{\cos(\omega_{D,IS}\tau)\cos^2(\varphi) + \sin^2(\varphi)\} + 2\hat{S}_y\hat{I}_x\sin^2\left(\frac{\omega_{D,IS}\tau}{2}\right)\sin(2\varphi) + \hat{S}_y\cos(\varphi)\sin(\omega_{D,IS}\tau)$
$2\hat{S}_x\hat{I}_y$	$2\hat{S}_x\hat{I}_y\{\cos^2(\varphi) + \cos(\omega_{D,IS}\tau)\sin^2(\varphi)\} + 2\hat{S}_x\hat{I}_x\sin^2\left(\frac{\omega_{D,IS}\tau}{2}\right)\sin(2\varphi) - \hat{S}_y\sin(\varphi)\sin(\omega_{D,IS}\tau)$
$2\hat{S}_y\hat{I}_x$	$2\hat{S}_y\hat{I}_x\{\cos(\omega_{D,IS}\tau)\cos^2(\varphi) + \sin^2(\varphi)\} + 2\hat{S}_y\hat{I}_y\sin^2\left(\frac{\omega_{D,IS}\tau}{2}\right)\sin(2\varphi) - \hat{S}_x\cos(\varphi)\sin(\omega_{D,IS}\tau)$
$2\hat{S}_y\hat{I}_y$	$2\hat{S}_y\hat{I}_y\{\cos^2(\varphi) + \cos(\omega_{D,IS}\tau)\sin^2(\varphi)\} + 2\hat{S}_x\hat{I}_y\sin^2\left(\frac{\omega_{D,IS}\tau}{2}\right)\sin(2\varphi) + \hat{S}_x\sin(\varphi)\sin(\omega_{D,IS}\tau)$

3.2.2. *D*-HETCOR sequences

3.2.2.1. Recoupling applied to the indirectly detected isotope.

As said before, the dipolar recoupling is applied to *I* spin, which is indirectly detected in this part, whereas the *S* spin is detected.

Fig.3.2(b) displays the pulse sequence of *D*-HMQC experiments in which the $SFAM_1$ scheme is applied to the indirectly detected spin (denoted HMQC-I-$SFAM_1$ hereafter). During the first $SFAM_1$ defocusing period, the in-phase *S*-spin magnetization ($\hat{S}_x$) for a pair of coupled *IS* spins evolves into antiphase one ($2\hat{S}_y\hat{I}_z$), which is converted into heteronuclear MQ coherences ($2\hat{S}_y\hat{I}_x$) by the π/2-pulse with phase y on the *I* channel (I-$\pi/2_y$ pulse hereafter). The isotropic shift is then encoded by allowing these MQ coherences to evolve during the evolution time, t_1. The S-π_y pulse applied in the middle of the t_1 period refocuses the evolution of the *S*-spin magnetization under isotropic shift during the τ and t_1 delays as well as its evolution under $J_{I\text{-}S}$ coupling. At the end of t_1, the MQ coherences are converted back into anti-phase *S*-spin magnetization by the I-$\pi/2_{-y}$ pulse and these coherences evolve during the second $SFAM_1$ refocusing period, into observable transverse *S*-spin magnetization. On a powder sample, the NMR signal of this experiment is proportional to [25]

$$S(\tau) \propto \frac{1}{2}\left\{1 - \frac{\pi\sqrt{2}}{4} J_{1/4}(\kappa b_{IS}\tau) J_{-1/4}(\kappa b_{IS}\tau)\right\} \tag{3.8}$$

where $J_{\pm 1/4}(x)$ denotes the Bessel functions of the first kind and ±1/4-order. In the absence of losses, the shorter τ value producing maximal $S(\tau)$ intensity is $\tau^{opt} = 2.36/(\kappa b_{IS})$.

Fig.3.2(a) displays the pulse sequence of *D*-HMQC-I experiments with the γ-encoded $|m| = 1$ RN_n^ν recoupling (denoted HMQC-I-RN_n^ν hereafter). During the defocusing delay, the in-phase *S*-spin magnetization is converted into heteronuclear MQ coherences, $2\hat{S}_y\hat{I}_{-\varphi}$, where $\hat{I}_{-\varphi} = \hat{I}_x\cos(\varphi) - \hat{I}_y\sin(\varphi)$. These coherences are encoded by isotropic shift during t_1. As seen in **Table.3.2**, $2\hat{S}_y\hat{I}_x$ and $2\hat{S}_y\hat{I}_y$ operators are converted back into $\hat{S}_x$ during the refocusing delay, with coefficients $-\cos(\varphi)$ and $\sin(\varphi)$, respectively. Hence, the NMR signal of this experiment is proportional to

$$S(\tau) \propto \langle\{\cos^2(\varphi) + \sin^2(\varphi)\}\sin^2(\omega_{D,IS}\tau)\rangle = \frac{1}{2}\left[1 - \langle\cos(2\omega_{D,IS}\tau)\rangle\right] \tag{3.9}$$

where the angular bracket $\langle \ldots \rangle$ denotes the powder average over all orientations of the *I*-*S* inter-nuclear vectors. As seen win Eq.(3.2), $\omega_{D,IS}$ does not depend on $\gamma_{PR}^{D,IS}$ angle and hence, the HMQC-I-RN_n^ν sequence is γ-independent. Using the closed analytical form for γ-encoded $|m| = 1$ recoupling sequence,[30] Eq.(3.9) can be recast as

$$S(\tau) \propto \frac{1}{2} - \frac{1}{3^{1/4}}\sqrt{\frac{\pi}{8\kappa b_{IS}\tau}}\left\{F_c\left(3^{1/4}\sqrt{\frac{2\kappa b_{IS}\tau}{\pi}}\right)\cos\left(\sqrt{3}\kappa b_{IS}\tau\right) + F_s\left(3^{1/4}\sqrt{\frac{2\kappa b_{IS}\tau}{\pi}}\right)\sin\left(\sqrt{3}\kappa b_{IS}\tau\right)\right\} \quad (3.10)$$

where $F_c(x)$ and $F_s(x)$ are the Fresnel cosine and sine integrals, respectively.[30] The shorter τ value producing maximal $S(\tau)$ intensity is $\tau^{opt} = 2.18/(\kappa b_{IS})$.

Given Eq.(3.4), the RN_n^ν recoupling can be replaced by a R^3 one bracketed by π/2-pulse with phases -y and y. Nevertheless, I-π/2 pulses applied at the beginning of the defocusing period and the end of the refocusing one do not affect the signal intensity since at such times, the terms in the density matrix which contribute to the signal, are proportional to $\hat{S}_x$ operator. Hence, these pulses can be removed and the sequence using R^3 recoupling on the indirectly detected channel (denoted HMQC-I-R^3 hereafter) is similar to that using $SFAM_1$ scheme. This sequence is γ-independent and its NMR signal is given by Eq.(3.10).

3.2.2.2. Recoupling applied to the detected isotope.

As said before, the dipolar recoupling is applied to *I* spin, which is detected in this part, whereas the S spin is indirectly detected.

Fig.3.2(c) displays the *D*-HMQC sequence using $SFAM_1$ recoupling (denoted HMQC-D-$SFAM_1$ hereafter). The evolution of the density matrix during this sequence is identical to that during HMQC-I-$SFAM_1$, and hence, the NMR signal is proportional to Eq.(3.8).

Fig.3.2(d) shows the pulse sequence of a novel through-space HETCOR experiments, named HUQC-RN_n^ν hereafter, in which the γ-encoded $|m| = 1$ RN_n^ν heteronuclear dipolar recoupling is applied to the detected spin. During the defocusing delay, the longitudinal magnetization of the *I* spin ($\hat{I}_z$) is converted into antiphase 1Q *I*-spin coherences, $2\hat{I}_{\frac{\pi}{2}+\varphi}\hat{S}_z$, where $\hat{I}_{\frac{\pi}{2}+\varphi} = \hat{I}_x\sin(\varphi) + \hat{I}_y\cos(\varphi)$. The simultaneous π/2-pulses on *I* and *S* channels partly convert these antiphase 1Q coherences into heteronuclear MQ coherences, $2\hat{I}_y\hat{S}_y\cos(\varphi)$, and antiphase 1Q *S*-spin coherences, $2\hat{I}_z\hat{S}_y\sin(\varphi)$. Therefore, this sequence is named *D*-HUQC since all coherences of the detected spin are allowed during the t_1 period. The isotropic shift is encoded by the evolution of these coherences during t_1 time. At the end of t_1, these coherences are converted back into $2\hat{I}_x\hat{S}_z$ and $2\hat{I}_y\hat{S}_z$ operators, which evolve into $\hat{I}_z$ one with coefficients sin(φ) and cos(φ), respectively. This longitudinal *I*-spin magnetization is converted into observable transverse *I*-spin magnetization by the last I-$\pi/2_y$ pulse. Therefore, the NMR signal

of HUQC experiment is proportional to Eq.(3.9), and hence to Eq.(3.10). In particular, the HUQC experiment using γ-encoded $|m| = 1$ RN_n^ν heteronuclear dipolar recoupling is γ-independent.

As explained above, the RN_n^ν recoupling can be replaced by a R^3 one bracketed by two π/2 pulses with phase -y and y. Hence, the sequence of HUQC experiment using R^3 recoupling (denoted HUQC-R^3 hereafter) is identical to the HMQC-D-SFAM$_1$ sequence (**Fig.3.2(c)**), but both heteronuclear MQ coherences and 1Q *S*-spin coherences evolve during the t_1 time.

We also introduce experiments using RN_n^ν or R^3 recoupling to correlate *I*-*S* MQ coherences with the *I*-spin 1Q ones. The pulse sequences of these variants of *D*-HMQC experiments (denoted HMQC-D-RN_n^ν and HMQC-D-R^3 hereafter) are shown in **Fig.3.3**. These sequences require the application of four I-π pulses during the t_1 period. In principle, their signals are identical to that of HUQC experiments. However, we show below using spin dynamics simulations that the additional I-π pulses decrease its robustness to CSA of the *I* spin (hereafter called CSA$_I$). Furthermore, in order to refocus the CSA$_I$, the four I-π pulses must be rotor-synchronized. Consequently, the period between defocusing and refocusing of the recouplings must be $4kT_R$, whereas that of HMQC-I and HUQC sequences is $2kT_R$, while the spectral width of the indirect dimension is equal to ν_R. The pulse programs corresponding to HMQC-I-RN_n^ν and HUQC are given in the Appendix.

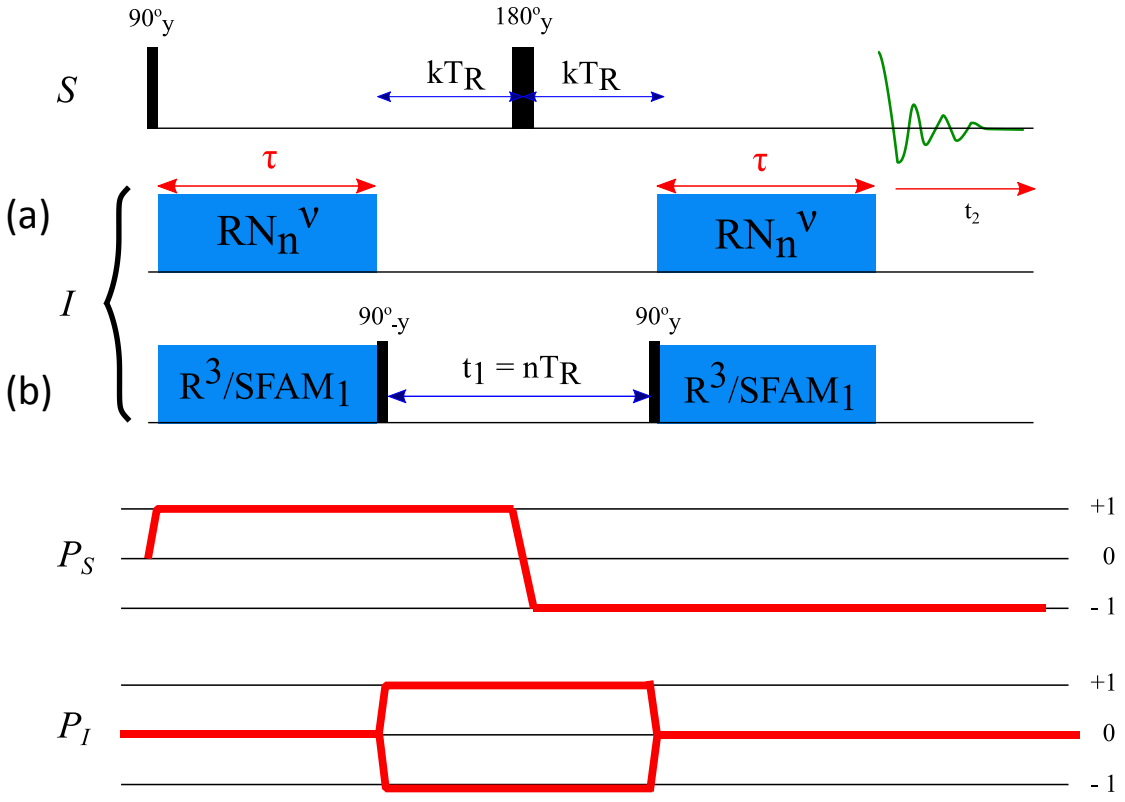

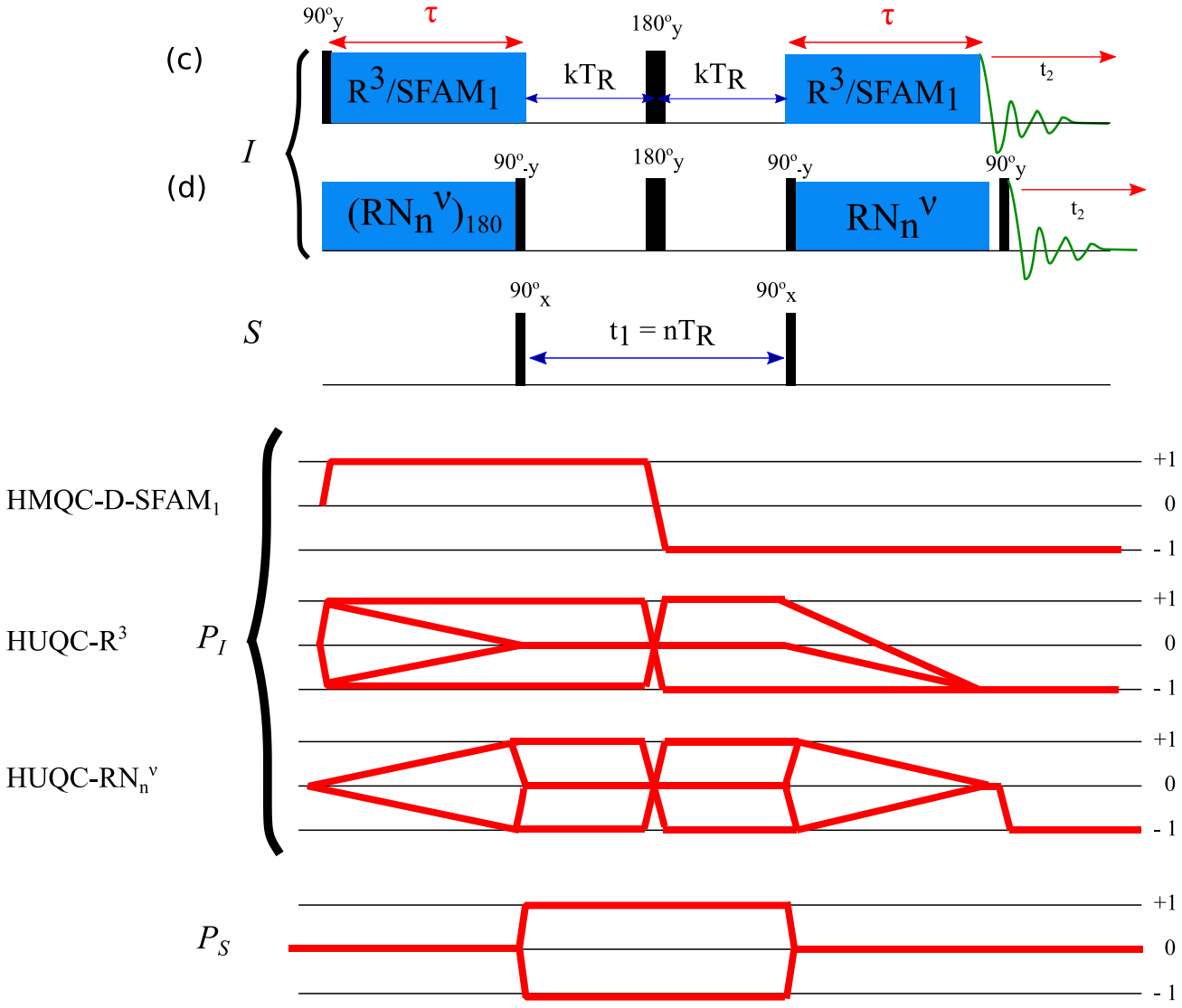

Fig.3.2. Pulse sequences and coherence transfer pathways of (a-b) HMQC-I experiment using (a) RN_n^ν and (b) R^3 or $SFAM_1$, (c) HMQC-D experiment using $SFAM_1$ as well as HUQC with R^3, and (d) HUQC using RN_n^ν. In (a) the coherence orders $p_I = \pm 1$ during the t_1 period are selected by a two-step phase cycling, in which the phase of the I-π pulses during the defocusing period and the phase of the receiver are incremented by 180°. Similarly in (b) the phases of $R^3/SFAM_1$ irradiation, the first I-$\pi/2_{-y}$ pulse and the receiver were incremented by 180° to select $p_I = \pm 1$ during t_1. For (b,c), $p_S = \pm 1$ was selected during t_1 by incrementing the phase of the first S-$\pi/2_x$ pulse and the receiver by 180°. Quadrature detection along the indirect dimension was achieved using the States-TPPI procedure,[48] by incrementing the phase of the I-pulses following the t_1 period.

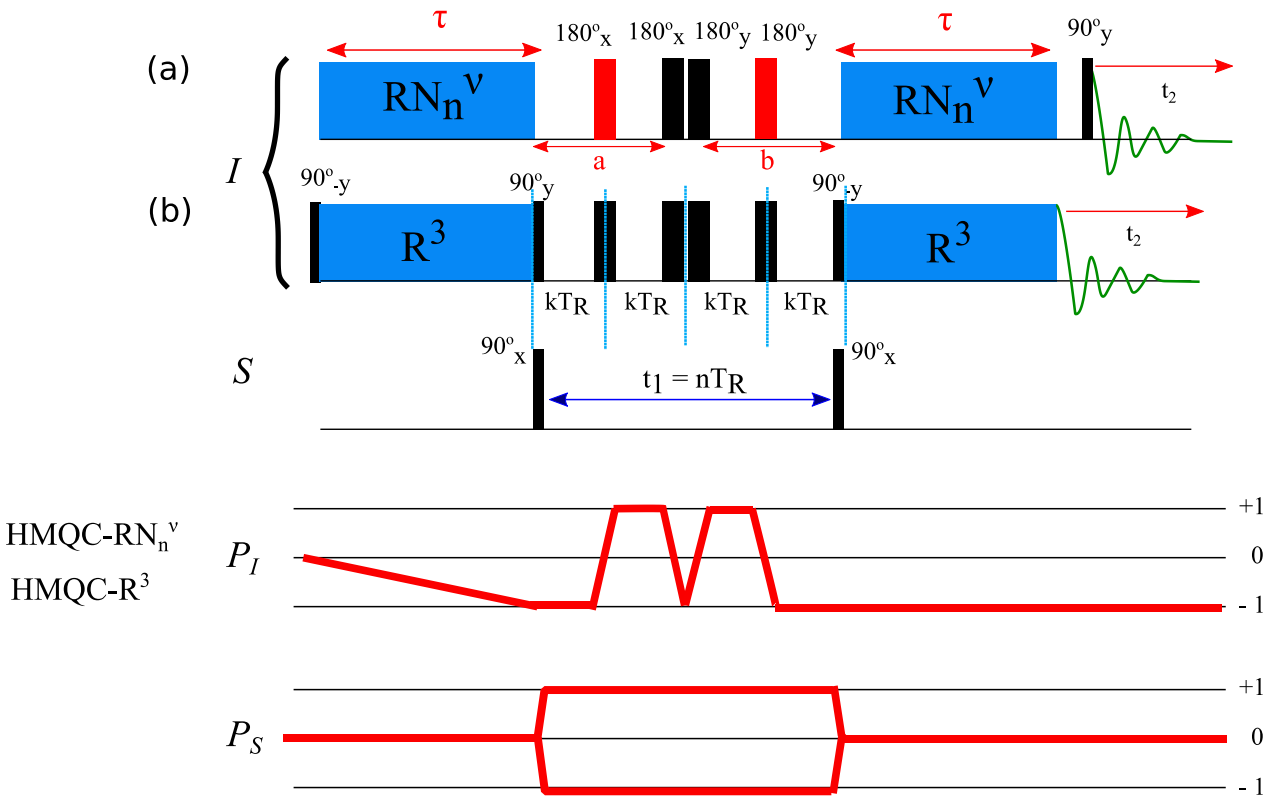

Fig.3.3. Pulse sequences and coherence transfer pathways of HMQC-D experiment using (a) RN_n^ν or (b) R^3 recoupling. The coherence orders of the *S*-spin, $p_S = \pm 1$, during the t_1 period were selected by incrementing the phase of the first S-π/2 pulse and the receiver by 180°. Quadrature detection along the indirect dimension was achieved using the States-TPPI procedure,[48] by incrementing the phase of the second S-π/2 pulse.

3.3. Simulations and experimental section

3.3.1. Numerical simulations for an isolated ^{13}C-^{15}N spin pair

All numerical simulations of spin dynamics were performed with the SIMPSON software (version 4.1.1).[36] The powder average was calculated using 168 $\{\alpha_{MR},\beta_{MR}\}$ pairs and 13 γ_{MR} angles. The 168 $\{\alpha_{MR},\beta_{MR}\}$ Euler angles, which relate the molecular and rotor frames, were selected according to the REPULSION algorithm,[37] while γ_{MR} angle was equally stepped from 0 to 360°. The spin system was an isolated ^{13}C-^{15}N spin pair. Simulations were performed for two spin-1/2 isotopes in order to limit the size of the density matrix and accelerate the simulations. The ^{13}C-^{15}N dipolar coupling constant was $b_{IS}/(2\pi)$ = 409 Hz, which corresponds to the typical ^{27}Al-^{31}P dipolar couplings for Al-O-P bonds found in alumino-phosphate materials. The CSA_I value is indicated in the figure captions, its asymmetry parameter is null, and the orientation of its principal axis systems with respect to the ^{13}C-^{15}N vector is described by the Euler angles (0, 30°, 0).

For all simulations, the static magnetic field was fixed at B_0 = 18.8 T ($\nu_{0,13C}$ = 201.2, $\nu_{0,15N}$ = 81.14 MHz). The MAS frequency was ν_R = 20 kHz, except in **Figs.3.11** - **3.14**. We simulated the powder averaged signal corresponding to HMQC-I sequence with ^{13}C detection, ^{13}C-{^{15}N} hereafter, using $SFAM_1$, $R18_4^5$, $R10_2^3$, $R16_3^5$, $R14_2^5$ and R^3 recoupling schemes. We also simulated ^{13}C-{^{15}N} HMQC-D sequences using the same recoupling schemes as well as ^{13}C-{^{15}N} HUQC using RN_n^ν and R^3 schemes. Except during the recoupling periods, the rf nutation frequencies were equal to 100 kHz during the pulses applied to ^{13}C and ^{15}N isotopes. The transfer efficiency is defined with respect to the ^{13}C signal detected after a spin echo. The rf nutation frequencies during the recoupling period were fixed to their theoretical value (see **Table 3.1**) for RN_n^ν schemes and ν_R for R^3 scheme, except in **Figs.3.6** - **3.8**. For $SFAM_1$, the peak rf amplitude, ν_1^{max}, and carrier frequency modulation, $\Delta\nu_{ref}^{max}$, were fixed to 70 and 50 kHz at ν_R = 20 kHz and 210 and 150 kHz at ν_R = 60 kHz, except in **Figs.3.6** - **3.8**. The pulses on both channels were always applied on resonance, except in **Figs**.**3.9** and **3.11**.

3.3.2. NMR experiments

Experiments were performed on a wide-bore 9.4 T and a narrow-bore 18.8 T Bruker spectrometers equipped with Avance II and III consoles, respectively. Spectra were recorded with 3.2 mm triple resonance HXY MAS probes. Rotors were fully filled with the sample.

3.3.2.1. ^{13}C-{^{15}N} correlations.

The ^{13}C and ^{15}N isotropic chemical shifts were directly referenced to 43.67 ppm and 32.3 ppm for α -Glycine peaks, respectively. ^{13}C-{^{15}N} HMQC-I, HMQC-D and HUQC experiments were performed on a sample of 98% [2-^{13}C,^{15}N] glycine ($C_2H_5NO_2$) containing a mixture of α and γ polymorphs. The sample was purchased from CortecNet and used without purification. The experiments were carried out at B_0 = 9.4 T and ν_R = 10 kHz except in **Figs.3.17**. The sequences of **Figs.3.2** and **3.3** have been combined with a preliminary ramped ^{1}H → ^{13}C CP transfer to create ^{13}C transverse magnetization, which was converted into ^{13}C longitudinal magnetization in the case of HMQC-I-RN_n^ν experiment (see **Fig.3.2(d)**). The CP contact time was 1.5 ms. The ^{13}C nutation frequency during CP was 44 kHz, whereas the ^{1}H nutation frequency was ramped from 54 to 77 kHz. During the remaining parts of the sequences, a SPINAL-64 decoupling with rf nutation frequency of 90 kHz was applied to the ^{1}H channel.[38] Except during the recoupling, the rf nutation frequencies of the π/2 and π pulses were $\nu_{1,13C}$ = 42 and $\nu_{1,15N}$ = 32 kHz. The rf nutation frequencies during the recoupling periods were fixed to their theoretical value (**Table.3.1**) for RN_n^ν scheme and $\nu_1 = \nu_R$ = 10 kHz for R^3 scheme. For SFAM$_1$ recoupling, the ν_1^{max} and $\Delta\nu_{ref}^{max}$ values were fixed to 16 or 26(for ^{15}N indirect or ^{13}C direct) and 40 kHz. The ^{13}C-{^{15}N} HMQC-I, HMQC-D and HUQC 1D and 2D spectra resulted from averaging 8 transients with a recycle delay of 3 s and 64 t_1 increments for the 2D ones. The spectral intensities were normalized with respect to those observed after the same ^{1}H → ^{13}C CP 1D spectrum.

3.3.2.1. ^{31}P-{^{27}Al} and ^{27}Al-{^{31}P} correlations.

The ^{31}P and ^{27}Al isotropic chemical shifts were referenced to 85% H_3PO_4 and a 1 M solution of $Al(NO_3)_3$, respectively. ^{27}Al-{^{31}P} HMQC-I, ^{31}P-{^{27}Al} HMQC-D and HUQC experiments were performed on two crystalline alumino-phosphate materials, VPI-5 ($Al_3(PO_4)_3(H_2O)_5$) and $Na_7(AlP_2O_7)_4PO_4$ (called (**1**) in the following) at ν_R = 20 kHz and B_0 = 9.4 T for VPI-5 and B_0 = 18.8 T for (**1**), which has been prepared according to the procedure previously reported.[39] Contrary to VPI-5, (**1**) contains ^{31}P sites subject to large CSA$_{31P}$ (up to 85 ppm).[25] The heteronuclear dipolar recoupling was always applied on the ^{31}P channel since the number of

pulses applied to the quadrupolar nucleus must be minimized. The rf nutation frequencies of $\pi/2$ and π pulses were $\nu_{1,^{31}P}$ = 74 and $\nu_{1,^{27}Al}$ = 9.3 kHz (to achieve selective excitation of the central transition (CT)). For ^{27}Al-{^{31}P} experiments, a preliminary Hyper-Secant (HS) pulse lasting 3 ms was used to enhance the polarization of the ^{27}Al CT by manipulating the population of satellite transitions.[40] The optimal HS enhancement was obtained with an rf field of 11 kHz and a frequency sweep from 180 to 160 kHz during 3 ms. The nutation frequencies during the recoupling periods were fixed to their theoretical value (**Table.3.1**) for RN_n^ν scheme and $\nu_1 = \nu_R$ = 20 kHz for R^3. For $SFAM_1$ recoupling, the ν_1^{max} and $\Delta\nu_{ref}^{max}$values were fixed to 42 and 60 kHz. The ^{27}Al-{^{31}P} HMQC-I, ^{31}P-{^{27}Al} HMQC-D and HUQC 1D and 2D spectra result from averaging 8/16 transients with a recycle delay of 1/20 s and 200/90 t_1 increments for the 2D ones. The intensities have been normalized with respect to that of either the ^{31}P signal after a $\pi/2$ hard-pulse (**Fig.3.18(b)**), or the ^{27}Al signal after a soft CT-selective $\pi/2$ pulse (**Fig.3.18(a)**).

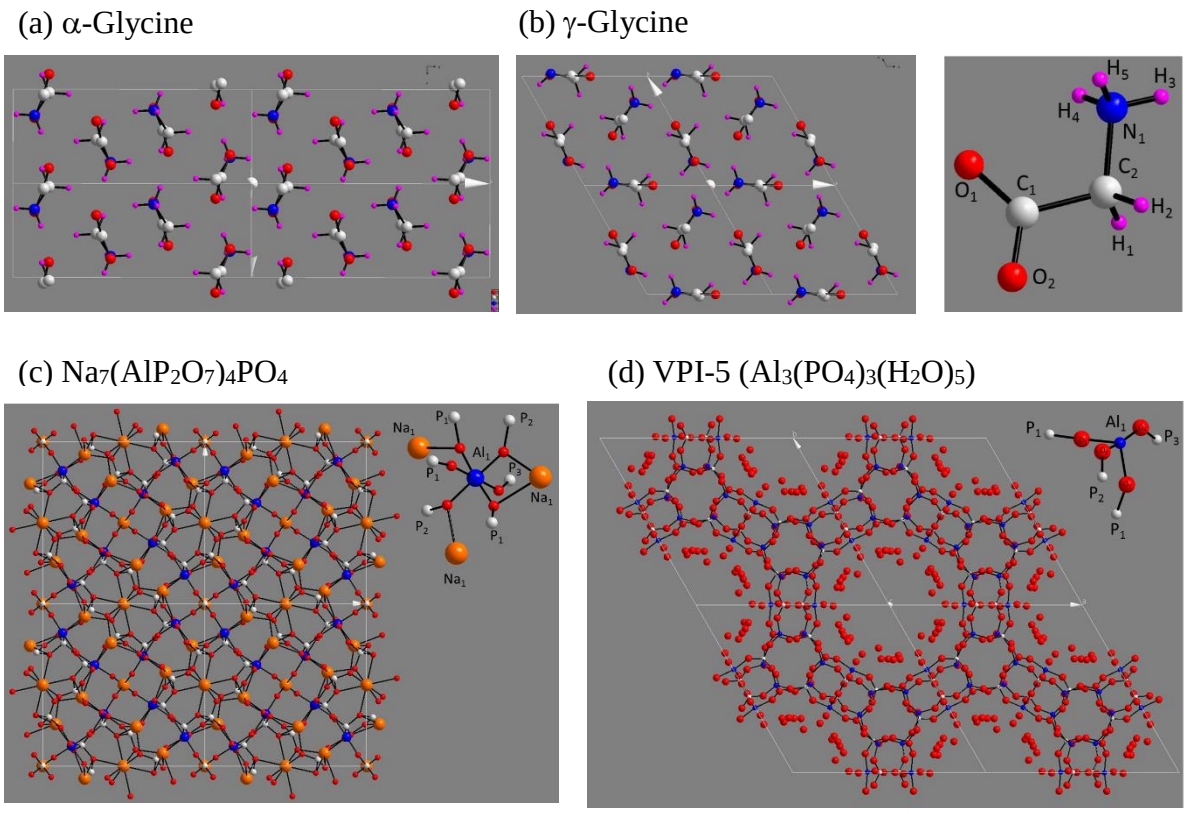

Fig.3.4. Crystal structure of (a) α-Glycine, (b) γ-Glycine, (c) $Na_7(AlP_2O_7)_4PO_4$ and (d) VPI-5 ($Al_3(PO_4)_3(H_2O)_5$). These figures are adopted from CIF files with Diamond software.

3.4. Results and discussion

3.4.1. Numerical simulations

3.4.1.1. Build up curves.

Fig.3.5 shows the simulated build-up curves of ^{13}C-{^{15}N} HMQC-I experiments for an isolated ^{13}C-^{15}N spin pair in the absence of any CSA. As expected, the reduced orientation dependence of γ-independent sequences, HMQC-I-RN_n^ν and -R^3, leads to a stronger oscillation of signal intensity versus τ than for HMQC-I-SFAM$_1$, the signal of which depends on $\gamma_{PR}^{D,IS}$ angle. Furthermore, the maximal transfer efficiency of γ-independent sequences is about 25% higher than that of HMQC-I-SFAM$_1$. These results are consistent with Eqs.(3.8) and (3.10). Furthermore, the optimal recoupling times agree with the τ^{opt} expressions and κ values given in the section II. Owing to its large scaling factor, R^3 scheme produces the fastest transfer and hence must be advantageous in the case of fast signal decay. We checked [not shown] that the build-up curves of HMQC-D and HUQC sequences are identical to their HMQC-I counterpart using the same recoupling schemes.

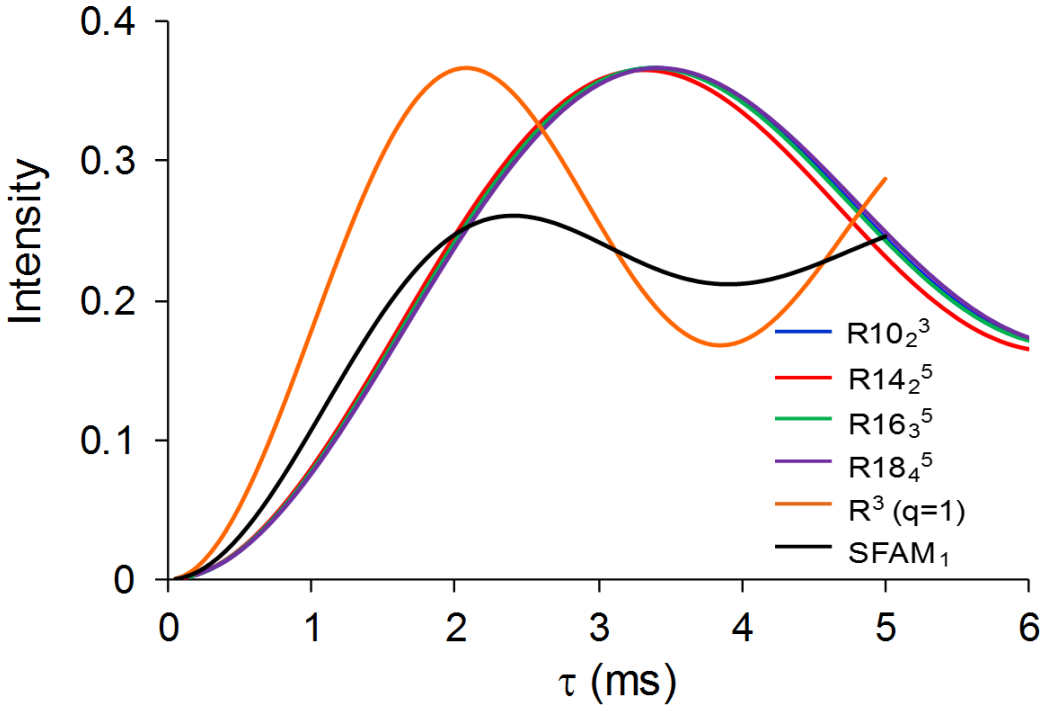

Fig.3.5. Simulated build-up curves of ^{13}C-{^{15}N} HMQC-I experiments of an isolated ^{13}C-^{15}N spin pair without any CSA, using SFAM$_1$, RN_n^ν and R^3 recoupling (see the labels of the curves on the right of the figure).

3.4.1.2. Robustness to rf inhomogeneity.

There exists an inherent distribution of rf field amplitudes in the sample coil of MAS probes, mostly along the axis of solenoid coil. Typically the rf field amplitude is maximal at the center of the coil and drops by about 50% near the edges.[41] The simulated signal intensity of ^{13}C-{^{15}N} HMQC-I, HMQC-D-SFAM$_1$ and HUQC experiments on an isolated ^{13}C-^{15}N spin pair is shown as function of ν_{1I} or ν_1^{max} shown either in absolute (**Fig.3.6**) or in relative (**Fig**.**3.7**) value. SFAM$_1$ exhibits the highest robustness to rf inhomogeneity owing to the modulation of the rf-field, whereas the R^3 scheme is the least robust. The RN_n^ν schemes, which are γ-encoded as R^3, are nevertheless more robust to rf-field variation. In the absence of CSA$_I$ (compare **Fig.3.6(a)** and **(c)** or **3.7(a)** and **(c)**), the robustness of RN_n^ν recoupling to rf-field is higher when the recoupling is applied to the indirectly detected spin. For both R^3 and RN_n^ν recoupling, the robustness to rf maladjustment or inhomogeneity increases when the irradiated spin is subject to CSA$_I$. Such effect has already been reported for R^3 irradiation.[23,26]

Similar simulations for HMQC-D-R^3 and -RN_n^ν experiments show that their efficiencies strongly decrease for CSA$_I$ = 10 kHz (**Fig.3.8**), and hence that the HUQC method should be preferred for direct recoupling. This limited efficiency of HMQC-D-R^3 and -RN_n^ν has been confirmed experimentally (not shown), and hence these sequences will not be analyzed anymore.

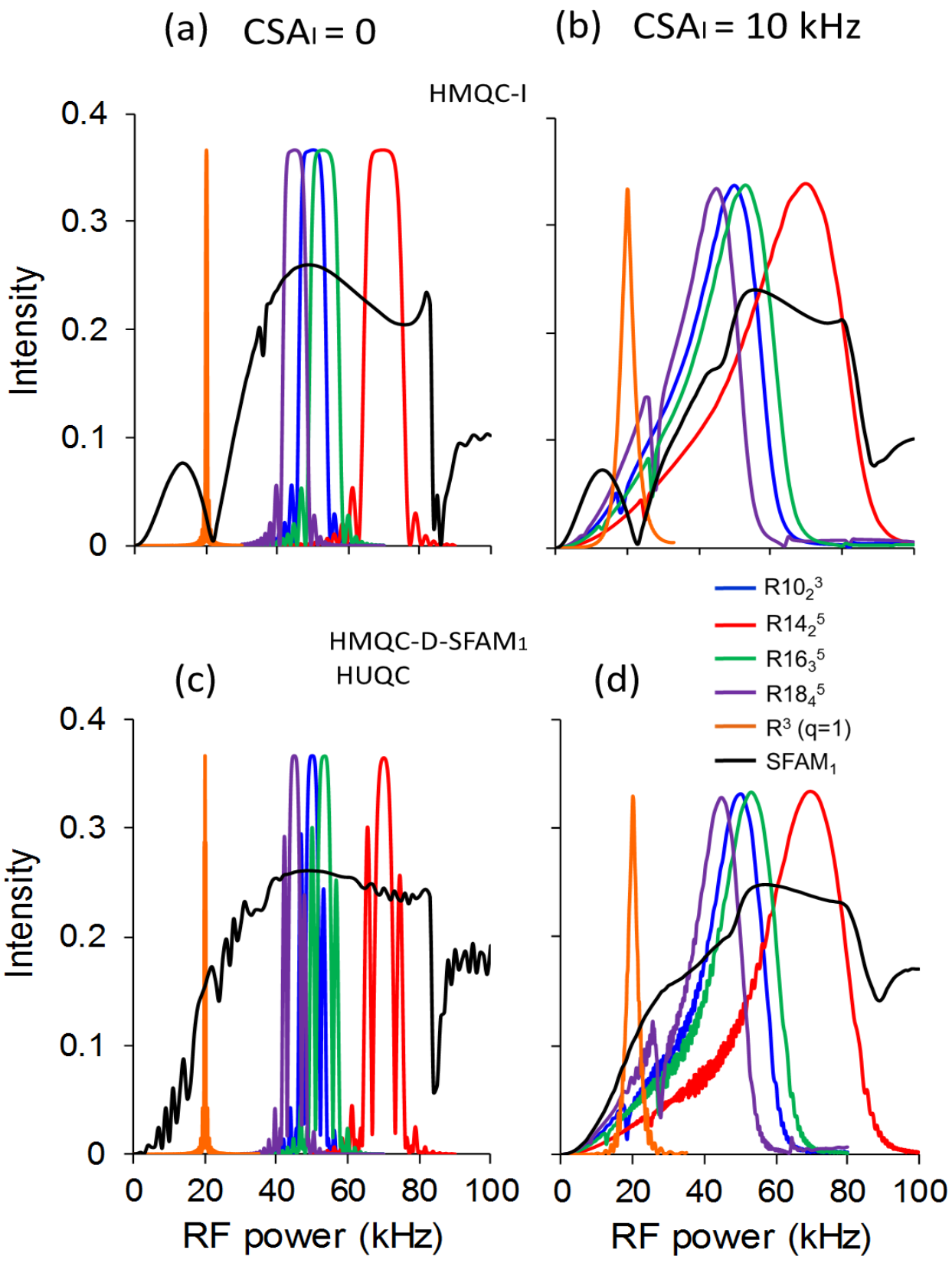

Fig.3.6. Simulated ^{13}C signal versus the applied rf field of the recoupling scheme, $\nu_1(RN_n^\nu$ or $R^3)$ or ν_1^{max} for SFAM$_1$, for ^{13}C-{^{15}N} experiments: (a,b) HMQC-I and (c,d) HMQC-D-SFAM$_1$ and HUQC using RN_n^ν and R^3 recoupling. CSA$_I$ = 0 (a,c) and 10 kHz (b,d). Recoupling times were fixed to their optimal values (**Figs.**3.5).

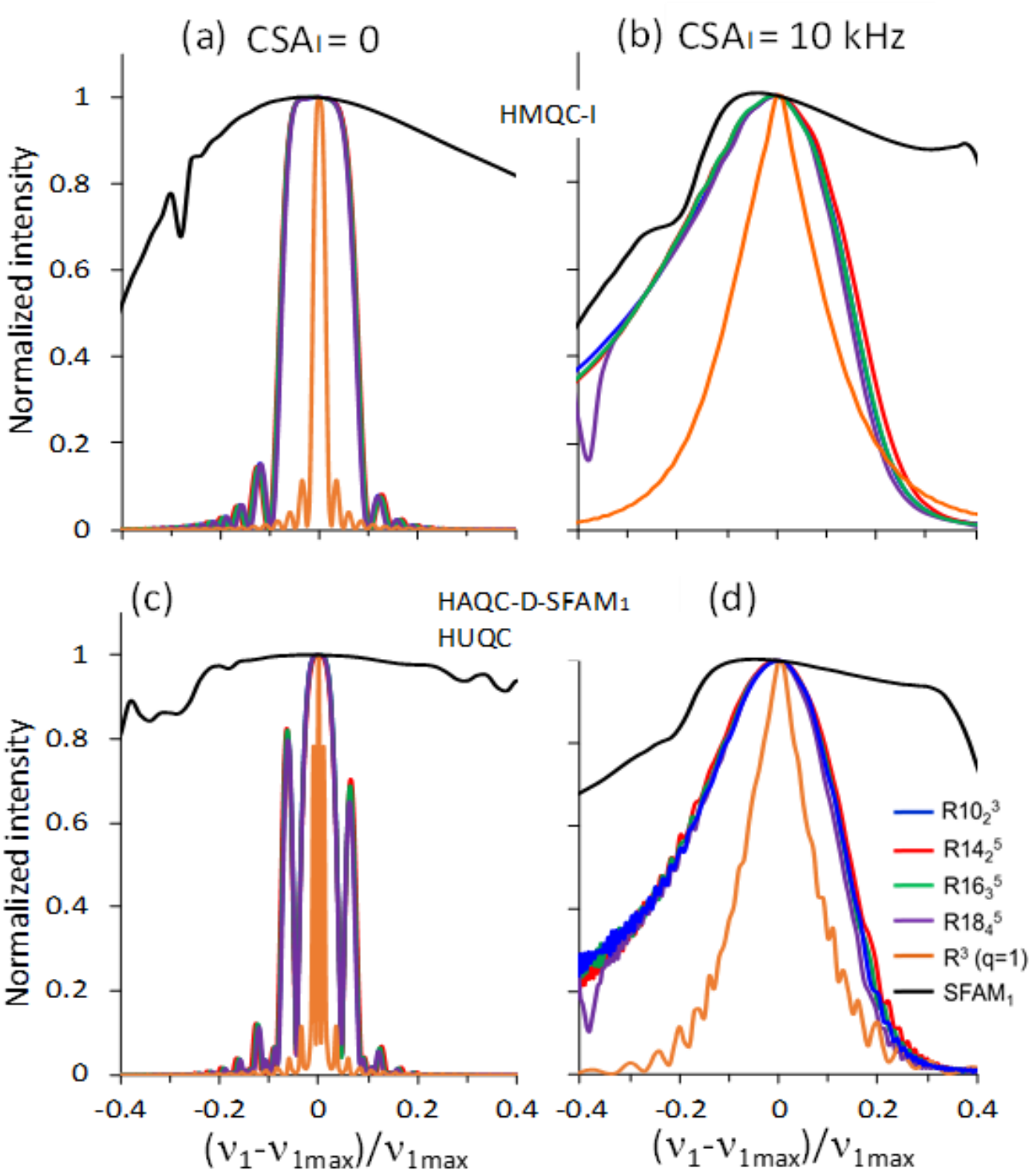

Fig.3.7. Simulated ^{13}C signal versus the ratio between the difference of the applied and nominal rf-fields and the nominal rf-field of the recoupling scheme for ^{13}C-{^{15}N} HMQC-I, HMQC-D-SFAM$_1$ and HUQC experiments for CSA$_I$ of (a,c) 0 and (b,d) 10 kHz. The recoupling times were fixed to their optimal values (**Figs.**3.5).

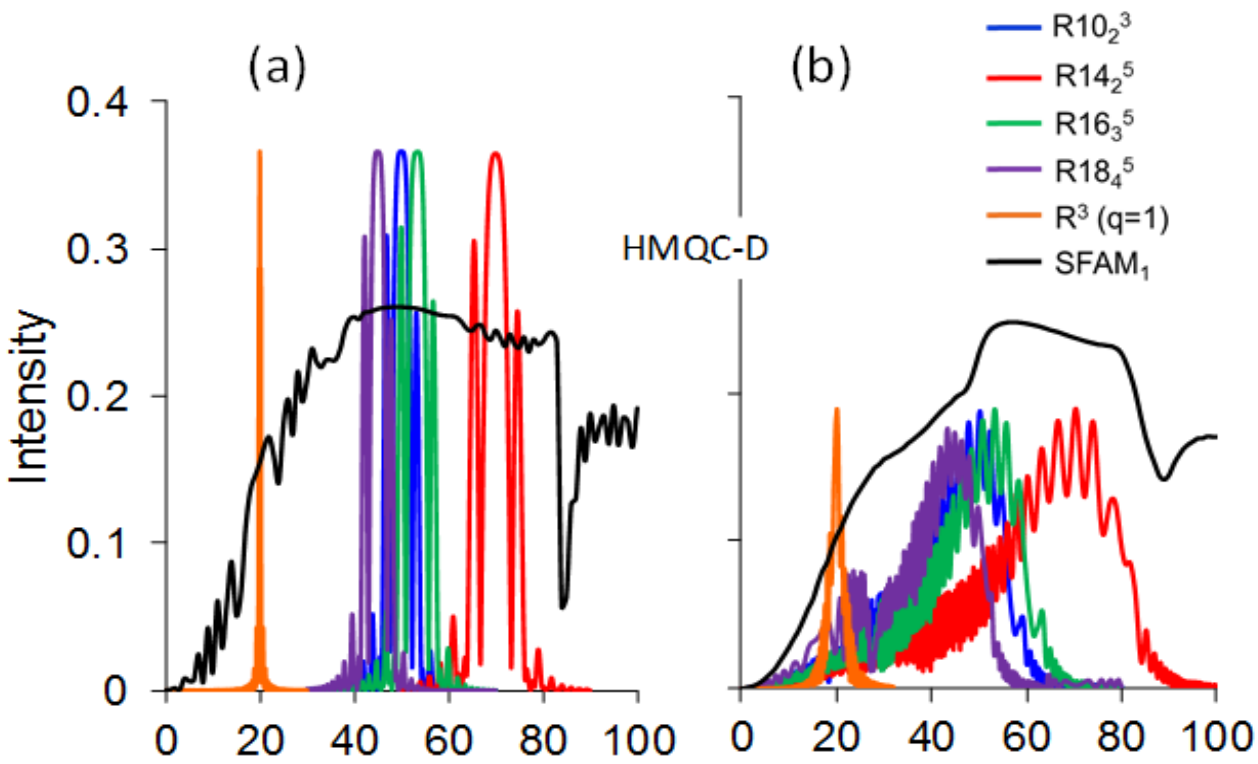

Fig.3.8. Simulated ^{13}C signal versus the applied rf field, $\nu_1(RN_n^\nu$ or $R^3)$ or ν_1^{max} for $SFAM_1$, of the recoupling scheme for ^{13}C-{^{15}N} HMQC-D experiments for CSA_{15N} = 0 (a) and 10 kHz (b). The recoupling times were fixed to their optimal values (**Figs.**3.5).

3.4.1.3. Robustness to offsets.

Fig.3.9 compares the robustness to offset of ^{13}C-{^{15}N} HMQC-I, HMQC-D-SFAM$_1$ and HUQC sequences. SFAM$_1$ recoupling is always the most robust sequence to resonance offset owing to the modulation of the carrier frequency position. Among the γ-encoded schemes, $R14_2^5$ and R^3 benefit respectively from the highest and lowest robustness to offset owing to their largest (**Table.3.1**) and smallest nominal rf-fields. The robustness to offset is globally similar when the recoupling is applied to the indirectly detected or detected isotope. As these recoupling schemes are rotor-synchronized, the offset bandwidth increases for increasing MAS frequency (**Fig.3.11**).

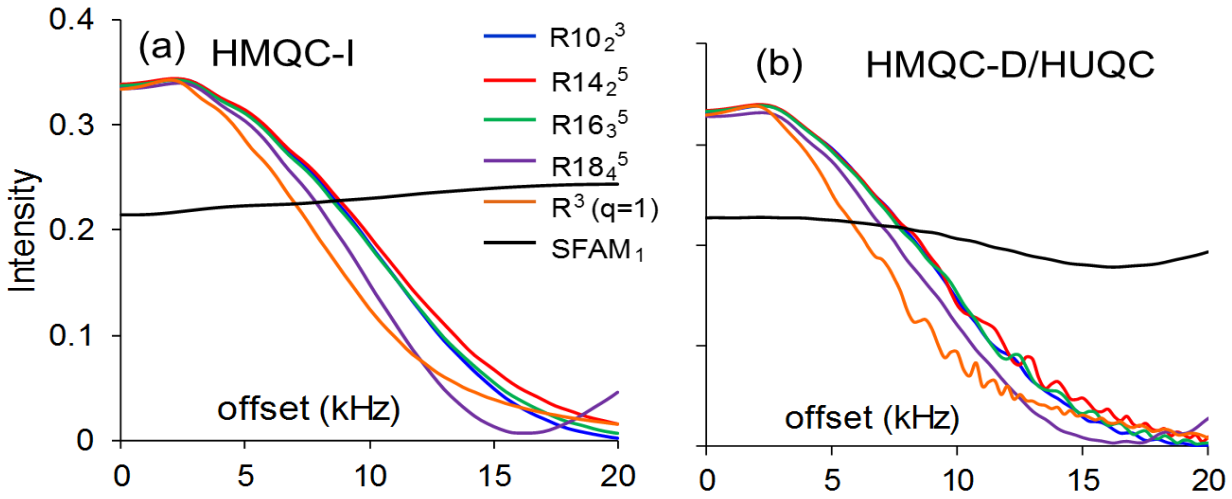

Fig.3.9. Simulated ^{13}C signal versus the resonance offset on the recoupled I channel for ^{13}C-{^{15}N} (a) HMQC-I experiments and (b) HMQC-D-SFAM$_1$ and HUQC with RN_n^ν and R^3 recoupling and CSA$_I$ = 10 kHz. Recoupling times were fixed to their optimal values (**Figs.3.5**).

3.4.1.4. Robustness to CSA$_I$.

Fig.3.10 shows the variation of the signal intensity of ^{13}C-{^{15}N} HMQC-I, HMQC-D-SFAM$_1$ and HUQC sequences versus CSA$_I$. SFAM$_1$ scheme is the least robust since its modulation during the rotor period interferes with the modulation of the rf carrier frequency. R^3 scheme benefits from the highest robustness to CSA$_I$ (see also **Fig.3.6** and **3.7**).

The robustness to CSA of RN_n^ν schemes is lower than that of R^3 since the CSA$_I$ results in imperfect π-pulses. Nevertheless, the deviation from the π-pulse is inverse proportional to ν_{1I}, and hence the robustness increases with the nominal rf-field. For the same reason, the robustness to CSA$_I$ increases with ν_R since the recoupling schemes are rotor-synchronized (**Fig.3.11(c)** and **(d)**).

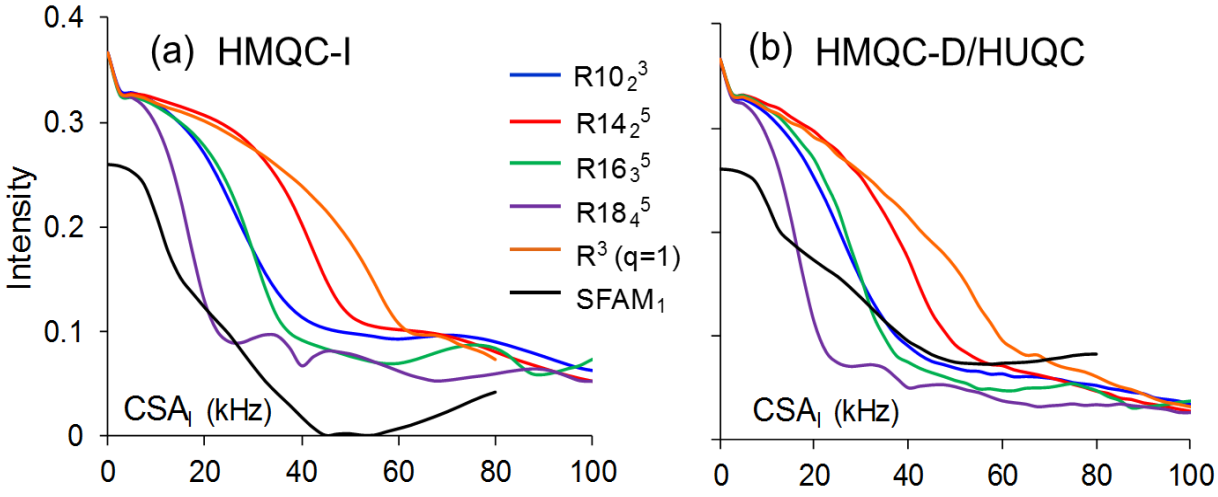

Fig.3.10. Simulated ^{13}C signal intensity versus CSA$_I$ for ^{13}C-{^{15}N} experiments: (a) HMQC-I and (b) HMQC-D-SFAM$_1$ and HUQC with RN_n^ν and R^3 recoupling. Recoupling times were fixed to their optimal values (**Figs.**3.5).

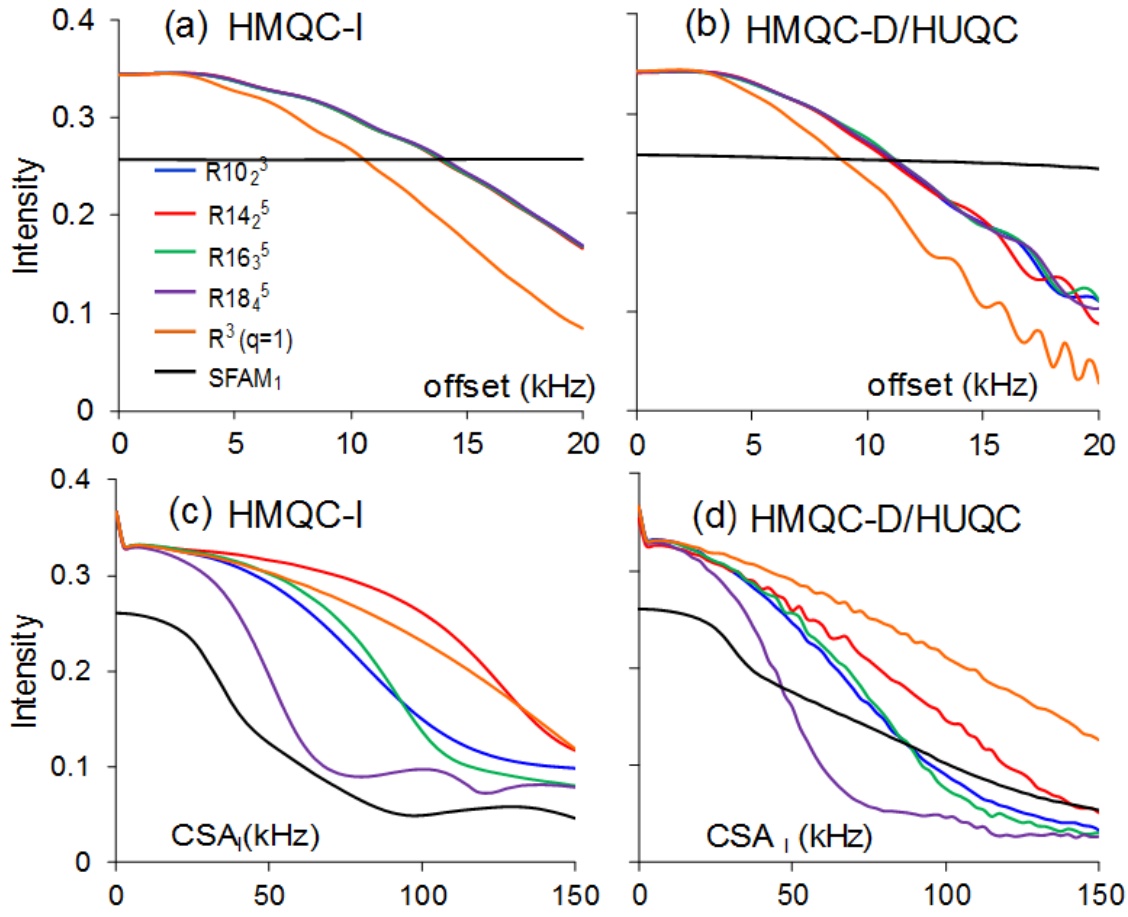

Fig.3.11. Simulated ^{13}C signal intensity at ν_R = 60 kHz versus (a,b) the resonance offset and (c,d) the CSA$_I$ of the irradiated isotope for ^{13}C-{^{15}N}: (a,c) HMQC-I experiments and (b,d) HMQC-D-SFAM$_1$ and HUQC using RN_n^ν and R^3 recoupling. In (a,b) CSA$_I$ = 10 kHz, whereas in (c,d), the recoupling is applied on resonance.

3.4.1.5. MAS frequency variations.

Fig.3.12 displays the variations of signal intensities of ^{13}C-{^{15}N} HMQC-I, HMQC-D-SFAM$_1$ and HUQC sequences versus ν_R. SFAM$_1$ scheme is most sensitive to variation in ν_R since it is non-γ-encoded. The sensitivity to MAS variations is especially high when the SFAM$_1$ recoupling is applied to the detected nucleus (**Fig.3.12(b)**) since in that case, the CSA$_I$ is imperfectly refocused when $\nu_R \neq 20$ kHz, which decreases the signal intensity. As expected the γ-encoded schemes exhibit better robustness to MAS fluctuations. Furthermore, for those recoupling methods, the robustness to ν_R is similar when the recoupling is applied to the detected or indirectly detected isotope (compare **Fig.3.12(a)** and **(b)**). As seen by comparing **Fig.3.12** and **3.13**, the tolerance to ν_R deviations does not depend on its value in Hz, and hence, the relative variations in MAS frequency must be smaller at high MAS frequency. In the case of larger CSA (29 kHz), R^3, R14$_2^5$ and R16$_3^5$ schemes are more robust to the ν_R fluctuations than the other sequences (**Fig.3.14**).

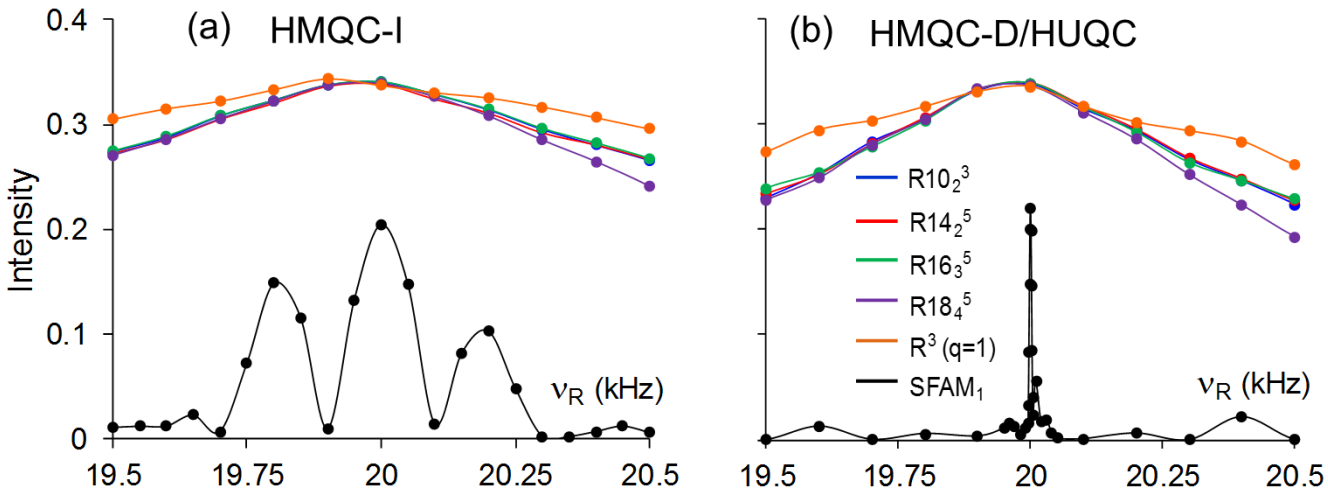

Fig.3.12. Simulated ^{13}C signal intensity versus ν_R for ^{13}C-{^{15}N} experiments: (a) HMQC-I and (b) HMQC-D-SFAM$_1$ and HUQC using RN_n^ν and R^3 recoupling with CSA$_I$ = 10 kHz. Recoupling times were fixed to their optimal values (**Figs.3.5**).

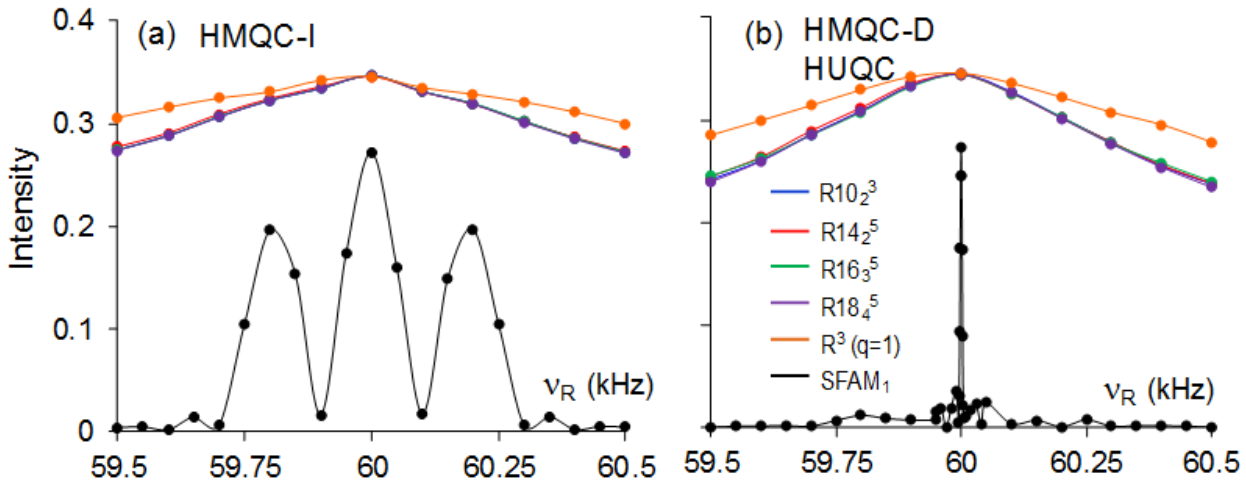

Fig.3.13. Simulated ^{13}C signal intensity around ν_R = 60 kHz for ^{13}C-{^{15}N} experiments: (a) HMQC-I and (b) HMQC-D-SFAM$_1$ and HUQC experiments using RN_n^ν and R^3 recoupling with CSA$_I$ = 10 kHz. The recoupling times were fixed to their optimal values (**Figs.3.5**).

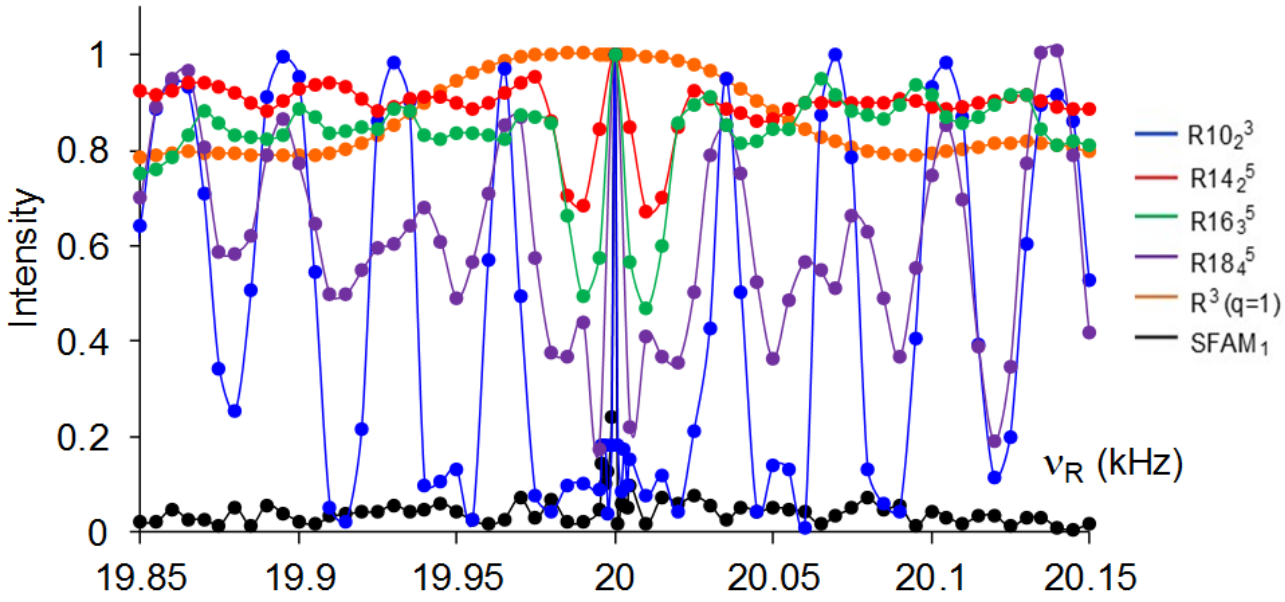

Fig.3.14. Simulated ^{13}C signal intensity around ν_R = 20 kHz for ^{13}C-{^{15}N} HMQC-D-SFAM$_1$ and HUQC experiments when CSA$_{13C}$ = 27.5 kHz, which is the shielding value of P$_1$ in sample (**1**) at 18.8 T.

3.4.2. Experimental verifications

3.4.2.1. ^{13}C-{^{15}N} D-HETCOR

Fig.3.15(a) displays the experimental build-up curves of the $^{13}C^{\alpha}$ signal of [2-^{13}C,^{15}N] glycine in 1D ^{13}C-{^{15}N} HMQC-I spectra. The CSA_{15N} of the NH_3^+ group is equal to 9.7 ppm, i.e. 400 Hz at B_0 = 9.4 T.[42] The experimental build-up curves agree well with the simulated ones shown in **Fig.3.5** with null CSA_{15N}. The major difference is the lower transfer efficiency for HMQC-I-R^3 sequence, which stems from its poor robustness to rf field inhomogeneity. For HMQC-I experiments, the highest signal intensity is achieved using RN_n^{ν} recoupling since these methods combine γ-encoding and higher robustness to rf-field than R^3 scheme.

Nevertheless, when the recoupling is applied to the detected ^{13}C nucleus, subject to CSA_{13C} = 19.43 ppm, i.e. 1.95 kHz at B_0 = 9.4 T,[43] $SFAM_1$, $R18_4^5$, $R10_2^3$ and $R16_3^5$ schemes produce similar intensities (**Fig.3.15(b)**) since the RN_n^{ν} recoupling techniques are less robust to rf inhomogeneity when applied to the detected spin (**Table.3.3**). **Fig.3.16(a)**,**(b)** and **(c)**,**(d)** show respectively the ^{13}C-{^{15}N} HMQC-I and HMQC-D/HUQC 2D spectra of glycine, which exhibit two cross-peaks, one correlating the de-shielded ^{13}C signal to the shielded ^{15}N one, assigned to α-glycine and the other one to γ-glycine.[44] As seen in ^{13}C slices of these 2D spectra, RN_n^{ν} recoupling schemes always produce higher signal intensity than $SFAM_1$ and R^3 schemes.

We measured experimentally the robustness to rf-field inhomogeneity and offset of the various recouplings and the results are given in **Table.3.3**. As already observed in numerical simulations, $SFAM_1$ recoupling exhibits the highest robustness to rf-field inhomogeneity and offset and RN_n^{ν} schemes are more robust to offset and rf inhomogeneity than R^3. Furthermore, the RN_n^{ν} recoupling schemes are more sensitive to the offset and rf field when they are applied to the detected isotope. Experiments also confirm that the non-γ-encoded $SFAM_1$ sequence is the least robust to variation in MAS frequency (**Fig.3.17**).

Table.3.3. Experimental robustness to rf-inhomogeneity, R_{rf}, and offsets, $\Delta\nu_{ref}$, for the $^{13}C^{\alpha}$ signal of [2-^{13}C,^{15}N] glycine in ^{13}C-{^{15}N} HMQC-I, HMQC-D-SFAM$_1$ and HUQC 1D experiments.

Scheme	HMQC-I		HMQC-D/HUQC	
	[a] R_{rf}	[b] $\Delta\nu_{ref}$/kHz	[a] R_{rf}	[b] $\Delta\nu_{ref}$/kHz
$R18^5_4$	0.29	9.8	0.20	7.5
$R10^3_2$	0.30	9.8	0.21	7.3
$R16^5_3$	0.28	9.8	0.23	7.0
$R14^5_2$	0.31	9.0	0.25	7.5
R^3	0.14	7.0	0.09	7.0
SFAM$_1$	1.01	35	1.46	20

[a] R_{rf}, is defined as the ratio between the total rf-range where the signal is larger than half its maximum and the nominal nutation frequency. [b] $\Delta\nu_{ref}$ is defined as the frequency offset range on the recoupled channel, for which the signal intensity is larger than the half maximum of the signal.

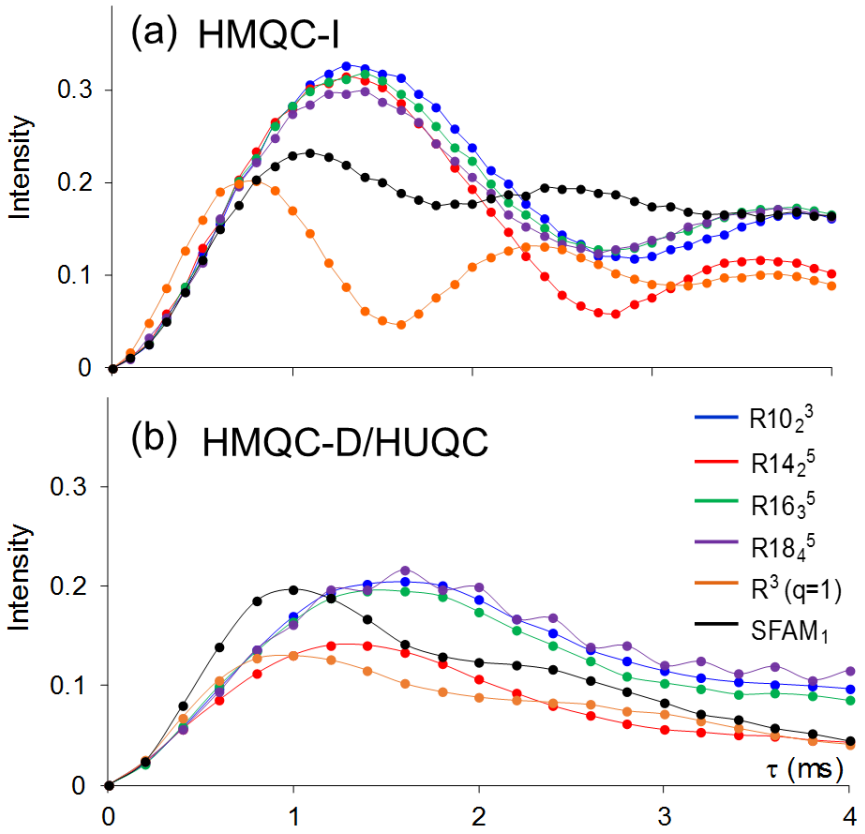

Fig.3.15. Experimental build-up curves of $^{13}C^{\alpha}$ signal of [2-^{13}C,^{15}N] α-glycine for ^{13}C-{^{15}N} 1D experiments: (a) HMQC-I, (b) HMQC-D-SFAM$_1$ and HUQC using RN_n^{ν} and R^3 recoupling.

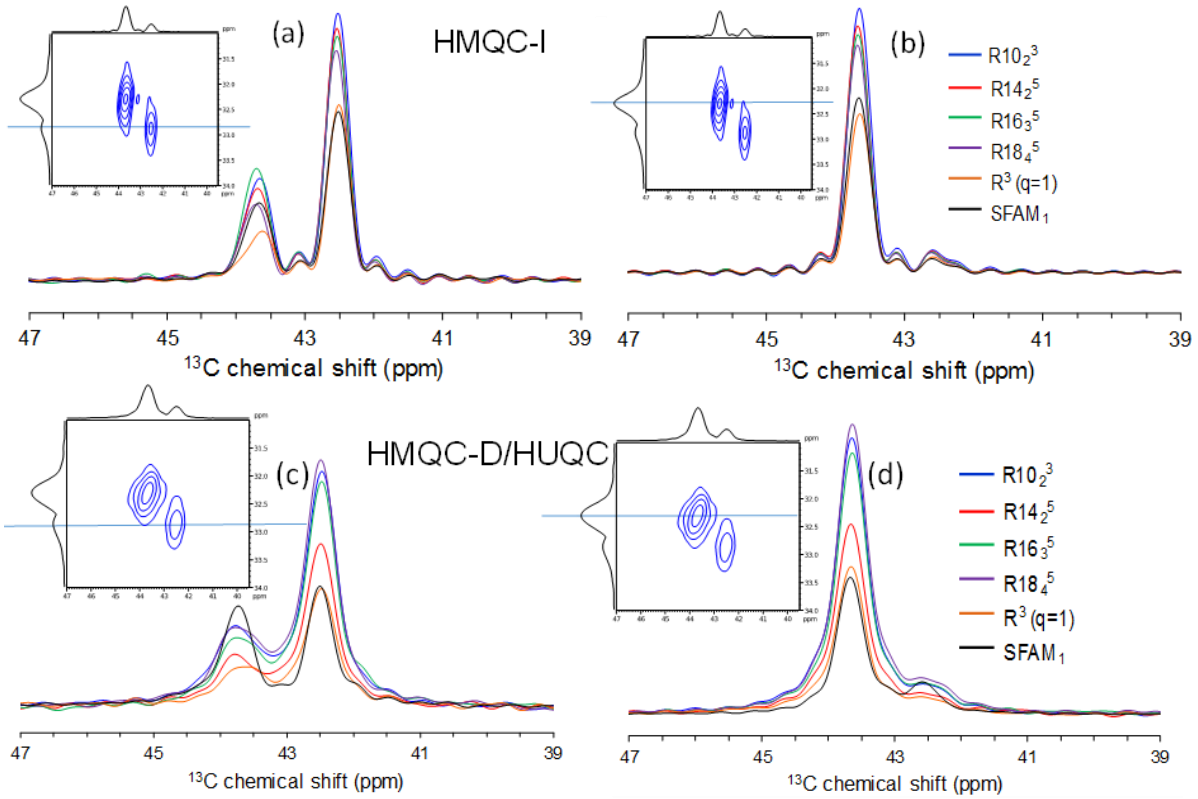

Fig.3.16. Experimental ^{13}C-{^{15}N} (a,b) HMQC-I and (c,d) HMQC-D-SFAM$_1$ and HUQC with RN_n^ν and R^3 recoupling 2D spectra of [2-^{13}C,^{15}N] glycine containing a mixture of α and γ polymorphs. The recoupling times were fixed to their optimal values determined from **Fig.3.15**.

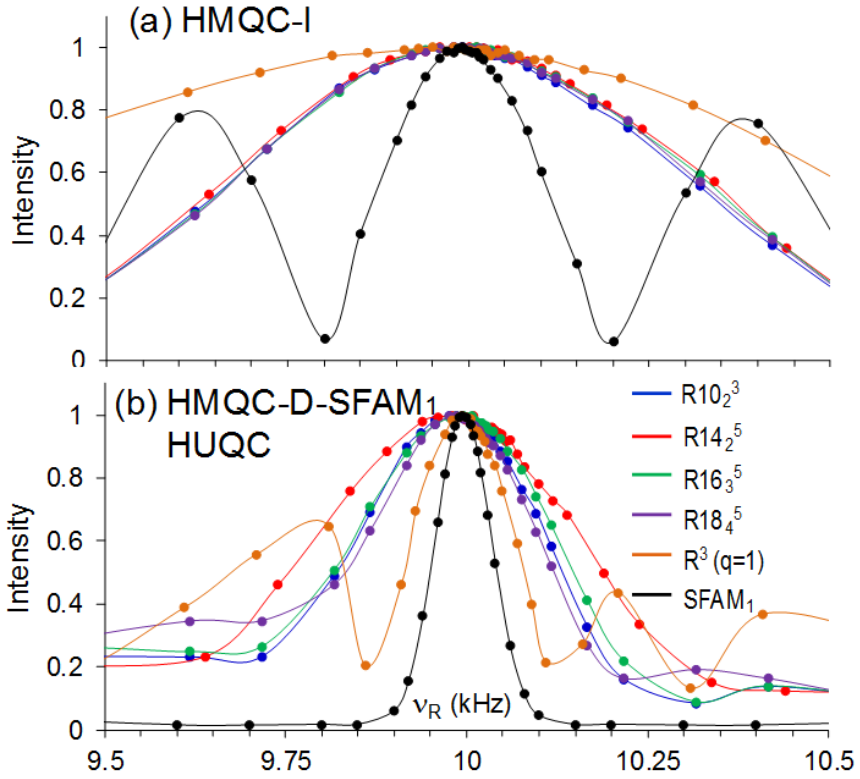

Fig.3.17. Experimental ^{13}C$^\alpha$ signal versus ν_R for ^{13}C-{^{15}N} experiments: (a) HMQC-I and (b) HMQC-D-SFAM$_1$ and HUQC experiments using RN_n^ν and R^3 recoupling. The recoupling times were fixed to their optimal values determined from **Fig.3.15**.

3.4.2.2. ^{27}Al-^{31}P *D*-HETCOR on VPI-5 at 9.4 T.

Hydrated VPI-5 contains three equally populated sites for Al and P, which are coordinated with each other through one bridging oxygen. Under MAS at 9.4 T, the ^{31}P resonances are well resolved, but only two ^{27}Al peaks are observable (Al_1 and $Al_{2,3}$). The resonance labeled Al_1 at ≈ -20 ppm represents a site between the fused four-membered rings. Two water molecules complete an octahedral coordination sphere for Al_1 and render inequivalent the tetrahedrally coordinated Al_2 and Al_3 sites at ≈ 40 ppm, as well as the phosphorus sites P_2 and P_3 in the six-membered rings. The CSA_{31P} are equal to 26.3, 33.7 and 34.6 ppm, i.e. 4.26, 5.46 and 5.60 kHz for P_1, P_2 and P_3 sites, respectively at B_0 = 9.4 T. ^{27}Al quadrupolar parameters are equal to (C_Q (MHz), η_Q) = (3.5,0.91), (1.1,0.3) and (2.2,0.8) for Al_1, Al_2 and Al_3, respectively [46]. The specific connectivities between various nuclei are as follows: Al_1 ($2P_1$, P_2, P_3), Al_2 (P_1, $2P_2$, P_3) and Al_3 (P_1, P_2, $2P_3$).

Fig.3.18 shows the build-up curves of $^{27}Al_{2,3}$ signal in ^{27}Al-{^{31}P} HMQC-I and $^{31}P_2$ signal in ^{31}P-{^{27}Al} HMQC-D-$SFAM_1$ and HUQC spectra of VPI-5, and **Fig.3.19** the corresponding 2D spectra and 1D slices. $SFAM_1$ recoupling always results in the fastest build-up (**Fig.3.18**). For HMQC-I experiments, the highest intensity is achieved using $SFAM_1$ (**Figs.3.18(a)** and **3.19(a)-(c)**). Conversely HMQC-D-$SFAM_1$ and HUQC-RN_n^ν sequences produce similar cross-peak intensities (Fig.**3.18(b)** and **3.19(d)**).

Table.3.4 compares the robustness to rf inhomogeneity and offset of the various recouplings in VPI-5. As already observed for ^{13}C-{^{15}N} D-HETCORs, $SFAM_1$ recoupling exhibits the highest robustness to offset and rf inhomogeneity. The RN_n^ν schemes are more robust to rf field variation than R^3. For RN_n^ν and R^3 methods, the robustness to rf inhomogeneity and offset is higher when the recoupling is applied to the indirectly detected spin.

Fig.3.20 compares the robustness to MAS frequency of all HMQC and HUQC sequences. For HMQC-I experiment, RN_n^ν and R^3 techniques benefit from the highest robustness to variations in MAS frequency (**Fig.3.20(a)**). In the case of recoupling schemes applied to the detected spin (**Fig.3.20(b)**), the highest robustness is achieved by R^3 scheme but RN_n^ν ones are also much more robust to MAS frequency fluctuations than $SFAM_1$.

Table. 3.4. Experimental robustness to rf-inhomogeneity, R_{rf}, and offsets, $\Delta\nu_{ref}$, observed in 1D experiments of VPI-5 for the $^{27}Al_{2,3}$ signal in ^{27}Al-{^{31}P} HMQC-I and for the $^{31}P_2$ signal of ^{31}P-{^{27}Al} HMQC-D-SFAM$_1$ and HUQC.

Scheme	HMQC-I		HMQC-D/HUQC	
	R_{rf}	$\Delta\nu_{ref}$/kHz	R_{rf}	$\Delta\nu_{ref}$/kHz
$R18^5_4$	0.41	22.3	0.33	16.7
$R10^3_2$	0.42	24.2	0.26	16.2
$R16^5_3$	0.45	22.6	0.27	16.2
$R14^5_2$	0.39	22.9	0.30	16.2
R^3	0.28	23.7	0.18	16.0
SFAM$_1$	1.15	27.5	1.61	25.0

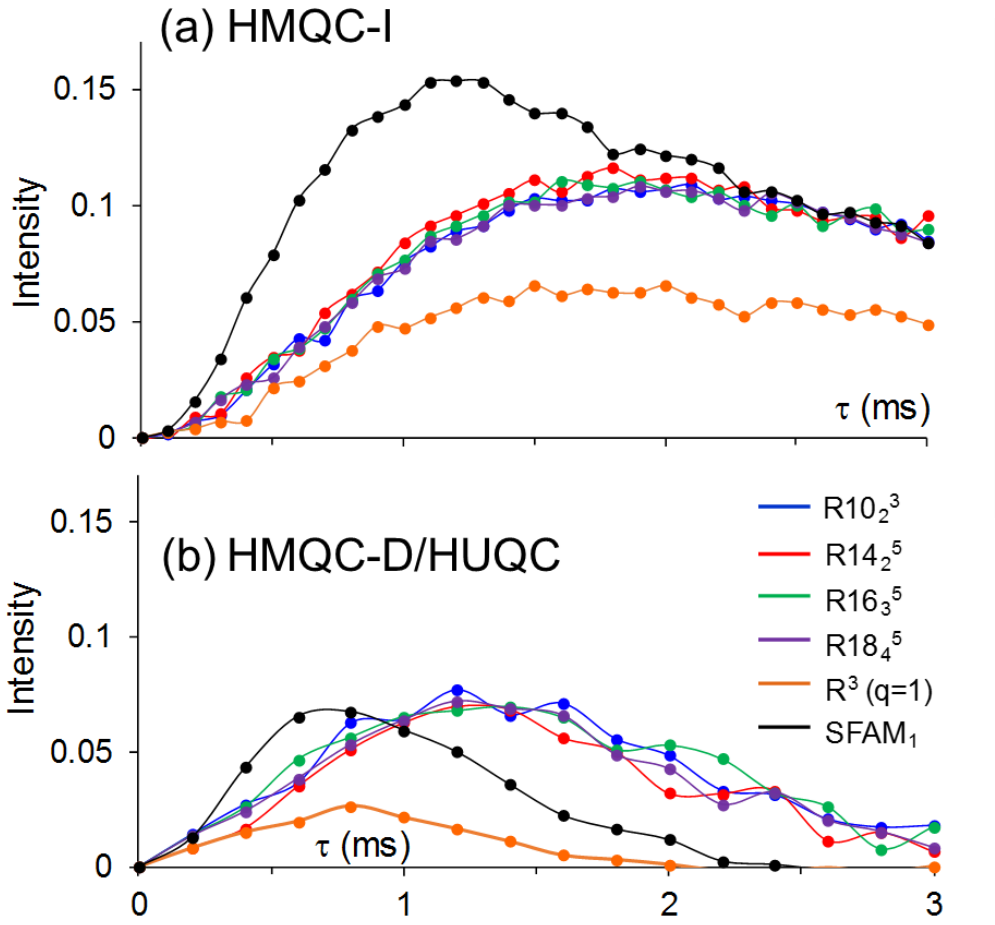

Fig.3.18. Experimental build-up curves observed with 1D experiments for VPI-5. (a) $^{27}Al_{2,3}$ signal with ^{27}Al-{^{31}P} HMQC-I and (b) $^{31}P_2$ signal with ^{31}P-{^{27}Al} HMQC-D-SFAM$_1$ and HUQC with RN^{ν}_{n} and R^3 recoupling.

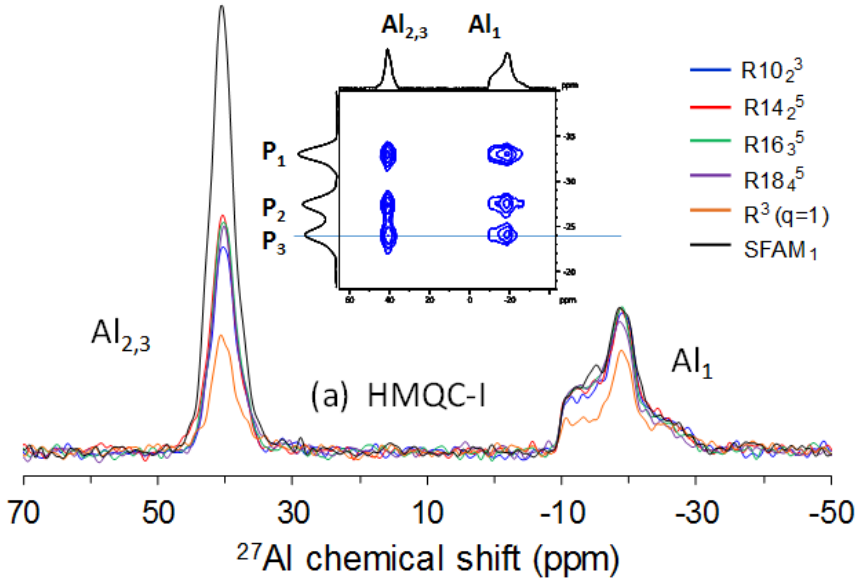

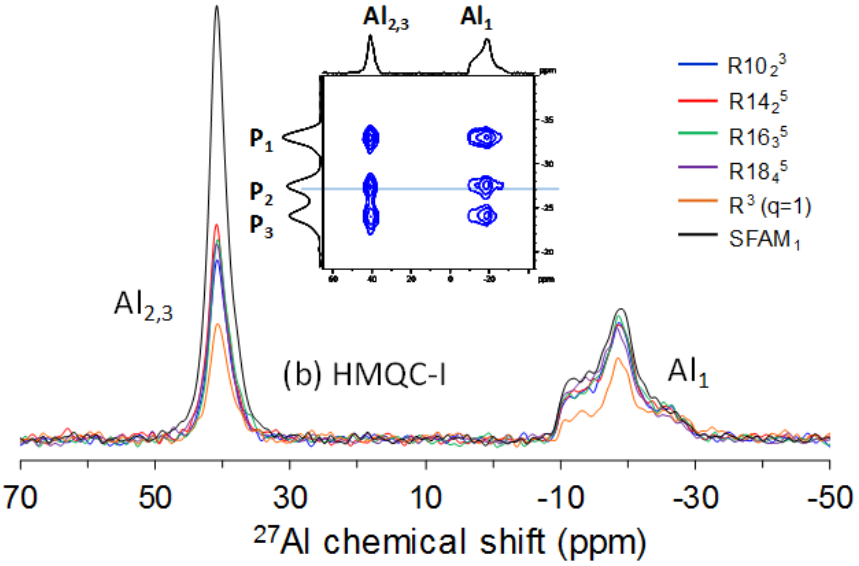

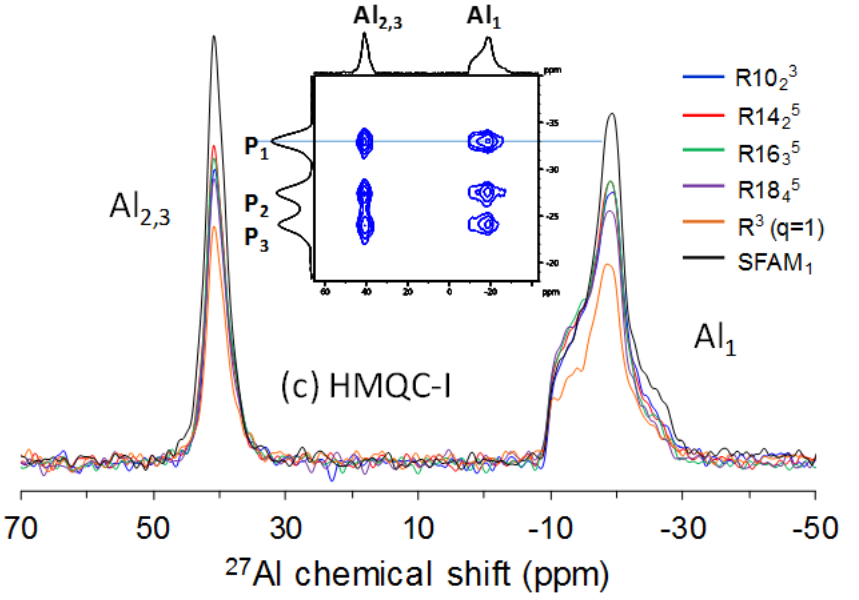

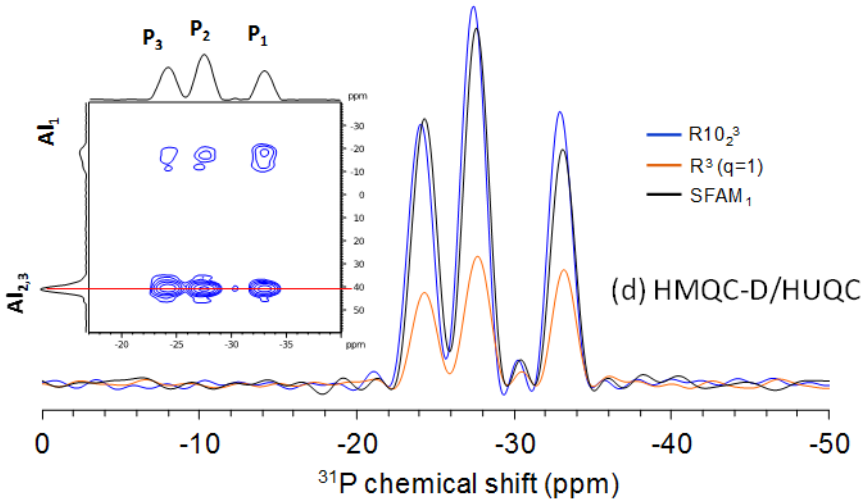

Fig.3.19. Experimental (a-c) ^{27}Al-{^{31}P} *D*-HMQC-I and (d) ^{31}P-{^{27}Al} HMQC-D-SFAM$_1$ and HUQC (R^3 and $R10^3_2$) 2D spectra and 1D slices of VPI-5 at B_0 = 9.4 T with ν_R = 20 kHz. The recoupling times were fixed to their optimal values (**Fig.3.18**).

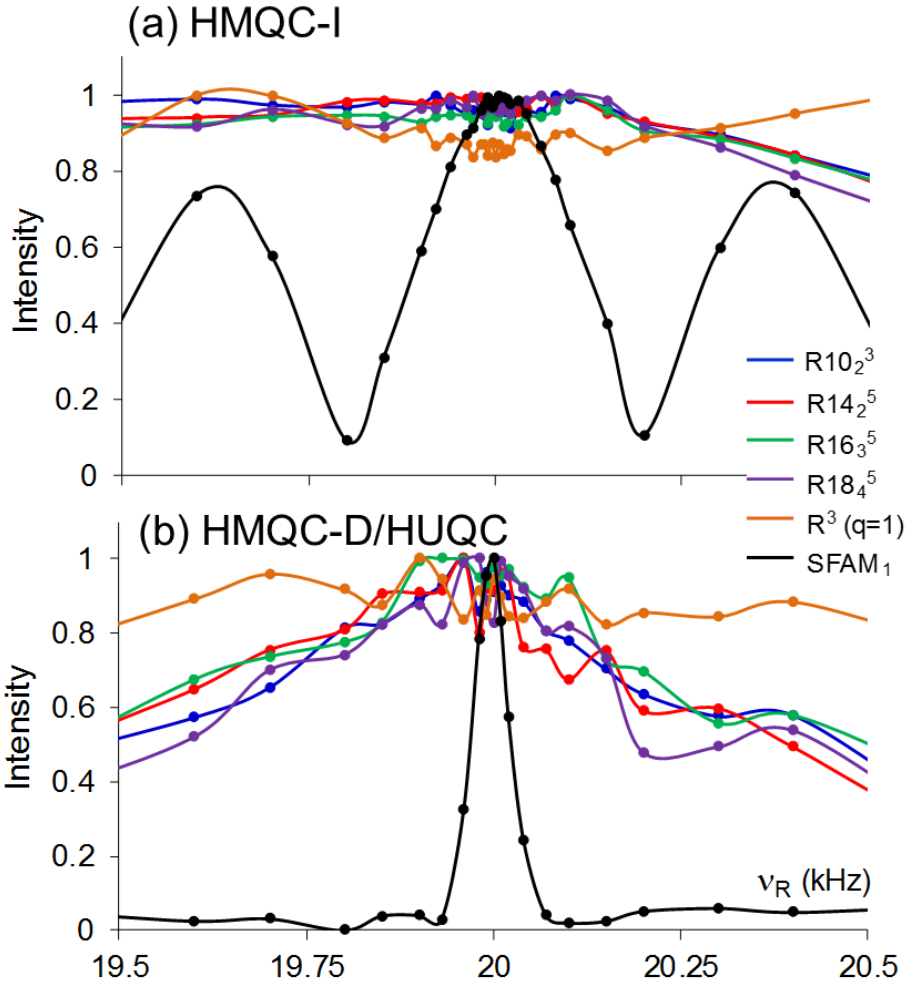

Fig.3.20. Experimental signal observed with 1D experiments of VPI-5 versus ν_R of (a) ^{27}Al$_{2,3}$ for ^{27}Al-{^{31}P} HMQC-I and (b) ^{31}P$_2$ for HMQC-D-SFAM$_1$ and HUQC with RN_n^ν and R^3 recoupling.

3.4.2.3. ^{31}P-{^{27}Al} HMQC-D-SFAM$_1$ and HUQC on $Na_7(AlP_2O_7)_4PO_4$ at 18.8 T.

Numerical simulations have shown that RN_n^ν schemes are more robust to CSA$_I$ than SFAM$_1$ recoupling. Therefore, the ^{31}P-{^{27}Al} sequences were tested with direct recoupling on $Na_7(AlP_2O_7)_4PO_4$ sample, called (**1**) hereafter, which contains three P sites with two of them subject to large CSA (**Fig.3.21**). Their CSA parameters are (δ_{aniso} (ppm), η_{CSA}) = (85, 0.6), (10.5, 0.85) and (75.7, 0.3) for P$_1$, P$_2$ and P$_3$ sites, respectively,[25] which is equivalent to CSA$_{31P}$ = 27.5, 3.4 and 24.5 kHz at 18.8 T. This sample also contains one ^{27}Al site with C_Q = 5.3 MHz and η_Q = 0.46.

Fig.3.22 compares the F1 slices of P$_1$ in sample (**1**), which presents the largest CSA$_{31P}$, for 2D spectra recorded with ^{31}P-{^{27}Al} HMQC-D-SFAM$_1$ and HUQC with RN_n^ν and R^3 recoupling. R^3 and $R10_2^3$ schemes produce the smallest and largest signal intensities, respectively. However, one notices the very large differences in the t_1-noise, lower for R^3, $R16_3^5$ and $R14_2^5$ schemes than for $R10_2^3$ and SFAM$_1$ since the former recouplings are more robust to ν_R than the latter ones. As a result, the S/N ratios are in the order: $R16_3^5 > R14_2^5 > R10_2^3 >> R18_4^5$. It must be noted that the order of the S/N is fully correlated to the robustness to spinning speed fluctuations (**Fig.3.13**), except for R^3 which is very sensitive to rf-inhomogeneity.

It has recently been shown that the t_1-noise is mainly related to the 2nd-order dipolar-CSA cross-terms, and that one way to decrease this noise is to slightly de-synchronize the sequence [47]. We have used this trick with the HUQC-$R10_2^3$ experiment by slightly increasing the spinning speed to ν_R = 20.1 kHz, without changing the pulse timing based on ν_R = 20 kHz. The corresponding F1 slices are shown in **Fig.3.23**. This de-synchronization slightly decreases the efficiency, but as expected largely improves the S/N ratio of the P$_1$ cross-peak. However, it introduces one additional parameter, the spinning speed which must be slightly optimized with respect to its theoretical value.

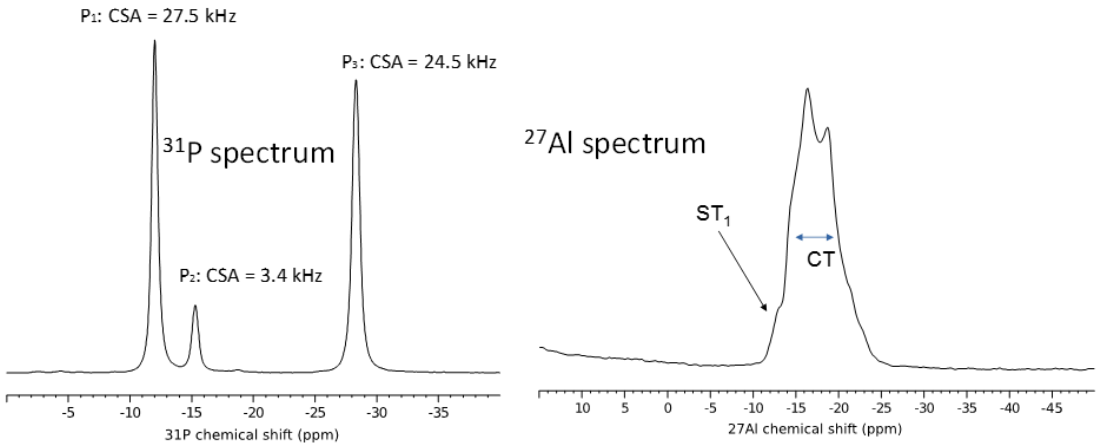

Fig.3.21. ^{31}P and ^{27}Al single hard-pulse spectra of $Na_7(AlP_2O_7)_4PO_4$ at B_0 = 9.4 T and ν_R = 20

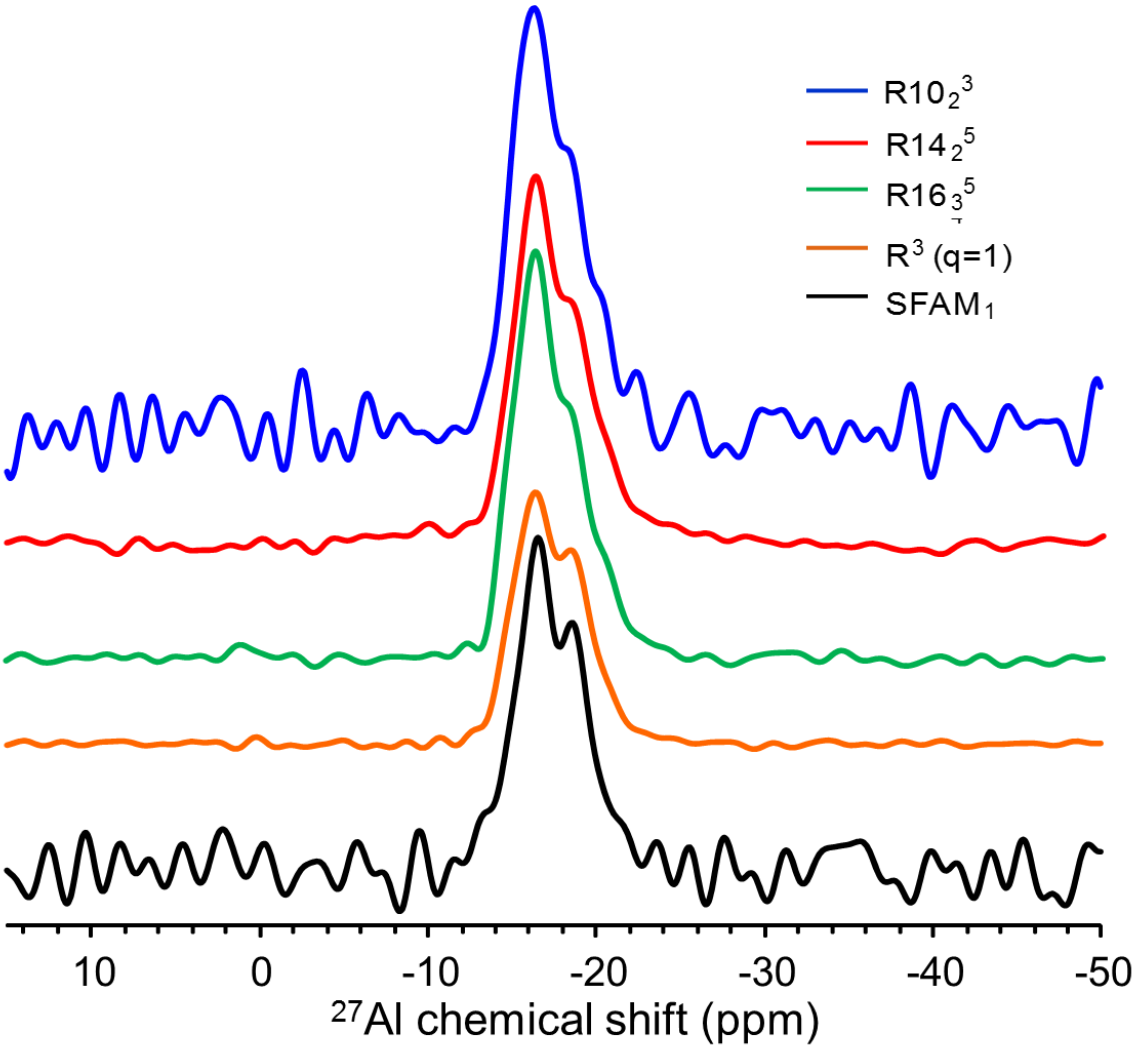

Fig.3.22. $Na_7(AlP_2O_7)_4PO_4$: experimental F1 slices observed for P_1, which presents the largest CSA_{31P} = 27.5 kHz, at B_0 = 18.8 T and ν_R = 20 kHz with HMQC-D-SFAM$_1$ and HUQC with R10$_2^3$, R16$_3^5$, R14$_2^5$ and R^3 recoupling. One observes very large differences in sensitivity, with HUQC-R10$_2^3$ and -R16$_3^5$ providing the largest and the smallest S/N, respectively.

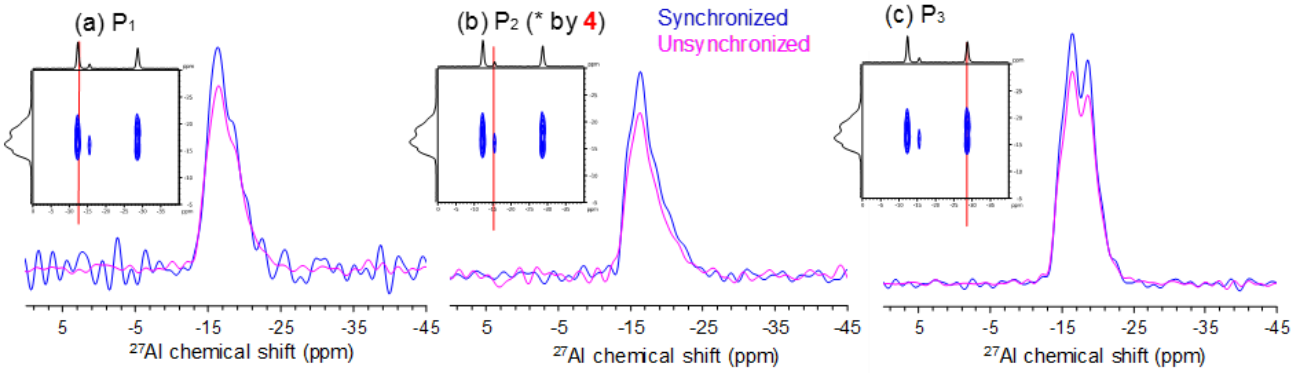

Fig.3.23. Experimental F1 slices of ^{31}P-{^{27}Al} HUQC-R10$_2^3$ of $Na_7(AlP_2O_7)_4PO_4$ at B_0 = 18.8 T, either synchronized or unsynchronized with ν_R = 20 or 20.1 kHz, respectively, both with the same τ values based on ν_R = 20 kHz

3.5. Conclusion

We have introduced symmetry-based heteronuclear dipolar recoupling schemes, which are γ-encoded and result in rapid dipolar dephasing by reintroducing the space component $|m| = 1$ for the heteronuclear dipolar coupling. These recoupling schemes have been incorporated into novel sequences to correlate half-integer spin quadrupolar nuclei and spin-1/2 isotopes, other than ^{1}H and ^{19}F. These heteronuclear correlation sequences are γ-independent and hence their signal is in principle 25% higher than that of their counterparts using non-γ-encoded recoupling schemes, such as $SFAM_1$. Furthermore, they are more robust to the CSA of the irradiated spin and the fluctuations of the MAS frequency. Such improved robustness reduces the t_1-noise in the case of spin-1/2 nuclei subject to large CSA. In addition, the γ-encoded $|m| = 1$ RN_n^v recoupling techniques, such as $R18_4^5$, $R10_2^3$, $R16_3^5$ and $R14_2^5$, are more robust to rf inhomogeneity than their R^3(q = 1) cousin. Nevertheless, the γ-encoded $|m| = 1$ recoupling techniques are less robust to rf inhomogeneity and offset than $SFAM_1$ method. ^{31}P-^{27}Al heteronuclear correlation experiments show that (i) $SFAM_1$ recoupling leads to higher transfer efficiency when the spin-1/2 nucleus is indirectly detected and subject to small CSA, whereas (ii) $R16_3^5$ scheme produces the highest *S/N* ratio in the case of detection via spin-1/2 nuclei subject to large CSA.

3.6. References

[1] J.P. Amoureux, J. Trébosc, L. Delevoye, O. Lafon, B. Hu, Q. Wang, Correlation NMR spectroscopy involving quadrupolar nuclei, Solid State Nucl. Magn. Reson. 35 (2009) 12–18. doi:10.1016/j.ssnmr.2008.11.004.
[2] M. Deschamps, D. Massiot, Correlation Experiments Involving Half-integer Quadrupolar Nuclei, in: eMagRes, John Wiley & Sons, Ltd, 2007. doi:10.1002/9780470034590.emrstm1207.
[3] G. Tricot, J. Trébosc, F. Pourpoint, R. Gauvin, L. Delevoye, Chapter Four - The D-HMQC MAS-NMR Technique: An Efficient Tool for the Editing of Through-Space Correlation Spectra Between Quadrupolar and Spin-1/2 (^{31}P, ^{29}Si, ^{1}H, ^{13}C) Nuclei, in: G.A. Webb (Ed.), Annu. Rep. NMR Spectrosc., Academic Press, 2014: pp. 145–184. doi:10.1016/B978-0-12-800185-1.00004-8.
[4] J.M. Egan, R.M. Wenslow, K.T. Mueller, Mapping aluminum/phosphorus connectivities in aluminophosphate glasses, J. Non-Cryst. Solids. 261 (2000) 115–126. doi:10.1016/S0022-3093(99)00606-7.
[5] G. Tricot, L. Delevoye, G. Palavit, L. Montagne, Phase identification and quantification in a devitrified glass using homo- and heteronuclear solid-state NMR, Chem. Commun. (2005) 5289–5291. doi:10.1039/B511207A.
[6] G. Tricot, O. Lafon, J. Trébosc, L. Delevoye, F. Méar, L. Montagne, J.-P. Amoureux, Structural characterisation of phosphate materials: new insights into the spatial proximities between phosphorus and quadrupolar nuclei using the D-HMQC MAS NMR technique, Phys. Chem. Chem. Phys. 13 (2011) 16786. doi:10.1039/c1cp20993k.
[7] G. Tricot, O. Mentré, S. Cristol, L. Delevoye, Fine Hierarchy of the V–O Bonds by Advanced Solid State NMR: Novel Pb4(VO2)(PO4)3 Structure as a Textbook Case, Inorg. Chem. 51 (2012) 13108–13113. doi:10.1021/ic300966r.
[8] B. Bouchevreau, C. Martineau, C. Mellot-Draznieks, A. Tuel, M.R. Suchomel, J. Trébosc, O. Lafon, J.-P. Amoureux, F. Taulelle, High-Resolution Structural Characterization of Two Layered Aluminophosphates by Synchrotron Powder Diffraction and NMR Crystallographies, Chem. Mater. 25 (2013) 2227–2242. doi:10.1021/cm4004799.
[9] B. Bouchevreau, C. Martineau, C. Mellot-Draznieks, A. Tuel, M.R. Suchomel, J. Trébosc, O. Lafon, J.-P. Amoureux, F. Taulelle, An NMR-Driven Crystallography Strategy to Overcome the Computability Limit of Powder Structure Determination: A Layered Aluminophosphate Case, Chem. – Eur. J. 19 (2013) 5009–5013. doi:10.1002/chem. 201203767.
[10] C.A. Fyfe, K.C. Wong-Moon, Y. Huang, H. Grondey, K.T. Mueller, Dipolar-Based 27Al .fwdarw. 29Si Solid-State NMR Connectivity Experiments in Zeolite Molecular Sieve Frameworks, J. Phys. Chem. 99 (1995) 8707–8716. doi:10.1021/j100021a041.
[11] S. Cadars, R. Guégan, M.N. Garaga, X. Bourrat, L. Le Forestier, F. Fayon, T.V. Huynh, T. Allier, Z. Nour, D. Massiot, New Insights into the Molecular Structures, Compositions, and Cation Distributions in Synthetic and Natural Montmorillonite Clays, Chem. Mater. 24 (2012) 4376–4389. doi:10.1021/cm302549k.
[12] S. Alahraché, M. Deschamps, J. Lambert, M.R. Suchomel, D. De Sousa Meneses, G. Matzen, D. Massiot, E. Véron, M. Allix, Crystallization of Y2O3–Al2O3 Rich Glasses: Synthesis of YAG Glass-Ceramics, J. Phys. Chem. C. 115 (2011) 20499–20506. doi:10.1021/jp207516w.
[13] J.W. Wiench, G. Tricot, L. Delevoye, J. Trebosc, J. Frye, L. Montagne, J.-P. Amoureux, M. Pruski, SPAM-MQ-HETCOR: an improved method for heteronuclear correlation

spectroscopy between quadrupolar and spin-1/2 nuclei in solid-state NMR, Phys. Chem. Chem. Phys. 8 (2006) 144–150. doi:10.1039/B512246E.
[14] F. Pourpoint, Y. Morin, R.M. Gauvin, J. Trébosc, F. Capet, O. Lafon, J.-P. Amoureux, Advances in Structural Studies on Alkylaluminum Species in the Solid State via Challenging 27Al–13C NMR Spectroscopy and X-ray Diffraction, J. Phys. Chem. C. 117 (2013) 18091–18099. doi:10.1021/jp4055044.
[15] F. Pourpoint, A.S.L. Thankamony, C. Volkringer, T. Loiseau, J. Trébosc, F. Aussenac, D. Carnevale, G. Bodenhausen, H. Vezin, O. Lafon, J.-P. Amoureux, Probing ^{27}Al–^{13}C proximities in metal–organic frameworks using dynamic nuclear polarization enhanced NMR spectroscopy, Chem Commun. 50 (2014) 933–935. doi:10.1039/C3CC47208F.
[16] S. Li, F. Pourpoint, J. Trébosc, L. Zhou, O. Lafon, M. Shen, A. Zheng, Q. Wang, J.-P. Amoureux, F. Deng, Host–Guest Interactions in Dealuminated HY Zeolite Probed by 13C–27Al Solid-State NMR Spectroscopy, J. Phys. Chem. Lett. 5 (2014) 3068–3072. doi:10.1021/jz501389z.
[17] G. Qi, Q. Wang, J. Xu, J. Trébosc, O. Lafon, C. Wang, J.-P. Amoureux, F. Deng, Synergic Effect of Active Sites in Zinc-Modified ZSM-5 Zeolites as Revealed by High-Field Solid-State NMR Spectroscopy, Angew. Chem. Int. Ed. 55 (2016) 15826–15830. doi:10.1002/anie.201608322.
[18] C.A. Fyfe, H. Grondey, K.T. Mueller, K.C. Wong-Moon, T. Markus, Coherence transfer involving quadrupolar nuclei in solids: aluminum-27 .tautm. phosphorus-31 cross-polarization NMR in the molecular sieve VPI-5, J. Am. Chem. Soc. 114 (1992) 5876–5878. doi:10.1021/ja00040a069.
[19] A. Vega, CPMAS of quadrupolar S = 3/2 nuclei, *Solid State NMR*, 1 (1992) 17-32. (b) J.P. Amoureux, M. Pruski, Theoretical and experimental assessment of single- and multiple quantum cross-polarizations in solid state NMR, *Molec. Phys*. 100, 10 (2002) 1595-1613; (c) S.E. Ashbrook, S. Wimperis, Spin-locking of half-integer quadrupolar nuclei in NMR of solids: second-order quadrupolar and resonance offset effects, *J. Chem. Phys*. 131 (2009) 194509.
[20] Z. Gan, 13C/14N heteronuclear multiple-quantum correlation with rotary resonance and REDOR dipolar recoupling, J. Magn. Reson. 184 (2007) 39–43. doi:10.1016/j.jmr.2006.09.016.
[21] J. Trebosc, B. Hu, J.P. Amoureux, Z. Gan, Through-space R3-HETCOR experiments between spin-1/2 and half-integer quadrupolar nuclei in solid-state NMR, J. Magn. Reson. 186 (2007) 220–227. doi:10.1016/j.jmr.2007.02.015.
[22] Y. Ishii, R. Tycko, Sensitivity Enhancement in Solid State 15N NMR by Indirect Detection with High-Speed Magic Angle Spinning, J. Magn. Reson. 142 (2000) 199–204. doi:10.1006/jmre.1999.1976.
[23] B. Hu, J. Trébosc, J.P. Amoureux, Comparison of several hetero-nuclear dipolar recoupling NMR methods to be used in MAS HMQC/HSQC, J. Magn. Reson. 192 (2008) 112–122. doi:10.1016/j.jmr.2008.02.004.
[24] O. Lafon, Q. Wang, B. Hu, F. Vasconcelos, J. Trébosc, S. Cristol, F. Deng, J.-P. Amoureux, Indirect Detection via Spin-1/2 Nuclei in Solid State NMR Spectroscopy: Application to the Observation of Proximities between Protons and Quadrupolar Nuclei, J. Phys. Chem. A. 113 (2009) 12864–12878. doi:10.1021/jp906099k.
[25] X. Lu, O. Lafon, J. Trébosc, G. Tricot, L. Delevoye, F. Méar, L. Montagne, J.P. Amoureux, Observation of proximities between spin-1⁄2 and quadrupolar nuclei: Which heteronuclear dipolar recoupling method is preferable?, J. Chem. Phys. 137 (2012) 144201. doi:10.1063/1.4753987.

[26] C. Martineau, B. Bouchevreau, F. Taulelle, J. Trébosc, O. Lafon, J.P. Amoureux, High-resolution through-space correlations between spin-1/2 and half-integer quadrupolar nuclei using the MQ-D-RINEPT NMR experiment, Phys. Chem. Chem. Phys. 14 (2012) 7112–7119. doi:10.1039/C2CP40344G.
[27] G. Hou, S. Paramasivam, I.-J.L. Byeon, A.M. Gronenborn, T. Polenova, Determination of relative tensor orientations by γ-encoded chemical shift anisotropy/heteronuclear dipolar coupling 3D NMR spectroscopy in biological solids, Phys. Chem. Chem. Phys. 12 (2010) 14873–14883. doi:10.1039/C0CP00795A.
[28] G. Hou, I.-J.L. Byeon, J. Ahn, A.M. Gronenborn, T. Polenova, Recoupling of chemical shift anisotropy by R-symmetry sequences in magic angle spinning NMR spectroscopy, J. Chem. Phys. 137 (2012) 134201. doi:10.1063/1.4754149.
[29] M.H. Levitt, Symmetry-Based Pulse Sequences in Magic-Angle Spinning Solid-State NMR, in: eMagRes, John Wiley & Sons, Ltd, 2007. doi:10.1002/9780470034590. emrstm0551.
[30] G. Pileio, M. Concistrè, N. McLean, A. Gansmüller, R.C.D. Brown, M.H. Levitt, Analytical theory of γ-encoded double-quantum recoupling sequences in solid-state nuclear magnetic resonance, J. Magn. Reson. 186 (2007) 65–74. doi:10.1016/j.jmr.2007.01.009.
[31] M. Edén, Advances in Symmetry-Based Pulse Sequences in Magic-Angle Spinning Solid-State NMR, in: eMagRes, John Wiley & Sons, Ltd, 2007. doi:10.1002/9780470034590. emrstm1326.
[32] M. Carravetta, M. Edén, X. Zhao, A. Brinkmann, M.H. Levitt, Symmetry principles for the design of radiofrequency pulse sequences in the nuclear magnetic resonance of rotating solids, Chem Phys Lett. 321 (2000) 205–215.
[33] A. Brinkmann, M.H. Levitt, Symmetry principles in the nuclear magnetic resonance of spinning solids: Heteronuclear recoupling by generalized Hartmann-Hahn sequences, J Chem Phys. 115 (2001) 357–384.
[34] A. Brinkmann, M. Edén, M.H. Levitt, Synchronous helical pulse sequences in magic-angle spinning nuclear magnetic resonance: double quantum recoupling of multiple-spin systems, J Chem Phys. 112 (2000) 8539–8554.
[35] A. Brinkmann, M. Edén, Second order average Hamiltonian theory of symmetry-based pulse schemes in the nuclear magnetic resonance of rotating solids: Application to triple-quantum dipolar recoupling, J Chem Phys. 120 (2004) 11726–11745.
[36] R. Fu, S.A. Smith, G. Bodenhausen, Recoupling of heteronuclear dipolar interactions in solid-state MAS NMR by simultaneous frequency and amplitude modulation, *Chem. Phys. Lett*. 272 (**1997**) 361-369.
[37] M. Bak, J.T. Rasmussen, N.C. Nielsen, SIMPSON: a general simulation program for solid-state NMR spectroscopy, J Magn Reson. 147 (2000) 296–330.
[38] M. Bak, N.C. Nielsen, REPULSION, a novel approach to efficient powder averaging in solid-state NMR, J Magn Reson. 125 (1997) 132.
[39] B.M. Fung, A.K. Khitrin, K. Ermolaev, An Improved Broadband Decoupling Sequence for Liquid Crystals and Solids, J. Magn. Reson. 142 (2000) 97–101. doi:10.1006/jmre.1999.1896.
[40] M. de la Rochère, A. Kahn, F. d'Yvoire, E. Bretey, Crystal structure and cation transport properties of the ortho - diphosphates Na7(MP2O7)4PO4 (M = Al, Cr, Fe), Mater. Res. Bull. 20 (1985) 27–34. doi:10.1016/0025-5408(85)90023-6.
[41] R. Siegel, T.T. Nakashima, R.E. Wasylishen, Signal enhancement of NMR spectra of half-integer quadrupolar nuclei in solids using hyperbolic secant pulses, Chem. Phys. Lett. 388 (2004) 441–445. doi:10.1016/j.cplett.2004.03.047.

[42] R. Gupta, G. Hou, T. Polenova, A.J. Vega, RF inhomogeneity and how it controls CPMAS, Solid State Nucl. Magn. Reson. 72 (2015) 17–26. doi:10.1016/j.ssnmr.2015.09.005.
[43] K. Kalakewich, R. Iuliucci, K.T. Mueller, H. Eloranta, J.K. Harper, Monitoring the refinement of crystal structures with 15N solid-state NMR shift tensor data, J. Chem. Phys. 143 (2015) 194702. doi:10.1063/1.4935367.
[44] A. Brinkmann, J. Schmedt auf der Günne, M.H. Levitt, Homonuclear Zero-Quantum Recoupling in Fast Magic-Angle Spinning Nuclear Magnetic Resonance, J Magn Reson. 156 (2002) 79–96.
[45] H. Kimura, K. Nakamura, A. Eguchi, H. Sugisawa, K. Deguchi, K. Ebisawa, E. Suzuki, A. Shoji, Structural study of α-amino-acid crystals by $^1\textrmH$ CRAMPS NMR spectroscopy, J Mol Struct. 447 (1998) 247–255.
[46] C. Fernandez, C. Morais, J. Rocha, M. Pruski, Solid State Nucl. Magn. Reson. 21 (**2002**) 61-70.
[47] K.O. Tan, M. Rajeswari, P.K. Madhu, M. Ernst, Asynchronous symmetry-based sequences for homo-nuclear dipolar recoupling in solid-state nuclear magnetic resonance, *J. Chem. Phys*., 142, 6 (**2015**) 065101.
[48] D. Marion, M. Ikura, R. Tschudin, A. Bax, Rapid recording of 2D NMR spectra without phase cycling. Application to the study of hydrogen exchange in proteins, J. Magn. Reson. 1969. 85 (1989) 393–399. doi:10.1016/0022-2364(89)90152-2.

Chapter 4: General conclusion and perspectives

4.1. General conclusion

This thesis has focused on the development and application of novel through-bond and through-space correlation solid-state NMR experiments involving half-integer quadrupolar nuclei. We have notably improved the sensitivity of the correlation experiment and extended the application range of the correlation experiment involving half integer spin quadrupolar nuclei. In main two part, main achievement and new insights are as follow:

(1) ^{77}Se{^{71}Ga} *J*-RINEPT-CPMG, ^{71}Ga{^{77}Se} *J*- and *D*-HMQC-QCPMG and ^{71}Ga split-t_1 z-filter STMAS-QCPMG sequences were developed and applied to investigate the structure of gallium selenide materials. As a result, ^{77}Se-^{71}Ga HETCOR and ^{71}Ga STMAS experiments were acquired within reasonable experimental time using the developed sequences. The analytical expressions for heteronuclear *J* coupling estimation were extended to inorganic materials with 3D bond connectivity. ^{77}Se-^{71}Ga HETCOR experiment indicates that the sample of β-Ga_2Se_3 crystal is composed of Annealed phase and Quenched phase. This Quenched phase only contains Se^{III} sites and ^{71}Ga nuclei located in symmetrical environment but exhibiting a large distribution of isotropic chemical shifts. In the case of $20Ga_2Se_3$-$80GeSe_2$ glass sample, 2D HETCOR ^{77}Se projection spectra was deconvoluted into 6 distinct Se sites bonded to Ga atom. These results have never been reported previously, notably because of the lack of sensitivity of HETCOR experiment. The combination with CPMG acquisition can open the door to the new application for HETCOR and STMAS experiments.

(2) Novel Dipolar-Heteronuclear Universal Quantum Correlation with γ encoded heteronuclear dipolar recoupling on direct channel (*D*-HUQC-DR) was developed in order to increase the sensitivity, compared to conventional *D*-HMQC with R^3. MAS fluctuation cause t_1 noise for 2D experiment in solid and t_1 noise reduces the sensitivity of 2D experiment. *D*-HUQC experiment with γ encoded *R* symmetry-based recoupling reintroducing $m = 1$ spatial component of heteronuclear dipolar couplings has similar robustness to MAS fluctuation than the one using R^3 recoupling. Hence, this method overcomes the t_1 noise problem for the aluminophosphate materials with large CSA. Furthermore, R symmetry recoupling with $m = 1$ spatial component has much better robustness to RF inhomogeneiy than R^3 recoupling which lead to 3 times higher efficiency. This new pulse sequence partially solves the t_1 noise issue and will be useful for the condition of ultra-high field (> 18.8 T), in which CSA could be very large, and unstable MAS frequency (such as very fast MAS and DNP experiment).

4.2. Perspectives

4.2.1. Correlation experiment for Gallium Selenide material

DFT calculation of β-Ga_2Se_3 crystal and Ga_2Se_3-$GeSe_2$ glass

It is revealed that the structure of β-Ga_2Se_3 crystal possesses complicated structure including Quenched phase. It may be possible to reveal the detailed structure by performing DFT calculation using the information of ^{71}Ga and ^{77}Se chemical shifts, ^{71}Ga-^{77}Se *J* coupling constants, ^{71}Ga quadrupolar parameters (C_Q and η_Q) and ^{77}Se CSA. Similarly, DFT calculation will be useful to support the assignment of ^{77}Se signals for 2D HETCOR ^{77}Se projection spectrum in glass sample.

HETCOR experiment with population transfer at higher field

Further sensitivity improvement of ^{71}Ga-^{77}Se HETCOR can be performed at higher magnetic field. The CT spectrum of half-integer quadrupolar nuclei will be narrowed and population transfer pulse could be applied at the beginning of HETCOR sequence. Population transfer pulse was not applied to the present experiment in the thesis because of too broad ^{71}Ga line width at 9.4 T. If the combination population transfer and high field is possible, the sensitivity could be further increased, even if CSA and chemical shift distribution, which broaden the ^{77}Se spectrum, is also increased. The improved resolution and sensitivity at high magnetic field can provide additional details on the nature of molecular patterns in gallium selenide materials.

Application to Ga_2Se_3-$GeSe_2$ glass-ceramics

Ga_2Se_3-$GeSe_2$ glass-ceramics material benefits from higher mechanical strength than the glass sample, while keeping IR transparency. Moreover, the lens made of glass-ceramics can be molded as those made of glass material. For a glass-ceramics sample, narrow peak occurs in ^{71}Ga 1D MAS spectra. This narrow peak is similar to that of β-Ga_2Se_3 crystal. The chemical structure and the mechanism of the nucleation could be clarified by using ^{71}Ga-^{77}Se HETCOR experiment and DFT calculation.

Application to other system

Present proposed *J*-RINEPT-CPMG and *J*/*D*-HMQC-QCPMG sequence could be applied not only to gallium selenide materials but also other difficult system exhibiting broad NMR spectra. Here, CPMG acquisition enhances sensitivity when the observed nuclei possess the property of (i) low natural abundance, (ii) short FID, (iii) long T_2'. Nevertheless, as mentioned in the introduction part, modified CPMG protocol proposed by R. Siegel et al may make the CPMG acquisition more efficient in non-dilute system. Similarly to *J*-RINEPT sequence, *D*-RINEPT sequence could be combined with CPMG acquisition as well as PRESTO-III-QCPMG

sequence. *D*-RINEPT sequence is complementary to *J*-RINEPT for extracting both through space and through bond information in the material. In *D*-RINEPT sequence, appropriate heteronuclear dipolar recoupling sequence could be chosen depending on the application (e.g. $SR4_1^2$ and SFAM instead of R^3).

4.2.2. γ independent *D*-HMQC pulse sequence

Utilization of dipolar truncation effect

As mentioned in the introduction, the recoupling method used in *D*-HMQC was mostly non-γ encoded recoupling except for R^3. Since these method enables long-range correlation, it is effective for observing the correlation between all spins. On the other hand, γ-encoded recoupling has a dipolar truncation effect. Therefore, in principle it is possible to obtain the correlation of only the nearest neighbor nucleus. By employing the two types of recoupling complementarily, it will be useful for editing the correlation spectrum and it will be possible to obtain more detailed material structure.

The correlation experiment at very high field and with DNP

NMR magnet with very high magnetic fields are being developed. They will notably improve the resolution of half-integer quadrupole nuclei. In the Lille, 1.2 GHz NMR spectrometer is planned to be installed in 2020. On the other hand, a high magnetic field increases the CSA. For non-γ-encoded recoupling, larger CSA decreases the robustness to MAS frequency fluctuations, thus generating larger t_1 noise. The γ-encoded recoupling proposed in this thesis should allow the suppression of t_1 noise even under high magnetic field conditions. In the experiment of DNP, usually carried out at 100 K, MAS fluctuation are also significantly larger than for conventional NMR experiments. DNP-enhanced *D*-HUQC spectra can be acquired, for instance by initially transferring the DNP-enhanced 1H polarization to the detected isotope using CP. The use of *D*-HUQC method under DNP conditions will reduce the t_1 noise and thus improve the sensitivity, allowing the observation of small correlation peaks.

HUQC *m* = 2 recoupling

D-HMQC-DR sequence has been used for the indirect detection of quadrupolar nuclei, such as ^{14}N, or spin-1/2 isotope exhibiting wide NMR signal, such as ^{195}Pt, via ^{1}H nuclei. Heteronuclear dipolar recoupling used here must have the property of homonuclear dipolar decoupling, and $SR4_1^2$ recoupling is often chosen. However, again, high t_1 noise occurs since this recoupling is non-γ-encoded. For these systems, it is expected that this t_1 noise could be suppressed by applying R symmetry recoupling with m = 2 component having the property of homonuclear dipolar decoupling.

Curriculum Vitae

Hiroki NAGASHIMA

Date of Birth: 22/08/1984
Notionality: Japanese
CNRS UMR 8181, UCCS; University of Lille 1 Science and Technology, 59652 Villeneuve d'Ascq,France
Phone: +336-4312-5041
Email: hiroki.nagashima@etudiant.univ-lille1.fr
nhiroki0822@gmail.com

Education

PhD: 2014 – 2017, Chemistry, University of Lille 1 Sciences and Technologies
MS: 2007 - 2009, Material Science, The University of Tokyo
BS: 2003 - 2007, Physics, Toho University

Work Experience

Research scientist: 2018 –, IRC3, AIST, Japan
Postdoctoral researcher: 2017 – 2018, University of Lille Sciences and Technologies
Researcher: 2009 – 2014, Central Research Analytical Department, Bridgestone. Co., Japan

Research Topics

2018 -: Research scientist at IRC3, AIST, Japan
Development and application of DNP-NMR and advanced SS-NMR methodology for industrial materials
2017 – 2018: Postdoctoral researcher at University of Lille Sciences and Technologies, Supervisor: Prof Olivier Lafon
2014 - 2017: University of Lille Sciences and Technologies, Supervisor: Prof Olivier Lafon
(i) The development of the 2D HETCOR between spin-1/2 and half-integer quadrupolar nuclei
(ii) Applications of Dynamic Nuclear Polarization for inorganic materials
2009 – 2014: Bridgestone. Co., Japan
Characterization of composite material in the tire using advanced SS-NMR methodology
2007 – 2009: The University of Tokyo, Supervisor: Prof Masashi Takigawa
The study of strongly correlated electron spin system by SS-NMR
2006 – 2007: Toho University, Supervisor: Prof Yutaka Nishio
Specific heat study of 2D organic superconductor.

Publications

1) **Hiroki Nagashima,** Grégory Tricot, Julien Trébosc, Olivier Lafon, Jean-Paul Amoureux, Frédérique Pourpoint " 3D correlation NMR spectrum between three distinct heteronuclei for the characterization of inorganic samples: application on sodium alumino-phosphate materials" *Solid state Nuclear Magnetic Resonance* (2017) **84,** 1664-170 (2017)
2) **Hiroki Nagashima**, Aany S. Lilly Thankamony, François Méar, Lionel Montagne, Julien Trébosc, Frédérique Pourpoint, Olivier Lafon, Jean-Paul Amoureux "Gamma encoded heteronuclear correlation between spin-1/2 and quadrupole nuclei in solids" *Solid state Nuclear Magnetic Resonance*, **84,** 216-226 (2017)
3) **Hiroki Nagashima**, Frédérique Pourpoint, Julien Trébosc, François Méar, Lionel Montagne, Jean-

Paul Amoureux, Laurent Calvez, Olivier Lafon " ^{71}Ga-^{77}Se through-bond and through-space connectivities analyzed by solid-state NMR in chalcogenide glasses "*Journal of Magnetic Resonance*, **282,** 71-82 (2017)

4) **Hiroki Nagashima**, Julien Trébosc, Olivier Lafon, Frédérique Pourpoint, Piotr Paluch, Marek Potrzebowski , Jean-Paul Amoureux, " Imaging the spatial distribution of radiofrequency field, sample and temperature in MAS NMR rotor " *Solid State Nuclear Magnetic Resonance*, ***in press***
5) **Hiroki Nagashima**, Torsten Gutmann, Shantanu Lanke, Aany S. Lilly Thankamony, Frédérique Pourpoint, Hervé Vezin, Gerd Buntkowski, Vivek Polshettiwar, Olivier Lafon "Dynamic Nuclear Polarization enhanced NMR spectroscopy of fibrous silica (KCC-1) nanoparticles" ***in preparation***
6) **Hiroki Nagashima**, François Méar, Julien Trébosc, Frédérique Pourpoint, Hervé Vezin, Lionel Montagne, Olivier Lafon "Optimization of paramagnetic dopants to enhance the sensitivity of solid-state NMR" ***in preparation***
7) **Hiroki Nagashima**, Aany S. Lilly Thankamony, François Méar, Lionel Montagne, Julien Trébosc, Frédérique Pourpoint, Jean-Paul Amoureux, Gwendal Kervern, Olivier Lafon, "Heteronuclear dipolar recoupling using adiabatic inversion pulses**" *in preparation***
8) **Hiroki Nagashima**, Frédérique Pourpoint, Julien Trébosc, François Méar, Lionel Montagne, Olivier Lafon "NMR spectroscopy of glass thin-films enhanced by Dynamic Nuclear Polarization*" in preparation***
9) Zhehong Gan, Ivan Hung, Yusuke Nishiyama, Olivier Lafon, **Hiroki Nagashima**, Julien Trébosc, Jean-Paul Amoureux, Ilya Kuprov "Theory of ^{14}N overtone nuclear magnetic resonance of rotating solids" ***in preparation***
10) **Hiroki Nagashima**, Charlotte Martineau, Grégory Tricot, Julien Trébosc, Frédérique Pourpoint, Jean-Paul Amoureux, Olivier Lafon, "Recent developments in NMR studies of aluminophosphate" ***in preparation***
11) **Hiroki Nagashima**, Shantanu Lanke, Julien Trébosc, Frédérique Pourpoint, Jean-Paul Amoureux, P. K. Madhu, Vivek Polshettiwar, O. Lafon "Dynamic Nuclear Polarization enhanced NMR spectroscopy of hybrid and inorganic materials" ***in preparation***
12) **Hiroki Nagashima**, Frédérique Pourpoint, Julien Trébosc, François Méar, Lionel Montagne, Olivier Lafon, "The review of glass thin film NMR"

Presentations

1) **Hiroki Nagashima**, Julien Trébosc, Frédérique Pourpoint, François Mear, Laurent Calvez, Olivier Lafon, Jean Paul Amoureux, "^{71}Ga-^{77}Se connectivities and proximities in gallium selenide materials probed by solid state NMR" Société Chimique de France (SCF) 2017, Montpellier (France), November 8– 10 2017 *Oral presentation*
2) **Hiroki Nagashima**, Aany S. Lilly Thankamony, Julien Trébosc, Frédérique Pourpoint, Jean-Paul Amoureux, Olivier Lafon, "Correlation between spin-1/2 and quadrupolar nuclei: high robustness to Magic-Angle Spinning fluctuations" Euromar 2017, Warsaw (Poland), July 2– 6 2017 *Oral presentation*
3) **Hiroki Nagashima**, Julien Trébosc, Frédérique Pourpoint, François Mear, Laurent Calvez, Olivier Lafon, Jean Paul Amoureux, "^{71}Ga-^{77}Se connectivities and proximities in gallium selenide materials probed by solid state NMR" Euromar 2017, Warsaw (Poland), July 2– 6 2017 *Poster presentation*

4) Hiroki Nagashima, Frédérique Pourpoint, Julien Trébosc, Jean-Paul Amoureux, Olivier Lafon, Solid-state ionics 21, "Insights into atomic-level structure of materials from Dynamic Nuclear Polarization-enhanced NMR spectroscopy", Padua (Italy), June 2017
5) **Hiroki Nagashima,**" ^{71}Ga-^{77}Se connectivities and proximities in gallium selenide materials probed by solid state NMR", NMR Grand Basin Parisien meeting, Paris (France), July 2017 *Oral presentation*
6) Hiroki Nagashima, Julien Trébosc, Frédérique Pourpoint, François Mear, Laurent Calvez, Olivier Lafon, Philippe Corcos, Jean Paul Amoureux, "^{71}Ga-^{77}Se through-bond and through-space connectivities analyzed by solid-state NMR", 58th ENC, California(USA), March 26-31,2017
7) Hiroki Nagashima, Frédérique Pourpoint, Julien Trébosc, Jean-Paul Amoureux, Olivier Lafon, "Probing structures and interactions in heterogeneous catalysts using solid-state (DNP)-NMR", Symposium Catalysis by Design using NMR, Villeneuve d'Ascq (France), March 2017
8) Hiroki Nagashima, Frédérique Pourpoint, Julien Trébosc, Jean-Paul Amoureux, Olivier Lafon,"Probing proximities between spin-1/2 and quadrupolar isotopes: novel concepts and new insights into the catalysts structure", 8th Annual User Meeting of IR-RMN-THC, Paris (France), October 2016
9) **Hiroki Nagashima**, Aany S. Lilly Thankamony, Julien Trébosc, Frédérique Pourpoint, Jean-Paul Amoureux, Olivier Lafon, "Gamma encoded heteronuclear correlation between spin-1/2 and quadrupole nuclei", NMR Grand Basin Parisien meeting, Renes(France), September2016 *Oral presentation*
10) Hiroki. Nagashima, F. Pourpoint, J. Trébosc, J.-P. Amoureux, O. Lafon,"Ultra-high field NMR: shining light on the dark sites of heterogeneous catalysts and advanced materials" ICMRBS satellite workshops (Kyoto), August 2016
11) Hiroki Nagashima**,** Julien Trebosc, Frederique Pourpoint, Jean-Paul Amoureux, Olivier Lafon "The insight into the Activity of Heterogeneous Catalysits from high-field (DNP)-NMR" Euromar 2016, Aarhus (Denmark), July 3 – 7 2016
12) **Nagashima H**, Takigawa M, Nagao Y,Hiroi Z "Magnetic order and dynamics of Pyrochlore oxide $Cd_2Os_2O_7$ with metal-insulator transition", The Physical Society of Japan Spring meeting, Tokyo, Japan, 2009 *Oral presentation*
13) **Nagashima H**, Takigawa M, Nagao Y, Hiroi Z, "^{17}O-NMR measurement of Pyrochlore oxide $Cd_2Os_2O_7$", The Physical Society of Japan Spring meeting, Osaka, Japan, 2008 *Oral presentation*
14) **Nagashima H**, Takigawa M, Tajima H, Matsuda M, Hanasaki T, Naito T, Inabe T, " ^{15}N-NMR measurement of organic conductor TPP [Fe(Pc) $(CN)_2]_2$ ", The Physical Society of Japan Autumn meeting, Hokkaido, Japan, 2007 *Oral presentation*
15) **Nagashima H**, Nishio Y, Sasaki T, Kajita K, " Specific heat in the deuterium substitution system of κ-$(BEDT\text{-}TTF)_2Cu[N(CN)_2]Br$ ", The Physical Society of Japan Spring meeting, Kagoshima, Japan, 2007 *Oral presentation*

Appendix: Bruker Pulse Program

A.1. *D, J*-HMQC (with indirect recoupling)-QCPMG pulse sequence

This sequence was used on AV-II Bruker console driven by topspin2.1.

```
;hmqcIR-CPMG.jt
; hmqc with indirect dipolar recoupling and CPMG detection
; Reference sequence : hmqcIR.jt
; CPMG works on Avance-II. It need to modify for Avance-III
; version 1.0 (published online XXX)
; ----------------
; DESCRIPTION :
; hmqc experiment using SFAM (simultaneous frequency and
; amplitude modulation) or SR4 to generate heteronuclear multiple
; quantum correlation spectra
; you need to run SFAM AU program to generate correct shape pulse
;
;AUTHOR
; Julien TREBOSC / Hiroki NAGASHIMA
;$COMMENT=HMQC with dipolar recoupling on indirect channel
;$CLASS=Solids
;$DIM=2D
;$TYPE=
;$SUBTYPE=
;$OWNER=Trebosc

;************************ Parameters *****************
;ns : 64*n min, 128*n  max
;d1 : recycle delay
;pl1 : =119 dB, not used
;pl21 : RF power level p3/p4
;pl3 : RF power level p1
;pl23 : SFAM/SR4 power level
;p3 : 90 degree pulse @ pl21
;p4 : 180 degree pulse @ pl21
;p1 : 90 degree pulse @pl3
;p16 : SFAM/SR4 dipolar recoupling time
;cnst3 : shape pulse resolution in ns (300ns)
;cnst30 : SFAM offset amplitude
;cnst31 : =MAS spin rate
;cnst0 : factor for second pulse
;l3 : SFAM mode (l3=1 or 2 for homo dipol decoupl)
;l22 : # of echos to be acquired
;d3 : time to allow pulse ringdown, 10 to 100 us
;d6 : enter duration of FID
;FnMODE : States or States-TPPI
;l0 : set to 0 automatrically
;ZGOPTNS : -DPRESAT -DdecF3 -DdecF2t1 -DdecF2aq -D_DFS -Dopt1D
; -DPRESAT : send presaturation pulses on F1 can be replaced with DS=1 or 2
; -DdecF3 : applyies decoupling during aq on F3
; -DdecF2aq : applyies decoupling during aq on F2 (1H)
; -DdecF2t1 : applyies decoupling during t1 on F2 (1H)
; -D_SR4 : use SR4 recoupling
; -D_SFAM : use SFAM recoupling (default)
; -D_DFS : add DFS enhancement pre-pulse
; -Dopt1D : select only +1 pathway : 1D only, not to be used for 2D

#include <Avancesolids.incl>

;************************ PRESAT *****************
#ifdef PRESAT
#include "presat.incl"
#else
#define PRESAT1(f1)
#define presatPH
```

```
#endif

;*********************** Decoupling *****************

#ifdef decF3
#define dec
#define decF3on cpds3:f3
#define decF3off do:f3
#else
#define decF3on
#define decF3off
#endif

#ifdef decF2t1
#define decF2
#define decF2t1on cpds2:f2
#else
#define decF2t1on
#endif

#ifdef decF2aq
#define decF2
#define decF2aqon cpds2:f2
#else
#define decF2aqon
#endif

#ifdef decF2
#define dec
#define tppm
#define decF2off do:f2
#else
#define decF2off
#endif

#ifdef dec
#include "decouple.incl"
#endif

;*********************** DFS *****************
#ifdef _DFS
;p2 DFS/HS pulse
;cnst1 : (kHz) Start DFS sweep freq.
;cnst2 : (kHz) End DFS sweep freq.
;cnst3 : (ns) time resolution of shape sp1
;spoffs1 HS offset (spoffs1 < 1/cnst3)
;spnam1 DFS/HS shape : use HS.jt of DFS.jt to regenerate
;sp1 DFS/HS shape power
define delay showInASED
"showInASED=cnst1+cnst2+cnst3"
#define DFSpulse (5u p2:sp1 ph0 5u):f1
#else
#define DFSpulse
#endif

;*********************** CPMG delays calculation *****************
define delay del3
"del3=d3-2u"
define loopcounter tmpD3
define delay d3best
define delay cycle
define loopcounter tmpTD
define loopcounter TDtot
define delay rest
define delay Spik_int
define delay showInASED2
define delay ratioOK
```

```
; Calculate best d3 for rotor synchronisation
"tmpD3=(d6+p4/2)*cnst31"
"d3best=(1s*(tmpD3+1)/cnst31)-d6-(p4/2.0)"

;calculate minimum TD to set
"tmpTD=0.5*(((d6*2+d3*2+p4)*l22)+d6+d3)/dw"
"TDtot=(tmpTD+1)*2"

"rest=abs(aq-(TDtot*dw))"
"Spik_int=1s/(d6*2+d3*2+p4)"
"cycle=d6*2+d3*2+p4"
"ratioOK=cycle/(2*dw)"
; to make TDtot, etc. show up in ased
"showInASED2=TDtot+d3best+Spik_int+cycle+ratioOK"

;**************** calculation of t1 delays ******************
define delay Dmin
define loopcounter lmin
define delay delA
define delay delAa
define delay delAb
define delay delB
"Dmin=(2*p1+d0+2u)+0.4u"
"lmin=(Dmin*cnst31)+1"
"delA=(((1s*lmin)/cnst31)-2u-p4)/2.0"
"delB=(((1s*lmin)/cnst31)-2u-d0-p1*2.0)/2.0"
"delAa=1s/cnst31+0.5s*(lmin%2)/cnst31-p3/2"
"delAb=1s/cnst31+0.5s*(lmin%2)/cnst31"

define loopcounter LCounter
define delay dummy

#ifndef _SR4
#define _SFAM
#endif

#ifdef _SFAM
"p6=1s/cnst31"
"LCounter=(p16*cnst31/1e6+0.5)"
"p17=LCounter*p6"
"dummy=cnst31+cnst30+cnst3+l3+p17"
#endif

#ifdef _SR4
"p6=(0.25s/cnst31)"
"LCounter=(p16*cnst31/1e6+0.5)"
"p17=LCounter*p6*4"
"dummy=p17"
#endif

; counter for cycling SR4
"l0=0"

;topspin 2.1 only
"in0=inf1"

;duty cycle
define delay pulsef1
define delay scandelay
"pulsef1=p2*2+p3+p4*(l22+2)"
"scandelay=d1+p16+aq+100m"
"cnst60=pulsef1/scandelay"

;*************** experiment block ********************
1 ze
2 100m decF2off decF3off
```

```
"Dmin=(2*p1+d0+2u)+0.4u"
"lmin=(Dmin*cnst31)+1"
"delA=(((1s*lmin)/cnst31)-2u-p4)/2.0"
"delAa=1s/cnst31+0.5s*(lmin%2)/cnst31-p3/2"
"delAb=1s/cnst31+0.5s*(lmin%2)/cnst31"
"delB=(((1s*lmin)/cnst31)-2u-d0-p1*2.0)/2.0"

;SR4 manual cycling
10u iu0

#ifdef _SR4
#ifndef opt1D
"cnst47=180*(((l0-1)/4)%2)"
"cnst46=180*(((l0-1)/16)%2)"
#else
"cnst47=180*(((l0-1)/8)%2)"
"cnst46=180*(((l0-1)/32)%2)"
#endif
10u ip16+cnst46
10u ip17+cnst47
#endif
  PRESAT1(f1)

  d1
  STARTADC
  RESETPHASE
  1u REC_BLK
  1u SGU3_pulse

  DFSpulse
  5u pl21:f1 pl23:f3
  (p3 ph1):f1
  delAa decF2t1on

;----------- D,J-HMQC -----------------
#ifdef _SFAM
SFAMl1, (p6:spf5 ph4):f3
lo to SFAMl1 times LCounter
#endif
#ifdef _SR4
sr4_1, (p6 ph16^):f3
       (p6 ph16^):f3
       (p6 ph16^):f3
       (p6 ph16^):f3
  lo to sr4_1 times LCounter
#endif

  1u
  (delB pl3 p1 ph11 d0 p1 ph12 delB):f3 (delA p4 ph2  delA ):f1
  1u pl23:f3

#ifdef _SFAM
SFAMl2, (p6:spf5 ph5):f3
lo to SFAMl2 times LCounter
#endif
#ifdef _SR4
sr4_2, (p6 ph17^):f3
       (p6 ph17^):f3
       (p6 ph17^):f3
       (p6 ph17^):f3
  lo to sr4_2 times LCounter
#endif

  delAb decF2off
;----------- CPMG acq -----------------
  d6 decF2aqon decF3on
  2u
  del3
```

```
  (p4 ph7):f1
  del3
  1u DWL_CLK_ON
  1u SGU3_observe
  d6 REC_UNBLK
3 d6 REC_UNBLK
  1u REC_BLK
  1u
  del3 SGU3_pulse
  (p4 pl21 ph8):f1
  2u
  del3 SGU3_observe
  d6 REC_UNBLK
  lo to 3 times l22
  d6
  del3 REC_BLK

  rest decF3off decF2off
  1u DWL_CLK_OFF
  rcyc=2
 ; go=2 ph31 decF2aqon decF3on

  1u decF3off decF2off

  100m mc #0 to 2 F1PH(ip11,id0)
exit


#ifndef opt1D
;phase cycling for 2D
ph0=0
;ph1={0 0 2 2}*2
ph1=0
;ph2=1
ph2={0 0}^2^1^3
ph4={0}*16 {2}*16
ph5={0}*8 {2}*8
ph7=1
ph8=1
;ph7={1}*16 {3}*16
;ph8={1}*32 {3}*32
ph11=0
ph12=0 2
;ph12=0 0
ph30=0
;ph31={{{{0 2 2 0}*2}*2}^2}^2 ; over 64 phases
ph31={0 2}^0^2^2; over 64 phases ph31=ph12+2*ph2+0*ph4+0*ph5
;ph31={0 0 2 2}*2 {3 1 1 3}*2
ph16=(360) 90 270 90 270 270 90 270 90 210 30 210 30 30 210 30 210 330 150 330 150
150 330 150 330
ph17=(360) 90 270 90 270 270 90 270 90 210 30 210 30 30 210 30 210 330 150 330 150
150 330 150 330
#else
; phase cycling for 1D optimization
ph0=0
ph1={0 0 0 0 2 2 2 2}*2
ph2=1
ph4={0}*16 {2}*16
ph5={0}*8 {2}*8
ph7={1}*32 {3}*32
ph8={1}*64 {3}*64
ph11=0
ph12=0 2 1 3
ph30=0
ph31={{{{0 2 1 3 2 0 3 1}*2}*2}^2}^2
ph16=(360) 90 270 90 270 270 90 270 90 210 30 210 30 30 210 30 210 330 150 330 150
150 330 150 330
```

```
ph17=(360) 90 270 90 270 270 90 270 90 210 30 210 30 30 210 30 210 330 150 330 150
150 330 150 330
#endif

; set phases for presat : ph19 and ph20
presatPH
```

A.2. *J*-RINEPT-CPMG pulse sequence

This sequence was used on AV-II Bruker console driven by topspin2.1.

```
;ineptrd_cpmg.jt
; J-RINEPT with cpmg detection
; CPMG works on Avance-II. It need to modify for Avance-III
; with decoupling during acquisition
; AUTHOR
; Julien TREBOSC / Hiroki NAGASHIMA

;********************** Parameters *****************
;pl1 : power level for p1,p2
;pl21 :  power level for p3,p4
;pl22 :  power level for p5 (CPMG)
;pl12: f2 channel - power level for CPD/BB decoupling
;pl13: f2 channel - power level for CPD/BB decoupling
;p1 : 90 degree @ pl1
;p2 : 180 degree @ pl1
;p3 : 90 degree @ pl21
;p4 : 180 degree @ pl22 for CPMG
;p5 : 180 degree @ pl21
;d1 : relaxation delay; 1-5 * T1
;d4 : J-inept mixing delay/2
;d44 : J-inept mixing delay
;     1/(6J(XH))  XH, XH2, XH3 positive
;     1/(4J(XH))  XH only
;     1/(3J(XH))  XH, XH3 positive, XH2 negative
;d5 : J-inept refocusing delay/2
;d55: J-inept refocusing delay
;     1/(4J(XH))
;d6 FID decay time for CPMG
;d3 dead time for CPMG
;l22 number of CPMG echoes
;cnst31 : spinning speed (Hz)
;ZGOPTNS : -DPRESATf3 -DPRESATf1 -DdecF2aq -DdecF2mix -DdecF2t1 -D_DFS -DnoDelSync
;NS: 32 * n, total number of scans: NS * TD0
;DS: 16
;cpdprg1: decoupling during mix
;cpdprg2: decoupling during t1/AQ
;cpdprg3: decoupling during AQ
;pcpd2: cpd pulse on channel f2


;duty cycle
define delay pulsef1
define delay pulsef3
define delay scandelay
"pulsef1=p2*2+p1+p4*(l22+1)"
"pulsef3=(p3+p5)*2"
"scandelay=d1+d4+d5+aq+3m+30m"
"cnst63=pulsef1/scandelay"

#include <Avancesolids.incl>

;********************** PRESAT *****************
#include "presat.incl"
#ifndef PRESATf3
#undef PRESAT2(f3)
```

```
#define PRESAT2(f3)
#endif

#ifndef PRESATf1
#undef PRESAT1(f1)
#define PRESAT1(f1)
#endif

;********************** Decoupling *****************
#include "decouple.incl"
#ifdef decF3aq
#define decF3on cpds3:f3
#define decF3off do:f3
#else
#define decF3on
#define decF3off
#endif

#ifdef decF2all
#define decF2mix
#define decF2t1
#define decF2AQ
#endif

#ifdef decF2mix
#define decF2
#define decF2mixon cpds1:f2
#else
#define decF2mixon
#endif

#ifdef decF2t1
#define decF2
#define decF2t1on cpds2:f2
#else
#define decF2t1on
#endif

#ifdef decF2aq
#define decF2
#define decF2aqon cpds2:f2
#else
#define decF2aqon
#endif

#ifdef decF2
#define decF2off do:f2
#else
#define decF2off
#endif

;**************** DFS of HS *****************
#ifdef _DFS
;p10 DFS/HS pulse
;spname0 DFS/HS shape pulse
;sp0 DFS/HS shape power
#define DFSpulse (5u p10:sp0 ph10 5u):f3
#else
#define DFSpulse
#endif

;********************** CPMG delays calculation *****************

define delay del3
"del3=d3-2u"
define loopcounter tmpD3
define delay d3best
define delay cycle
```

```
define loopcounter tmpTD
define loopcounter TDtot
define delay rest
define delay Spik_int
define delay showInASED2
define delay ratioOK
define delay t1delay
; Calculate best d3 for rotor synchronisation
"tmpD3=(d6+p4/2)*cnst31"
"d3best=(1s*(tmpD3+1)/cnst31)-d6-(p4/2.0)"

;calculate minimum TD to set
"tmpTD=0.5*(((d6*2+d3*2+p4)*l22)+d6+d3)/dw"
"TDtot=(tmpTD+1)*2"

"rest=abs(aq-(TDtot*dw))"
"Spik_int=1s/(d6*2+d3*2+p4)"
"cycle=d6*2+d3*2+p4"
"ratioOK=cycle/(2*dw)"
; to make TDtot, etc. show up in ased
"showInASED2=TDtot+d3best+Spik_int+cycle+ratioOK+cnst63"

;*********************** Mixing time calculation *****************
"p5=p3*2"

"d0=0"
#ifdef _synct1
"t1delay=d0+(1s/cnst31)-p3/2"
#else
"t1delay=d0"
#endif


#ifndef noDelSync
"l4=d4*cnst31"
"d14=(1s*l4/cnst31)-p3/2.0-larger(p2,p5)/2.0-1u"
"d24=(1s*l4/cnst31)-larger(p3,p1)/2.0-larger(p2,p5)/2.0"
#else
"d14=d4"
"d24=d4"
#endif
"d44=2.0s*l4/cnst31"

#ifndef noDelSync
"l5=d5*cnst31"
"d15=(1s*l5/cnst31)-larger(p3,p1)/2.0-larger(p2,p5)/2.0"
"d25=(1s*l5/cnst31)-larger(p2,p5)/2.0-1u"
"d55=2.0s*l5/cnst31"
#else
"d15=d5"
"d25=d5"
#endif

"in0=inf1"

;*************** experiment block ********************
1 ze
2 30m decF3off decF2off
#ifdef _synct1
"t1delay=d0+(1s/cnst31)-p3/2"
#else
"t1delay=d0"
#endif
  PRESAT2(f3)
  d1
  STARTADC
  RESETPHASE
  1u REC_BLK
```

```
  1u SGU1_pulse

  PRESAT1(f1)
  DFSpulse

; ----------- INEPT part -------------
  10u pl21:f3 pl1:f1
  0.1u decF2t1on
  (p3 ph1):f3
  t1delay
  1u decF2off
  d14 decF2mixon
  (center (p5 ph2):f3 (p2 ph4):f1 )
  d24
  (center (p3 ph3):f3 (p1 ph5):f1 )
  d15
  (center (p5 ph2):f3 (p2 ph6):f1 )
  d25
  1u decF2off

; ----------- CPMG acq ---------------
  d6 decF2aqon
  2u
  del3
  (p4 pl22 ph7):f1
  del3
  1u DWL_CLK_ON
  1u SGU1_observe
  d6 REC_UNBLK
3 d6 REC_UNBLK
  1u REC_BLK
  1u
  del3 SGU1_pulse
  (p4 pl22 ph7):f1
  2u
  del3 SGU1_observe
  d6 REC_UNBLK
  lo to 3 times l22
  d6
  del3 REC_BLK
  d6 decF2off
  rest decF2off

  1u DWL_CLK_OFF
  rcyc=2
  30m mc #0 to 2 F1PH(ip1,id0)
exit


;Phase cycling
ph1 = 0 2
ph2=0
ph3=1
ph4={{0}*2}^2
ph5={{0}*4}^2
ph6={{0}*8}^2^1^3
ph7=0
ph31= {{{0 2}^0}^2}^0^2^2
ph30=0
ph10=0

; set phases for presat : ph19 and ph20
presatPH
```

A.3. Split-t*1* STMAS with z filter and QCPMG pulse sequence

This sequence was used on AV-III Bruker console

```
;stmas_split_t1_Zcpmg.jt
; pulse sequence for (satellite transition) STMAS spectroscopy
; on 3/2 nuclei only
; with coherence transfer pathway 0 -> +1/-1 -> +2/-2 -> 0 -> -1/+1
; uses split t1 technique and z-filter
;then a cpmg train is added
; see J. Trebosc, J.-P. Amoureux, and Zhehong Gan, SSNMR 31 (2007) 1-9
; see  JP Amoureux et al JMR 175,285 (2005)
; written by julien trebosc
; CHANGES :

;*************** parameters ********************
;ns : 16 * n
;p1 : excitation pulse
;p2 : mixing pulse
;p3 : selective  90 degree pulse
;p4 : selective 180 degree pulse
;p7 : set delay such that delB>0.3u and delA>0
;pl1 : =119 dB, not used
;pl11 : power for hard pules
;pl21 : power for selective pulse
;l1 : first d0 span l1 Tr
;l7 : run time test counter
;d1 : recycle delay
;d4 : z-filter delay, typ. 20 us
;d23 : offset for d10/d11 calculation not being negative
;d6 : cpmg half echo delay
;d3 : for dead time
;p60:  storage of cpmg cycle time
;cnst31 : spinning frequency
;in0 : =1/spinning frequency for rotor synchronisation,
;      or half of it for half rotor synchronisation
;FnMode : States or States-TPPI

;$COMMENT=stmas for 3/2 spins with t1 split and cpmg acquisition
;$CLASS=Solids
;$DIM=2D
;$TYPE=half integer quadrupoles
;$SUBTYPE=STMAS
;$OWNER=Trebosc

#include <Avancesolids.inc>

;*************** PRESAT ********************
#ifdef PRESAT
#include "presat.incl"
#else
#define PRESAT1(f1)
#define presatPH
#endif

;*************** Decoupling ********************
#ifdef decF2
#define decF2on cpds2:f2
#define decF2off do:f2
#include "decouple.incl"
#else
#define decF2on
#define decF2off
#endif

;*************** QCPMG delay ********************
"p4=2*p3"
define delay del1
```

```
define delay del3
"del3=d3-2u"
"del1=del3+2u-((p3)/2)"

define loopcounter tmpD3
define delay d3best
;d3best set d3 to this value for rotr synchronized echoes
define loopcounter tmpTD
define loopcounter TDtot
;TDtot set TD to this value + dig filter to record all echoes
define delay rest
define delay Spik_int
define delay showInASED
define delay cycle
define delay PTSperCycle

; Calculate best d3 for rotor synchronisation
"tmpD3=(d6+p4/2)*cnst31"
"d3best=(1s*(tmpD3+1)/cnst31)-d6-(p4/2.0)"
;"d3=d3best"
;calculate minimum TD to set
"tmpTD=0.5*(((d6*2+d3*2+p4)*l22)+2*d6+2*d3+p4+4u)/dw"
"TDtot=(tmpTD+1)*2"
"cycle=(d6*2+d3*2+p4)"
"p60=cycle"
"PTSperCycle=cycle/(2*dw)"
"rest=aq-(TDtot*dw)"
"Spik_int=1s/(d6*2+d3*2+p4)"
; to make TDtot, etc. show up in ased
"showInASED=TDtot+d3best+Spik_int+p60+PTSperCycle"

;*************** Split-t1 STMAS delay ********************
#ifdef Sync
#define SyncP1   0.3u trigpe4 \n\
                 delA
#define SyncP2     if "d11-halfTr <= 0" goto 72419 \n\
                   0.3u trigpe4
#else
#define SyncP1
#define SyncP2
#endif

define delay halfTr
define delay delA
define delay delB
"halfTr=0.5s/cnst31"
"delB=p7"
"delA=delB+(p2-p1)/2.0"

"d0=1s*(l1*1/cnst31)"
"d10=d0/9.0 -p1/2 -p4/2 +d23"
"d11=8*d0/9.0 - p2/2 - p4/2 -d23 -delB"

"in0=inf1"
"in11=8.0*in0/9.0"
"in10=in0/9.0"

dwellmode auto

;*************** Experimental block *******************
1 ze
"showInASED=1us"
2 100m
"d10=d0/9.0 -p1/2 -p4/2 +d23"
"d11=8*d0/9.0 - p2/2 - p4/2 -d23 -delB"

#ifdef Sync
if "d11-halfTr <= 0" goto skipSync
```

```
;/* redefine d11 for allowing rotor syncing when d11 is longer than half rotor
period. Else syncing is skipped */
"d11=8*d0/9.0 - p2/2 - p4/2 -d23 -delB -halfTr"
skipSync, 1u
#endif

;presaturation only if -DPRESAT in ZGOPTNS
 PRESAT1(f1)
  d1
  (1u pl11 ph1):f1

  STARTADC
  RESETPHASE

  SyncP1

  (p1 ph1):f1         ; first pulse

  d10 decF2on         ; ST1Q evol

  (p4 pl21 ph2):f1    ; DQ filter

  d11                 ; ST2Q evol
  SyncP2
72419 (delB pl11 ph3):f1

  (p2 pl11 ph3):f1   ; reconversion pulse
  50u  ; Z filter delay
  (p3 pl21 ph4):f1   ; SPAM pulse
  d6                 ; +1/-1 evolution for echo creation
  del1
  (p4 pl21 ph5):f1
  del3 START_NEXT_SCAN
  1u
  1u
  d6 RG_ON
3 d6 RG_ON
  2u
  del3 RG_OFF
  (p4 pl21 ph6):f1
  del3
  2u
  d6 RG_ON
  lo to 3 times l22
  d6
  del3 RG_OFF
  rest decF2off
  1u
  rcyc=2

  100m mc #0 to 2 F1PH(ip1,id0)
exit

ph30=0
ph1= 0 2
ph2= {{0}*2}^2
ph3= {{0}*4}^1^2^3
ph4={{0}*16}^2
ph5= 1
ph6= 1
ph31={{{0 2}^2}^2^0^2}^2 ; cycling of 32
;ph31=-ph1-ph2+2*ph3+ph4 for +1 +2 +1 -1 pathway
; phase of presat
presatPH
```

A.4. D-HUQC (with RN_n^ν recoupling) pulse sequence

```
;huqcDR-m1.jt
;for topspin 1 and 2
;for topspin 3 and more check for trunc function in lmin calculation

; huqc with direct dipolar recoupling
; version 1.0 (published online XXX)
; ----------------
; DESCRIPTION :
; huqc experiment using m = 1 gamma-encoded pulse sequences
;AUTHOR
; Olivier Lafon, Julien Trebosc, Hiroki Nagashima
;MODIFICATIONS :
;$COMMENT=HMQC with dipolar recoupling on direct channel
;$CLASS=Solids
;$DIM=2D
;$TYPE=
;$SUBTYPE=
;$OWNER=Trebosc

; ------------
;PARAMETERS:
;ns... see below in phase cycling section
;d1 : recycle delay
;d4 : z-filter delay
;pl1 : RF power level p4/p5
;pl3 : RF power level p7
;pl23 : recoupling power level
;p4 : 90 degree pulse @ pl1
;p5 : 180 degree pulse @ pl1
;p6 : 180 degree pulse  @ pl23
;p7 : 90 degree pulse @ pl3
;p16 : dipolar recoupling time [in us]
;cnst31 : =MAS spin rate
;FnMODE : States or States-TPPI
;
;ZGOPTNS : PRESATf1 PRESATf3 decF3 decF2t1 decF2aq
; PRESAT : send presaturation pulses on F1 can be replaced with DS=1 or 2
; decF3 : applyies decoupling during aq on F3
; decF2aq : applyies decoupling during aq on F2 (1H)
; decF2t1 : applyies decoupling during t1 on F2 (1H)

;*********************** PRESAT *****************
#include "presat.incl"
#ifndef PRESAT
#undef PRESAT1(f2)
#define PRESAT1(f2)
#endif

#ifndef PRESATf1
#undef PRESAT2(f1)
#define PRESAT2(f1)
#endif

;********************** Decoupling *****************
#ifdef decF3
#define dec
#define decF3on cpds3:f3
#define decF3off do:f3
#else
#define decF3on
#define decF3off
#endif

#ifdef decF2t1
#define decF2
#define decF2t1on cpds2:f2
```

```
#else
#define decF2t1on
#endif

#ifdef decF2aq
#define decF2
#define decF2aqon cpds3:f2
#else
#define decF2aqon
#endif

#ifdef decF2
#define dec
#define tppm
#define decF2off do:f2
#else
#define decF2off
#endif

#ifdef dec
#include "decouple.incl"
#endif


;**************** calculation of R symmetry ******************

define delay dummy

#define ZGOPNTS_ERROR

#ifndef _R1425
#ifndef _R1635
#ifndef _R1845
#ifndef _R1023
#ifndef _R3
#undef ZGOPTNS_ERROR
#define ZGOPTNS_ERROR you must use ZGOPTNS -D_R1425 or -D_R1635 or -D_R1845 or -
D_R1023 or -D_R3
#endif
#endif
#endif
#endif
#endif
ZGOPNTS_ERROR

#ifdef _R1023
;this is R1023 symmetry
"p6=(2.0/10)*1s/cnst31"
"l23=trunc(p16/((2.0e6/cnst31)/5)+0.5)"
#define RNphase1 23400
#define RNphase2 12600
#define RNphase3 5400
#define RNphase4 30600
#endif

#ifdef _R1425
;this is R1425 symmetry
"p6=(2.0/14)*1s/cnst31"
"l23=trunc(p16/((2.0e6/cnst31)/7)+0.5)"
#define RNphase1 24429
#define RNphase2 11571
#define RNphase3 6429
#define RNphase4 29571
#endif

#ifdef _R1635
;this is R1635 symmetry
"p6=(3.0/16)*1s/cnst31"
```

```
"l23=trunc(p16/((3.0e6/cnst31)/8)+0.5)"
#define RNphase1 23625
#define RNphase2 12375
#define RNphase3 5625
#define RNphase4 30375
#endif

#ifdef _R1845
;this is R1845 symmetry
"p6=(4.0/18)*1s/cnst31"
"l23=trunc(p16/((4.0e6/cnst31)/9)+0.5)"
#define RNphase1 23000
#define RNphase2 13000
#define RNphase3 5000
#define RNphase4 31000
#endif

#ifdef _R3
;this is R3 symmetry
"p6=(1.0/4.0)*1s/cnst31"
"l23=trunc(p16/((1e6/cnst31)/2)+0.5)"
#define RNphase1 18000
#define RNphase2 18000
#define RNphase3 0
#define RNphase4 0
#endif

;**************** calculation of delay ******************
"p5=2*p4"
"p17=(l23)*p6*2"
"dummy=p17"
define delay Dmin
define loopcounter lmin

#ifdef d0sync
"d0=1.0s/cnst31-p7"
#endif

"Dmin=(2.0*p7+d0+0.1u)/2.0"
"lmin=trunc(Dmin*cnst31)+1"
"d62=((1s/cnst31)*lmin-p7-d0/2.0)"
"d63=((1s/cnst31)*lmin-p4-p5/2.0)"

;topspin 2.1 and more only
"in0=inf1"

"dummy=p17+l23"

;*************** experiment block ********************

1 ze

#ifdef optMAS
; just for VCLIST to appear in ASED and saved with status acq params
12435 1u
lo to 12435  times c
#endif

2 100m decF2off decF3off

"Dmin=(2.0*p7+d0+0.1u)/2.0"
"lmin=trunc(Dmin*cnst31)+1"
"d62=((1s/cnst31)*lmin-p7-d0/2.0)"
"d63=((1s/cnst31)*lmin-p4-p5/2.0)"

PRESAT2(f1)
d1
```

```
  10u pl23:f1 pl3:f3

  0.5u fq=cnst29:f1
  0.5u decF2t1on
RN_1, (p6 pl23 ph21):f1
        (p6 pl23 ph22):f1
  lo to RN_1 times l23

  (d62 p7 pl3 ph6 d0 p7 pl3 ph7 d62):f3 (p4 pl1 ph14 d63 p5 pl1 ph4 d63 p4 pl1
ph15):f1

RN_2, (p6 pl23 ph23):f1
        (p6 pl23 ph24):f1
  lo to RN_2 times l23
(p4 pl1 ph8):f1

   0.5u decF2off

  go=2 ph31  decF3on decF2aqon
  6.35u decF3off decF2off
  100m mc #0 to 2 F1PH(ip6, id0)
exit


#ifdef opt1D
;phase cycling for 1D
;ns : 8 * n
ph4={{1}*4}^2
ph6=0 2 1 3; use to select p= -1 between the two p7 pulses
ph7=0
ph8=1
ph14=3
ph15=3
ph21=(36000) RNphase1
ph22=(36000) RNphase2
ph23=(36000) RNphase3
ph24=(36000) RNphase4
ph31=0 2 1 3
#else
;phase cycling for 2D
;ns : 4 * n
ph4={{1}*2}^2
ph6=0 2 ; use to select p= 1 or -1 between the two p7 pulses
ph7=0
ph8=1
ph14=3
ph15=3
ph21=(36000) RNphase1
ph22=(36000) RNphase2
ph23=(36000) RNphase3
ph24=(36000) RNphase4
ph31={0 2}
#endif

ph0=0
; set phases for presat : ph19 and ph20
presatPH
```

A.5. D-HUQC (with R^3 recoupling) pulse sequence

```
;huqcDR-R3.jt
; version 1.0 (published online XXX)
; ----------------
; DESCRIPTION :
; huqc experiment using R3
;
```

```
;AUTHOR
; Julien TREBOSC, Olivier Lafon, Hiroki Nagashima
; MODIFICATIONS :
;$COMMENT=HUQC with R3
;$CLASS=Solids
;$DIM=2D
;$TYPE=
;$SUBTYPE=
;$OWNER=Trebosc

; ------------
;PARAMETERS:
;ns : 4 * n
;d1 : recycle delay
;pl1 : RF power level p1/p2
;pl3 : RF power level p3
;pl23 : SFAM power level
;p1 90 degree pulse @ pl1
;p2 180 degree pulse @ pl1
;p3 90 degree pulse @pl3
;p16 : R3 dipolar recoupling time
;cnst31 : =MAS spin rate
;cnst0 : factor for second pulse
;FnMODE : States or States-TPPI
;ZGOPTNS : PRESATf1 PRESATf3 decF3 decF2t1 decF2aq
; PRESAT : send presaturation pulses on F1 can be replaced with DS=1 or 2
; decF3 : applyies decoupling during aq on F3
; decF2aq : applyies decoupling during aq on F2 (1H)
; decF2t1 : applyies decoupling during t1 on F2 (1H)

;*********************** PRESAT *****************
#include "presat.incl"
#ifndef PRESAT
#undef PRESAT1(f2)
#define PRESAT1(f2)
#endif

#ifndef PRESATf1
#undef PRESAT2(f1)
#define PRESAT2(f1)
#endif

;********************** DECOUPLING *****************
#ifdef decF3
#define dec
#define decF3on cpds3:f3
#define decF3off do:f3
#else
#define decF3on
#define decF3off
#endif

#ifdef decF2t1
#define decF2
#define decF2t1on cpds2:f2
#else
#define decF2t1on
#endif

#ifdef decF2aq
#define decF2
#define decF2aqon cpds2:f2
#else
#define decF2aqon
#endif

#ifdef decF2
#define dec
```

```
#define decF2off do:f2
#else
#define decF2off
#endif

#ifdef dec
#include "decouple.incl"
#endif

;**************** calculation of delays ******************
#ifdef d0sync
"d0=1s*l1/cnst31-p3"
#endif

define delay Dmin
define loopcounter lmin
define delay delA
define delay delB
"Dmin=(2*p3+d0+2u)"
"lmin=(Dmin*cnst31/2.0)+1"
"delA=((1s*lmin)/cnst31)-1u - p2/2.0"
"delB=(((2s*lmin)/cnst31)-2u-d0-p3*2.0)/2.0"

define delay RF
define loopcounter LCounter
define delay dummy

"cnst0=2.0"
"p2=p1*cnst0"

;**************** calculation of R3 ******************
#ifdef _R3
"p6=1s/cnst31"
"l11=p16/(p6)"
"p17=p6*l11"
"RF=l3*500000/p6"
"dummy=RF+p17"
#endif

"in0=inf1"

;**************** experiment block ******************

1 ze

#ifdef optMAS
; just for VCLIST to appear in ASED and saved with status acq params
12435 1u
lo to 12435  times c
#endif

2 100m decF2off decF3off

"Dmin=(2*p3+d0+2u)"
"lmin=(Dmin*cnst31/2.0)+1"
"delA=((1s*lmin)/cnst31)-1u - p2/2.0"
"delB=(((2s*lmin)/cnst31)-2u-d0-p3*2.0)/2.0"

  PRESAT2(f1)

  d1
  1u rpp3 rpp6
  10u pl1:f1 pl3:f3
  (p1 ph1):f1
  0.5u fq=cnst29:f1
  1u pl23:f1 decF2t1on

#ifdef _R3
```

```
R3_1, (p6 ph4):f1
  lo to R3_1 times l11
#endif

  1u
  (delB pl3 p3 ph11 d0 p3 ph12):f3 (delA pl1 p2 ph2  delA ):f1
  1u pl23:f1

#ifdef _R3
R3_2, (p6 ph5):f1
  lo to R3_2 times l11
#endif

  1u decF2off

  go=2 ph31 decF2aqon decF3on
  1u decF3off decF2off
  100m mc #0 to 2 F1PH(ip11,id0)
exit

;phase cycling
ph0=0
ph1=3
ph4=2
ph5=0
ph12=0
#ifdef opt1D
ph2={{1}*4}^2
ph11=0 2 1 3
ph31={0 2 1 3}
#else
ph2={{1}*2}^2
ph11=0 2
ph31=0 2
#endif
ph30=0
ph3=0
ph6=0
; set phases for presat : ph19 and ph20
presatPH
```

A.6. Including file (preset.incl) and AU program (for DFS and SFAM)

Include file presat.incl

```
;$COMMENT=presaturation loops
;$CLASS=Solids INCL
;$DIM=
;$TYPE=presaturation
;$SUBTYPE=
;$OWNER=Trebosc
;Presat include file ************************************
;d20 : delai between Presat pulses (p20)
;pl20 : power of Presat pulses (p20)
;l20 : number of Presat pulses (p20)
;p20 : Presat pulses
;ph20 : phase of Presat pulses (p20)
; second presat parameters
;d19 : delai between Presat2 pulses (p21)
;pl19 : power of Presat2 pulses (p19)
;l19 : number of Presat2 pulses (p19)
;p19 : Presat2 pulses
;ph19 : phase of Presat2 pulses (p19)
#define PRESAT1(ch) 983547 d20 pl20:ch \n\
(p20 ph20^):ch \n\
lo to 983547 times l20
```

```
#define PRESAT2(ch) 9835472 d19 pl19:ch \n\
(p19 ph19^):ch \n\
lo to 9835472 times l19
#define PRESAT11(ch) 9835479 d20 pl20:ch \n\
(p20 ph20^):ch \n\
lo to 9835479 times l20
#define PRESAT22(ch) 98354729 d19 pl19:ch \n\
(p19 ph19^):ch \n\
lo to 98354729 times l19
#define presatPH ph19= 0 \n ph20= 0
```

DFS generator AU program

```
/*************************************************************/
/*     dfs.jt              16.11.2011                        */
/*************************************************************/
/*     Short Description :                                   */
/*     Program to calculate shape file for double frequency  */
/*     sweep and subsequent data-acquisition                 */
/*************************************************************/
/*     Keywords :                                            */
/*     adiabatic sweep, shaped pulse, MQMAS                  */
/*************************************************************/
/*     Description/Usage:                                    */
/*     This program runs with xaua from within poptau or     */
/*     paropt etc.                                           */
/*     This means it can be used to optimise the parameters  */
/*     for the sweep in an automatic way.                    */
/*     Do ased first to make sure that the parameters listed */
/*     below are set appropriately:                          */
/*                                                           */
/*     p2 : duration of the sweep                            */
/*     sp1 : power level of the sweep                        */
/*     spnam1 : DFSjt is always used as default name         */
/*     cnst1 : (in kHz) Startfrequency of the sweep          */
/*     cnst2 : (in kHz) Endfrequency of the sweep            */
/*     cnst3 : (in ns) currently used to define the timing   */
/*           resolution of the sweep                         */
/*     Make sure that a customer-made pulse program uses     */
/*     these parameters for the same purpose!                */
/*     The file which is created contains a comment line like:     */
/*     ##USAGE= Frequency sweep of 100 kHz in 100 usec             */
/*     to be able to remember what sweep had been used             */
/*     This AU program is suitable to be used with the       */
/*     following library pulse programs:                     */
/*     dfs90sel :   sweep followed by 90 degree sel. pulse   */
/*************************************************************/
/*     Author(s) :                                           */
/*     Name         : Stefan Steuernagel                     */
/*     Organisation : Bruker Analytik                        */
/*     Email        : stefan.steuernagel@bruker.de           */
/*************************************************************/
/*     Name         Date   Modification:                     */
/*     ste          000817 created                           */
/*     ste          031128 changed to allow sweep of  */
/*                         fractions of rotor periods */
/*                         by setting l0 = 1, 2, or 4 */
/*                         blank character included for     */
/*                         npoints in parameter part  */
/*     jt           111116  modification to match JT syntax */
/*************************************************************/
/*
$Id: zg_dfs,v 1.4 2003/12/03 10:05:07 es Exp $
*/

FILE *fwave;
char outfile[256],outputfile[256],filename[256];
```

```
double PI=3.14159265359;
double amplitude, t, Startfreq, Endfreq;
float Anfang, Ende;
float phase=0;
int npoints;

GETCURDATA

/* read parameters for sweep calculation from acqu-file     */
/* and store filename for shaped pulse               */

(void)strcpy(outfile,"DFSjt");
STOREPAR("SPNAM1",outfile);

// pulse length in us
FETCHPAR("P 2",&f1);
//printf("p2=%f",f1);

/* used for timing resolution of sweep in ns*/
/* must not be less than 50 ns */
FETCHPAR("CNST 3",&f2);

/* get start- and end-frequencies in kHz*/
FETCHPAR("CNST 1",&Anfang);
FETCHPAR("CNST 2",&Ende);
Startfreq=(double)Anfang;
Endfreq=(double)Ende;

/* calculate number points in the file */
npoints=round(f1/(f2*1e-3));
f2=f1/npoints*1000;

/* open outputfile for shaped pulse                  */
(void)sprintf(outputfile,"%s%s",getstan(0,"lists/wave/user/"),outfile);
if ((fwave=fopen(outputfile, "w+")) == NULL ) {
       Perror(DEF_ERR_OPT,outfile);
       ABORT;
       }

/* store amplitude values in shaped pulse file       */

fprintf(fwave,"##TITLE= %s\n",outputfile);
fprintf(fwave,"##USAGE= Frequency sweep from %4.1f kHz to %4.1f kHz in %4.1f usec
with resolution %4.1f ns\n",Startfreq,Endfreq,f1,f2);
fprintf(fwave,"##JCAMP-DX= 5.00 $$ Bruker JCAMP library\n");
fprintf(fwave,"##DATA TYPE= Shape Data\n");
fprintf(fwave,"##ORIGIN= Bruker BioSpin GmbH\n");
fprintf(fwave,"##DATE= 00/01/20\n");
fprintf(fwave,"##TIME= 08:15:00\n");
fprintf(fwave,"##MINX= -1.000000e+02\n");
fprintf(fwave,"##MAXX= 1.000000e+02\n");
fprintf(fwave,"##MINY= 0.000000e+00\n");
fprintf(fwave,"##MAXY= 0.000000e+00\n");
fprintf(fwave,"##$SHAPE_EXMODE= None\n");
fprintf(fwave,"##$SHAPE_TOTROT= 0.000000e+00\n");
fprintf(fwave,"##$SHAPE_BWFAC= 0.000000e+00\n");
fprintf(fwave,"##$SHAPE_INTEGFAC= 7.460936e-01\n");
fprintf(fwave,"##$SHAPE_MODE= 1\n");
fprintf(fwave,"##NPOINTS= %d\n",npoints);
fprintf(fwave,"##XYPOINTS= (XY..YX)\n");
TIMES(npoints)
       t=(loopcount1*f1*1e-6)/npoints;
       d1=2*PI*Startfreq*1000*t;
       d2=(2*PI*((Startfreq*1000)-(Endfreq*1000))*t*t)/(2*f1*1e-6*(npoints-
1)/npoints);
       amplitude=cos( d1 - d2 );
       if (amplitude<0) {
              amplitude*=-1;
```

```
            phase=180.0;
      } else { phase=0.0;}
      fprintf(fwave,"%3.6f, %3.6f\n",amplitude*100,phase);
END
fprintf(fwave,"##END\n");
fclose(fwave);
(void) sprintf(text,"parameters and waveform file stored!");
Show_status(text);

QUIT
```

SFAM generator AU program

```
/*************************************************************
parameters:
cnst0: max offset
cnst31: approximate spinning speed (rounded to match shape requirements)
cnst3:       resolution
l3: n=1 or 2
*************************************************************/
FILE *fwave;
char outfile[256],outputfile[256],filename[256];
double PI=3.14159265359;
int points=0;
int ph=0;
int n=1;
float off,spin,step;
float plength;
int n50,n350,max;
/*********
CNST:  float
L      int1
********/

GETCURDATA
FETCHPAR("CNST 30",&off);
FETCHPAR("CNST 31",&spin);
FETCHPAR("L 3",&n);
FETCHPAR("CNST 3",&step);

// interval must be at least 350ns
// interval must be a multiple of 50ns
// pulse length must be a multiple of interval
// thus pulse length must be a multiple of 50ns

//calculate plength depending on spinning speed
plength=1e9/spin;
// we want to split plength in at least 20 steps
max=(int) (plength/20/50+0.5);

n50=(int) (plength/50.0+0.5);
//
printf("plengthini=%f,n50i=%f,rn50=%d,plength=%f\n",plength,plength/50.,n50,n50*50.
);
// find closed n50 that is multiple of at least 7 (so that step=n350*50>=350)
n50=findclosest(n50,max);
// plength is now a multiple of 50ns
plength=n50*50;
// step is a multiple of 50ns and is greater or equal than 350ns
n350=mult(n50,max);
step=n350*50;
// number of points is plength/step=n50/350
points=n50/n350;

//recalculate the spinning speed after rounded plength :
spin=1e9/plength;
```

```
// printf("\npulse de %fns decoupe en %d intervales de
%fns\n",plength,points,step);

//store back possibly modified spinning speed and step
STOREPAR("CNST 31",spin);
STOREPAR("CNST 3",step);

/* read parameters for sweep calculation from acqu-file     */
/* and store filename for shaped pulse               */

(void)strcpy(outfile,"sfam2");
STOREPAR("SPNAM5",outfile);

/* open outputfile for shaped pulse                  */
(void)sprintf(outputfile,"%s%s",getstan(0,"lists/wave/"),outfile);
if ((fwave=fopen(outputfile, "w+")) == NULL ) {
       Perror(DEF_ERR_OPT,outfile);
       ABORT;
       }

/* store amplitude values in shaped pulse file       */

fprintf(fwave,"##TITLE= %s\n",outputfile);
fprintf(fwave,"##USAGE=SFAM\n");
fprintf(fwave,"##CNST31=%f\n",spin);
fprintf(fwave,"##CNST30=%f\n",off);
fprintf(fwave,"##CNST3=%f\n",step);
fprintf(fwave,"##L3=%d\n",n);
fprintf(fwave,"##JCAMP-DX= 5.00 $$ Bruker JCAMP library\n");
fprintf(fwave,"##DATA TYPE= Shape Data\n");
fprintf(fwave,"##ORIGIN= Bruker BioSpin GmbH\n");
fprintf(fwave,"##DATE= 00/01/20\n");
fprintf(fwave,"##TIME= 08:15:00\n");
fprintf(fwave,"##MINX= -1.000000e+02\n");
fprintf(fwave,"##MAXX= 1.000000e+02\n");
fprintf(fwave,"##MINY= 0.000000e+00\n");
fprintf(fwave,"##MAXY= 0.000000e+00\n");
fprintf(fwave,"##$SHAPE_EXMODE= None\n");
fprintf(fwave,"##$SHAPE_TOTROT= 0.000000e+00\n");
fprintf(fwave,"##$SHAPE_BWFAC= 0.000000e+00\n");
fprintf(fwave,"##$SHAPE_INTEGFAC= 7.460936e-01\n");
fprintf(fwave,"##$SHAPE_MODE= 1\n");
fprintf(fwave,"##NPOINTS= %d\n",points);
fprintf(fwave,"##XYPOINTS= (XY..YX)\n");

int i;
double amp1,ph1,z;
for (i=0;i<points;i++){
       amp1=sin(n*(i*1.0)/((points)*1.0)*2*PI)*100;
       ph1=sin(n*(i*1.0)/((points)*1.0)*2*PI)*off/(n*spin)*360/2/PI;
       if (amp1<0) { amp1=-amp1;ph1=ph1+180;}
       fprintf(fwave,"%12.6f, %12.6f\n",amp1,ph1);
}
fprintf(fwave,"##END\n");
fclose(fwave);

(void) sprintf(text,"%s file stored!offset=%3.6f spin=%3.6f points=%i
step=%f",outfile,off,spin,points,step);
Show_status(text);
sleep(1);


/* start acquisition */
QUIT

// function that returns the first multiple of n50 greater or equal than 7
// but lower than max
```

```
int mult(int n50,int max) {
int i=7;
while ((n50%i)!=0) { i++;if (i>max) {i=0;break;}}
// printf("pour n50=%d n350=%d",n50,i);
return i;
}

int findclosest(int n50,int max) {
int i,j;
 for (i=0; i<n50 ; i++) {
  for (j=-1;j<=1;j+=2) {
//     printf("fc : n50=%d j=%d,i=%d\n",n50+j*i,j,i);
     if (mult(n50+j*i,max)!=0) {return n50+j*i;}
   }
 }
}
```

Abstract

My PhD thesis focuses on the development of the through-bond and through-space correlation solid state NMR experiments involving half-integer quadrupolar nuclei in order to characterize chemical structure of inorganic material at atomic level. This thesis consists of two part.

First, we introduce two-dimensional (2D) ^{71}Ga-^{77}Se through-bond and through-space heteronuclear correlation (HETCOR) experiments. Such correlations are achieved using (i) the *J*-mediated Refocused Insensitive Nuclei Enhanced by Polarization Transfer (*J*-RINEPT) method with ^{71}Ga excitation and ^{77}Se Carr-Purcell-Meiboon-Gill (CPMG) detection, as well as (ii) the *J*- or dipolar-mediated Heteronuclear Multiple-Quantum Correlation (*J*- or *D*-HMQC) schemes with ^{71}Ga excitation and quadrupolar CPMG (QCPMG) detection. These methods are applied to the crystalline β-Ga_2Se_3 and the $0.2Ga_2Se_3$-$0.8GeSe_2$ glass. We also report 2D ^{71}Ga Satellite Transition Magic-Angle Spinning (STMAS) spectrum of β-Ga_2Se_3 using QCPMG detection at high magnetic field, high Magic-Angle Spinning frequency, and high rf-field.

Second, we introduce novel sequences using indirect detection to correlate quadrupolar nuclei and spin-1/2 isotopes, other than ^{1}H and ^{19}F. These sequences use γ-encoded symmetry-based RN_n^v schemes that reintroduce the space component $|m| = 1$ of the heteronuclear dipolar coupling. These schemes can be applied to the indirectly detected spin in Dipolar-mediated Heteronuclear Multiple-Quantum Correlation (*D*-HMQC) sequence or to the detected isotope in a novel sequence, named Dipolar-mediated Heteronuclear Universal-Quantum Correlation (*D*-HUQC). The performance of the sequences have been compared to conventional *D*-HMQC with R^3 and SFAM recoupling via SIMPSON simulations and NMR experiments, including ^{13}C-{^{15}N} heteronuclear correlation on glycine and ^{31}P-^{27}Al ones on VPI-5 and $Na_7(AlP_2O_7)_4PO_4$.